The Heating of the Solar Corona by Kink Instabilities

A thesis submitted to The University of Manchester for the degree of
Doctor of Philosophy
in the Faculty of Engineering and Physical Sciences

2012

Michael Bareford
School of Physics and Astronomy

Contents

The University of Manchester

ABSTRACT OF THESIS submitted by Michael Bareford
for the Degree of Doctor of Philosophy and entitled
The Heating of the Solar Corona by Kink Instabilities. January 2012

The million-degree temperature of the solar corona might be due to the combined effect of barely distinguishable energy releases, called nanoflares, that occur throughout the solar atmosphere. Unfortunately, the high density of nanoflares, implied by this hypothesis, means that conclusive verification is beyond present observational capabilities. Nevertheless, it might be possible to investigate the plausibility of nanoflare heating by constructing a magnetohydrodynamic (MHD) model; one that can derive the energy of nanoflares, based on the assumption that the ideal kink instability of a twisted coronal loop triggers a relaxation to a minimum energy state. The energy release depends on the current profile at the time when the ideal kink instability threshold is crossed. Subsequent to instability onset, fast magnetic reconnection ensues in the non-linear phase. As the flare erupts and declines, the field transitions to a lower energy level, which can be modelled as a helicity-conserving relaxation to a linear force-free state. The aim of this thesis is to determine the implications of such a scheme with respect to coronal heating.

Initially, the results of a linear stability analysis for loops that have net current are presented. There exists substantial variation in the radial magnetic twist profiles for the loop states along the instability threshold. These results suggest that instability cannot be predicted by any simple twist-derived property reaching a critical value. The model is applied such that the loop undergoes repeated episodes of instability followed by energy-releasing relaxation. Photospheric driving is simulated as an entirely random process. Hence, an energy distribution of the nanoflares produced is collated. These results are discussed and unrealistic features of the model are highlighted. Subsequently,

confirmation of the plasma relaxation process is sought from a numerical analysis.

A sample of marginally unstable and current-neutralised coronal loops are simulated within a non-linear three-dimensional MHD code. Loops that carry zero net current are preferred since the photospheric motions that twist the loop and thereby create azimuthal field are spatially localised; outside the loop boundary the field is purely axial. The results of these simulations show the dynamics of the relaxation process. A new localised relaxation model is developed which fits the simulation data.

The revised relaxation model is combined with a linear stability analysis such that nanoflare energy distributions can be produced from ensembles of loops driven by random photospheric twisting motions. Different loop aspect lengths are considered, as well as the spatial correlation of the twisting motions and the level of radial expansion that may accompany loop relaxation. The range of active-region heat fluxes extracted from all the different scenarios is $0.09\text{–}1 \times 10^7\,\mathrm{erg\,cm^{-2}\,s^{-1}}$. When the relaxation radius is increased, the flux approaches $10^7\,\mathrm{erg\,cm^{-2}\,s^{-1}}$, regardless of the aspect ratio and of the randomness of the path to instability — this is sufficient for coronal heating. The distribution of energies has a Gaussian form when the twisting motions are correlated across the loop radius. Uncorrelated motions yield power-law distributions with gradients of approximately -2.

Declaration

I declare that no portion of the work referred to in the thesis has been submitted in support of an application for another degree or qualification of this or any other university or other institute of learning.

Copyright Statement

(i) The author of this thesis (including any appendices and/or schedules to this thesis) owns certain copyright or related rights in it (the “Copyright”) and s/he has given The University of Manchester certain rights to use such Copyright, including for administrative purposes.

(ii) Copies of this thesis, either in full or in extracts and whether in hard or electronic copy, may be made **only** in accordance with the Copyright, Designs and Patents Act 1988 (as amended) and regulations issued under it or, where appropriate, in accordance with licensing agreements which the University has from time to time. This page must form part of any such copies made.

(iii) The ownership of certain Copyright, patents, designs, trade marks and other intellectual property (the “Intellectual Property”) and any reproductions of copyright works in the thesis, for example graphs and tables (“Reproductions”), which may be described in this thesis, may not be owned by the author and may be owned by third parties. Such Intellectual Property and Reproductions cannot and must not be made available for use without the prior written permission of the owner(s) of the relevant Intellectual Property and/or Reproductions.

(iv) Further information on the conditions under which disclosure, publication and commercialisation of this thesis, the Copyright and any Intellectual Property and/or Reproductions described in it may take place is available in the University IP Policy (see `http://www.campus.manchester.ac.uk/medialibrary/policies/intellectual-property.pdf`), in any relevant Thesis restriction declarations deposited in the University Library, The University Library’s regulations (see `http://www.manchester.ac.uk/library/aboutus/regulations`) and in The University’s policy on presentation of Theses.

Remember that all models are wrong; the practical question is
how wrong do they have to be to not be useful.

George E. P. Box and Norman R. Draper, **Empirical Model-Building and Response Surfaces** (1987)

During the height of the late 1870s' discussion of sunspots and climate connections,
Schuster had reported that the years of good wine vintage in western Europe occurred
in intervals of approximately eleven years. Whether this was a real connection or
some undergraduate devilment remains unknown.

Stuart Clark, **The Sun Kings** (2007)

Dedication

To Vivien and Christopher.

To Sarah.

Acknowledgements

First, I would like to thank my supervisor, Philippa Browning, for her enthusiastic support throughout my three years and one month at the Jodrell Bank Centre for Astrophysics.

I am also thankful to Ronald Van der Linden for his assistance with using the linear stability code; thanks also to Alan Hood and Mykola Gordovskyy for their support regarding the numerical analysis.

Codes cannot run without computers; so thank you to Anthony Holloway and Bob Dickson for helping me to use the COMA cluster, which was required for the linear stability analysis. And thank you to Herbert Früchtl for getting me started on the new St. Andrews MHD cluster — this hardware was used to run three-dimensional magnetohydrodynamic simulations.

Finally, thank you to Matthew Penny for proofreading the introductory chapters.

The Author

Michael Bareford graduated from the University of Manchester with a first class degree in Physics with Astrophysics (B.Sc) in 2008. He then began a PhD, under the supervision of Professor Philippa Browning, concerning the importance of magnetic field instability with regard to coronal heating.

Supporting Publications

1. The Flux-energy Distributions Generated by Kink-unstable Ensembles of Zero-net-current Coronal Loops

M. R. Bareford, P. K. Browning and R. A. M. Van der Linden, Sol. Phys., 273, 93 (2011).

2. A Nanoflare Distribution Generated by Repeated Relaxations Triggered by Kink Instability

M. R. Bareford, P. K. Browning and R. A. M. Van der Linden, A&A, 521, A70 (2010).

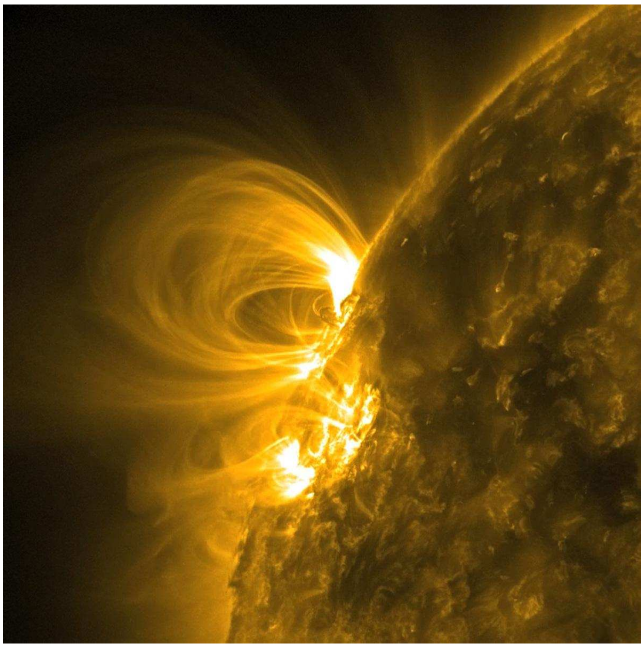

Figure 1: A snapshot of the magnetic field structure above an active region on the north-eastern solar limb. Courtesy of the Solar Dynamics Observatory (SDO) and the Atmospheric Imaging Assembly (AIA) consortium, NASA.

1

Introduction

This thesis is concerned with the importance of magnetic field instability with respect to the dramatic temperature inversion that occurs in the atmosphere of the Sun. The introduction begins with a basic description of the Sun, preparatory to a discussion of the solar magnetic field: the likely means by which it is created and how it is manifested above the solar surface. Next, the problem of coronal heating is more formally introduced together with an outline of the different classes of heating theory.

Subsequent chapters will describe the theoretical foundation on which a model, used to investigate the dissipation of magnetic energy within the corona, will rest (see abstract for further details). The purpose of this model is to simulate the consequences of the magnetic kink instability for coronal heating. The results (e.g., heating-event distributions) are mainly derived from linear analyses, however numerical studies are performed for specific field configurations; one of the aims of this work is to discover if the assumptions implicit in the linear analysis are justified.

1.1 The Turbulent Sun

At the most basic level the Sun is a massive ball of plasma that increases in density towards its centre. The plasma ions are mainly hydrogen (~90%) and helium (~10%); heavier elements make up less than 1% of the solar mass (Priest 1987). The

Sun is powered by nuclear fusion, which, together with the known solar luminosity ($L_\odot = 3.8 \times 10^{33}$ erg), implies a core temperature of around 15 MK. High-energy photons, produced by the fusion of hydrogen nuclei in the core, are randomly absorbed and emitted by ions in the radiative zone (Figure 1.1). The temperature of the solar interior must fall with radius: it declines from 7 to 2 MK across the radiative zone (Christensen-Dalsgaard et al. 1996). Helioseismology data is routinely used to infer the conditions inside the Sun, which can then be checked against the predictions of solar models (Mullan 2010). Hence, the temperature profile is known with some certainty. At around two thirds of the solar radius, the temperature is low enough for photons to be absorbed but not re-emitted; convection becomes the main mode of energy transport. This boundary is also known as the tachocline: the uniform rotation of the radiative zone gives way to the differential rotation of the convective layer (Kosovichev et al. 1997). The shearing produced by the faster moving equatorial flows creates a ring current, which, through Ampères law, generates a global dipole magnetic field. Furthermore, the presence of a magnetic field will promote further separation of opposite charges and the fields carried by these secondary currents will modify the dipole field.

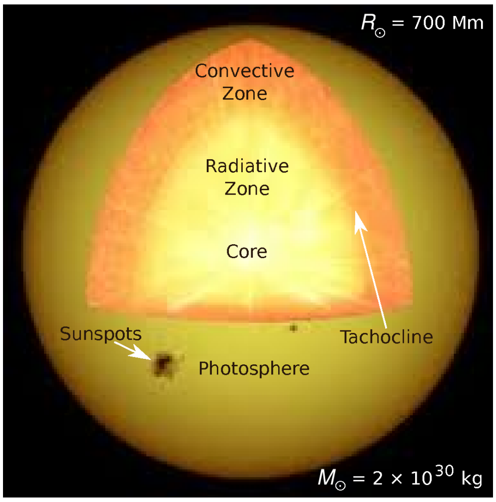

Figure 1.1: A cartoon of the solar interior. Approximate values for the solar radius ($R_\odot$) and mass ($M_\odot$) are also given. On this scale, the Earth is the size of the dot over the letter i. Courtesy of Hathaway, D. H., NASA.

The quasi-random and self-reinforcing behaviour of the *solar dynamo* are thought to produce the solar magnetic cycle (Kippenhahn 1994).

Interior ring currents generate magnetic fields that can force an expansion of a magnetic flux tube (Bellan 2006), until pressure balance is achieved with the thermal pressure of the surrounding plasma. Therefore, the density within such a region of magnetic field is lower than the external density. As a result of this buoyancy, flux tubes can rise through the convective zone and break through the solar surface.

The photosphere is the *surface* of the Sun; it is simply the region over which the Sun becomes transparent to optical radiation. This region has a thickness that is one thousandth of the solar radius and has an average temperature of 5800 K (Aschwanden 2009). The photosphere exhibits a continuously changing pattern of granulation. The granules shown in Figure 1.2 are convection cells. These bodies of plasma are thousands of kilometres across, but their lifetimes are short (between five and ten minutes). The darker cell boundaries mark the sinking of cooler gas beneath the photosphere. Magnetic fields that have risen above the surface represent the most buoyant part of a magnetic flux tube; one that was created near the tachocline or higher up in the convective zone. Such a field will intersect the photosphere at two separate regions (of

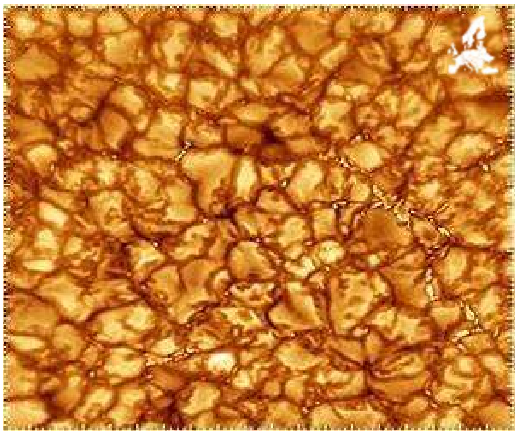

Figure 1.2: Convective granulation on the solar surface. An outline of the European continent is shown for scale in the top right corner — the entire image is roughly 20 Mm across. Courtesy of the Big Bear Solar Observatory, New Jersey Institute of Technology.

opposite polarity), which are buffeted by the turbulence of rising and falling plasma. These regions are called footpoints when the fields in question reach as high as the corona.

Magnetic structures permeate the corona and act as conduits for the transmission of energy to the solar atmosphere: the source is the kinetic energy of convective motions occurring at the footpoints. Understanding the details of this interaction between magnetism and photospheric turbulence could explain why upper atmospheric temperatures are so much hotter than those observed at the surface (coronal temperatures are typically measured to be in the 1–6 MK range).

1.2 The Solar Corona

The corona is a diffuse magnetised plasma that surrounds the Sun. Although it is somewhat inhomogeneous, it can be divided into those parts that feature open magnetic field lines, namely coronal holes[1], and those that contain closed fields as illustrated by coronal loops (Figures 1,1.3). Coronal holes are mainly found over the solar poles Golub and Pasachoff (1997); here plasma is extremely rarefied, since it is efficiently transported along the field, away from the Sun. The parts of the corona featuring

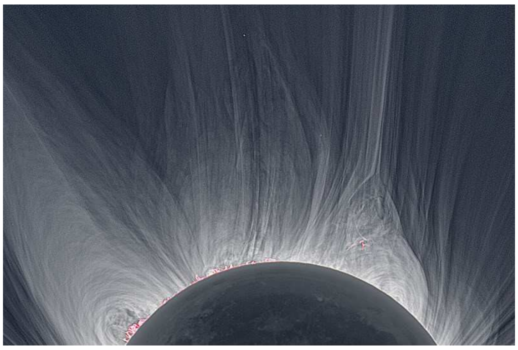

Figure 1.3: The solar eclipse of 2008 revealed magnetic fields of open and closed shape. ©2008 Miloslav Druckmüller, Martin Dietzel, Peter Aniol, Vojtech Rušin

---

[1] The field lines associated with coronal holes are assumed to close on scales appropriate to the heliosphere (~15 Million Mm).

closed magnetic fields occur above two types of photospheric region, active and quiet Sun. Active regions contain intense and non-uniform magnetic fields ($\langle B \rangle \approx 100$–$300\,\mathrm{G}$ and $B_{\mathrm{max}} \approx 2000$–$3000\,\mathrm{G}$, Aschwanden 2009), which are closed on scales of between 10 Mm and 100 Mm. These regions appear as sunspot groups and are typically found within a 40° band either side of the solar equator, and are most numerous during solar maxima. At this stage in the magnetic cycle, the quiet Sun still covers the majority of the solar surface. Compared to active regions, quiet-Sun magnetic fields *appear*[2] to be weaker, by at least an order of magnitude. Nevertheless, many dynamic and energetic events occur over the quiet Sun, such as microflares (Aschwanden et al. 2000a) and mini-coronal mass ejections (Innes et al. 2009).

Historically, direct study of the corona has required some ingenuity. Light from the solar atmosphere is emitted via Thomson scattering of photospheric light, however, since the corona is diffuse ($n \approx 10^{15}\,\mathrm{m}^{-3}$), coronal light is easily outshone by that arriving direct from the solar surface. These problems were mitigated by the development of coronagraphs (an occulting device combined with a spectroheliograph), which permitted the corona to be observed at specific frequencies (Grotian 1939), including ultraviolet (UV) when observing from the Pyrenees (Lyot 1939). Shortly afterwards, Edlén (1943) confirmed that the hitherto unidentified UV emission lines were in fact emitted by highly-ionised iron atoms. This finding revealed the high coronal temperature compared to the photosphere. Decades later, observations from instruments on board spacecraft — starting with Skylab (NASA) and latterly, Solar and Heliospheric Observatory (SOHO), Transition Region and Coronal Explorer (TRACE), Solar Dynamics Observatory (SDO) — showed that the corona is much brighter than the photosphere in the extreme ultraviolet (EUV) and X-ray parts of the spectrum. EUV radiation corresponds to temperatures in the range 0.15 to 1.5 MK (Figure 1.4). Coronal radiation is primarily bremsstrahlung and magneto-bremsstrahlung emission. Elec-

---

[2] The latest observational evidence indicates that the disorganisation of quiet Sun fields makes it harder to resolve the magnetic fields and therefore field strengths are underestimated (Sánchez Almeida and Martínez González 2011).

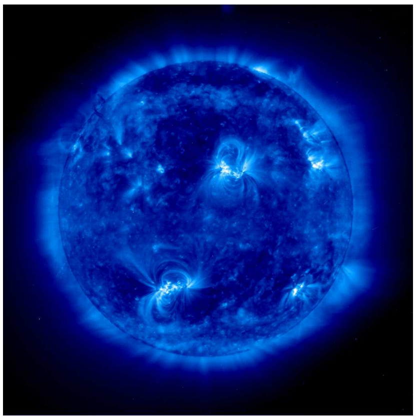

Figure 1.4: The Sun in EUV. The emission shown here is from the resonance lines of eight and nine times ionized iron (Fe IX,X). Courtesy of SOHO and the EUV Imaging Telescope (EIT), ESA & NASA.

trons are decelerated and deflected by the electric fields produced by ions and thereby lose kinetic energy through bremsstrahlung emission. In a magnetised plasma, charged particles gyrate around the field lines and this gives rise to magneto-bremsstrahlung or gyro-emission. This type of emission may be absorbed by other particles that subsequently gyrate at the next harmonic frequency — this is called gyro-resonance. Also, the corona is optically thin and so, the emission measure (the amount of plasma that is emitting radiation) is proportional to the density squared integrated along the line of sight. The density at different temperature regions of the corona can be estimated using different spectral lines. Other properties of the solar atmosphere can be inferred by matching the synthetic emission calculated by atmospheric models with emission levels that have actually been observed. Selhorst et al. (2008) have developed a 3D solar atmospheric model that reproduces brightness temperatures at radio frequencies. This model incorprates bremsstrahlung and gyro-resonance — the magnetic field is extrapolated from surface magnetograms taken by the MDI instrument onboard SOHO. The results, presented in Figure 1.5, agree qualitatively with those produced by models that have been matched against different parts of the radiation spectrum (Aschwanden 2009).

Figure 1.5 illustrates the magnitude of the coronal heating problem. The sudden

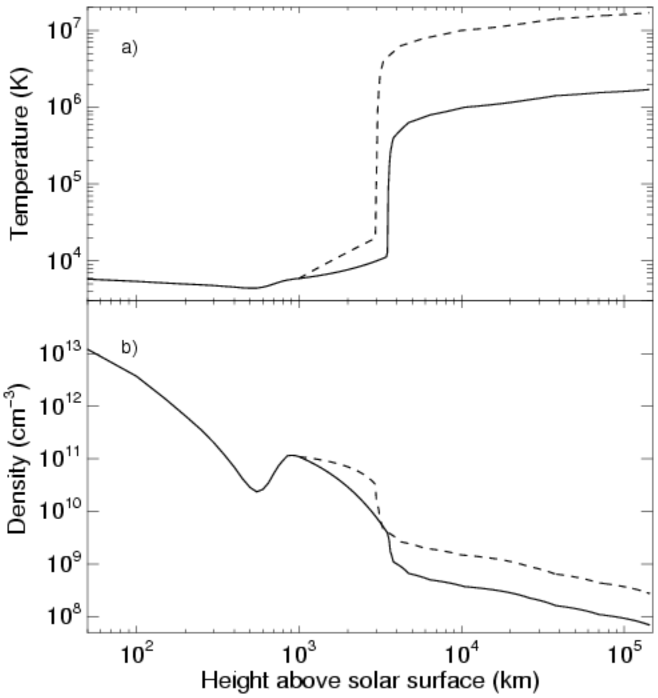

Figure 1.5: Comparison between the quiet-Sun atmosphere (solid line) and active-region atmosphere (dashed line) for (a) temperature and (b) particle density. Courtesy of Selhorst et al. (2008).

change in temperature (coincident with a drop in density) marks the beginning of the corona; farther out, at 1 AU, the temperature drops to 10^5 K. In addition, the chromosphere — a 2000 km-thick atmospheric layer immediately above the surface — is also hotter than expected. The reduction in density means that any heat input at coronal heights has a more drastic effect, and perhaps explains why the chromospheric heating problem is less pronounced than the coronal one. The steepest part of the temperature gradient is referred to as the Transition Region, which separates the chromosphere from the corona. Above this layer matter is fully ionised.

The differences in the quiet-Sun and active-region plots of Figure 1.5 hint at a far less orderly picture; in fact, the stratification implied by the use of the term *layer* should not be taken too seriously. For instance, the actual height of the coronal base ($\approx$ 2500 km) varies according to the strength of the solar magnetic field directly below. This magnetic variability also alters the electron density: $n_e \approx 10^{15}\ \mathrm{m}^{-3}$ above the quiet

Sun and 10^{17} m^{-3} above active regions. Surface conditions cease to have an impact in the upper corona (a height of 1 $R_\odot$), where $n_\mathrm{e} \approx 10^{12}$ m^{-3}.

All strategies for answering the coronal heating problem have so far been based on the idea that non-thermal forms of energy (i.e., magnetism) are somehow expressed as heat in the corona. The magnetic fields that fill this region are rooted at the photosphere, since the density there is much higher. Convective motions may disturb a field to such an extent that an instability is initiated (or equilibrium is lost) and a spatially-confined explosion (a solar flare) heats the surrounding atmosphere. Alternatively, convective motions might act as sources of waves that, guided by magnetic fields, travel to the corona before releasing energy. These two ideas are examined in the sections that follow.

Clearly, this problem is a fundamental one; the physics responsible are continuously occurring throughout the corona and perhaps need to be uncovered before other solar phenomena can be fully understood. For example, the ability to predict Coronal Mass Ejections and thereby protect the power networks and satellites vitally important to our civilisation, may first require a solution to the problem of coronal heating.

1.3 Coronal Loops

The corona is dominated by a pervasive and dynamic magnetic field. Its presence is clear on large scales, such as during a solar eclipse (Figure 1.3), and on smaller scales. Closed arch-like fields are strikingly apparent when observing in EUV (Figure 1.6). Coronal loops come in a range of sizes, from 1 Mm bright points within inter-granular lanes to 1000 Mm trans-equatorial arches (Reale 2010). At coronal heights, the gas within loops is fully ionised and so interacts with the magnetic field. The ratio of thermal pressure to magnetic pressure,

$$\beta = \frac{P_\mathrm{th}}{P_\mathrm{m}} = \frac{2n_\mathrm{e}k_\mathrm{B}T_\mathrm{e}}{B^2/8\pi}, \tag{1.1}$$

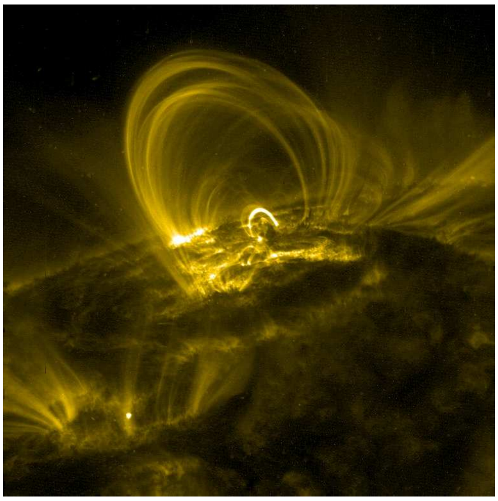

Figure 1.6: An arcade of coronal loops observed in EUV (171 Å). The loop apexes are aligned above the magnetic polarity inversion line that divides the active region. The largest loops have a height of ≈ 200Mm. Courtesy of TRACE, Stanford-Lockheed Institute for Space Research, NASA.

is much lower than unity in the corona, this means the plasma is constrained to follow the magnetic field. The bright regions of Figure 1.6 indicate higher electron density: the higher the density, the brighter the bremsstrahlung emission. The magnetic field implied by the positions of coronal loops is usually different to the field extrapolated from surface magnetograms (Feng et al. 2007; Sandman et al. 2009). This is especially true for field extrapolations that assume a linear force-free environment; i.e., the currents are parallel to the field and a single value suffices for the ratio of current density and magnetic field strength. In fact, more complex fields are likely to exist below the Transition Region[3], where $\beta > 1$, which would explain why actual coronal loops are more curved and non-planar when compared to the extrapolated field lines. A further difference is the fact that the cross-sectional areas of loops vary little with height. Klimchuk (2000) studied a collection of soft X-ray loops observed by the Yohkoh spacecraft and found that loop width increased by just 30% between the (chromospheric) footpoint and apex; also, these modest increases in width were evenly distributed along

---

[3] The Transition Region can be defined as the height where the enthalpy flux changes from cooling the plasma to heating the plasma (Bradshaw and Cargill 2010).

the loop length. Potential field lines should expand within the low-density corona, so coronal loops have to be non-potential and the currents associated with these twisted fields would oppose expansion. The radius of the loop is determined when the inward tension force, created by the azimuthal field, ($F_{\rm t} \propto B_\theta^2/R$) is balanced by the axial field pressure ($F_{\rm p} \propto B_z^2/R$). The axial and the twist-related azimuthal components have the following relationship,

$$\frac{B_\theta}{B_z} = R\left(\frac{d\phi}{dz}\right), \qquad (1.2)$$

where $d\phi/dz$ is the angular rotation of the magnetic field per unit axial length. Klimchuk et al. (2000) used this expression to show that the ratio of $F_{\rm t}$ to $F_{\rm p}$ scales as R^2; hence, wider loops undergo greater constriction. Alas, the level of constriction actually observed implies twists that approach the theoretical limit for kink instability (Section 2.2). Interestingly, circular cross sections are achieved for twists less than 2π (Klimchuk et al. 2000); the majority of coronal loops appear to have this property. DeForest (2007) argues that the constant width is a consequence of indequate instrument resolution: any expansion will not be seen if the apex width is comparable to the point-spread function of the telescope. It is also possible that line-of-sight effects (such as loop overlap) confound width measurements. However, other workers have asserted strongly that the constancy of loop diameters is real (López Fuentes et al. 2008). If this is the case, perhaps coronal loops are actually by-products of magnetic reconnection, namely separators (Plowman et al. 2009), see Section 2.3.3. It should not be forgotten that the *observed* coronal loops are those loops (or strands within loops) that have been heated, otherwise these structures would not stand out against the coronal background. Above an active region, there might be many *invisible* coronal loops, i.e., magnetic curvilinear structures that expand as expected with height, but are in the process of reaching some threshold that enables then to be heated and so, for the time being, these loops are not observable.

The optically thin nature of the corona means that loop observations are fraught with difficulties; this is particularly true if one wishes to discern the temperature structure within loops. For instance, if a loop is multi-thermal, the measured temperature will be a complicated average along the line-of-sight, which is weighted for the (highly non-linear) instrument response. Invariably, there will also be other structures that intersect the line-of-sight, adding noise to the observation. Somewhat perplexingly, workers have claimed to observe multi-thermal (Patsourakos and Klimchuk 2007) and iso-thermal (Noglik et al. 2008) structure over the same temperature ranges (1–3 MK). It is not known if hot loops cool and are then observed as warm loops (1–2 MK), or if warm loops are simply a consequence of a lower than average heating input (Reale 2010). Observations of high temperature loops (> 2 MK) seem to have been most successful in detecting multi-thermal structure (Schmelz et al. 2005; Reale et al. 2007). Such work strongly suggests that hot loops are multi-stranded, where each strand is a filament of heated plasma that runs the entire length of the loop. A typical loop of diameter 2 Mm is therefore a bundle of several hundred strands and at any instant most of the strands are cooling but some are being heated. Many workers have considered the possibility that these strands are brought into existence by nanoflares, see Section 1.4.2. Ordinarily, flares are so energetic that the magnetic structure of the surrounding medium is significantly altered. However, flares of much lower energy might leave the loop intact — the loop is heated but regains equilibrium. The energy of a nanoflare is relative to the magnetic field strength of the coronal loop (10^{24} erg for a loop of 10 G or 10^{26} erg for a 1 kG loop).

Although some coronal loops exhibit transient phenomena such as flares, most remain stable beyond the plasma cooling time and can exist for hours. There is substantial evidence for a correlation between loop transience and temperature: high temperature loops appear steady with a low level of fluctuation (Warren et al. 2010), but cooler loops appear to be highly transient (Kopp et al. 1985; Di Giorgio et al. 2003). Loop equilibrium is of course closely related to loop heating, which is best explained by describing the life-cycle of a loop. Some form of heating (e.g., nanoflaring) is rapidly transmitted, via the magnetic field, to the whole loop. Shortly after, an evaporative phase occurs, whereby cooler chromospheric material is evaporated into the loop, increasing the plasma density. Subsequently, thermal conduction, again guided by the magnetic field, smooths out any differences in temperature and therefore restores stability. A hot steady loop can only exist if the heating time scale is shorter than the cooling time scale, so called steady heating. Alternatively, if the loop is composed of many heated/cooling strands then impulsive heating may have the same effect. It does not matter if the heating is episodic (i.e., the gap between heating events is comparable to the cooling time) because there will always be some strands that are heated and therefore emitting in the X-ray.

Identifying the heating mechanisms responsible for the observed loop variability will be crucial in determining which coronal heating theories are worth pursuing. Unfortunately, coronal loops are diverse and often appear crowded together. The technical challenges that these problems present, mean that observations are not yet sufficiently conclusive to constrain theory.

1.4 Coronal Heating

The corona loses energy by radiation, by conduction to the lower atmosphere and by mass loss (flowing outwards in the form of solar wind and/or flowing downwards into the chromosphere). The sizes of these different losses have been estimated by atmospheric models that have been constrained by EUV spectral line intensities and radio brightness temperatures. In a review of such work, Withbroe and Noyes (1977) presented values of $10^7\,\mathrm{erg\,cm^{-2}\,s^{-1}}$ for active regions and $3\times10^5\,\mathrm{erg\,cm^{-2}\,s^{-1}}$ for the quiet Sun. More recently, Aschwanden and Acton (2001) measured the soft X-ray emission from the entire corona (out to a radius of $2R_\odot$). Their estimates of the energy lost through radiation are $0.2-2\times10^6\,\mathrm{erg\,cm^{-2}\,s^{-1}}$ (active regions) and $0.1-2\times10^5\,\mathrm{erg\,cm^{-2}\,s^{-1}}$ (quiet Sun), which are in agreement with the radiative losses given by Withbroe and Noyes (1977, Table 1). These estimates show that active regions are responsible for at least 80% of the energy losses — the coronal heating problem is most severe above sunspot groups.

The explanation as to why the corona has multi-million degree temperatures may have several complications, some of which were hinted at in the previous section. It is quite possible that not all loops are heated in the same way: the heating of the quiet Sun and of active regions might be governed by different mechanisms. Furthermore, the diffuse (inter-loop) corona may be heated by yet another process; in fact very recent observations made using the SDO/AIA telescope have indicated that for active regions, most of the emission ($\gtrsim 65\%$) is from diffuse areas (Viall and Klimchuk 2011).

This thesis is concerned with how coronal loops are heated and in particular, it will explore theoretical ideas that are thought to be pertinent to active-region loops. It has been generally assumed (Klimchuk 2006) that convectively-driven flows of plasma in and below the photosphere are the source of the energy that heats the corona. The challenge therefore is to explain how flows of plasma lead to the unexpectedly high coronal temperatures. Clearly, the energy that drives the seething photosphere can be carried into the corona via any closed magnetic fields that reach the outer atmosphere. Disturbances at the surface can excite ions, which in turn disturb the local magnetic field. Thus, oscillations, involving plasma ions and the magnetic field, are established. These Alfvénic[4] waves can propagate along coronal loops, from footpoint to footpoint. The wave frequency is low compared to the ion-cyclotron frequency ($\omega_{\rm ic} = Bq_{\rm i} / m_{\rm i}$) and the wave velocity is given by $v_{\rm A} = B / \sqrt{\mu_0 \rho}$, which for a typical active-region coronal loop (e.g., $B = 100\,\rm G$, $n = 10^{15}\,\rm m^{-3}$, $L = 50\,\rm Mm$), gives an Alfvén time ($t_{\rm A}$) of 5–10 seconds. Broadly speaking, coronal-heating theories are divided by how $t_{\rm A}$ compares to the time scale associated with photospheric motions, $t_{\rm ph}$.

1.4.1 Wave Dissipation

Heating that occurs through wave dissipation ($t_{\rm ph} \approx t_{\rm A}$) is referred to as alternating-current (AC) heating. Turbulent convection excites a large and diverse flux of up-

---

[4] Alfvén waves involve a uniform magnetic field, whereas the corona clearly has an inhomogeneous magnetic field; hence, the term Alfvénic is used here.

wardly propagating waves. Some of these waves transmit acoustically, whereas other types also involve the magnetic field, such as magnetosonic waves (slow and fast) and Alfvénic waves. This last type also covers waves that transmit along entire magnetic structures, e.g., torsional, kink and sausage perturbations (Figure 2.2).

Wave fluxes have been calculated numerically and also inferred from observations. Narain and Ulmschneider (1996) reviewed the wave fluxes produced by a wide variety of solar convection models, as well as those derived from the velocity and brightness fluctuations of spectral lines. In general, the fluxes are in excess (sometimes considerably so) of $10^7\,\mathrm{erg\,cm^{-2}\,s^{-1}}$ — the heating flux required for active regions. However, not all of this flux may reach the corona since longitudinal waves cannot negotiate easily the temperature gradients present in the solar atmosphere.

Above the surface, the temperature goes down before it rises sharply within the transition region (Figure 1.5). The sound speed is proportional to $\sqrt{T}$; hence, longitudinal waves passing through the chromosphere may become shocked on reaching the temperature minimum. The height of the temperature minimum will of course fluctuate in time and in space, which may exacerbate the damping of acoustic and slow magnetosonic waves. Nevertheless, there have been many observations of slow-mode waves propagating to coronal heights of 1-2 $R_\odot$ (Nakariakov and Verwichte 2005), although the associated energy flux is far below that required for coronal heating (de Moortel 2009). In the transition region, an increasing temperature raises the sound speed and fast-mode waves travelling in a non-radial direction can be refracted downwards.

Alfvénic Waves

Refraction is less of a problem for Alfvénic waves, which, guided by the magnetic field, are able to penetrate the corona. In addition, their transverse nature means that shocks are avoided. The Alfvénic wave flux has been estimated from the turbulent velocities of network bright points (NBPs). These features appear within the intergranular lanes surrounding photospheric convection cells (Figure 1.2) and appear to be a good proxy for coronal loop footpoints (Falconer et al. 1998). Muller et al. (1994)

measured a NBP mean speed of 1.4 km s^{-1} for the quiet Sun, and calculated from this an energy flux greater (by an order an magnitude) than the quiet Sun heating requirement. This excess is greater still when one considers that the number of loop footpoints is underestimated by the NBP count: footpoints only become bright in response to converging granular flows.

It is possible that heating by Alfvénic waves is only applicable to quiet-Sun conditions. The periodicity of photospheric agitation (50 – 300 s) constrains the periods of the Alfvénic waves excited by this motion. Hence, the dissipation length mostly depends on the local Alfvén speed ($v_{\mathrm{A}} \propto B/n^{1/2}$). Parker (1991) argues that for low-density coronal holes, the dissipation lengths of Alfvénic waves are several multiples of the solar radius (5–10 $R_{\odot}$); i.e., too long to heat the corona. Minimal dissipation should also be associated with regions of high magnetic field. However, the presence of complex closed fields create the conditions for at least two types of wave resonance. Phase mixing can occur wherever there is a gradient in v_{A} across the wave front (this could be caused by a variation in plasma density). The opportunities for energy dissipation are greatly enhanced when adjoining sections of magnetic field carry oscillations that are out of phase (Heyvaerts and Priest 1983). In addition, any coherent magnetic field structure, such as a coronal loop, will resonate at particular frequencies; but if a loop has a variable density profile, $\rho(r)$, the resonance will be confined to those threads of magnetic field that have the right density. This process, known as resonant wave absorption (Klimchuk 2006), can lead to impulsive heating, since localised heating alters the density profile and as a consequence, threads at other locations are preferentially heated.

Alfvénic waves have been seen propagating along magnetically-confined jets of plasma that extend out into the chromosphere. These jets, otherwise known as spicules (Figure 1.7) have been likened to prairie grass being buffeted by strong winds. Recently, SDO has observed these features in unprecedented detail and in great profusion. McIntosh et al. (2011) have discovered that fast Alfvénic wave phenomena previously seen only in the chromosphere also reach the corona.

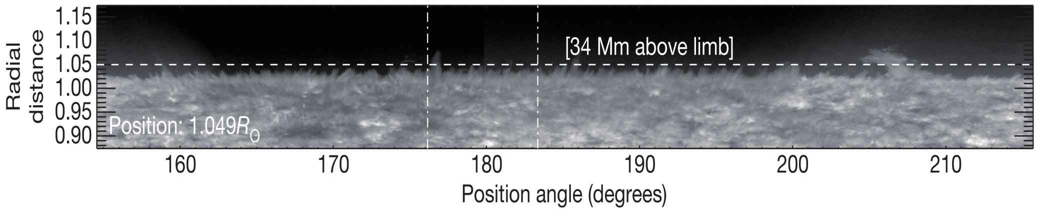

Figure 1.7: Spicules, imaged at 304 Å (He II), undergoing Alfvénic perturbations. Courtesy of McIntosh et al. (2011) and SDO/AIA, NASA.

Through the use of Monte-carlo simulations, McIntosh et al. have been able to determine the wave periods and speeds that best match observations. They were then able to estimate the energy fluxes for quiet Sun conditions and for coronal holes. Their results show that Alfvénic waves carried by spicules could, assuming that dissipation takes place, heat the corona above the aforementioned regions (although, the reasons why these waves are excited is not yet fully understood). McIntosh et al. also estimated the energy flux from a single active region and found it to be insufficient (by an order of magnitude) to heat the corona.

Active regions have much stronger magnetic fields ($\gtrsim 1$ kG) and therefore, these regions should produce Alfvénic waves of longer wavelength, which would have shorter dissipation lengths that are perhaps still too long to heat the corona. The Hinode spacecraft has recently observed *coronal rain* in such detail that there is now tentative evidence against Alfvénic-wave heating for active regions. When a coronal loop is heated, material is evaporated from the chromosphere and the temperature starts to decline as the density of the loop plasma increases. At some point the loop will start to cool radiatively and this cooling will be catastrophic ($t_R \propto T^{3/2}/n$) because the loop is now so dense. These are the pre-conditions for coronal rain (Schrijver 2001; de Groof et al. 2005), the descent of cold plasma. Antolin et al. (2010) have used magnetohydrodynamic simulations to show how this phenomenon implies the absence of Alfvénic-wave heating. This form of heating promotes loops that are steady in temperature and density; i.e., the conditions for catastrophic collapse cannot be reached.

1.4.2 Dissipation of Magnetic Stresses

Direct current (DC) heating is caused by photospheric flows operating for much longer than the Alfvén time. Essentially, these convectively-driven motions can shear/rotate the footpoints of coronal loops and/or take a collection of footpoints on separate but overlapping random walks. Whatever happens, work is done on the coronal magnetic field, increasing its free energy. The rate at which this energy accumulates is given by the Poynting flux, $F = \frac{1}{4\pi} B_z B_\perp \cdot v_\perp$, where B_z is the field parallel to the surface normal and the $\perp$ subscript denotes the transverse direction.

The greater the turbulence at the photosphere the more energy available for coronal heating. A way to quantify photospheric turbulence is to perform a two-dimensional (2D) Fourier transform of B_z over some area of interest, e.g., an active region. Integrating the square of the transform over wave number space gives a power spectrum, $E(k) \approx k^{-\gamma}$; the higher the power index (γ) the more turbulent the photosphere. Abramenko et al. (2006) calculated power indices for 104 active regions and found that the power index correlated positively with the soft X-ray flux (as well as emission measure and temperature). This work demonstrates an encouraging correlation between energy added at the photosphere and energy radiated in the corona.

Mackay et al. (2011) have attempted to determine a value for the energy input by DC heating. They followed a single active region, producing a series of line-of-sight magnetograms (of 49-minute cadence) in order to capture how the surface field changes in response to convective flows. At each step, they extrapolated the coronal field and were thus able to estimate the growth rate of the free energy; this increase in energy was enough to explain radiative losses. The authors comment that the photospheric field did not appear to be subject to any shearing or vortical motions during the 4-day observation period. Perhaps this explains why the extrapolated coronal fields did not evolve further away from a potential field and thereby accrue more free energy.

Parker (1988) incorporated the idea of magnetic stress dissipation into a theory of coronal heating, based on minimal energy releases. He first considered the footpoint of an elemental magnetic thread (a coronal loop may contain many such structures). Initially, the footpoint field is normal to the photosphere: it has a B_z component only. A random convective flow causes the footpoint to move with respect to the rest of the thread. The footpoint field acquires a transverse component and therefore magnetic tension ($B_z B_\perp / 4\pi$). This magnetic shear can be expressed in two ways,

$$\frac{B_\perp}{B_z} \approx \frac{v_\theta\, t}{l} = \tan(\varphi)\,, \tag{1.3}$$

$$\frac{B_\perp}{B_z} \approx \frac{4\pi}{B_z^2\, v_\theta} F\,, \tag{1.4}$$

where v_θ is an average surface flow velocity, t is the flow duration, l is the thread length, φ is the angle between the thread axis and the surface normal, and F is the energy flux into the corona. Photospheric flow velocities have been measured by tracking NBPs via G-band emission (4305 Å): Berger and Title (1996) obtained $v_\theta = 1\text{–}5\,\mathrm{km\,s^{-1}}$ for NBPs in an active region and Utz et al. (2010) found, using an automated tracking algorithm, that $v_\theta = 1\text{–}2\,\mathrm{km\,s^{-1}}$ for quiet-Sun NBPs. The average B_z has been estimated at 100 G for active regions (Klimchuk 2006). So, if we conservatively choose the lower bound for v_θ, the level of shear required to produce an active-region energy flux ($10^7\,\mathrm{erg\,cm^{-2}\,s^{-1}}$) is approximately 0.12 ($\varphi \approx 7°$). Using Equation 1.3, the time taken to achieve this critical shear is 5000 s (the footpoint travels 5000 km). The quicker this time, the greater the efficiency of energy dissipation via magnetic stresses; however, less energy will be released since less tension is created. A less effective dissipation would actually result in a hotter corona: the magnetic tension is greater at the point of energy release.

Parker went further and estimated the size of these energy releases; he assumed that the path to critical shear comprises a sequence of steps. Each step has a duration of 500 s (the lifetime of a granule in the photosphere) and therefore a length, λ, of 500 km. This means a thread footpoint takes around 10 steps before the shear exceeds 7°. At each step more of the thread is displaced, hence Δl, the incremental displaced length is $L\,/\,N$, where N is the number of steps. The expression of the energy release is thus,

$$W \approx \frac{B_{\perp}^{2}}{8\pi}\lambda^{2}\Delta l\,N\,. \qquad (1.5)$$

The transverse field strength, $B_{\perp}$, is simply $0.12B_{z}$. So, using the values given, the size of an elemental energy release is around $7{\times}10^{24}$ erg. This argument implies that something happens to a thread once the shear gets to a certain point, i.e., the local field becomes unstable, energy is released and a (nano)flare results — a strand of heated plasma traces the original thread. Parker's nanoflare heating hypothesis states that the corona is heated by vast numbers of continually occurring but barely detectable flares. The size of a nanoflare is related to the properties of the host thread, namely its length and axial field strength.

Berger and Title (1996) comment that NBPs have a lifetime equivalent to that of a granule (6–8 mins), and conclude that magnetic threads (or flux tubes) cannot survive for more than 500 s, which is the time for a single step in Parker's theory. Compatibility between observation and theory is restored if one assumes that the network bright points observed by Utz et al. (2010), Berger and Title (1996) and Muller et al. (1994) are nanoflaring threads. A NBP lifetime is the duration of a flare hosted by an elemental thread; before such an event, the thread is acquiring the necessary shear and is not yet emitting in the G-band.

AC heating appears to be a viable explanation for the hot corona above coronal holes and above the quiet Sun. Many observations have confirmed the existence of wave phenomena in the corona (De Moortel et al. 2002; Banerjee et al. 2004; Brynildsen et al. 2004; McIntosh et al. 2011); however, the problem is in showing that the wave is unambiguously excited by some mechanism that is not itself caused by heating. Secondly, in order for a wave to be damped in the corona it must have specific properties, some of which may be difficult to determine from observations. Wave heating models will not be considered further here. The heating model proposed by this thesis is a DC-heating model, concerned with investigating how the high coronal temperatures *above active regions* could be maintained. Nanoflares are a form of DC heating, assuming these heating events are created by a particular type of coronal-loop instability (Sec. 2.2). Indeed, nanoflares could heat the corona, but these small energy releases would need to occur in far greater numbers than the much larger flares (Figure 1.8) that are commonly detected — this is the subject of the next section.

1.4.3 Flare Heating

A typical solar flare (i.e., one that is easily observed) can release up to 10^{25} J over a period of hours[5]. The observed occurrence rate of large flares is far too small to sustain coronal temperatures. Flares like the one shown in Figure 1.8 have an occurrence rate that reaches a peak of several times a day during periods of high activity. Solar observers have discovered a power law relationship between flare frequency and flare energy that spans the X-ray and EUV frequencies:

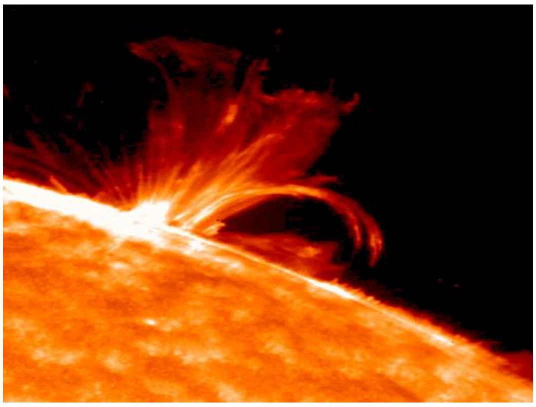

Figure 1.8: A solar flare reaching to a height of approximately 150 Mm. Courtesy of TRACE, Stanford-Lockheed Institute for Space Research, NASA.

$$N(E) \quad \propto \quad E^{-m}\,, \tag{1.6}$$

where $N(E)$ is the frequency distribution of flare energies, E is the flare energy and m is the flare population gradient. Equation 1.6 can be used to calculate the total energy

---

[5] This colossal amount of energy is just $\frac{1}{10}$% of the energy emitted by the Sun every second.

contribution from flares of all sizes:

$$W = \int_{E_{\min}}^{E_{\max}} EN(E)\, dE \propto \frac{1}{2-m}\left[E_{\max}^{2-m} - E_{\min}^{2-m}\right], \tag{1.7}$$

where $E_{\min}$ and $E_{\max}$ are the minimum and maximum solar flare energies. This contribution is dominated by small flares (i.e., those of energy $E_{\min}$) if $m > 2$ (Hudson 1991). If this condition is not met, nanoflares cannot be responsible for heating the corona. The results of a flare energy *census* covering eight orders of magnitude (from

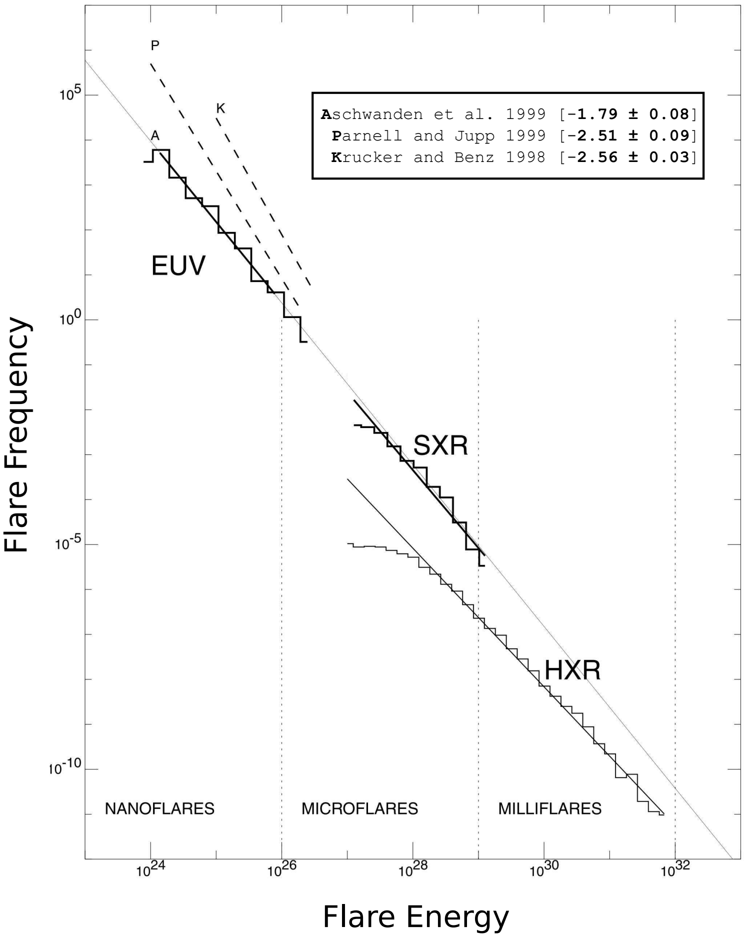

Figure 1.9: The logarithmic variation of flare occurrence frequency with flare energy. The letters (A, P and K) are used to label best-fit lines to three sets of nanoflare emission data. The slopes of these lines are the population gradients. These gradients are shown in brackets alongside the original reference for each dataset (the letter labels are the first letters of the lead authors). Courtesy of Aschwanden et al. (2000b)

nanoflares to large milliflares) have been compiled by Aschwanden et al. (2000b), see Figure 1.9. The best-fit lines, labelled A, P and K in Figure 1.9, give different values for the nanoflare population gradient. Two studies (P and K) give values above 2, but the gradient determined by study (A) is below 2. Aschwanden et al. attribute this lower value to methodical differences. They conclude that their methods for deciding when a solar event qualified as a flare were stricter than those used by the other studies. Three aspects of experimental procedure were cited as having caused the discrepancies in population gradient. First, was the coincidence criterion: events associated with the same flare occur within a specified period of time. Study A (Aschwanden et al. 2000b) used a coincidence criterion of two minutes, whereas studies P (Parnell and Jupp 2000) and K (Krucker and Benz 1998) used a zero coincidence criterion. Thus, multiple low-energy flare events overlapping in time (and space) would not all be counted by study A, resulting in a shallower population gradient. Second, was the flare-selection criterion; Aschwanden et al. argue that compared to studies P and K, their study discounted a greater number of non-flaring variabilities (especially prevalent when measuring low flare fluxes). Third, studies P and K were essentially 2D: the region of flare emission was assigned a constant column depth, the variable dimensions being the width and length. Study A modelled the flare region as a semi-circular cylindrical loop; hence, the column depth varied as the line of sight moved away from the loop axis. Aschwanden et al. found that they calculated greater flare energies since their results were based on entire loop volumes.

There is some debate over when observational data constitutes a nanoflare and how the size of the nanoflare should be determined. The reasons for using a two-minute coincidence criterion are not obvious; although the radiative cooling times for nanoflares are estimated to be of the order of minutes (Aschwanden et al. 2000b, p.1058), Aschwanden et al.'s approach is safe only if they are observing isolated nanoflares. In general, the effect of methodical differences increase in significance as one moves into the EUV range, and the spatio-temporal separations become less sharp. Different assumptions about what constitutes a nanoflare can give values above and below -2 for the same set of data (Parnell 2004). The detection of a discrete nanoflare will always be problematic if it is embedded in a region of intense flaring activity (this is likely to be the case if nanoflares *are* sufficiently numerous to heat the corona), so the population of this flare species will need to be determined indirectly.

Nanoflare Signatures

Understanding the origin of nanoflares only reveals part of the picture that shows how nanoflares contribute to coronal heating. What also needs to be considered is how the coronal plasma responds to the nanoflare; such details may help identify the observational signatures that reveal the characteristics of the underlying nanoflare population.

Nanoflare population gradients have been expressed as properties of X-ray fluctuations within a numerical model (Vekstein and Katsukawa 2000; Vekstein and Jain 2003). The energy dissipation sites within coronal loops can be described as filamentary structures (i.e., strands) whose dimensions are derived from a simple pressure balance equation:

$$2nk_{\mathrm{B}}T = \frac{|B|^2}{2\mu_0}, \tag{1.8}$$

where the left-hand-side (LHS) represents the thermal pressure within the strand and the right-hand-side (RHS) represents the external magnetic field pressure. The initial strands are formed by thin reconnecting current sheets, see Section 2.3. After equilibrium has been reached, a two-phase cooling mechanism (conduction followed by radiation) is used to estimate the strand's lifetime. X-ray fluctuations are therefore the superposition of many hot strands that have been created by randomly occurring (temporally and spatially) nanoflares. Vekstein and Katsukawa (2000) developed a model based on these ideas and applied it to set of active region loops that had previously been observed. The measured properties (temperature, length and emission measure) were then used to infer the magnetic field strength, energy flux and the filling factor (the proportion of the loop occupied by strands) for each loop. The results supported nanoflare heating for those loops with strong magnetic field ($B > 10\,\mathrm{G}$).

The advantage of this model, is that a determination of the nanoflare population gradient can be made without having to perform a direct count of nanoflares from observational data. Instead, a dynamic population of strands can be simulated according to an imposed population gradient. The time histories of density and temperature distribution that result from these simulations can then be convolved with the temperature response function of a soft X-ray telescope (SXRT); specifically, the one used on board the Yohkoh spacecraft. By following this procedure Vekstein and Jain (2003) discovered a qualitative relationship between the population gradient and the variation in amplitude of X-ray fluctuations (Figure 1.10). When the population gradient is steep there are many more smaller nanoflares than larger ones; hence, nearly all fluctuations originate from small nanoflares resulting in a narrow variation of fluctuation amplitude. As the gradient becomes shallower, there is an increased chance of fluctuations from large nanoflares contributing to the measurement: the measured fluctuations have a wider variation of amplitude. Surprisingly, analysis of data from Yohkoh's SXRT (Katsukawa and Tsuneta 2001) seemed to indicate the possibility of two independent populations of nanoflares. The intensity profile of the low energy half (in the nanoflare range) corresponded to high population gradients with $m > 3$; however, for the high

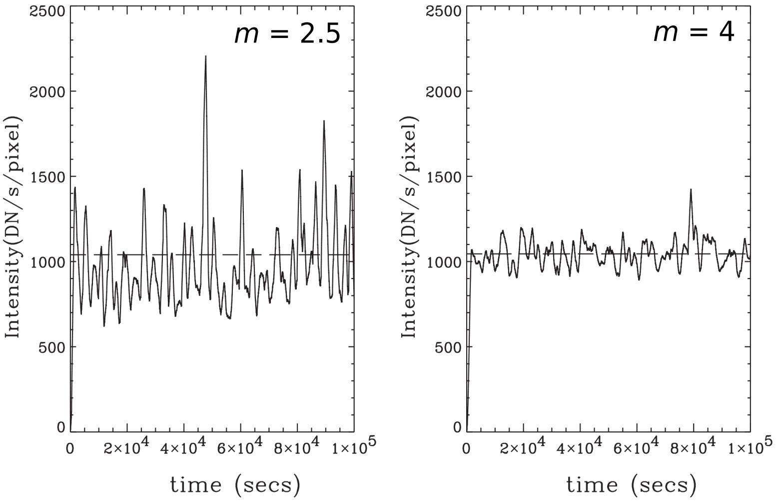

Figure 1.10: The time histories of X-ray intensity computed for two population gradients ($m = 2.5$ and $m = 4$). Courtesy of Vekstein and Jain (2003)

energy half, $m \leq 3$. Vekstein and Jain state that further observations are required by other telescopes before this complication can be accepted. This forward-modelling technique has also been used to select a mean nanoflare energy that matches the fluctuations in EUV emission. Vekstein (2009) obtained an estimate of 2×10^{24} erg using TRACE observations of two active regions.

Terzo et al. (2011) have looked at X-ray fluctuations in a slightly different way. A nanoflare strand cools quasi-exponentially over a time period much longer than the heating phase. As a result, the mean intensity is higher than the median value. The X-ray telescope on board the Hinode spacecraft was used by Terzo et al. to measure the intensity variations over an entire active region; this involved 32000 pixels at 1 arcsecond resolution ($\sim 700\,\mathrm{km}$). The fluctuation statistics were presented in the form of normal distributions, one for the mean and one for the median intensity. Terzo et al. found that the peak value for the median distribution was indeed lower than that for the mean (this result is robust against Poisson noise). Essentially, Terzo et al.'s work is a confirmation of impulsive heating; assuming that nanoflaring is the cause then in the future, this signature type could be used to constrain loop substructure (e.g., strand diameter).

Direct counting of nanoflares is evidently impractical, but there has been some encouraging work that has examined how the characteristics of nanoflare populations are uncovered through statistical analysis. However, the techniques used by the aforementioned workers require their models to be run with prescribed nanoflare populations. What if it was possible to construct a model that *created* ensembles of nanoflares? The next chapter explains how this could be done: it presents the basic elements of theory that could be used to simulate the ideal kink instability for a coronal loop. The instability is the outcome of successive perturbations applied at the loop footpoints and it leads to the non-ideal resistive instabilities that reconfigure the magnetic field, thereby releasing energy for heating coronal plasma.

2

Theoretical Background

2.1 Magnetohydrodynamics

Coronal loops can be considered as regions of strongly magnetised plasma; hence, each loop is essentially a discrete mini-atmosphere defined by its magnetic field and bounded by the solar surface. Loops are millions of metres in length (i.e., 10–1000 Mm) and since this length scale is far larger than the mean-free-path for plasma particles, $l_{\mathrm{mfp}} \approx 100\,\mathrm{km}$, (Bellan 2006), the magnetised plasma can be treated as a quasi-neutral fluid that is non-relativistic (Priest 1987; Goedbloed and Poedts 2004).

The magnetohydrodynamic (MHD) equations incorporate two of Maxwell's equations $\left(\nabla \cdot \vec{B} = 0,\, \nabla \times \vec{B} = \mu_0 \vec{j}\right)$, the perfect gas law and a simplified (single fluid) Ohm's law,

$$\vec{j} \;=\; \sigma\left(\vec{E} + \vec{v} \times \vec{B}\right), \tag{2.1}$$

where j is the current, $\vec{v}$ is the plasma flow velocity and σ is the conductivity. Conservation of mass and energy are enforced by the following expressions,

$$\frac{\partial \rho}{\partial t} \;+\; \nabla \cdot (\rho \vec{v}) \;=\; 0\,, \tag{2.2}$$

$$\frac{\rho^{\Gamma}}{\Gamma - 1}\frac{DP}{Dt} \;=\; -\mathscr{L}\,, \tag{2.3}$$

where ρ is the plasma density, P is the plasma pressure, Γ is the ratio of specific heats, $D/Dt = \partial/\partial t + v \cdot \nabla$ is the convective derivative, and $\mathscr{L}$ is the energy loss function (Priest 1987). The induction equation relates the magnetic field to plasma flow:

$$\frac{\partial \vec{B}}{\partial t} \quad = \quad \nabla \times \left(\vec{v} \times \vec{B}\right) + \eta \nabla^2 \vec{B}\,, \tag{2.4}$$

where η is the magnetic diffusivity: $\eta = \frac{1}{\mu_0 \sigma}$. In a fully-ionised plasma, such as the corona, $\sigma \approx 7{\times}10^{-4}\, T^{3/2}\, \Omega^{-1}\,\mathrm{m}^{-1}$ for temperature T. At coronal temperatures (~ 1 MK), the conductivity is approximately $700\,000\,\Omega^{-1}\,\mathrm{m}^{-1}$ and $\eta \approx 1.1\,\mathrm{m}^2\,\mathrm{s}^{-1}$. The induction equation can be used to estimate the time it takes for magnetic energy to resistively decay (due to ohmic diffusion of currents). For a loop of radius 1 Mm, the diffusion time, t_d, is $L^2/\eta \approx 30$ millennia: thus, magnetic diffusion is far too slow to be a driver for coronal heating. There must be faster processes that cause loops to release their magnetic energy, see Section 2.3.

The magnetic Reynolds number, R_m, is the ratio of the two terms on the RHS of the induction equation — it is the strength of the coupling between the plasma flow and the magnetic field. When the diffusion term is very low ($\partial\vec{B}/\partial t \approx \nabla \times (\vec{v} \times \vec{B})$), as is typical for coronal environments, R_m is extremely high ($\approx 10^{10}$). This leads to an important property of coronal loops, the conservation of magnetic flux (Alfvén 1943). In other words, the flux is *frozen* to the plasma. Whenever the plasma moves so does the magnetic field; even if the field energy is exceeded by the kinetic energy of the plasma flow, as is the case in the photosphere.

The forces acting on a coronal loop are described by the momentum equation:

$$\rho\left(\frac{\partial \vec{v}}{\partial t} + \vec{v} \cdot \nabla \vec{v}\right) \quad = \quad -\nabla P + \vec{j} \times \vec{B} + \rho \vec{g}_\odot\,, \tag{2.5}$$

where $\vec{g}_\odot$ is the acceleration due to the Sun's gravity (other forces may also be present, such as the viscous force). It is helpful to use an order-of-magnitude analysis to derive the characteristic velocity, the Alfvén speed, associated with the magnetic field (pressure and gravity terms are ignored);

$$\rho\left(\frac{v}{t_\mathrm{p}} + \frac{v^2}{L}\right) \quad \approx \quad \rho\left(\frac{v^2}{L}\right) \quad \approx \quad \frac{1}{\mu_0}\frac{B^2}{L}\,, \tag{2.6}$$

where t_p is the plasma flow time scale and L is the length scale. By replacing t_p with L/v it is quickly seen that the two terms on the LHS are of the same order. This leads to an expression for the Alfvén speed,

$$v_\mathrm{A} = \frac{B}{\sqrt{\mu_0 \rho}}, \tag{2.7}$$

which is the transmission speed of magnetic field perturbations.

If v_A is much larger than the plasma flow speed, the LHS of the momentum equation can be set to zero. The pressure gradient can usually also be neglected, in light of the fact that plasma-β (Equation 1.1) is small within the corona. Further analysis shows, that for large gravitational-scale-heights[1], the pressure term dominates the gravitational term. The solar scale height is of the order 10^6 m (Aschwanden 2009), so $\vec{j}\times\vec{B}$ is even more dominant when compared to $\rho\vec{g}_\odot$, except for very long loops. Equation 2.5 can now be revised for the corona such that only the Lorentz term remains:

$$\vec{j}\times\vec{B} \;=\; 0\,. \tag{2.8}$$

The loop therefore exists in a state of force-free equilibrium. This conclusion is confirmed by observations: coronal loops have been seen to maintain their shape over periods of many hours (López Fuentes et al. 2007). Equation 2.8 implies the current and magnetic field are parallel and so can be rewritten in the following form,

$$\nabla\times\vec{B} \;=\; \alpha(\vec{r})\vec{B}, \tag{2.9}$$

where the scalar $\alpha = (\mu_0\vec{j}\cdot\vec{B})/(|B|^2)$ is the ratio of current density to magnetic field and $\vec{r}$ is a position vector. Converting to cylindrical polar coordinates gives,

$$\nabla\times\vec{B} \;=\; \left(\frac{1}{r}\frac{\partial B_z}{\partial\theta} - \frac{\partial B_\theta}{\partial z}\right)\hat{r} \;+\; \left(\frac{\partial B_r}{\partial z} - \frac{\partial B_z}{\partial r}\right)\hat{\theta} \;+\; \frac{1}{r}\left(\frac{\partial(rB_\theta)}{\partial r} - \frac{\partial B_r}{\partial\theta}\right)\hat{z}\,. \tag{2.10}$$

Evaluation of the magnetic field vectors implied by the force-free equation for straightened line-tied coronal loops, shows that all radial variation takes place within small

---

[1] The gravitational force declines as $1/r^2$; the gravitational-scale-height is reached when gravity has reduced by a factor of e.

boundary layers at the end of the loop (Zweibel and Boozer 1985; Browning and Hood 1989). Hence, to a good approximation, the radial component can be neglected and a one-dimensional (1D) force-free field can be used instead;

$$\vec{B} \;=\; B_\theta(r)\hat{\theta} + B_z(r)\hat{z}\,. \tag{2.11}$$

Thus, $\partial\vec{B}/\partial\theta = \partial\vec{B}/\partial z = 0$, and for constant α ($\partial\alpha/\partial r = 0$), Equation 2.10 simplifies to,

$$\nabla \times \vec{B} \;=\; -\frac{\partial B_z}{\partial r}\,\hat{\theta} \;+\; \left(\frac{B_\theta}{r} + \frac{\partial B_\theta}{\partial r}\right)\hat{z} \;=\; \alpha B_\theta\,\hat{\theta} \;+\; \alpha B_z\,\hat{z}\,. \tag{2.12}$$

The expressions formed by equating the $\hat{\theta}$ and $\hat{z}$ coefficients of Equation 2.12 are coupled. By differentiating the $\hat{\theta}$-coefficient equation with respect to r and by making appropriate substitutions, it is possible to express the $\hat{z}$-coefficient equation without using B_θ. Multiplying through by αr^2 and rearranging yields Equation 2.13, which is a Bessel differential equation involving B_z,

$$r^2\frac{\partial^2 B_z}{\partial r^2} \;+\; r\frac{\partial B_z}{\partial r} \;+\; \alpha^2 r^2 B_z \;=\; 0\,. \tag{2.13}$$

A similar expression can be found for the azimuthal field: Equation 2.14 is obtained by rewriting the $\hat{\theta}$-coefficient equation such that B_z does not appear,

$$r^2\frac{\partial^2 B_\theta}{\partial r^2} \;+\; r\frac{\partial B_\theta}{\partial r} \;+\; \left(\alpha^2 r^2 - 1\right)B_\theta \;=\; 0\,. \tag{2.14}$$

Hence, assuming $\alpha(r)$ is uniform or piecewise constant, the magnetic field can be expressed in terms of Bessel functions, see Section 3.1.

The minimum energy state occurs when $\alpha = 0$ throughout the loop volume; i.e., the loop is potential and has no azimuthal field ($B_\theta = 0$). Over time, the magnetic field is twisted in response to the continuous and random convection motions of the plasma at the loop footpoints. This twisting of the field introduces currents (via Ohm's law) and creates a non-zero $\alpha(r)$ profile. The extra azimuthal field created by these currents is accumulated by the loop as free magnetic energy. In addition to a rising α, field perturbations are continually been transmitted along the loop. Crucially, the time that these disturbances take to travel from one footpoint to the other (seconds) is usually much faster than the time scale for photospheric motions (minutes–hours). The disturbances have time to decay before the loop is again perturbed from the photosphere; hence, the loop moves through a series of force-free equilibrium states. At some point however, presumably when the magnetic twist (Equation 2.16) has exceeded some threshold value, the loop will thermalise some of its magnetic energy through a flare-like event. For such a heating event (or some other dissipation process) to occur, the diffusion term in the induction equation (Equation 2.4) must become significant.

2.2 Coronal Loop Instabilities

A dynamical system, such as a coronal loop, is unstable if it can move to a state of lower potential energy. The loop loses or gains potential energy when it is perturbed. If all possible perturbations add potential energy, the loop is considered stable, since it will experience a restoring force that returns it to the equilibrium position. The two situations (stability and instability) are illustrated by Figure 2.1. Instability occurs when the sign of the change in potential energy (δW) is negative. The system is marginally stable when $\delta W = 0$ and stable when $\delta W > 0$. This is known as the energy principle (Priest 1987; Goedbloed and Poedts 2004).

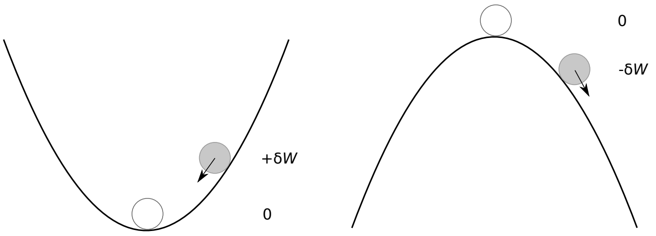

Figure 2.1: An object (shaded circle) is displaced from its original position (empty circle). The black arrows indicate the direction of the resultant force that now acts on the object. **Left**, the system is linearly stable, the resultant force acts to restore the object to its original position. **Right**, the system is linearly unstable.

An instability is ideal when magnetic diffusivity is zero. Resistive instabilities are driven by some finite resistivity; however, since the corona is nearly perfectly conducting, the resistive time scale is very long. Ideal instabilities on the other hand are sufficiently fast to be compatible with flare observations; such disturbances involve a pinching or distortion of the plasma column defined by the loop (Figure 2.2).

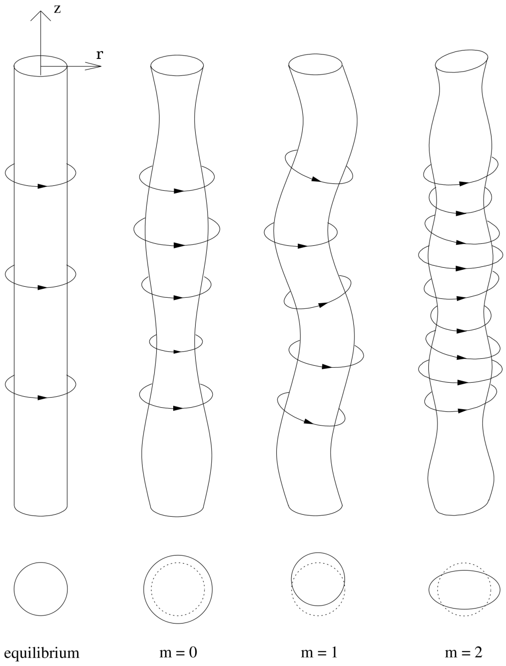

Figure 2.2: The three ideal instability modes are sausage ($m = 0$), kink ($m = 1$) and fluting ($m > 1$). Courtesy of Braithwaite (2006)

The sausage mode is the result of a self-reinforcing pinching (due to the Lorentz force) of the azimuthal field. In response to this compression, plasma is evacuated into the areas of lower gas pressure either side of the pinch. This mode is stabilised by the presence of an axial field, B_z, and by preventing plasma from escaping through the loop boundaries or footpoints. The kink mode involves a bending of the entire plasma column. Magnetic pressure is increased on the inside of the bend and decreased on the outside, promoting further growth of the instability. Again, stabilisation can be achieved if B_z is sufficiently strong (a high $|B_z|$ will provide a pressure force that will oppose the kinking of the loop); however, this may not prevent a helical kink instability, since the axial pressure now has to counteract kinking in both dimensions perpendicular to the loop axis. A loop is also stabilised if it is line-tied (Hood 1992); i.e., field lines are prevented from moving across a *fixed* footpoint plane. Hence, during a perturbation, energy is now required to compress the high-tension field at the footpoints, which means there is less energy to drive the instability. Finally, the fluting modes ($m > 1$) produce simple longitudinal oscillations that do not lead to runaway instabilities.

Forcing a loop to be line-tied, replicates the severe density gradient that exists between the corona and the photosphere: coronal densities are eight orders of magnitude lower than those at the photosphere and so any perturbations are almost completely damped at the footpoints (Raadu 1972). Hood and Priest (1979) performed a MHD stability analysis, using the energy method, on a variety of straightened line-tied coronal loops by subjecting them to ideal perturbations. The changes to a loop's magnetic energy (δW) as a result of a perturbation were represented by an energy integral,

$$\delta W \;=\; -\frac{1}{2}\int \xi \cdot F(\xi)\; dV\,, \tag{2.15}$$

where ξ is the displacement ($v_1 = \partial\xi/\partial t$ is the perturbed velocity) and F is the linearised force function derived from the momentum equation. This integral was minimised so that the smallest perturbations could be analysed. If there exists one perturbation such that $\delta W < 0$ then the loop is unstable. In this way, Hood and Priest were able to show that the instability with the highest growth rate was the kink ($m = 1$) mode. There is more than one way to solve the linearised MHD equations: the normal mode method assumes that all perturbations are of the form, $\xi(r,t) = \xi(r)e^{i\gamma t}$, where γ is the growth rate of the instability. This method will be explained further in the next chapter (Section 3.2), where it will be used to uncover a 2D thresold for linear kink instablity.

Hood and Priest were also interested in whether the magnetic twist of a loop (i.e., the angle through which a field line rotates from one end of the loop to the other) can be used as a proxy for kink instability onset, since the twist,

$$\phi \;=\; \frac{LB_\theta}{RB_z}\,, \tag{2.16}$$

where L is the loop length and R is the radius, is directly related to rotational photospheric motions. They found that the critical twist, ϕ_{crit}, varies according to the aspect ratio (L/R), plasma-β and the transverse magnetic structure (i.e., the radial twist profile). In general, short fat loops (low aspect ratio) have low critical twists, whereas long thin loops (high aspect ratio) have high critical twists. Subsequent work (Hood and Priest 1981) revealed that a particular type of loop (aspect ratio 10, zero β and *uniform* twist profile) possessed a critical twist of 2.49π. This figure is often quoted as a general result. The stability of loops with variable twist profiles have also been studied (Mikic et al. 1990; Velli et al. 1990; Baty 2001); but, this work will be discussed in the next chapter (Section 3.5.1), so that it can be directly compared with the results of the loop model presented in this thesis.

Many numerical experiments have been run to uncover the dynamics that occur within a loop during a kink instability. The non-linear simulations of (Browning et al. 2008) showed the emergence of current surfaces that were concentrated in the form of helical ribbons (Figure 2.3). These structures are a precursor for magnetic reconnection and therefore, the dissipation of magnetic energy, see next section, Figure 2.8.

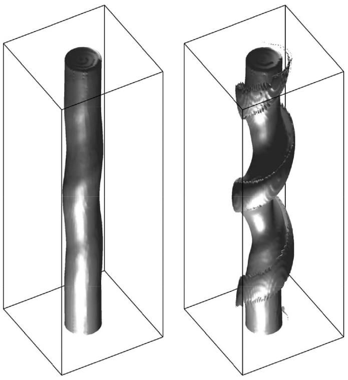

Figure 2.3: Isosurfaces of current just before and after the initiation of a kink instability. The loop configuration chosen was one known to be linearly kink unstable according to Figure 3.2.

Other workers have sought an understanding of how a kink unstable loop could be confirmed observationally. Haynes and Arber (2007) focussed on short coronal loops of 10 Mm — those that might be responsible for coronal bright points — and looked at how a kink instability would be viewed by the EUV instrument on board the TRACE spacecraft. Their synthetic observations revealed diagonal density depletions at the main reconnection site internal to the loop, see the top row of Figure 2.4. After magnetic reconnection the field untwists and matter is transported towards the footpoints: the density is lower with respect to the volume either side of the reconnection site. Density *gaps* have indeed been seen in observations taken by the 171 Å TRACE filter. Srivastava et al. (2010) observed what they called double structure in a flaring loop, which they believe to be a signature of kink instability (Figure 2.4, bottom row). Furthermore, the authors claim that this density variation does not occur for the sausage mode instability. There are of course significant differences between the simulated

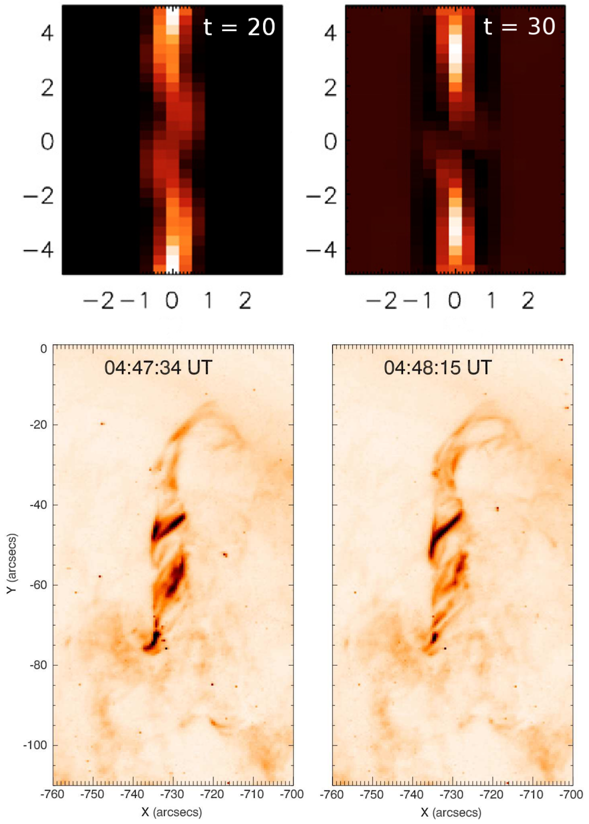

Figure 2.4: The top row shows the diagonal density depletions resulting from a numerically simulated kink instability (Haynes and Arber 2007) — the loop is straight and has an aspect ratio of 10. An active-region loop was observed by Srivastava et al. (2010) and exhibited a similar density pattern, see bottom row — this loop was considered to be kink unstable. The simulated and observed loops appear to have opposite twists.

loop and the real one; the latter was curved and also significantly longer — the aspect ratio of this loop was double that of the one modelled by Haynes and Arber.

Ideal instabilities initiate slow diffusion of magnetic energy; without some sort of resistive process, the rate of diffusion will be insufficient to power a flare. Nevertheless, through a kink instability, a coronal loop may be deformed such that magnetic flux surfaces are brought together. Consequently, magnetic fields are made to approach (but not necessarily arrive at) an anti-parallel configuration and therefore, magnetic reconnection can take place (Priest 1987; Aschwanden 2009). Resistive MHD shows that magnetic field can diffuse faster in the compressed areas than in the unperturbed regions.

Another instability that a coronal loop could be prone to is the ballooning instability (Tsap et al. 2008; Aschwanden 2009). This possibility arises because coronal loops are curved: at the apex, the gas pressure is higher on the inside of the loop compared to the outside. The pressure differential forces the outer edge of the loop apex to expand upwards, assuming there is no counteracting magnetic tension. The loop models presented in this thesis are force-free (plasma-$\beta \ll 1$) and so the ballooning instability will not be considered further. Thermal instabilities (Aschwanden 2009) will also be disregarded.

2.3 Reconnection

One way for the diffusion term to soar in value is for the length scale to shorten drastically, since $\eta\nabla^2 B \sim \eta B/L^2$. Such a possibility can arise in a phenomenon called magnetic reconnection (Priest 1987; Priest and Forbes 2000; Gurnett and Bhattacharjee 2005; Birn and Priest 2007), see Figure 2.5. Reconnection relies (in its basic form) on the drawing near of anti-parallel magnetic fields, driven by opposing plasma flows. As the separation between the fields becomes ever smaller, a current sheet is formed in response to the steepening magnetic gradient. The dimensions of the sheet are specified by its thickness (l), width (w) and length (L) — illustrations of reconnection usually

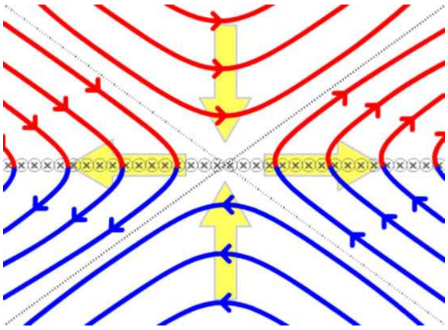

Figure 2.5: The reconnection of magnetic fields (red and blue lines). An increasingly severe magnetic gradient, caused by the inward flows, creates a current sheet perpendicular to the magnetic field (the line of crossed circles marks the edge of the sheet). Plasma flows are indicated by the yellow arrows. Courtesy of Wikimedia Commons, ChamouJacoN.

arrange the sheet width to be in the horizontal direction and the thickness in the vertical (Figure 2.5). Notice how the pattern of field lines will describe an X-shape when w is small; in this situation, the area of null magnetic field is referred to as an X-point.

The energetics of reconnection can be estimated by a simple application of the Poynting vector equation:

$$\vec{S} = \frac{1}{\mu_0}\left(\vec{E} \times \vec{B}\right), \tag{2.17}$$

where $\vec{E} = \vec{v} \times \vec{B}$ is the electric field generated by the plasma inflow. Hence, the magnitude of the Poynting vector is approximately:

$$S \approx \frac{vB^2}{2\mu_0}, \tag{2.18}$$

and so the amount of power available for dissipation as heat can be expressed as,

$$W = 2\,S\,L^2 = \frac{vB^2L^2}{\mu_0}\,. \tag{2.19}$$

The squared terms show that the heating delivered by reconnection increases non-linearly with the magnetic field strength.

During reconnection, two forms of magnetic energy release are possible; ohmic dissipation caused by the resistivity of the current sheet (oriented perpendicular to the magnetic fields) and the release of magnetic tension in the reconnected field. The latter process converts magnetic energy to the kinetic energy of plasma particles. Both processes diffuse the same amount of magnetic energy if the current sheet has constant resistivity across its width. This scenario, described as Sweet-Parker reconnection (Birn and Priest 2007), has been observed in laboratory plasmas (Figure 2.6); however, the time scale for Sweet-Parker reconnection in the corona is four orders of magnitude longer than that associated with solar flares (Yamada et al. 2010). The slowness of Sweet-Parker reconnection is due to the width of the current sheet, since the reconnection rate, v_R, scales as $(l/w)v_A$. Petschek (1964) proposed that slow shocks form in the outflow region, thereby accelerating plasma outflow and increasing the reconnection rate. Space for these shocks is provided by limiting the width of the current sheet. Following work has shown that it is not just the thinness of the current sheet that ensures magnetic diffusion, rather, it is the variation in resistivity across the current sheet that acts as a trigger for the dissipation of magnetic energy (Yamada et al. 2010). Slight variations in the resistivity will cause approaching field lines to bend relative to where the resistivity is higher. The bending creates a tension in the magnetic field and when this tension is released, plasma particles are accelerated. Hence, magnetic energy is converted to kinetic energy, which can be converted to heat via plasma viscosity. In essence, the current sheets have a shorter width, that is limited by the scale

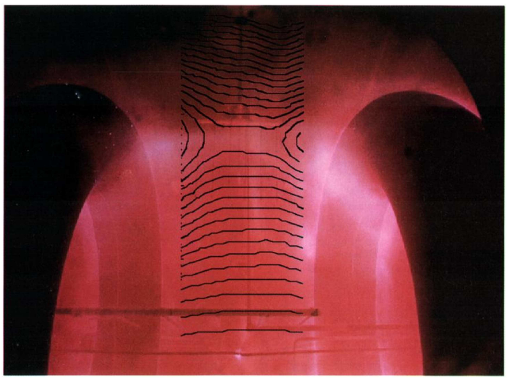

Figure 2.6: The Magnetic Reconnection Experiment (MRX) device was used to create driven reconnection discharges within a hydrogen plasma. Flux contours (black) were calculated from measurements taken by magnetic probes. Courtesy of Yamada (1999).

size of the resistivity. Most of the magnetic diffusion now occurs via kinetic energy. An important caveat is that, in order to attain reconnection speeds compatible with solar flares, the dimensions of the current sheet need to be much smaller than coronal scales ($L \sim 10\,\mathrm{Mm}$): the thickness is of the order of 10 m and the width 1000 m. These sizes fall below the resolution of MHD numerical simulations and more importantly, the coronal plasma is not collisional on these scales.

2.3.1 Collisionless Reconnection

Reconnection does not necessarily require a collisional plasma. Indeed, reconnection becomes collisionless when the current sheet thickness falls below the ion skin depth — the depth to which ion flows can penetrate a body of magnetised plasma. The plasma pressure is balanced by the magnetic field and so the skin depth is of the same order as the ion gyroradius, $\omega_{\mathrm{ic}} r_{\mathrm{i}} = \sqrt{k_{\mathrm{B}} T_{\mathrm{i}} / m_{\mathrm{i}}}$ (Yamada et al. 2010). When the sheet thickness is less than the ion gyroradius, ions escape the magnetic field and become demagnetised; this is not the case for electrons, which have tighter gyroradii. The plasma separates into two fluids (electrons and ions); hence, the MHD regime is no longer applicable.

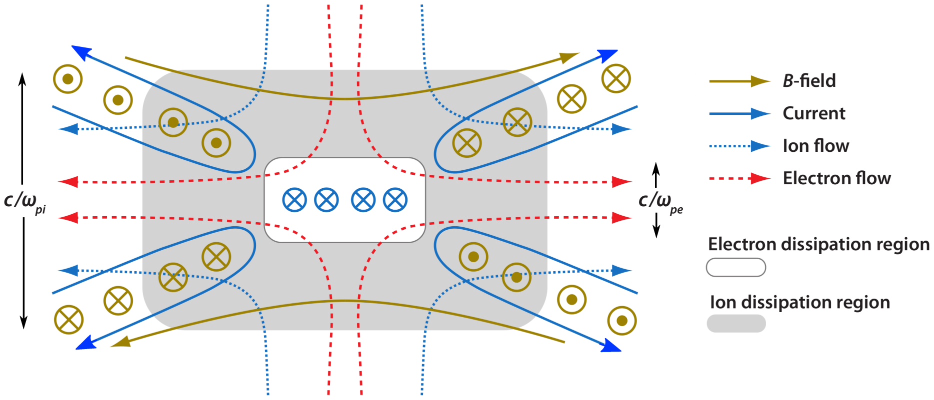

Figure 2.7: The Magnetic field geometry in collisionless reconnection. The ions separate from the electrons at a distance equivalent to the ion skin depth, $\delta_{\mathrm{i}} = c/\omega_{\mathrm{pi}}$, where $\omega_{\mathrm{pi}} = \sqrt{4\pi n_{\mathrm{p}} e^2 / m_{\mathrm{p}}}$ is the proton plasma frequency. Courtesy of Zweibel and Yamada (2009).

Figure 2.7 shows the ions entering the neutral sheet; those that become demagnetised take the direction of reconnection outflow. However, the still-magnetised electrons migrate towards the centre in accordance with $\vec{E} \times \vec{B}$ motion, where $\vec{E}$ is the reconnection electric field into the plane of the figure. This drift (E_y/B_x) is enhanced by the weakening magnetic field. Some of the electrons will join the current sheet and some will be captured by reconnected field and ejected in the direction of reconnection outflow. The pattern of current flow illustrated by Figure 2.7 creates a secondary out-of-plane magnetic field. Its quadrupolar form is a signature of the Hall effect; it is this effect that speeds up the reconnection rate. There is however a second dissipation mechanism, namely anomalous resistivity. This is the name for the microturbulence that occurs when the current density (within the inner diffusion region) exceeds a certain threshold. Experiments involving the MRX device (Figure 2.6) have shown the presence of both dissipation mechanisms (Ji et al. 2004).

2.3.2 Reconnection in the Corona

The relevance of reconnection to the corona has been explored by Uzdensky (2007), who argues that magnetic dissipation continually switches between Sweet-Parker and collisionless (Petschek-like) reconnection. He defines the nanoflare (Section 1.4.2) to be a product of collisionless reconnection. Uzdensky then explains how the nanoflare causes heating, which evaporates chromospheric material and increases the plasma density, thereby *switching off* the physics that created the original nanoflare. Reconnection still takes place but only according to the much slower Sweet-Parker scheme. Eventually, the plasma will start to cool radiatively, the density falls and once again collisionless reconnection becomes possible. The implication here is that the conditions for flaring are controlled by cooling. This thesis will argue that the kink instability (2.2) is a pre-requisite for fast collisionless reconnection.

Magnetic flux is continually emerging from the photosphere and into the corona where it will interact with the pre-existing field. Flux emergence combined with the convection and differential rotation of the solar surface, create many opportunities for magnetic reconnection (Aschwanden 2009). How could this phenomenon be caused by a coronal loop instability? When a loop experiences more and more twisting as a result of convective motions, the opportunities for reconnection events increase. Several three-dimensional (3D) numerical MHD studies of straightened loops (Velli et al. 1997; Lionello et al. 1998; Baty 2000; Browning et al. 2008; Hood et al. 2009) have shown how a non-linear kink instability can achieve heating via reconnection. Browning et al. (2008) used a resistive MHD code; although, in their simulations, the background resistivity was zero, an anomalous resistivity[2] was applied as soon as the current exceeded a threshold value. Figure 2.8 shows the results of one of these simulations. The drop in magnetic energy is coincident with the rise in internal energy caused in part by ohmic and viscous heating. Kinetic energy also increases at the same time. Note, the energy is not strictly conserved during energy conversion: the increase

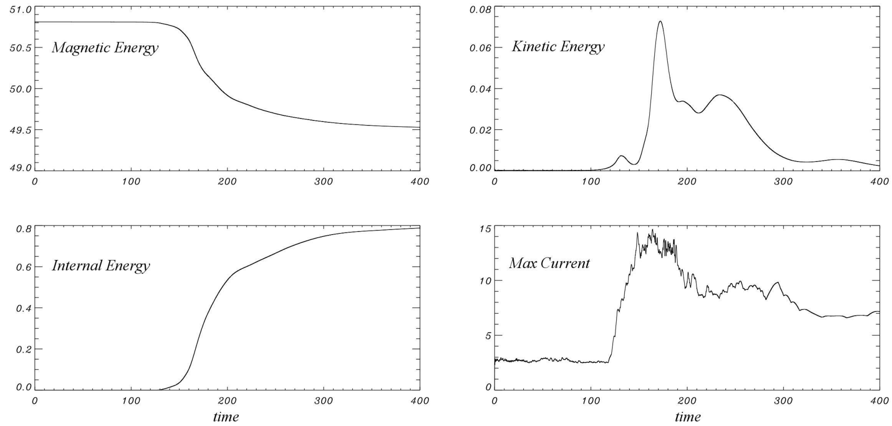

Figure 2.8: Results from a 3D MHD numerical simulation of a cylindrical coronal loop conducted by Browning et al. (2008) showing the change in magnetic energy (top left), kinetic energy (top right), internal energy (bottom left) and the maximum current (bottom right). The time axis is in units of the Alfvén time.

---

[2] This is an artifical term used by Browning et al. (2008) to compensate for limited spatial resolution (see Section 4.1), it is *not* the same as the anomalous resistivity discussed in the section on collisionless reconnection (2.3.1).

in internal energy is less than two thirds of the magnetic energy loss. This is because the energy released by the instability amounts to barely more than 2% of the original field; at these levels, numerical inaccuracies become apparent.

Figure 2.9 (left) is a schematic of the magnetic reconnection geometry that might be associated with a large-scale flare. This figure shows the reconnection region occurring above the coronal loop. In addition, particles are accelerated downwards along the field lines towards the footpoints, where the denser atmosphere will produce bremsstrahlung emission. The Ramaty High Energy Solar Spectroscopic Imager (RHESSI) spacecraft has provided evidence for these processes (Lin et al. 2003), see Fig 2.9 (right). The contours mark the areas of emission, which are consistent with those shown in the left figure. Strong evidence for reconnection has also been found in observations of other large-scale flares (Fletcher 2009; Qiu 2009).

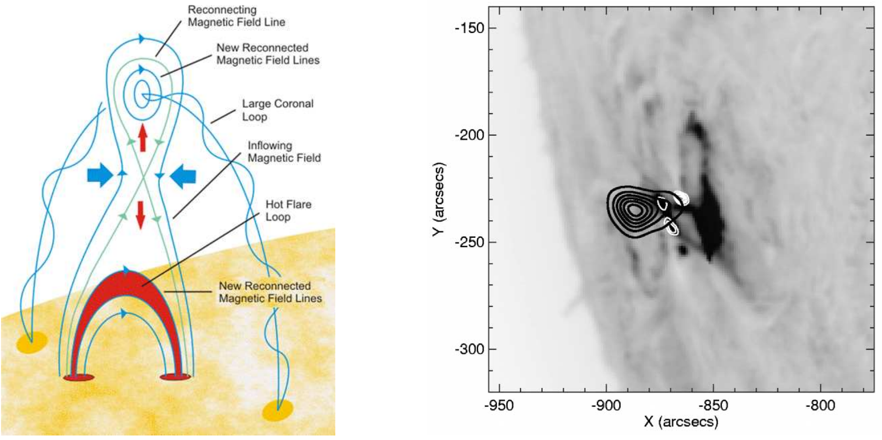

Figure 2.9: **Left**, the geometry of an eruptive flare driven by magnetic reconnection according to the CSHKP model (Svestka et al. 1992). Courtesy of Gordon Holman, Goddard Space Flight Center, NASA. **Right**, hard X-ray emission of two coronal loops merged at the southernmost footpoint. Black contours indicate emission in the range 12–18 keV and white contours cover the energy range 30–80 keV. The RHESSI contour data has been superimposed on a Hα image from the Big Bear Solar Observatory. Courtesy of Lin et al. (2003).

2.3.3 3D Reconnection

Unlike the corona, the cartoon of Figure 2.9 is not truely 3D. In order to understand the possibilities for 3D reconnection, new terminology is required. Separatrix surfaces (Figure 2.10, left) represent the extent of a magnetic domain; i.e, a volume containing uniform magnetic connectivity. A separator is the line of intersection between two separatrix surfaces. Any field line that connects two null points (places of zero magnetic field) qualifies as a separator — null points also occur wherever separators intersect each other. Merging unipolar fields (Figure 2.10, right) are best described in terms of a symmetry axis (or spine) and a fan dome, the surface of which divides the two fields. The basic types of 3D reconnection can be classified in terms of the concepts introduced above (Priest and Forbes 2000; Aschwanden 2009) and of course other topologies, involving myriad forms of reconnection, can be created by combining more and more dipolar and unipolar fields.

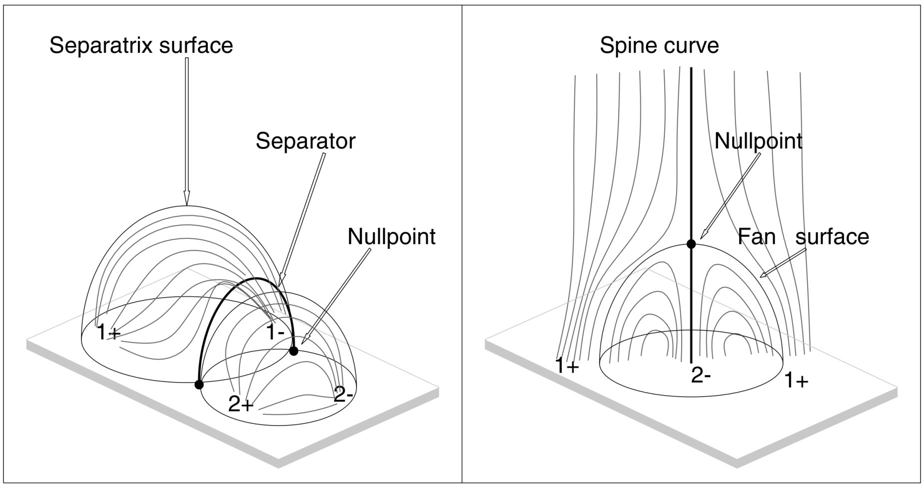

Figure 2.10: **Left**, an emerging dipole (2+,2-) joins an established dipole (1+,1-). Magnetic nulls (bold dots) are indicated where the resulting separator intersects the photosphere. **Right**, a unipolar region (2-) emerges within an open field of opposite polarity (1+). The two regions are separated by a fan surface. A magnetic null occurs where this surface intersects the spine. Courtesy of Aschwanden (2009).

Priest and Titov (1996) constructed the skeleton for a single null point (i.e., a spine and a fan surface) in order to explore the possibilities for reconnection relating to footpoint motions. In this context, footpoints are the intersection points of field lines with some bounding surface; e.g., a cylinder. Priest and Titov found three kinds of reconnection. For example, fan reconnection was caused by footpoint motions at the ends of a bounding cylinder (the fan is situated at the midplane of the cylinder and the spine is coincident with the cylinder axis). Separators were also found to be closely associated with reconnection. It was noticed that field lines within planes perpendicular to separators tend to have X-type topology (Figure 2.5); the collapse of such an arrangement generates currents along the separator. Parnell et al. (2010) investigated this type of reconnection further by allowing the magnetic domains created by two flux sources of opposite polarity to pass each other without intersecting (Figure 2.11). This work has shown that, unlike 2D reconnection (Figure 2.5), the local field structure differs from the global topology. Also, separator reconnection is not confined to the ends (i.e., at

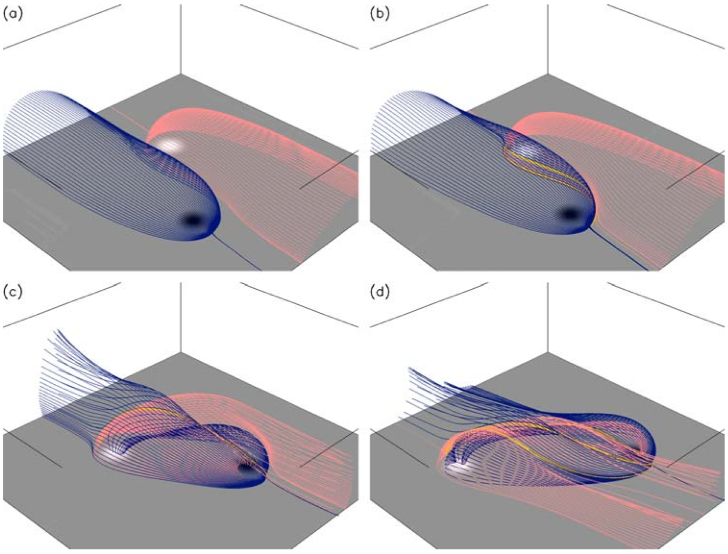

Figure 2.11: Snapshots — (a) is the earliest and (d) the latest — of the magnetic skeleton as two flux sources (white is positive and black is negative) pass each other. The separatrix surfaces are pink (positive) and blue (negative). Separators are indicated by the yellow lines. Courtesy of Parnell et al. (2010).

the null points), but can also occur at various points along the separator. Thus, the opportunities for reconnection and energy release were found to be greater than expected; especially as, at particular times during the simulation, the separatrix surfaces crossed each other multiple times (Parnell 2007).

Clearly, separators are more than just a topological concept. Plowman et al. (2009) claim that separators are, when heated by reconnection, mistakenly classified as coronal loops. Their argument rests on the idea that the coronal part of the separator has more or less constant magnetic field strength; hence, flux conservation does not require a significant expansion of the separator width. Plowman et al. measured the characteristics of the field lines derived from a planar arrangement of point charges. The field lines were divided into separators and non-separators, which were classed as coronal loops. Then, expansion-factor distributions were plotted for the two classes of field line. Coronal loops exhibited a wide range of expansion factors centred on ≈ 3, whereas the separator distribution peaked around unity. The coronal loops described in this thesis cannot be classed as separators. Reconnection is initiated when a loop achieves kink instability in response to photospheric driving. This is not possible for separators because these structures are cut off from the photosphere (due to the zero magnetic field at the separator ends). Regardless, if one considers the independent motions of the threads of magnetic field within a loop, separatix surfaces and separators can be created (Priest et al. 2005), and therefore, energy release via reconnection becomes possible.

The idea that small-scale reconnection events heat the corona (Levine 1974) was the starting point for the nanoflare heating hypothesis (Section 1.4.2). Reconnection could be the means by which a coronal loop transitions to a lower energy state. Identifying this state numerically is computationally expensive (both in time and in computer memory), notwithstanding the compromises that need to be made in order to accommodate the disparate spatial scales. Fortunately, there exists a theory that determines the relaxed state without having to model the complex reconnection dynamics.

2.4 Relaxation Theory

Relaxation theory states that when a magnetic field reaches instability (or is otherwise disrupted) it will evolve towards a minimum energy state such that the total magnetic axial flux and the *global* magnetic helicity are conserved (Taylor 1974, 1986). The relaxed state is the well known constant-α or linear force-free field:

$$\nabla \times \vec{B} \;=\; \alpha \vec{B}. \tag{2.20}$$

The original intention of this theory was to explain laboratory plasma phenomena; but latterly, it has been frequently applied to the solar corona (Heyvaerts and Priest 1984; Browning et al. 1986; Vekstein et al. 1993; Zhang and Low 2003; Priest et al. 2005). During relaxation, the helicity, K, and the axial flux, ψ, are conserved — K/ψ^2 is the conserved dimensionless combination of these two properties. The helicity measures the self-linkage of the magnetic field (Berger 1999) and is defined thus,

$$K \;=\; \int_V \vec{A} \cdot \vec{B} \, dV \,, \tag{2.21}$$

where $\vec{B}$ is the magnetic field and $\vec{A}$ is the vector potential ($\vec{B} = \nabla \times \vec{A}$). A modified expression for this quantity needs to be used since the field lines cross the photospheric boundaries, which creates a non-zero normal flux and therefore removes gauge invariance. Relative helicity (Berger and Field 1984; Finn and Antonsen 1985) is the difference between the helicity of the actual field and that of some reference field (the dashed terms in Equation 2.22) with the same normal flux distribution,

$$K \;=\; \int_V (\vec{A} + \vec{A}') \cdot (\vec{B} - \vec{B}') \, dV \,. \tag{2.22}$$

As a rule, the reference field is chosen to be potential for convenience. In ideal MHD, the helicity of every flux region is conserved. Taylor proposed that in the presence of reconnection all such local invariants are destroyed, whilst the global helicity is conserved.

Helicity conservation is not absolute. During relaxation, helicity is still subject to global resistive diffusion, but the change in helicity is negligible when compared to the drop in magnetic energy, so long as dissipation predominantly occurs within thin current sheets. The rates of dissipation for helicity and magnetic energy (W) are

$$\frac{dK}{dt} = -2\eta \int_V j \cdot B \, dV \approx -\frac{2\eta}{\mu_0} B^2 \frac{L^3}{l}, \tag{2.23}$$

$$\frac{dW}{dt} = -\eta \int_V j \cdot j \, dV \approx -\frac{\eta}{\mu_0^2} B^2 \frac{L^3}{l^2}, \tag{2.24}$$

where $j = \nabla \times B/\mu_0$ is the current density, l is the length scale of magnetic variation (i.e., current sheet thickness), L is the global length scale and η is the resistivity (Browning 1988). Using $K \approx B^2 L$ and $W \approx B^2/2\mu_0$, the ratio of the dissipation rates reduces to l/L. Hence, $d_t K/K \ll d_t W/W$ (where $d_t \equiv d/dt$) if $l \ll L$, which is expected to be well satisfied for reconnecting current sheets within the highly conductive corona, where *global* resistive diffusion of helicity and energy are negligible. The relative sizes of the dissipation rates have been confirmed by MHD simulations, despite the coarseness of numerical grids (the difference between dissipation rates becomes more pronounced as the resistivity becomes smaller and falls below numerical precision). Browning et al. (2008) showed that during the relaxation of a marginally (kink) unstable loop, $\delta K/K \sim 10^{-4}$ and $\delta W/W \sim 10^{-2}$. Detailed estimates of coronal helicity dissipation are given by Berger and Field (1984); further justification for helicity-conserving relaxation is provided by laboratory experiments (Taylor 1986; Heidbrink and Dang 2000).

Prior to relaxation, the motions at the footpoints need to generate a significantly non-linear force-free field (Equation 2.9), in order for there to be a significant energy release (Heyvaerts and Priest 1984). The maximum energy release occurs when the field relaxes to a potential state ($\alpha = 0$); however, the time scale for complete relaxation is usually too slow (requiring complete dissipation of all currents) and instead the relaxed state is the linear force-free field (constant α). Heyvaerts and Priest found that the plausibility of DC heating (Section 1.4.2) is sensitive to certain ratios; namely, a scale-length ratio (magnetic footpoint structure to photospheric flow) and a time-scale ratio (reconnection/relaxation time to photospheric flow). When the latter is greater than one, the coronal loop develops a non-linear force-free field; thus, the energy accrued during the path to catastrophe can be released.

Helicity conservation and the invariant nature of the relaxed α-profile, imply that helicity has simply become more evenly distributed within the loop. The relaxed α can be calculated, which means the amount of magnetic energy liberated during relaxation can also be determined. Such a calculation gives an upper limit to the heating event energy, since a strictly linear force-free state may not be attained. Furthermore, how much of the energy released goes into heating, depends on the plasma response, which is outside the scope of the model presented later.

Observing plasma relaxation in the corona is a huge challenge; this is mainly down to the difficulty in making reliable measurements of the coronal magnetic field and in determining the current profile within individual loops. Evidence suggestive of relaxation has come in measuring/estimating the correlation between changes in magnetic free energy and the occurrence of X-class flares (Figure 1.8). Jing et al. (2009) estimated the temporal variation in free magnetic energy using a non-linear force-free extrapolation of photospheric magnetograms taken by the Big Bear Solar Observatory. They found that each X-class[3] flare in a set of four occurred after a sustained ($\sim$15 min) decline in magnetic free energy, the inference being that each decline was the result of plasma relaxation.

A more direct claim for Taylor relaxation has been made by Nandy et al. (2003). They collected magnetogram data by conducting repeated observations of 82 active regions. Within each region, the component of α along the line of sight ($\alpha_z = \mu_0(J_z/B_z)$) was measured at separate positions (wherever the transverse magnetic field was sufficiently free from noise). Hence, each region was assigned a value for the α_z variance, which was then recalculated as the active region moved across the solar disk. Nandy et al. also examined the X-ray fluxes over the same time period for the same active regions. This enabled them to compare flare-productivity measures, which they call integrated flare energy fluxes (Figure 2.12), with α_z variances. The authors report a

---

[3] Solar flares are rated according to the peak X-ray flux (0.1–0.8 nm) measured by satellites in Earth orbit. X-class flares have fluxes $\geq 10^{-4}$ W m^{-2}.

negative correlation coefficient (the stated confidence level is 98.95%) between these two properties: the more productive an active region is in terms of flaring, the closer it will be to a fully relaxed state. Nandy et al. go further and attempt to estimate a

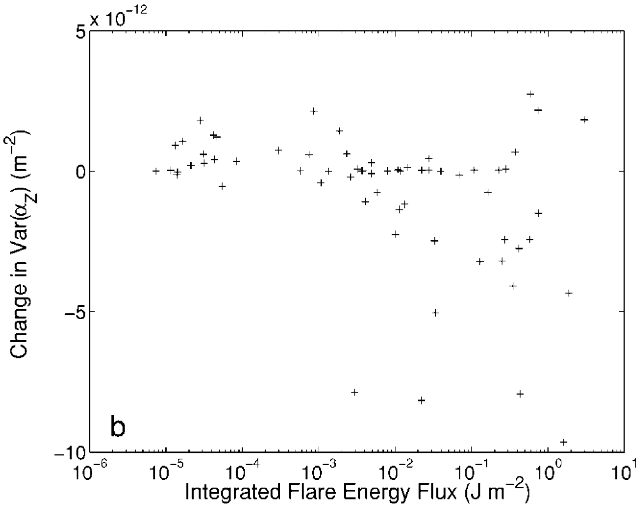

Figure 2.12: Each cross represents an active region. The smaller the variance in α_z, the closer a region is to a fully relaxed state. The higher the flare energy flux the greater the number of flares observed over the active region. Courtesy of Nandy et al. (2003).

time scale for relaxation, which they find to be significantly longer (∼1 week) than that observed for photospheric footpoint motions (∼1 day). These findings are consistent with the idea that relaxation can only happen once magnetic stresses have accrued to a certain level. It will be interesting to see if other workers reach the same conclusions when they investigate other groups of active regions.

We are now ready to combine the theoretical ideas discussed in this chapter (all of which have experimental/observational support) into an analytical model. The aim of this model is to understand the conditions for coronal loop kink instability, and to explore the relationship between a coronal loop ensemble and the distribution of heating events (i.e., the nanoflare population) that it produces. In this way, it can be determined if the ideas presented here could explain the coronal heating that transpires above active regions.

This model, representing an ensemble of coronal loops, is presented in the next chapter. It incorporates random photospheric driving, linear kink instability, energy release and Taylor relaxation. In Chapter 4, the assumptions regarding non-linear instability and relaxation theory are tested by a non-linear 3D MHD code. At this point, a more realistic loop configuration is introduced, one that is compatible with localised photospheric twisting. The findings of Chapter 4 are then used to improve the ensemble model. Other enhancements are also included, all of which are discussed in Chapter 5, along with the revised results.

3

The Heating Caused by Continual Relaxations Triggered by Kink Instability

Coronal heating is strongest in active regions (Section 1.4). An investigation of whether or not this unexplained heating could be (partly) related to magnetic field instability, first requires a model that represents a collection of magnetic structures common to active regions. These structures will need to be simplified versions of the field geometries associated with coronal loops — the widely-used cylindrical geometry gives analytical expressions for fields and related quantities.

This thesis defines a coronal loop as a section of closed magnetic field that, when brought to some instability, heats the corona and illuminates the general shape of the field. Before then, the coronal loop is considered to evolve through equilibria as it is driven by photospheric footpoint motions. The reader should view the 171 Å images (Figures 1, 1.6) as bundles of strands that are located at the places within loops where heating has occurred.

Sustained photospheric driving will eventually cause a loop to undergo some type of energy-releasing catastrophe. This is modelled here by the ideal MHD kink instability: an ideal instability is necessary in order to be consistent with the observed rapidity of flare onset. Ideal conditions mean there is no resistivity to dissipate magnetic energy; nevertheless, many 3D MHD models have shown how coronal loops exhibit current sheet formation during the non-linear growth of said instability (Baty and Heyvaerts 1996; Velli et al. 1997; Arber et al. 1999; Baty 2000). Essentially, helical current sheets become the site of ohmic dissipation, resulting in a heating event. Further simulations have revealed the appropriate correlation between magnetic energy dissipation and ohmic heating (Browning et al. 2008; Hood et al. 2009). Once a linear instability has achieved a positive growth rate, it will soon become non-linear: at this point, current sheets will form wherein fast reconnection of the magnetic field can take place. These expectations are justified by the results of the cited numerical simulations and by the results that will be presented in the next chapter. The kinds of magnetic field considered by this thesis (Chapters 3–5) have simple topologies that describe single isolated loops — this work disregards the heating caused by magnetic reconnection between loops or by a loop reconnecting with an overlying coronal field.

In summary, a relaxation event is triggered when the loop's field becomes linearly unstable (Browning and Van der Linden 2003). Relaxation theory is the means by which energy releases are estimated; this approach is generally supported by the results from non-linear simulations, especially pertinent examples are shown in Chapter 4. This chapter mostly represents the work published in Bareford et al. (2010) — it extends the work of Browning and Van der Linden (2003) and Browning et al. (2008) by allowing a loop to *repeatedly undergo relaxation* as it evolves within a 2D parameter space.

3.1 Equilibrium Fields

The magnetic field is $\vec{B} = B_\theta(r)\hat{\theta} + B_z(r)\hat{z}$ (Section 2.1) and the α-profile ($\nabla\times\vec{B} = \alpha(r)\vec{B}$) is approximated by a piecewise-constant function featuring two parameters (Browning and Van der Linden 2003). This design, first proposed by Melrose et al. (1994), is readily extensible: extra layers of constant α can be inserted to obtain more realistic profiles. The ratio of current to magnetic field is α_1 in the core, α_2 in the outer layer and zero in the potential envelope. Any α-profile that might result from random convective motions can be approximated by some combination of α_1 and α_2. Note, the magnetic field is continuous everywhere (though the current has discontinuities). Recent work indicates that these α discontinuities do not introduce artificial effects. Hood et al. (2009) simulated linearly unstable loops described by continuous and discontinuous α-profiles. The differences in the results generated by the two types of loop (e.g., energy release and final magnetic field) were found to be qualitatively similar.

An idealised model of a straight cylindrical loop with constant radius (Figure 3.1, left) is used with the photosphere represented by two planes at $z = 0, L$; however, the essential physics should apply to more complex geometries. The loop model shown in Figure 3.1 was first used by Browning and Van der Linden (2003) and then extended by Browning et al. (2008) to include a potential envelope. Here, this model is expanded

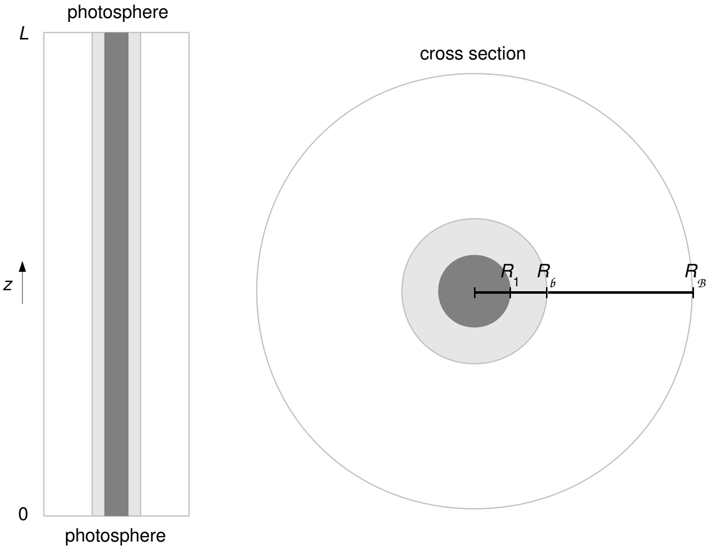

Figure 3.1: Schematic of a straightened coronal loop in the r-z plane (left) and in the r-θ plane (right). The loop, comprises a core (dark grey) and an outer layer (light grey); it is embedded in a potential envelope (white). The core radius is half the loop radius and 1/6 the envelope radius (R_1:$R_{\mathscr{b}}$:$R_{\mathscr{B}}$ = 0.5:1:3). The loop's aspect ratio ($L/R_{\mathscr{b}}$) is 20.

further so that it encompasses a particularly homogeneous loop ensemble: all loops have the same size and undergo the same type of photospheric driving. In addition, the loops are isolated from one another and each carries a net current (i.e., there is azimuthal field outside the loop). At this stage, the ensemble is deliberately simplistic. This has two benefits: it is easier to check for errors in the code that represents the initial model and secondly, as more realistic features are incorporated, it should be possible to gauge which of these are most important to coronal heating.

Without an envelope, the loop's outer surface (located at $R_{\mathscr{b}}$) is surrounded by a conducting wall (Browning and Van der Linden 2003). This is unrealistic in the context of the solar corona; the loop would be more stable than it might be otherwise. Browning et al. (2008) plotted the relationship between the growth rate of the instability and the distance to the outer surface of the potential envelope (i.e., a more distant conducting wall). They found that for six unstable loop states the growth rate was invariant once the outer surface of the envelope ($R_{\mathcal{B}}$) exceeded $\frac{3}{2}\,R_{\mathscr{b}}$. The $R_{\mathcal{B}}$ boundary is placed at twice this value.

The equilibrium identified by Equations 2.9 and 2.11 can be expressed in the form of Bessel differential equations (Section 2.1), which in turn lead to the field equations.

$$
\begin{aligned}
B_{1z} &= B_1 J_0(|\alpha_1| r)\,, && && (3.1)\\
B_{1\theta} &= \sigma_1 B_1 J_1(|\alpha_1| r)\,, && 0 \le r \le R_1\,, && (3.2)
\end{aligned}
$$

$$
\begin{aligned}
B_{2z} &= B_2 J_0(|\alpha_2| r) + C_2 Y_0(|\alpha_2| r)\,, && && (3.3)\\
B_{2\theta} &= \sigma_2 (B_2 J_1(|\alpha_2| r) + C_2 Y_1(|\alpha_2| r))\,, && R_1 \le r \le R_{\mathscr{b}}\,, && (3.4)
\end{aligned}
$$

$$
\begin{aligned}
B_{3z} &= B_3\,, && && (3.5)\\
B_{3\theta} &= \sigma_2 \frac{C_3}{r} R_{\mathscr{b}}\,, && R_{\mathscr{b}} \le r \le R_{\mathcal{B}}\,. && (3.6)
\end{aligned}
$$

These expressions will change slightly whenever α_1 or α_2 become negative; these alterations are captured by σ symbols: $\sigma_1 = \frac{\alpha_1}{|\alpha_1|}$, $\sigma_2 = \frac{\alpha_2}{|\alpha_2|}$ and $\sigma_{1,2} = \sigma_1 \sigma_2$. (The sign of an α value merely denotes the orientation of the azimuthal field.) Also, the fields must be continuous at the radial boundaries, R_1 and $R_{\mathscr{b}}$. Therefore, the constants B_2, B_3, C_2 and C_3 can be expressed like so:

$$B_2 = B_1 \frac{\sigma_{1,2} J_1(|\alpha_1|R_1) Y_0(|\alpha_2|R_1) - J_0(|\alpha_1|R_1) Y_1(|\alpha_2|R_1)}{\Delta}, \tag{3.7}$$

$$C_2 = B_1 \frac{J_0(|\alpha_1|R_1) J_1(|\alpha_2|R_1) - \sigma_{1,2} J_1(|\alpha_1|R_1) J_0(|\alpha_2|R_1)}{\Delta}, \tag{3.8}$$

$$B_3 = B_2 F_0(|\alpha_2|R_{\mathscr{b}}), \tag{3.9}$$

$$C_3 = B_2 F_1(|\alpha_2|R_{\mathscr{b}}), \tag{3.10}$$

where

$$\Delta = Y_0(|\alpha_2|R_1) J_1(|\alpha_2|R_1) - Y_1(|\alpha_2|R_1) J_0(|\alpha_2|R_1) = \frac{2}{\pi|\alpha_2|R_1}, \tag{3.11}$$

$$F_{0,1}(x) = J_{0,1}(x) + \frac{C_2}{B_2} Y_{0,1}(x). \tag{3.12}$$

At all times, the total magnetic flux (through the loop and envelope) is conserved:

$$\begin{aligned} \psi &= \int_0^{R_{\mathscr{B}}} 2\pi r B_z \, dr = \frac{2\pi B_2}{|\alpha_2|} R_{\mathscr{b}} F_1(|\alpha_2|R_{\mathscr{b}}) \\ &\quad + 2\pi R_1 B_1 J_1(|\alpha_1|R_1) \left(\frac{1}{|\alpha_1|} - \frac{\sigma_{1,2}}{|\alpha_2|} \right) \\ &\quad + \pi B_2 F_0(|\alpha_2|R_{\mathscr{b}}) \left(R_{\mathscr{B}}^2 - R_{\mathscr{b}}^2 \right). \end{aligned} \tag{3.13}$$

In the model, the total flux is dimensionless and set to one; hence, B_1 can be determined (noting that, in Equation 3.13, B_2 is a function of B_1). The loop length is expressed in units of the loop radius, $R_{\mathscr{b}}$. As the random motions of the photosphere proceed, the loop evolves through a series of force-free equilibrium states until it becomes linearly unstable. In this chapter, the results for the profiles (Equation 3.1–3.6) are discussed, which in general carry a *net* loop current. Hence, $B_\theta \neq 0$ in the potential envelope (except for special combinations of α_1 and α_2, see Hood et al. (2009)). Profiles with *zero* net current are discussed later (Chapter 5). The next section discusses the calculation of instability onset.

3.2 Linear Kink Instability Threshold

Coronal loop stability is enhanced by the line-tying of the photospheric footpoints (Hood 1992). This means all unstable modes are required to vanish at the loop ends ($z = 0, L$). A linear perturbation can be decomposed as a sum, $\sum_{m=0}^{\infty} \tilde{f}(r, z)e^{im\theta}e^{\gamma t}$, where f represents any perturbed quantity and γ is the growth rate of the instability. However, we need only consider the $m = 1$ term since this azimuthal mode is the least stable (Van der Linden and Hood 1999). The effects of such perturbations on the coronal loop are represented by the standard set of linearised ideal MHD equations (the original forms of these equations are given in Section 2.1),

$$\frac{\partial \rho_1}{\partial t} + \rho_0\left(\nabla \cdot \vec{v}_1\right) = 0\,, \tag{3.14}$$

$$\rho_0 \frac{\partial \vec{v}_1}{\partial t} = \frac{1}{\mu_0}\left(\nabla \times \vec{B}_1\right) \times \vec{B}_0 - \nabla P_1\,, \tag{3.15}$$

$$\frac{\partial P_1}{\partial t} - \frac{\Gamma P_0}{\rho_0}\frac{\partial \rho_1}{\partial t} = 0\,, \tag{3.16}$$

$$\frac{\partial \vec{B}_1}{\partial t} = \nabla \times \left(\vec{v}_1 \times \vec{B}_0\right), \tag{3.17}$$

$$\nabla \cdot \vec{B}_1 = 0\,, \tag{3.18}$$

where ρ is the plasma density, v is the plasma flow velocity, B the magnetic field and P the thermal pressure. Background and perturbed terms are denoted by the 0 and 1 subscripts respectively. Adiabatic conditions are assumed (Equation 3.16) and Γ, the ratio of specific heats, is $\frac{5}{3}$ for an ionised plasma.

A linear instability occurs when the growth rate, γ, transitions from a negative value to a positive one. The instability threshold is therefore a curve in 2D α-space (α_1, α_2). The properties of the loop (e.g., α_1 and α_2) at these threshold points can be found by substituting the perturbation function into the linearised MHD equations, leading to an eigenvalue equation for the growth rates (Priest 1987, Chap. 7). Equation 3.15 can be expressed in terms of v_1, γ and the background quantities. In fact v_1 appears in every term, which allows the equation of motion to be expressed in matrix form,

$$\mathbb{A} - \gamma^2 \mathbb{B} \begin{bmatrix} r v_{1r} \\ v_{1\perp} \end{bmatrix} = 0\,, \tag{3.19}$$

where $\mathbb{A}$ and $\mathbb{B}$ are matrices that contain the radial and perpendicular (with respect to the magnetic field) components of the equation of motion, and v_{1r} and $v_{1\perp}$ are the radial and perpendicular components of the velocity perturbation. The parallel component can be ignored if the thermal pressure is assumed to be negligible.

The growth rates and eigenfunctions of the most unstable modes are found numerically, for line-tied fields, with the CILTS code, described in Van der Linden (1991); Brennan (2000); Browning and Van der Linden (2003); Browning et al. (2008). This code uses a bicubic Hermite finite element method to discretise the r and z dependencies. Since the background magnetic field is expressed in terms of α_1 and α_2, CILTS can determine a relationship between the growth rate of the instability and the α-parameters. The inverse iteration method is used to calculate the growth rate for a given (α_1, α_2). An initial guess is supplied to the procedure and the guess is improved after each iteration. However, if the first guess is too high, the procedure will fail to converge[1] and a solution cannot be produced. CILTS has been automated so that when this occurs, the guess is reduced according to a user-specified scheme, until convergence is achieved or until the initial guess reaches a defined limit. A disadvantage of the inverse iteration method is that non-convergence does not imply stability; nevertheless stability is assumed if the method does not converge for an initial squared growth rate of 10^{-8}.

---

[1] CILTS was configured to iterate no more than twenty times.

The 2D parameter space represented by α_1 and α_2 is stable (to kink perturbations) near the origin, but will be unstable for sufficiently high α values. Typically, CILTS starts with one of these unstable configurations, determines the growth rate and then moves towards the α_2-axis (keeping α_2 constant). The code declares a stable configuration when the real part of the growth rate falls below zero or when the initial guess becomes too low. In this way, a threshold for linear kink instability can be located. The generation of such maps has revealed that non-converged stable points are always discovered after true stable points (i.e., closer to the α_2-axis).

The left plot of Figure 3.2 shows the closed instability threshold curve mapped by the CILTS code (see also Figure 5 of Browning et al. (2008)). The threshold curve has symmetry: it is invariant when rotated by π radians. It is sufficient therefore, to show how various properties (e.g., magnetic twist and energy release) vary along the top half of the threshold curve. For ease of plotting, this half of the threshold is converted to a one-dimensional (1D) form: the filled circles and bold numbers shown in the right plot of Figure 3.2 represent the tick marks and labels for the 1D threshold point axis, see Figures 3.6 – 3.9. It is important to remember that the threshold only applies to the specific loop geometry outlined above. A new threshold would need to be calculated should the structure of the loop (or envelope) change as a consequence

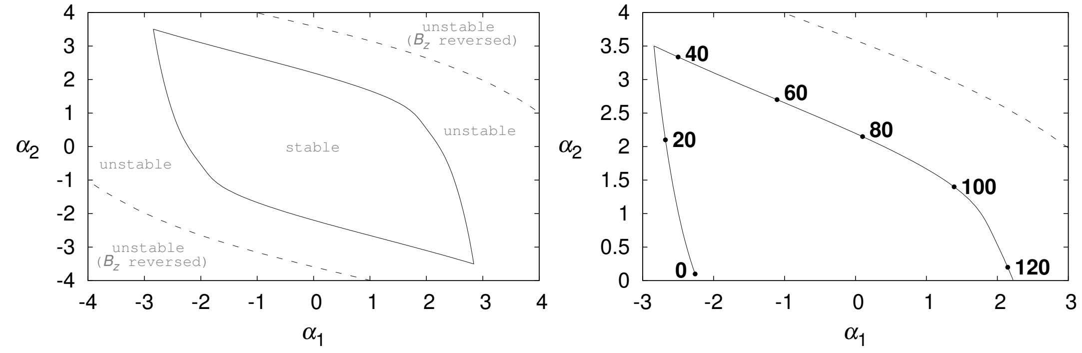

Figure 3.2: The left plot shows the closed instability threshold (solid) with the B_z reversal lines (dashed). The top half of the threshold (where $\alpha_2 > 0$), annotated with threshold point numbers, is shown in the right plot.

of some activity. Another caveat is that there are some points in α-space that yield singularities when calculating quantities such as helicity or magnetic energy (Section 3.4). These arise when the axial field (B_z) has a significant region of reversal (this is a consequence of the oscillatory behaviour of the underlying Bessel functions). The (dimensionless) magnetic flux is normalised and conserved: $\psi = \psi_* B_1 = 1$, where ψ_* is the unnormalised flux. As ψ_* tends to zero, B_1 approaches infinity, as do helicity and magnetic energy. Fortunately, the instability threshold does not enter the region where B_z begins to pass through zero (see dashed lines in Figure 3.2), so these singularities are not encountered.

3.3 Random walk

When a loop undergoes stochastic twisting motions at the photosphere, it performs a random walk through the α-space enclosed by the instability threshold (Figure 3.3). This traversal of α-space is modelled as a series of steps, random in direction but constant in length (initially, the dimensionless step-length, $\delta\alpha$, is set to 0.1). Clearly, the nature of this random walk depends on the statistical properties of the driving photospheric motions; in later chapters, different forms of random driving will be investigated, but for now, the simplest assumptions are taken.

The time unit τ is the step time, the time taken for α to change by $\delta\alpha / R_б$ (in dimensional units). A time scale for this process can be roughly estimated as follows. First, we derive an approximate value for the axial twist: ϕ_0 is the limit of $LB_\theta(r')/rB_z(r')$ as $r' \rightarrow 0$. For the field within the loop core, $\nabla \times \vec{B} = \alpha_1 \vec{B}$ implies

$$\frac{1}{r}\left[\frac{d}{dr}\Big(rB_\theta(r')\Big)\right]\hat{z} \quad = \quad \alpha_1 B_z(r')\,\hat{z}\,, \tag{3.20}$$

where $B_z(r') \rightarrow B_1$, $B_\theta(r') \rightarrow Dr$ and D is a constant; thus, using Equation 3.20, $D = \alpha_1 B_1/2$ and $\phi_0 = \alpha_1 L/2$. Based on this ϕ_0 value, a change $\delta\alpha$ corresponds to a change in magnetic twist, $\delta\phi = (L/2)(\delta\alpha/R_б)$; taking $L/R_б = 20$ gives $\delta\phi = 1$. If this is caused by photospheric twisting motions of magnitude v_θ for a time interval τ, we find

$\tau = (\delta\phi)R_{\rm ft}/v_\theta$, where $R_{\rm ft}$ is the footpoint radius, which is likely to be significantly less than $R_{\mathcal{B}}$. Typical values of $R_{\rm ft} = 200\,\rm km$ and $v_\theta = 1\,\rm km\,s^{-1}$ give a time unit of $\tau = 200\,\rm s$; note, this is consistent with quasi-static evolution, justifying *a posteriori* our choice of random-walk step size.

The step time may also be identified with the correlation time of photospheric motions, which is likely to be rather longer than the value given above (hence, the initial choice for $\delta\alpha$ is perhaps unrealistically small); for example, a granule lifetime of 1000 s may be more appropriate (Zirker and Cleveland 1993). The effect of increasing the step length ($\delta\alpha$) is considered in Section 3.6.4 ($\lambda = 0.1$).

Eventually, the field will reach the instability threshold: it will become linearly unstable. At this point, the field releases energy and transitions to a lower energy state defined by Taylor relaxation; helicity is conserved and the α-profile relaxes to a single value.

3.4 Energy Release Calculation

Initially, a loop starts from a randomly-selected stable state. The field profile then undergoes a random walk until it crosses the instability threshold; whereupon, the loop relaxes and the profile transitions to the relaxation line ($\alpha_1 = \alpha_2$). The constant α-value (α_e) will vary depending on where the threshold was crossed. It is found by helicity conservation (Browning and Van der Linden 2003), from the roots of the following equation,

$$K(\alpha_e) - K(\alpha_{\rm i1}, \alpha_{\rm i2}) \;=\; 0\,, \tag{3.21}$$

where $\alpha_{\rm i1}$ and $\alpha_{\rm i2}$ are the coordinates of the instability threshold crossing, and α_e is the position on the relaxation line. (Conservation of axial flux is ensured through the normalisation $\psi = 1$.) The helicity can be expressed as follows:

$$K \;=\; 2L \int_0^{R_{\mathcal{B}}} \frac{I(r)\,\psi(r)}{r}\,dr\,, \tag{3.22}$$

where $I(r)$ is the current,

$$
\begin{aligned}
I &= r\sigma_1 B_1 J_1(|\alpha_1| r), & 0 \le r \le R_1\,, \qquad (3.23)\\
I &= r\sigma_2\Big[B_2 J_1(|\alpha_2| r) + C_2 J_1(|\alpha_2| r)\Big], & R_1 \le r \le R_{\mathscr{b}}\,, \qquad (3.24)\\
I &= \sigma_2 C_3 \frac{R_{\mathscr{b}}}{r}, & R_{\mathscr{b}} \le r \le R_{\mathscr{B}}\,, \qquad (3.25)
\end{aligned}
$$

and L is the loop length (Finn and Antonsen 1985). The equation for the magnetic energy contained within the loop and envelope is straightforward:

$$
W = \frac{L\pi}{\mu_0} \int_0^{R_{\mathscr{B}}} r B^2 \, dr\,, \qquad (3.26)
$$

where L is normalised to 20 (since $R_{\mathscr{b}} = 1$) and μ_0 is set to 1, see Appendix A for the full expressions. The energy difference between the unstable and relaxed states can be calculated as

$$
\delta W = W(\alpha_{\mathrm{i}1}, \alpha_{\mathrm{i}2}) - W(\alpha_e)\,. \qquad (3.27)
$$

This is the relaxation energy, the energy released as heat during the event.

Although the initial loop (before the random walk begins) is axisymmetric, it does not necessarily follow that the relaxed state — the aftermath of a non-linear kink instability — will also be symmetric. Taylor (1974, 1986) showed that the minimum (i.e., relaxed) energy state is helical for fields with large currents. The relaxed energy state is the cylindrical Bessel function field, as assumed by the model, if $\alpha_e R_e < 3.11$, where $R_{\mathscr{b}} \le R_e \le R_{\mathscr{B}}$ is the radius of the relaxed loop. If the helicity exceeds some critical value, the field with lowest energy has the fixed value $\alpha_e R_e \approx 3.11$ and is a combination of the axisymmetric and first helical modes. The helicity becomes critical if it is greater than or equal to the helicity of a relaxed loop where $\alpha_e = \frac{3.11}{R_e}$; in other words, $K_{\mathrm{crit}} = K_e(3.11/R_e)$, where K_e is the helicity from R_0 (axis) to R_e. The energy of the relaxed loop that features helical modes is as follows,

$$
W_e = \frac{|\alpha_e|}{2\mu_0}\left[|K_e| + \frac{L}{2\pi R_e}\frac{J_0(|\alpha_e| R_e)}{J_1(|\alpha_e| R_e)}\big(\psi_e\big)^2\right]. \qquad (3.28)
$$

This complication does not apply to the instability threshold of Figure 3.2: none of the threshold states map to helical (i.e., non-axisymmetric) relaxed states.

When the loop relaxes, the α-profile throughout the loop and envelope becomes constant. The envelope is no longer potential; it has acquired a residual current. In principle, as the main portion of the loop is twisted again by ongoing motions, a new equilibrium would develop with varying current (α_1, α_2) in the loop and a non-zero current (α_3) in the envelope. For some threshold sections, the consequent residual current is so small that the threshold shape would remain unchanged. However, the validity of the simulation process can only be safeguarded by including an extra stage, wherein the envelope dissipates its helicity so that it becomes potential again. The loop can now resume its random walk with respect to the same threshold and the overall process can repeat many times (as illustrated by Figure 3.3). Hence, a sequence of energy release events is generated, which can be collated to produce a nanoflare energy distribution, see Section 3.6.2. The whole process is performed by a computer model (written in C++) called TRoLE (**T**aylor **R**elaxation **o**f **L**oop **E**nsembles). Note, every

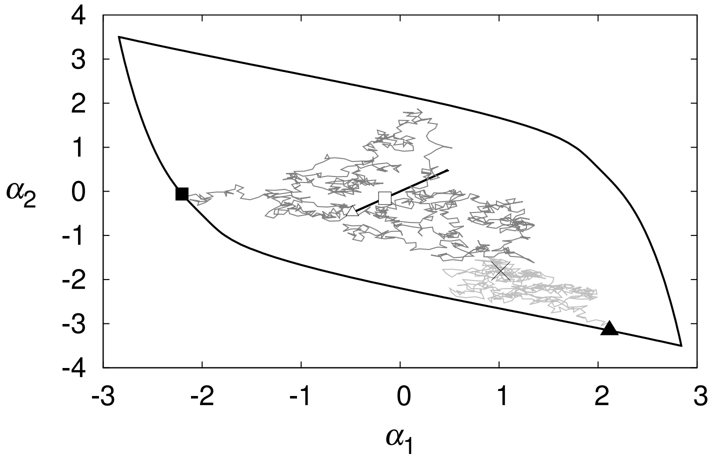

Figure 3.3: The instability threshold encloses the relaxation line, which is a subsection of the $\alpha_1 = \alpha_2$ line centred on the origin. The annotations illustrate the initial stages of a simulation that begins at the position marked by the cross. The first random walk is shown in light grey; it ends at the threshold position marked ▲ and the associated relaxation point is indicated by △, which is the starting point for a second random walk (dark grey). This walk attains instability onset at the position marked ■ and relaxes to the point labelled □ — the starting point for a third walk.

threshold point maps to a single point on the relaxation line, which fortunately does not intersect the threshold; otherwise, the loop that has the property $\alpha_1 = \alpha_2$ would not be able to relax.

Although the primary purpose of this model is to calculate the distribution of energy releases, in achieving this, some interesting new results on linear stability are also obtained, which are summarised in the next section. This is because, in order to explore the full parameter space of equilibrium current profiles, the linear stability properties are calculated for a much wider family of fields than previously investigated: in particular, fields with reversed twists.

3.5 Instability Threshold and Critical Twist

The evolution of the field profile through α-space is determined by photospheric perturbations which map to changes in the magnetic field, and hence, to changes in α_1 and α_2. A loop's magnetic twist (Equation 2.16) is more directly related to rotational photospheric motions. Thus, these motions determine the ϕ-profile, which in turn determine $\alpha(r)$ (and hence, in this model, α_1 and α_2). The magnetic twist of coronal loops is an observable feature (Kwon and Chae 2008). Portier-Fozzani et al. (2001) have even observed a loop's twist decreasing over time — evidence perhaps of a loop evolving towards a state of minimum energy.

3.5.1 Criteria for Instability

Many workers have looked at the idea that the closeness of a loop to kink instability could be deduced from measuring the magnetic twist. For example, a loop with a uniform twist profile has a critical twist of 2.49π (Hood and Priest 1981), see Section 2.2. The question arises as to whether there is any single parameter (such as peak or average twist) which determines instability onset for *all* twist profiles. Indeed, more generally, it would be desirable to have a single quantity determining instability onset even for more complex (non-cylindrical) fields (Malanushenko et al. 2009). It is possible to calculate the stability properties for an extensive family of equilibria (Figure 3.2), including fields with reversed twist (as well as simple monotonic-twist profiles as used by other workers). This provides a very useful test for any proposed criteria for instability onset.

Loops with variable-twist profiles have been studied; however, all such profiles generally have a similar form (Mikic et al. 1990; Velli et al. 1990; Baty 2001): the axial twist is the maximum, then the twist declines to a negligible value at the loop boundary. Velli et al. calculated that instability occurred when $\phi_0 = \phi(r{=}0) = 2.5\pi$; this agrees with Hood and Priest's result for a uniform twist profile. Mikić et al. calculated a critical axial twist of 4.8π, the loop's average twist however, was $\sim 2.5\pi$.

The idea of using magnetic twist as a marker for instability relies on the existence of some twist-derived parameter having a constant value for all the points on the instability threshold. Baty (2001) used a MHD stability code to show that for a small set of equilibria the average twist at instability is the same for several different magnetic configurations. However, there are several differences between Baty's work and the model presented here. First, the twist profiles defined for each equilibrium are all positive and none contain multiple peaks (Baty 2001, Figure 1). Furthermore, critical twist convergence arises when a normalised distance, d, is greater than 5 (Baty 2001, Figure 5), where

$$d = \frac{\phi_0 R_b}{L}. \tag{3.29}$$

In our equilibria, $d = \phi_0/20$; the threshold values of the absolute axial magnetic twist vary from zero to 9π, which means d varies from 0 to 1.42, and we are not in the regime where the critical axial twist should approximate to 2.5π. In fact, the large d regime cannot be attained for the parameters used in this model.

The idea of a single critical average twist seems unlikely when one examines the threshold presented here (Figures 3.2, 3.3). Clearly, at some threshold points α_1 and α_2 are of opposite sign; thus, one or two places on the threshold will have an average twist equal to zero, and yet they are unstable. Perhaps critical twist is achieved within a subsection of the loop; this idea is explored further in Sects. 3.5.2 and 3.5.3.

3.5.2 Radial Twist Profiles and Linear Eigenfunctions

In order to understand the nature of the instability, the twist profiles and eigenfunctions of the unstable mode, for different parts of the instability threshold, are investigated. The magnetic twist profiles for a selection of points just outside the threshold curve exhibit considerable variation, as Figure 3.4 demonstrates. For the unstable equilibrium labelled as point **b** ($\alpha_1 < 0, \alpha_2 > 0$), the corresponding twist profile (also labelled **b**) shows that the core field has a strong negative twist, whilst in most of the outer layer and in all of the envelope the field has positive twist. As one moves from **a** to **b**, the twist in the core becomes more negative, whilst the twist in the outer layer moves in the opposite direction. It appears that the increase in α_2 stabilises the negative core twist by providing additional reversed (i.e., positive) twist in the outer layer. The sharp corner at the top left of the threshold marks the point where instabilities driven within the core intersect those that originate from within the outer layer. Profiles **c** to **d** therefore, suggest instabilities driven in the outer layer, since $|\alpha_2| > |\alpha_1|$. The peak twist in

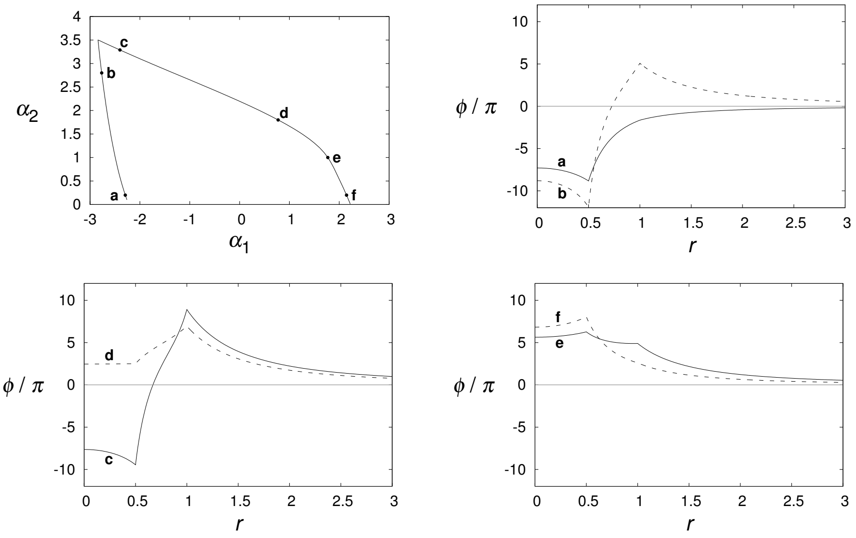

Figure 3.4: The radial twist profile at specific points along the threshold (labelled **a**–**f**).

the outer layer reduces as the core twist moves from negative to positive. Further along the threshold, where $\alpha_1 > \alpha_2$, the instabilities are likely to be driven in the core. Note, profiles **d**, **e** and **f** are always positive in sign; **d** has a twist peak near the loop edge while **e** and **f** are roughly monotonically decreasing. The corresponding magnetic field profiles for the six points **a**–**f** are given in Appendix B.1. It seems that instabilities are

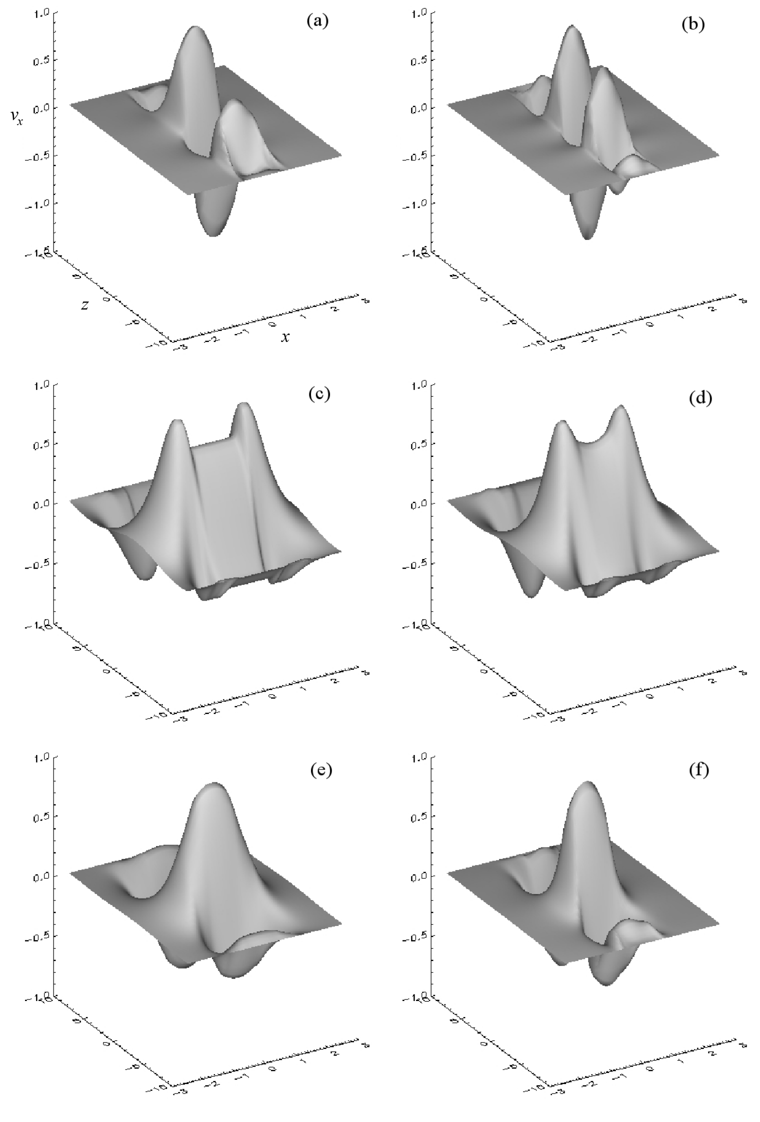

Figure 3.5: The linear eigenfunction, $v_x(x, y{=}0, z)$, for the α-space points profiled in Figure 3.4: these are **a** (top left), **b** (top right), **c** (middle left), **d** (middle right), **e** (bottom left) and **f** (bottom right). Cartesian coordinates are used, hence, the x-axis is equivalent to the radial axis.

driven mainly on or near the peak of largest absolute twist, but a twisted field region may be stabilised by an enclosing region of opposite twist. Furthermore, a twisted outer layer may need less twist to achieve instability if the core has the same twist orientation.

To investigate these ideas further, the unstable eigenfunctions obtained from CILTS for the same α-space points, **a** to **f**, are plotted. The eigenfunctions for profiles **a** and **b** (Figure 3.5, top row) show that the amplitude is strongest in the core. Interestingly, the amplitude for profile **a** has dropped to zero long before the envelope boundary at $R_{\mathscr{B}}$, which suggests that in the subsequent relaxation only inner regions will be affected, with little change in the potential envelope. There is a strong similarity between the eigenfunctions for profiles **c** to **d** (Figure 3.5, middle row) and the amplitude is highest near the $R_{\mathscr{b}}$ boundary, indicating an outer layer instability. Finally, the two plots in Figure 3.5 (profiles **e** and **f**, bottom row), clearly show a progression towards the eigenfunction calculated for **a** (albeit with a v_x of opposite sign). Notice also that the form of the eigenfunction changes significantly between **b** and **c**, indicating that different modes are going unstable. This is expected, since the α-space positions labelled **b** and **c** (Figure 3.4, top left) are either side of the intersection point formed by the two curves that describe the instability threshold.

3.5.3 Critical Twist Parameters

This section looks for a twist-related parameter that takes on a critical value whenever the loop reaches the threshold. As expected, the variation in axial twist, ϕ_0, is similar to the variation in $\phi(R_1)$, see Figure 3.6. None of the quantities suggests any single (constant) critical value. Perhaps, the average twist is less variable around the threshold?

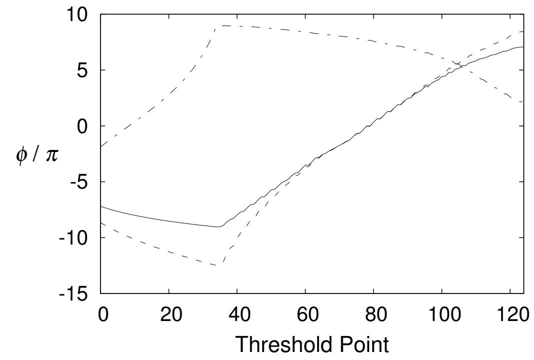

Figure 3.6: The variation in magnetic twist around the instability threshold (the threshold point axis is defined in Figure 3.2) for three radial positions. The solid line represents the variation in axial twist, ϕ_0; the dashed line is the variation in twist at the boundary between the core and the outer layer, $\phi(R_1)$; and the long-short dashed line is the variation in twist at the boundary between the outer layer and the potential envelope, $\phi(R_{\mathscr{b}})$.

There are several ways to calculate this property:

$$\langle\tilde{\phi}\rangle_{i,j} = \frac{\int_{R_i}^{R_j} LB_\theta(r)\,dr}{\int_{R_i}^{R_j} rB_z(r)\,dr} , \tag{3.30}$$

$$\langle\hat{\phi}\rangle_{i,j} = \frac{1}{R_j - R_i}\int_{R_i}^{R_j} \frac{LB_\theta(r)}{rB_z(r)}\,dr , \tag{3.31}$$

$$\langle\phi\rangle_{i,j} = \frac{1}{\pi(R_j^2 - R_i^2)}\int_{R_i}^{R_j} 2\pi r\,\frac{LB_\theta(r)}{rB_z(r)}\,dr , \tag{3.32}$$

where i is the radial lower bound and j is an upper bound (e.g., $R_{\mathscr{b}}$ or $R_{\mathcal{B}}$). The lower bound is dropped if it is zero; e.g., $\langle\phi\rangle_1$ is the average twist between the axis and R_1. Equation 3.32 is the average twist weighted by area. The other two equations (3.30 and 3.31) have been used by Velli et al. (1990) and Baty (2001). Note, Equation 3.30 can be calculated analytically, see Appendix A. $\langle\phi\rangle_{\mathscr{b}}$ denotes the average twist, weighted by area, over the core and outer layer. Similarly, $\langle\phi\rangle_{\mathcal{B}}$ denotes the same quantity but over the loop and potential envelope. The tilde (~) and hat ($\wedge$) symbols are used to indicate the other definitions of average twist.

When α_1 and α_2 are equal, there is no distinction between the loop regions; this occurs on the threshold when $\alpha_1 = \alpha_2 \approx 1.4$ — at this point $\langle\phi\rangle_\ell \approx 5\pi$. When $\alpha_1 \approx 2.2$ and $\alpha_2 = 0$, the loop is identical to the core with a bigger potential envelope and $\langle\phi\rangle_1 \approx 7.7\pi$. Thus, as expected, fatter loops like the first case, have lower instability twists than thinner ones. When the loop's core is potential (i.e., when $\alpha_1 = 0$ and $\alpha_2 \approx 2.2$), $\langle\phi\rangle_{1,\ell} \approx 4.5\pi$ is the average outer layer twist. In this configuration, the loop is less stable than the case when only the core is non-potential.

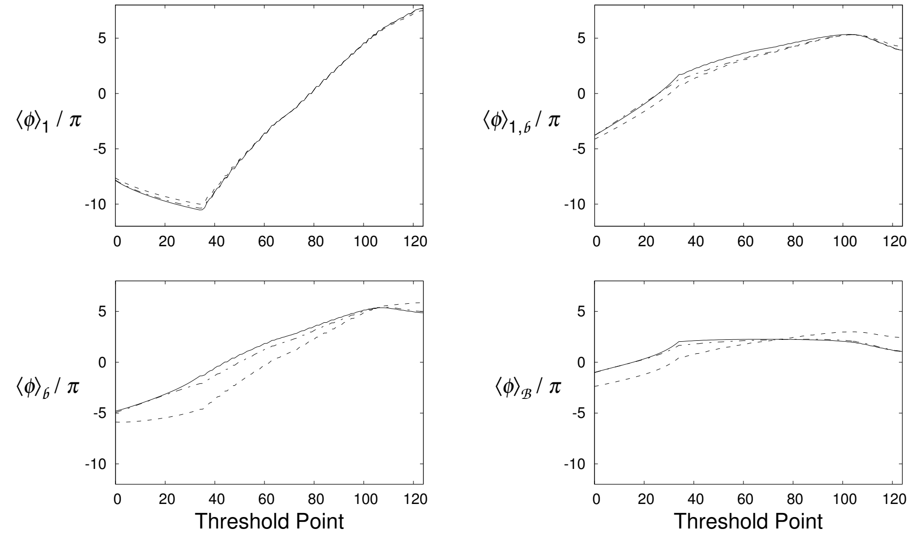

Figure 3.7: The variation in the average twist over the core, $0-R_1$ (top left), the outer layer, R_1-R_ℓ (top right), the loop, $0-R_\ell$ (bottom left) and the loop and envelope, $0-R_{\mathcal{B}}$ (bottom right). The solid lines were calculated according to Equation 3.32; the dashed according to Equation 3.31 and the long-short dashed according to Equation 3.30.

None of the twist averages (Figure 3.7) is invariant along the entire threshold. Although, $\langle\phi\rangle_{\mathcal{B}}$ and $\langle\tilde{\phi}\rangle_{\mathcal{B}}$ have approximately the same value ($\approx 2.2\pi$) between threshold points 40 and 90, all of which show a positive peak twist at R_ℓ. Hence, the envelope's contribution dominates the overall average twist. This is especially true for the $\langle\phi\rangle_{\mathcal{B}}$ case: the higher the radial coordinate the greater the weight of $\phi(r)$. Within the envelope, the twist declines as $1/r$ and so, the inclusion of the envelope twist averages out the final result. Notice also, that all the twist averages go through zero when the core and outer layer have opposite twists. It seems that these quantities do not reveal the detail necessary to understand why a particular loop configuration is on the point of instability, nor where in the loop that instability originates.

Finally, the proposal of Malanushenko et al. (2009) is considered; this states that a critical value of normalised helicity (equivalent, in the terms presented here, to the normalised loop helicity, K/ψ^2, over the range $0-R_6$) indicates instability onset. In fact, the normalised helicity is certainly not the same for every threshold point; this quantity passes through zero because α_1 and α_2 take on values of opposite sign along some sections of the threshold. For fields with single-signed twist, the normalised helicity gives an approximate threshold, but even here, the (absolute) critical value ranges from about $1.5-2.5$. Figure 3.8 shows that the idea of such a critical value breaks down for loops that feature regions of reversed twist.

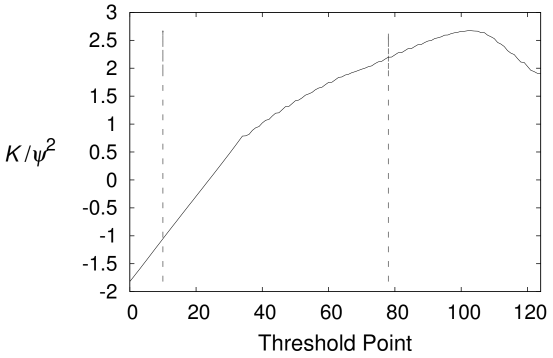

Figure 3.8: The variation in K/ψ^2 (over the range $0-R_6$) along the instability threshold. The threshold states between the vertical dashed lines feature reverse twist; outside the lines the twist is single-signed.

3.6 Distribution of Energies and Coronal Heating Considerations

The results of the main task of the loop ensemble model (TRoLE), which is to calculate the distribution of heating events generated by random photospheric driving, will now be shown.

3.6.1 Helicity and Energy

Figure 3.9 (top left) plots the total helicities of the threshold states. A total helicity (or flux) is one calculated over the range $0 - R_{\mathcal{B}}$, i.e., the loop and envelope. The helicity of these threshold configurations does not exceed the amount required for the relaxed state to feature helical modes (Taylor 1986) — all relaxed states are cylindrically symmetric. The bottom left plot confirms that each threshold state corresponds to a relaxed state. The maximum α_e is about 0.48; hence, there is a good chance that the envelope current after relaxation will not be insignificant. This result confirms the need to investigate how this current could be dissipated (although the maximum value is still significantly less than typical α_1 and α_2 threshold values).

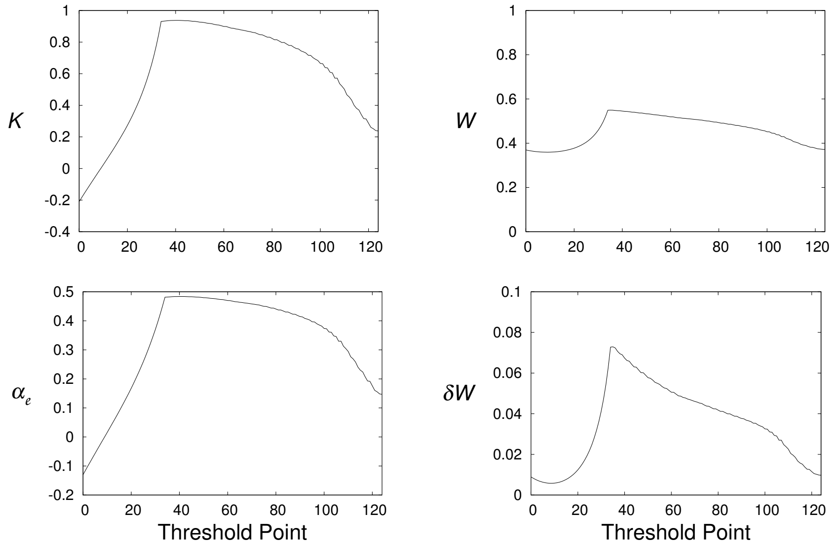

Figure 3.9: Helicity (top left), magnetic energy (top right), relaxed alpha (bottom left) and energy release (bottom right) along the 1D representation of the instability threshold. The energies, W and δW, are dimensionless quantities.

The energies shown in Figure 3.9 (right) are given as dimensionless quantities; in order to calculate the dimensional energy, it is first necessary to give the dimensional flux though the loop and envelope,

$$\psi^* = \int_0^{3R_{\rm cn}} 2\pi r^* B_z^* \, dr^* = R_{\rm cn}^2 \int_0^{R_{\mathcal{B}}} 2\pi r B_z^* \, dr \approx 9\pi R_{\rm cn}^2 B_{\rm cn} \, , \qquad (3.33)$$

where the asterisk superscripts denote dimensional variables. The dimensional constants, R_{cn} (the dimensionlised $R_{\mathcal{b}}$) and B_{cn} are the coronal loop radius and *mean* axial coronal field respectively. Since the flux is normalised such that $\psi = \int_0^{R_{\mathcal{B}}} 2\pi r B_z \, dr = 1$, the field strength can be dimensionlised thus,

$$\psi^* \int_0^{R_{\mathcal{B}}} 2\pi r B_z \, dr \;=\; R_{\mathrm{cn}}^2 \int_0^{R_{\mathcal{B}}} 2\pi r B_z^* \, dr \;\Rightarrow\; B^* \;\approx\; \frac{\psi^*}{R_{\mathrm{cn}}^2} B \,. \tag{3.34}$$

Hence, the dimensional energy release becomes

$$\delta W^* \;=\; \frac{1}{\mu_0} \left(\frac{\psi^*}{R_{\mathrm{cn}}^2} \right)^2 R_{\mathrm{cn}}^3 \, \delta W = \frac{81\pi^2}{\mu_0} \, R_{\mathrm{cn}}^3 B_{\mathrm{cn}}^2 \, \delta W \,. \tag{3.35}$$

Note, the loop length (as a multiple of $R_{\mathcal{b}}$) is incorporated within δW. This expression differs slightly from the one used by Browning and Van der Linden (2003): their dimensionless energy release is calculated per unit length and $R_{\mathcal{b}} = R_{\mathcal{B}}$. Assuming typical values ($R_{\mathrm{cn}} = 1\,\mathrm{Mm}$ and $B_{\mathrm{cn}} = 0.01\,\mathrm{T}$), dimensional energy values of $6 \times 10^{22}\, \delta W\,\mathrm{J} \equiv 6 \times 10^{29}\, \delta W$ erg are obtained. Thus, the top end of the δW scale (≈ 0.073) is equivalent to 4×10^{28} erg. This is in the microflare range, but nanoflare energies will be obtained for weaker fields or for smaller loops.

3.6.2 Flare Energy Distributions

Every time a random walk reaches the instability threshold, the relaxed state of the loop (i.e., its position on the relaxation line) and the associated energy release are calculated. The relaxed state is the start of a new random walk which will lead to another relaxation (and energy release). If this process is repeated often enough it can be shown that certain energy release sizes are more common than others. The flare energy distributions converge as the number of relaxation events simulated (see Section 3.4) is increased.

The gross features of the converged energy distribution can be explained by presenting the energy distribution for the highest number of flare events (Figure 3.10, bottom right) alongside the instability threshold in Figure 3.11. Both the distribution

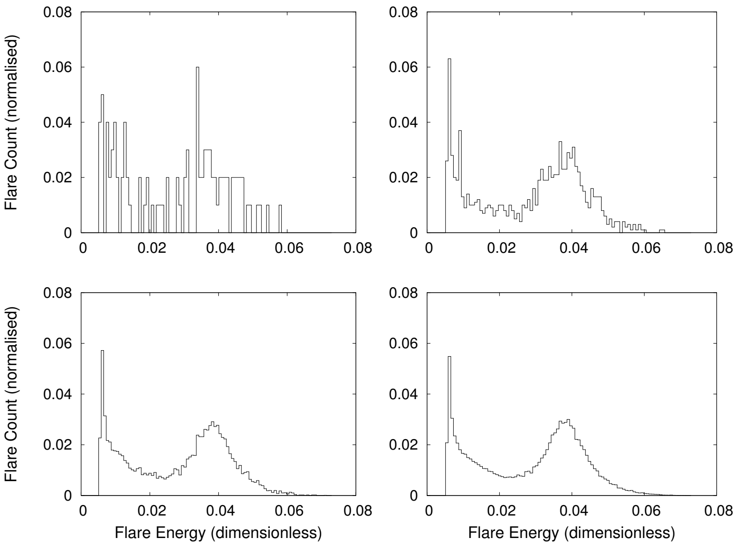

Figure 3.10: Flare energy distributions for 100 (top left), 1000 (top right), 10^4 (bottom left) and 10^5 (bottom right) relaxation events.

and the threshold are colour-coded according to event energy. The colour of the threshold point encountered by a coronal loop indicates the energy of the resulting flare and also the part of the distribution where the heating event falls. Dimensionlised values for the flare energies can be recovered by using typical loop parameters (see above).

The energy release changes as one moves along the threshold; i.e., there is an energy release gradient. This gradient is small for low energies, therefore, only a few bins cover the low energy sections of the threshold, see Figure 3.11. The low energy release events are divided amongst a small number of bins; hence, these bins contain many more events. The threshold sections corresponding to the profile minima are slightly longer than those associated with the first peak (≈ 1.5 times); but, the minima sections have a higher energy release gradient. The energy release events are divided amongst a higher number of bins and so each of these bins contain fewer events. As one moves into the threshold sections that correspond with the second profile peak (denoted by blue-green shades) the energy release gradient decreases, and so, one would expect the associated bins to have higher event counts. However, this increase is accentuated by the proximity of the corresponding relaxation points. Once a loop achieves a

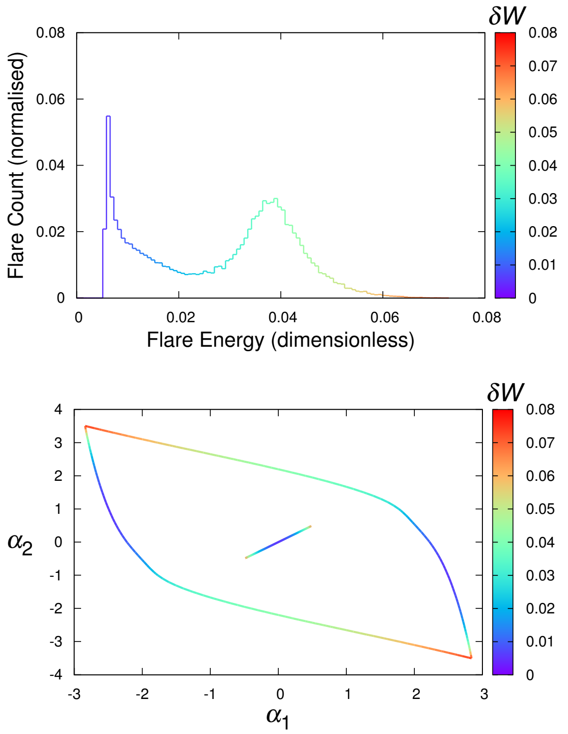

Figure 3.11: The flare energy distribution for 10^5 relaxation events and the instability threshold (with relaxation line). All lines are colour-coded according to energy release.

’blue-green’ instability, it will relax to a point (also coloured blue-green), which happens to be closest to the green section of the threshold. Subsequent walks will have a higher chance of crossing that section, thus, the corresponding distribution bins will contain even more events. The highest energy releases available on the threshold are farthest away from the relaxation line. In this part of the distribution, the chance of an energy release event is inversely proportional to the size of the energy release.

These results are not strongly tied to the loop lifetime, which is the number of relaxations a loop undergoes during the simulation. We can simulate loop replacement by randomly selecting a new position within the stability region after a certain number of relaxations. The top left distribution of Figure 3.12 is generated from a loop that is replaced after every 1000 relaxation events. As the loop lifetime is reduced so is the height of the second peak. However, this peak reduction is only noticeable for small lifetimes, e.g., < 10 relaxations. A minimum lifetime of 1 relaxation (Figure 3.12,

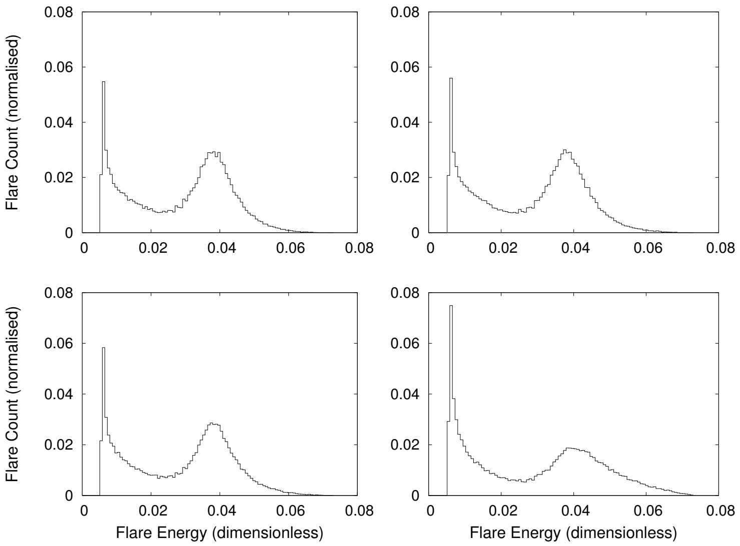

Figure 3.12: Flare energy distributions over 10^5 relaxation events for a variety of loop lifetimes. The lifetimes are 1000 relaxation events (top left), 100 relaxation events (top right), 10 relaxation events (bottom left) and 1 relaxation event (bottom right).

bottom right) still yields a two-peaked distribution, albeit with a reduced second peak. This result corresponds to finding the energy release from an ensemble of identical loops. It is also the most conservative in terms of total energy released.

The concept of a loop ensemble (a collection of 10^5 loops flaring simultaneously) is particularly useful, since it allows us to sidestep the complications that come with allowing loops to survive many relaxations. Otherwise, we would need to understand how a loop is affected by its energy release — a loop may shrink or implode after flaring (Janse and Low 2007). If the aspect ratio changes, the instability threshold would be invalidated. Therefore, the next section will examine in more detail the ensemble distribution.

3.6.3 Nanoflare Population Gradient and Heating Flux

The ensemble distribution (Figure 3.12, bottom right) does not yield a simple inverse power-law when converted to a log scale: there are two peaks in the profile. The trailing edge of the first peak equates to a power-law slope of ≈ -1.5. Its internal structure cannot currently be resolved, since one would need to increase the threshold point density. The trailing edge of the second peak gives a slope of ≈ -8.3; this is much greater than the critical gradient for nanoflare heating, $m \leq -2$.

These power-law figures are provisional and are likely to change as TRoLE is enhanced. For example, a more realistic α-space traversal function — one where $\delta\alpha_2$ is correlated with $\delta\alpha_1$ — will prefer walks parallel to the relaxation line; this will alter the distribution of heating events. Furthermore, only a single loop of fixed dimensions (or an ensemble of identical loops) is considered here. In reality, for any given large-scale loop structure, sub-loops of varying radii will be generated, depending on the horizontal scale-length of the driving photospheric motions. The distribution must then be averaged over a distribution of radii, as well as considering variations in length and field strength.

The primary aim of the TRoLE model is to calculate the distribution of nanoflares. In general terms, the heating rate will be similar to other calculations in the literature based on random photospheric twisting (Sturrock and Uchida 1981; Berger 1991; Zirker and Cleveland 1993; Abramenko et al. 2006). Within this approach, all the energy input from the photosphere must be dissipated, in a long-term time average over many events, since the build up of coronal magnetic field is limited by the instability threshold. The energy flux, F, can be expressed using Equation 3.35;

$$F = \frac{81\pi^2}{\mu_0}\,\frac{1}{N\tau}\,\frac{1}{2\pi R_{\mathrm{cn}}^2}\,R_{\mathrm{cn}}^3 B_{\mathrm{cn}}^2\,\langle\delta W\rangle = \frac{81\pi}{2\mu_0}\,\frac{R_{\mathrm{cn}} B_{\mathrm{cn}}^2}{\tau}\,\frac{\langle\delta W\rangle}{N}\,, \tag{3.36}$$

where N is the average number of steps taken to reach the threshold, τ is the time taken to complete each step in the random walk and $\langle\delta W\rangle$ is the average dimensionless energy release, given by

$$\langle\delta W\rangle = \frac{1}{10^5}\sum_{i=1}^{10^5}\delta W\,. \tag{3.37}$$

For the ensemble case, $\langle\delta W\rangle \approx 0.0293$ and $N \approx 264$. Applying previously used values ($B_{\mathrm{cn}} = 0.01$ T, $\tau = 200$ s and $R_{\mathrm{cn}} = 1$ Mm) yields a total flux of $6 \times 10^6\ \mathrm{erg\,cm^{-2}\,s^{-1}}$. This result is applicable to active regions (a value for the quiet Sun can be obtained by setting $B_{\rm cn} = 0.001\,\mathrm{T}$; this simply lowers F to $6 \times 10^4\,\mathrm{erg\,cm^{-2}\,s^{-1}}$). This result is slightly lower than $10^7\,\mathrm{erg\,cm^{-2}\,s^{-1}}$, Withbroe and Noyes (1977) estimate for active-region coronal heating losses. However, this shortfall vanishes if the random walk is conducted using larger step sizes, see following section.

3.6.4 Random Walks Revisited

So far, we have assumed photospheric motions to be somewhat temporally incoherent, with a short random walk step, $\delta\alpha = 0.1$, corresponding to $\tau = 200\,\mathrm{s}$. Here, the effect of varying this step length is considered; i.e., varying the coherence time of the photospheric motions. Figure 3.13, which should be compared with the bottom right plot of Figure 3.12, shows the distributions that result when $\delta\alpha$ is increased by factors of 10 and 40. For the latter case, the step is sufficiently long that, on average, just one step is required to reach the instability threshold: this corresponds to a temporally coherent twisting of the loop (although the spatial profile of the twisting varies randomly between heating events).

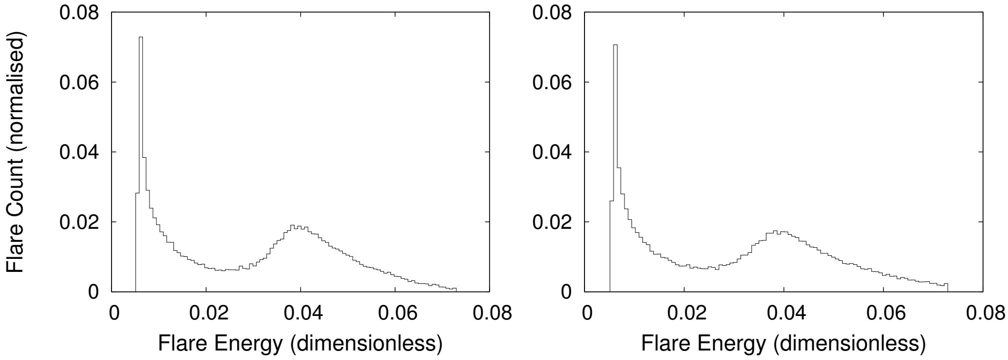

Figure 3.13: Flare energy distributions over 10^5 relaxation events for a step size of $\delta\alpha = 1$ (left) and $\delta\alpha = 4$ (right). Loop lifetime is one relaxation event.

It can be seen that the energy distribution is virtually independent of the random walk step size. Nevertheless, the heating flux *does* depend on this quantity. It is expected that the heating flux should be proportional to τ (Berger 1991). Equation 3.36 shows this to be the case, since the average number of steps, N, for the random walk to reach the threshold scales as $N \propto \tau^{-2}$ (Zirker and Cleveland 1993). In particular, for the limiting case of coherent twisting ($\tau = 8000$ s, $N \approx 1.13$ and $\langle \delta W \rangle \approx 0.0305$) the flux increases significantly, $F \approx 3 \times 10^7$ erg cm^{-2} s^{-1}.

Twist Space

The instability threshold can be expressed in terms of $\phi(R_1)$ and $\phi(R_6)$. This is more representative of the twist profile (see Section 3.5), which is directly generated by photospheric motions. These twist parameters are chosen to obtain a two-parameter representation of the family $\phi(r)$, since the twist profiles of Figure 3.4 usually show peak twists at the radial boundaries R_1 (0.5) and R_6 (1.0). The instability threshold can thus be plotted in *twist space* rather than *alpha space*, as in Figure 3.3. Given that the process is driven by chaotic photospheric motions, it is more realistic to assume the twist randomly evolves, rather than the α profile. Hence the calculations are repeated with a random walk in ϕ-space. When a simulation is run, for a sequence of heating events in ϕ-space, the resulting energy profile is more or less identical to that generated by an α-space simulation, see Figure 3.14 (right). The translation to ϕ-space results in a slight reorientation of the relaxation line with respect to the threshold. Consequently, the relaxation line is closer to the part of the threshold associated with the

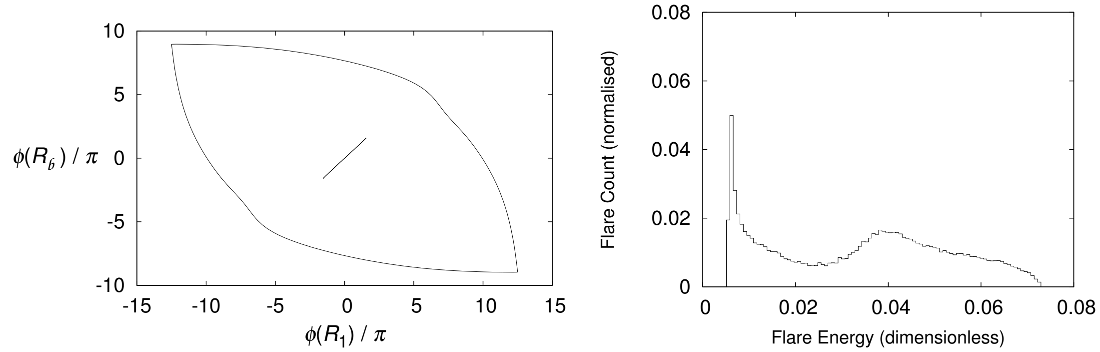

Figure 3.14: The instability threshold and relaxation line in ϕ-space (left), alongside the flare energy distribution for a 10^5 loop ensemble performed within ϕ-space (right). The random walk step size, $\delta\phi$, is approximately 0.32π, this corresponds to a step time of 200 s.

highest energies; this explains why the distribution has a thicker tail. The energy flux is $F \approx 4 \times 10^6\,\mathrm{erg\,cm^{-2}\,s^{-1}}$, which increases with step size in the same manner as shown for the α-space simulations.

3.6.5 Temporal Properties

In order to gain some insight into the temporal distribution of heating events, it is assumed that each step of a random walk in α-space takes the same arbitrary unit of time, corresponding to photospheric driving. The time axes of Figure 3.15 are shown in terms of random walk step number (i.e., step count or running step count). The time unit τ is the time taken for one step, which was estimated to be 200 s, see Section 3.3.

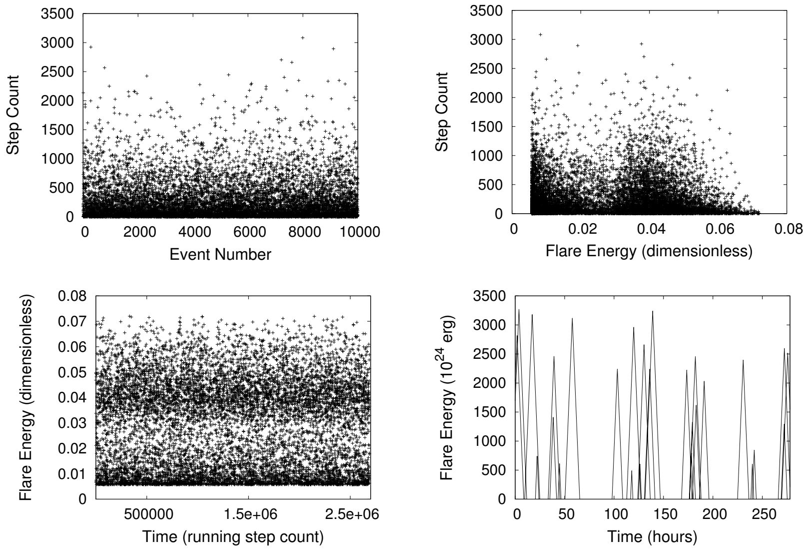

Figure 3.15: **Top Left**: the number of steps between relaxation and instability (i.e., time interval between heating events) for each event of a simulation comprising 10^4 events. **Top Right**: the number of steps taken to reach the threshold against the energy released. **Bottom Left**: the energy release as a function of time (running step count). **Bottom Right**: the 10^5 event simulation produced 10^5 flares of varying energies. The size of the flares are shown in a way that is reminiscent of actual flare/microflare/nanoflare observations: the bigger the event, the wider the base of the triangle used to represent that flare. The figure covers a time sequence equal to 5000 steps, taken from a random position within the simulation data.

The probability that a flare event will have occurred after a particular number of steps in α-space is invariant with time, see Figure 3.15 (top left). This is also true for the probability that a flare event will have a particular energy: the flare energy is not dependent on where in the simulation it occurs. The two horizontal bands shown in the bottom left plot are consistent with the peaks shown in Figures 3.12–3.13.

There does appear to be a slight relationship between the flare interval time (i.e., the number of steps taken to reach the threshold) and the flare energy, see Figure 3.15 (top right); but, no positive correlation is evident. Observations strongly suggest that these two properties are uncorrelated (Wheatland 2000). The top right plot echoes the shape of the energy release distributions. The instability threshold has an energy release gradient, which means that sections of threshold that have a more or less constant energy release (low gradient) will be visited by more loops. The higher the number of visiting loops, the wider the range of step counts associated with that section of the threshold. Thus, Figure 3.15 (top right) is in agreement with observations. Finally, the simulated energy releases can also be represented as a time series of flare energies, again see Figure 3.15 (bottom left).

3.6.6 Critical Magnetic Shear

Parker (1988) explains that a magnetic flux bundle rooted in the photosphere (i.e., a coronal loop) will be stressed as photospheric motions move the footpoints in a direction transverse to the original magnetic field. The coronal heating requirements for active regions and for the quiet Sun can be converted to equivalent magnetic stresses, which can in turn be converted to magnetic shears (B_θ/B_z), see Equation 1.4: this gives approximately 0.12 ($\sim 7^\circ$) for active regions where the mean B_z is of order 100 G.

Thus, for coronal heating to *work*, there must be some mechanism which restricts the shear to around these levels. If dissipation occurs at lower levels of shear the energy flux cannot maintain coronal temperatures. Conversely, if the shear can build up to much larger levels, the energy input would be higher than required. This model provides an explanation for these critical shear values. Two types of mean magnetic shear are calculated along the threshold, the mean absolute shear and the root mean square shear:

$$T_{\text{MABS}} = \frac{2}{R_6^2}\int_0^{R_6} r\left|\frac{B_\theta}{B_z}\right| dr\,, \tag{3.38}$$

$$T_{\text{RMS}} = \sqrt{\frac{2}{R_6^2}\int_0^{R_6} r\left(\frac{B_\theta}{B_z}\right)^2 dr}\,. \tag{3.39}$$

Both quantities are area-averaged. The plot (Figure 3.16) shows that the values of T_{MABS} and T_{RMS} are comparable with those derived above. In general, the average shear at the threshold is slightly higher than the limit suggested by Parker. Perhaps more shear is required, since not all of the magnetic energy released during relaxation will be converted to heat. Figure 3.16 suggests that the apparent limiting value for magnetic shear is determined by the linear instability. It should be mentioned that the work of Dahlburg et al. (2009), provide an alternative explanation of this shear dependency involving an explosive "secondary instability". They have used a 3D viscoresistive MHD code to simulate the shearing of a line-tied flux tube. The results of this code have revealed that the secondary instability requires a critical shear for onset.

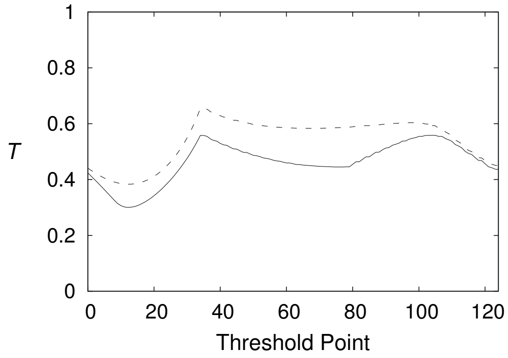

Figure 3.16: The mean absolute (solid) and root mean square (dashed) of the magnetic shear along the instability threshold. The shears are calculated over the loop volume, 0–R_6.

3.7 Interim Conclusions

A distribution of heating events has been calculated, both for a single loop which undergoes repeated stressing and relaxation, and for an ensemble of identical loops which are randomly stressed (and for intermediate cases). For a sufficiently large number of events, a statistically-stable distribution of event sizes is obtained. As expected, the smallest events are the most common, and there is (as noted by Browning and Van der Linden (2003)) a minimum event size for given loop parameters, perhaps corresponding to an 'elemental nanoflare'. More surprisingly, there is a second peak of event frequency at intermediate magnitudes, although this is somewhat reduced in size if an ensemble of loops is considered. This can be explained as follows. The first peak (at minimum energy) occurs simply because the range of energies near the minimum naturally encompasses the largest part of the instability threshold curve (because of the flatness of the minimum). The second peak is found because the instability threshold is most likely to be crossed in the part near to the region of constant-α.

An ensemble of identical loops — in which each individual loop starts from a randomly chosen initial state and is stressed until it undergoes a single relaxation event — is investigated in more detail. The distribution of heating events is qualitatively similar, although, the secondary peak of event frequency is much lower, and the decay of frequency with increasing energy is much flatter. A significant result is that, although the distribution is not a simple power law, the high-energy part of the distribution *is* well approximated by a power law with an index of around -8.3, which is considerably steeper than the minimum required for nanoflare heating to be effective (-2).

The TRoLE model requires that the field is sometimes unstable — although most of the time, the field profile will be well within the stable region. Typically, the dimensionless α value is of magnitude $1-2$, leading to dimensional values of $\alpha \approx 1-2\,\mathrm{Mm}^{-1}$ (for a loop radius of 1 Mm). Note, this is the maximum value which could be found, and usually we would expect lower values. This is consistent with observations; for example Régnier and Priest (2007) find α magnitudes around $1\,\mathrm{Mm}^{-1}$. Furthermore, a consequence of the fact that the fields are predicted to fluctuate between stable and unstable states, is that we predict a value for the average horizontal field component (on average, this will be somewhat less than the value at marginal stability). At threshold $B_{\perp}/B_z$ is around 0.5, which means that its average value should be around 0.25. This agrees very well with the limit on this quantity required by Parker (1988), in order for the Poynting flux from the photosphere to match coronal heating requirements — the kink instability appears to explain the critical shear value predicted by Parker. This also implies that the average heating flux derived from the model will be sufficient for coronal heating. Indeed, the fluxes derived from these results agree (especially if the correlation time for photospheric motions is increased) with the required values.

Relaxation theory makes no prediction about the spatial distribution of energy dissipation. However, this can be determined from numerical simulations. Hood et al. (2009) have shown that heating is well-distributed across the loop volume, as the current sheet, associated with the non-linear kink instability, stretches and fragments, thereby filling the loop cross section. This has implications for the observed emission.

A further important consideration is that so far, a single loop of fixed dimensions has been studied, with repeated stressing and relaxation. In practice, coronal heating events will occur in regions of field of varying sizes. A large flare will inevitably involve a large magnetic field volume, whereas nanoflares may involve small sets of field lines. This could be accounted for by allowing the loop aspect ratio to be randomly distributed also; the effect would be to convolve several energy distributions. A second limitation of the calculation is that a uniform random walk in α space has been assumed. This is not realistic, since photospheric twisting motions are likely to be correlated across the loop cross section and therefore changes in which the twist in the outer layer is similar to that in the core are much more likely: in other words, there should be a positive correlation between changes in α_1 (the core current) and changes in α_2 (the current in the outer layer), rather than these being independent random variables, as assumed here. This will be considered further in Chapter 5. Also, TRoLE will be enhanced such that there is, more realistically, zero net current carried by the loop. At present, in most cases the potential layer outside the loop contains azimuthal field. A current neutralisation layer will be inserted between the loop and the envelope — external magnetic fields will have an axial direction only (Hood et al. 2009), representing a response to localised photospheric twist motions.

The TRoLE model has included a number of simplifications and so is really a 'proof of principle', showing that a distribution of heating events can be produced from an (almost) *ab initio* coronal heating model. These initial results demonstrate the viability of the TRoLE model for further research and also act as a baseline against which the significance of later enhancements can be appraised. At this stage, it is also necessary to examine how a loop behaves after a kink instability and how well Taylor relaxation explains the final loop state. This is the purpose of the next chapter; it demonstrates the use of a 3D non-linear MHD code with regard to the more realistic current-neutralised loop. It is expected that during the aftermath of an instability, the loop will maintain zero net current, but again the details need to be revealed before this thesis can repeat the linear analysis for ensembles of zero-net-current loops.

4

3D Non-linear Simulations of Zero-net-current Coronal Loops

The coronal loop model demonstrated by the previous chapter incorporates a 2D configuration space. This space encompasses a large family of linearly stable and unstable loops with varying current profiles. Essentially, any current profile that could result from random photospheric flows is represented (albeit approximately) at some point within the configuration space. However, all of these loops carry net current, which blurs the distinction between the loop boundary and the background field. If the twisting motions are confined to some localised region, the untwisted field surrounding the loop should be purely axial. The currents generated by the twisting of the fields within the loop should close locally, such that the loop carries zero net current — Hood et al. (2009) undertook 3D numerical simulations with initial fields taken as twisted states with zero net current. The intention of this chapter is to first, define a new current-neutralised loop model (i.e., one that has zero net current) and second, to conduct non-linear numerical simulations for a small number of zero-net-current loops that have been identified as kink unstable. The results of these simulations will be tested against relaxation theory.

Numerical modelling requires far greater computational resources than those available with a standard desktop machine. Fortunately, the author has access to the one of the UK MHD Computer Clusters; it is hosted by the Solar and Magnetospheric MHD Theory Group at the School of Mathematics and Statistics, University of St Andrews.

4.1 Numerical Code

The non-linear simulations are conducted using a 3D MHD Lagrangian Remap Cartesian code, called LARE3D (Arber et al. 2001). It is written in Fortran 90 and uses the Message Passing Interface (MPI) to achieve parallelisation. More details are given in Section 4.1.1.

LARE3D solves the resistive MHD equations given by

$$\frac{\partial \rho}{\partial t} = -\nabla \cdot (\rho \vec{v}), \tag{4.1}$$

$$\frac{\partial}{\partial t}(\rho \vec{v}) = -\nabla \cdot (\rho \vec{v}\vec{v}) + \frac{1}{\mu_0}\left(\nabla \times \vec{B}\right) \times \vec{B} - \nabla P, \tag{4.2}$$

$$\frac{\partial \vec{B}}{\partial t} = \nabla \times \left(\vec{v} \times \vec{B}\right) - \nabla \times \left(\eta \frac{\nabla \times \vec{B}}{\mu_0}\right), \tag{4.3}$$

$$\frac{\partial}{\partial t}(\rho \epsilon) = -\nabla \cdot (\rho \epsilon \vec{v}) - P \nabla \cdot \vec{v} + \eta j^2, \tag{4.4}$$

with specific energy density,

$$\epsilon = \frac{P}{(\gamma - 1)\rho}, \tag{4.5}$$

where P is the thermal pressure, η is the resistivity (not magnetic diffusivity) — all other terms are as stated previously. Gravitational effects are ignored, as are thermal conduction and radiation. The neglect of gravity is justified by the fact that it is considerably weaker than the other forces pertinent to a coronal loop (e.g., magnetism and thermal pressure) when the loop height is less than the gravitational scale height. The simulations are concerned with how the magnetic field changes in response to the kink instability; specifically, how much energy is released and the nature of the field after the instability. It is only after the energy release that conduction becomes important (later, radiation is the dominant process). Nevertheless, numerical studies[1] have shown that conduction can act on MHD time scales (Botha et al. 2011). The amount of energy released from the field is unaffected, but kinetic energy parallel to the field is much reduced.

The MHD equations are made dimensionless by replacing the variables with dimensionless equivalents (the dimensional variables are again denoted by asterisks),

$$r = \frac{r^*}{r_0}, \quad B = \frac{B^*}{B_0}, \quad v = \frac{v^*}{v_A},$$

$$P = \frac{P^*}{P_0}, \quad t = \frac{t^*}{t_0}, \quad \rho = \frac{\rho^*}{\rho_0},$$

where $v_A = B_0/\sqrt{\mu_0\rho_0}$ is the Alfvén speed, $t_0 = r_0/v_\mathrm{A}$ is the Alfvén transit time and $P_0 = B_0^2/\mu_0$ is the magnetic pressure, r_0 is the loop radius and B_0 is the initial axial field (i.e., the z-component at $r = 0$). In addition, the current is in units of $B_0/\mu_0 r_0$ and the resistivity is in units of $\mu_0 r_0 v_\mathrm{A}$ ($\mu_0 = 1$). The resistivity is taken to be non-uniform in these simulations,

$$\begin{aligned} \eta &= \eta_\mathrm{b}, & |j| &\leq j_\mathrm{crit}, \\ \eta &= \eta_\mathrm{b} + \eta_0, & |j| &> j_\mathrm{crit}, \end{aligned}$$

where η_b is the background resistivity (normally set to zero) and $\eta_0 = 0.001$ is the anomalous resistivity, which is only switched on when the current rises above j_crit. The value of j_crit is set so that it is significantly higher than the maximum current at the start of the simulation. Super-critical currents appear as the current sheets, associated with magnetic reconnection, begin to form and decrease in thickness. The anomalous resistivity is intended to capture the dissipation occurring at scales below the grid resolution: at this scale, resistivity is enhanced by small-scale plasma instabilities.

---

[1] The latest version (v2.3) of LARE3D includes thermal conduction.

The computational domain is a 3D staggered grid: physical properties are not calculated at the same place for each cell in the domain. This approach improves numerical stability and allows conservation laws to be included in the computation. The domain size is $L_x = L_y = 6$ (-3:+3) and $L_z = 20$ (-10:+10). Initially, the loop axis is coincident with the z-axis and the loop radius is $r = 1$; therefore, the simulated loops all have an aspect ratio of 20. The loop is line-tied at $z = -10, +10$, which means, at those z-coordinates, the velocity is set to zero. The velocity is also zeroed at the boundaries for the x and y directions. The gradients for magnetic field, energy and density are zeroed at all boundaries.

The simulations are run with two grid resolutions, these are $128^2 \times 256$ (low) and $256^2 \times 512$ (high). It is assumed that a result is not a numerical artefact if it is consistent across the two resolutions. If a low resolution is applied to a loop of length 20 Mm and radius 1 Mm, each cell represents a length of $\approx$ 47 km in the x and y directions and a length of $\approx$ 78 km in the z direction. These lengths are halved for the higher resolution. The reader will note that the electron diffusion region associated with collisionless reconnection (Section 2.3.1) has a thickness of around 2 km (assuming $n_e = 10^{15}$ m^{-3}); appropriately, this is below the grid resolution.

4.1.1 LARE3D Internals

Observations of coronal emission could not be taken if the corona was empty of matter. A computational model of the corona must be able to calculate accurately changes in thermal pressure, in order to provide data that could be compared with observations. However, the corona is a magnetically dominated environment — the thermal pressure is much smaller than the magnetic energy density. A low plasma-β (Equation 1.1) presents a serious issue: a modest error on the magnetic field ($\sigma_B/B = 0.001$) translates to an error on the thermal pressure of 200%. For this reason, the MHD equations cannot be used conservatively; i.e., the pressure cannot be calculated by simply subtracting the magnetic energy from the total energy. Furthermore, viscosity and resistivity are extremely low in the corona (Section 2.1); hence, special techniques must be employed to prevent numerical resistivity from causing the simulation to depart too far from coronal conditions. In particular, it is necessary to preserve MHD shocks by maintaining the pressure differential, usually through the use of some artificial means.

Any code that is intended to simulate a coronal atmosphere cannot avoid the issues mentioned above. The following sections will describe the concepts implemented by LARE3D (Arber et al. 2001) along with some of the computational techniques used within the code.

The Grid

At the start of each time step, the properties of Equations 4.1–4.4 (i.e., density, pressure, velocity, magnetic field and specific energy density) are calculated on an Eulerian grid comprised of 3D cells (Figure 4.1). The velocities, magnetic field and thermal pressure are all staggered with respect to one another. This arrangement avoids the

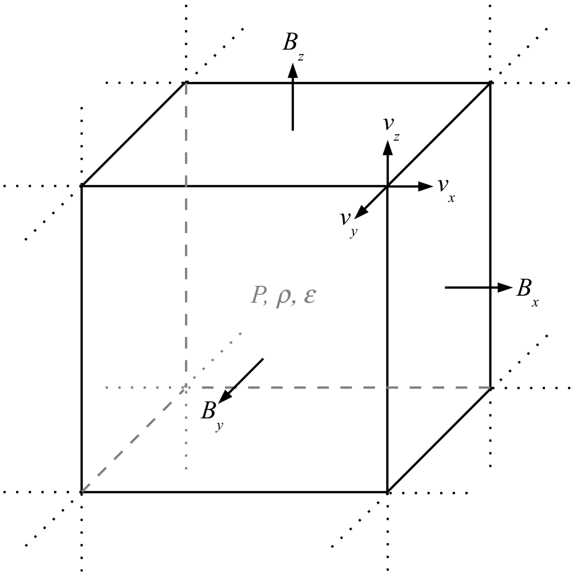

Figure 4.1: A single cell from the LARE3D grid. Pressure, density and specific energy are defined at cell centres, velocity components at cell vertices and magnetic field components at cell faces. Dotted lines indicate the neighbouring cells.

checkerboard instability, which can arise when one property depends on the spatial differential of a second property. Differentials are normally approximated by finite differencing: for example, within a 1D grid, a relationship such as $f(x) = \nabla \cdot g(x)$ could be represented as a *central* difference,

$$f_i \;=\; \frac{g_{i+1} - g_{i-1}}{2\Delta x}, \tag{4.6}$$

where the i subscript denotes the cell index. However, a cell-centred approach would create two coexisting solutions that are permanently decoupled: f_i at odd values of i would depend only on the differential of g estimated from even values of i and f_i at even i would depend on $\partial g/\partial x$ over odd i. Hence, plots of f would resemble a checkerboard pattern. The staggered arrangement of pressure and velocity avoids this problem; all grid points are coupled and the spatial differencing that results is second-order accurate. The magnetic field components are also staggered with respect to each other. Each field component is placed at the centre of a different cell face, so that $\nabla \cdot B = 0$ can be maintained during the Lagrangian step.

The Lagrangian Step

Initially, the cells are defined on the Eulerian grid and then the properties are updated to the next time step; but, because this is a Lagrangian step the grid itself moves with the plasma. All three dimensions are considered at once as each property is marched forward in time — the Lagrangian step is fully 3D.

The property updates are done according to a second-order accurate predictor-corrector scheme. First, predicted values are calculated at half a time step using finite backward differencing. For example,

$$\begin{aligned}\epsilon^{\delta t/2} \;=\; \epsilon - \left(\frac{\delta t}{2}\right)\frac{P}{\rho}\Bigg[&\frac{\langle v_x\rangle_{i,j,k} - \langle v_x\rangle_{i-1,j,k}}{dx} + \frac{\langle v_y\rangle_{i,j,k} - \langle v_y\rangle_{i,j-1,k}}{dy} \\ &+ \frac{\langle v_z\rangle_{i,j,k} - \langle v_z\rangle_{i,j,k-1}}{dz}\Bigg],\end{aligned} \tag{4.7}$$

where $\epsilon^{\delta t/2}$ is the predicted specific energy density at time $\delta t/2$, and dx, dy, dz are the cell dimensions — the omission of subscripts for all spatial terms implies the cell subscripts, i, j and k. Properties without a superscript are those defined on the Eulerian grid at the start of the Lagrangian step. The velocity components in Equation 4.7 are averaged values. Velocities are defined at cell vertices (Figure 4.1); a value for a cell face is simply the average of the four vertex values, and the velocity component at a cell centre is the average of the two opposing face values.

LARE3D now calculates the predicted force vectors at cell vertices, based on the *cell-centred* values for magnetic field and thermal pressure. In a 3D grid, each interior vertex is shared by eight cells. Hence, the force vector components are averages over an eight-cell control volume. The predicted vertex velocities can now be determined. Equation 4.8 gives the x-component of the vertex velocity at time $\delta t/2$,

$$v_x^{\delta t/2} \;=\; v_x + \left(\frac{\delta t}{2}\right)\frac{F_x^{\delta t/2}}{\rho^v}\,, \tag{4.8}$$

where $F_x^{\delta t/2}$ is the x-component of the vertex force vector and ρ^v is the Eulerian *vertex* value of the density for the same cell. The absence of sub-subscripts for v_x and F_x again implies i,j,k. Knowing the vertex velocities makes it possible to deduce how each cell is deformed over time.

The corrector step involves calculating the updates over the full time step. This is simple for the magnetic field because, for ideal MHD, magnetic flux moving with the plasma is conserved — non-ideal MHD physics can be applied separately. The corrector step starts with an update of the density control volume for each cell; i.e., the original Eulerian volumes used to calculate the cell-centred densities. Equation 4.9 gives the corrected specific energy density,

$$\begin{aligned}\epsilon^{\delta t} \;=\; \epsilon - (\delta t)\frac{P^{\delta t/2}}{\rho}\Bigg[&\frac{\langle v_x\rangle_{i,j,k}^{\delta t/2} - \langle v_x\rangle_{i-1,j,k}^{\delta t/2}}{dx} + \frac{\langle v_y\rangle_{i,j,k}^{\delta t/2} - \langle v_y\rangle_{i,j-1,k}^{\delta t/2}}{dy}\\ &+ \frac{\langle v_z\rangle_{i,j,k}^{\delta t/2} - \langle v_z\rangle_{i,j,k-1}^{\delta t/2}}{dz}\Bigg],\end{aligned} \tag{4.9}$$

where ρ is the original Eulerian density used here to ensure mass conservation. Other properties are corrected in a similar manner, see Arber et al. (2001) for details. Extra physics, such as resistivity and conduction, can be added at the start of the Lagrangian step, before the beginning of the predictor-corrector scheme.

The principle advantage of the Lagrangian step is that the density and magnetic fluxes sum to zero over each cell; only the velocity flux is non-zero. This makes it straightforward to incorporate any artificial mechanisms that are necessary for LARE3D to simulate coronal conditions. For example, artificial viscosity is used to dampen the non-physical oscillations that can occur behind a shock front:

$$q \;=\; 0.1\, c_{\rm f}\, \rho L\, |\, S\, | \;+\; 0.5\, \rho L^2\, S^{\,2}\,, \tag{4.10}$$

where q is the artifical viscosity taken from Wilkins (1980), L is the cell size, $c_{\rm f}$ is the fast magnetosonic wave speed, and S is the strain rate associated with the cell. This formulation can handle shocks propagating in any direction, since $c_{\rm f}$ is relative to the cell velocity.

The Remap Step

At the end of the Lagrangian step all the cells need to be remapped back to the original Eulerian grid before the simulation can continue. This step is entirely geometrical (it includes no physics or time dependence) and is dimensionally separated. Figure 4.2 illustrates the remapping for the x dimension. The density is remapped conservatively:

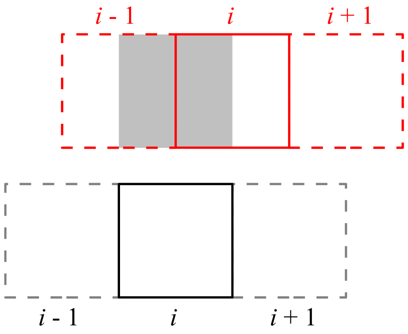

Figure 4.2: The 1D remapping of Lagrangian cell i (red) after one time step to the corresponding Eulerian cell (black). The shaded area in the Lagrangian cells demarcates the mass that is mapped to Eulerian cell i

the remapped mass within cell i of the Eulerian grid is equal to the mass within the corresponding Lagrangian cell, minus the mass that overlaps Eulerian $i + 1$ and plus the mass in Lagrangian $i - 1$ that overlaps Eulerian i (Figure 4.2).

Magnetic flux is unchanged during the Lagrangian step; however, during the remap step, small amounts of flux need to be transferred across the cell boundaries on the Eulerian grid. This is because LARE3D calculates the amount of remapped flux in such a way that $\nabla \cdot B = 0$ can be maintained to machine precision, according to Evans and Hawley constrained transport (Evans and Hawley 1988).

$$\begin{aligned} \psi'_y &= \psi_y(i,j,k) - \delta\psi_y(i,j,k) + \delta\psi_y(i-1,j,k)\,, && (4.11) \\ \psi'_x &= \psi_x(i,j,k) + \delta\psi_y(i,j,k) - \delta\psi_y(i,j-1,k)\,, && (4.12) \end{aligned}$$

$$\begin{aligned} \psi'_z &= \psi_z(i,j,k) - \delta\psi_z(i,j,k) + \delta\psi_z(i-1,j,k)\,, && (4.13) \\ \psi'_x &= \psi_x(i,j,k) + \delta\psi_z(i,j,k) - \delta\psi_z(i,j,k-1)\,. && (4.14) \end{aligned}$$

The Remapped fluxes (in the x direction) are indicated by the dashed ψ terms in Equations 4.11–4.14, similar expressions are used for the other dimensions.

Resolving MHD shocks is an important part of coronal simulations; this is the reason why LARE3D uses van Leer gradient limiters (van Leer 1979) as part of the remap step. This technique guarantees that monotonicity is preserved: minima do not decrease, maxima do not increase, and no new extrema are created during the remapping. The thick black slopes of Figure 4.3 are van Leer limited gradients. A limited gradient is less severe than the one it replaces and is calculated to fit better with

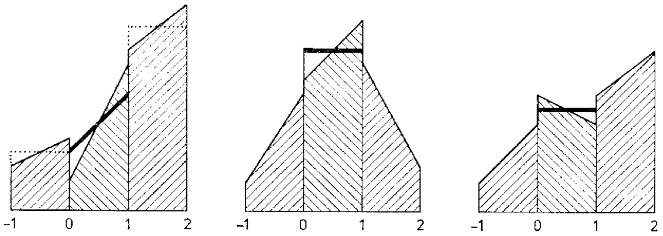

Figure 4.3: Three examples of the application of van Leer gradient limiters (thick lines). Courtesy of van Leer (1979).

the gradients of the neighbouring cells. Thus, shock fronts are less likely to fall below the grid resolution.

Arber et al. (2001) present a proof of energy conservation in the Lagrangian step; however, extra work is required to conserve energy during the remap step. Specifically, the change in kinetic energy is summed over all the cells and then added as a heating term to the internal energy. This conservation technique is not applied to magnetic energy.

When the remap step is complete, everything is once again defined on the Eulerian grid, and LARE3D begins the Lagrangian step for the next time increment. Now that the basics of how LARE3D operates have been covered, it is time to explain how this code has been used.

4.1.2 Initial Configuration

Some previous studies have used LARE3D to simulate the application of kink perturbations to a straightened line-tied coronal loop (Gerrard et al. 2002; Gerrard and Hood 2003; Browning et al. 2008; Hood et al. 2009). The model has been extended so that the loop has an outer current-neutralising layer to ensure the loop has (at least initially) zero net current: this improves on the model used in Chapter 3, which allowed loops to have net current (i.e., an azimuthal field was usually present in the potential envelope). All currents are now created by convective motions *local* to the loop footpoints. Hence, a current neutralisation layer is introduced here, defined such that the azimuthal field (B_θ) always falls to zero at the loop boundary (R_b); therefore, B_θ is zero in the potential envelope.

The loop's radial α-profile is approximated by a piecewise-constant function featuring three parameters (Figure 4.4): the ratio of current to magnetic field is α_1 in the core, α_2 in the outer layer, α_3 in the neutralisation layer and zero in the potential envelope. The free parameters are α_1 and α_2, whereas α_3 is dependent on the first two and is determined by the requirement of zero net current. The magnetic field is contin-

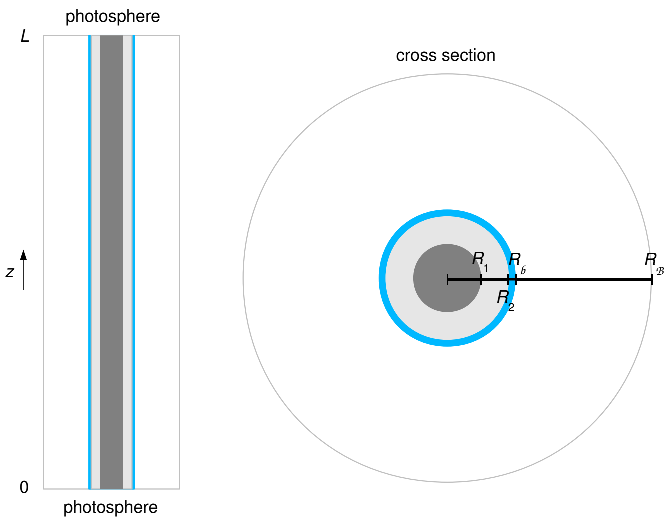

Figure 4.4: Schematic of a straightened coronal loop in the r-z plane (left) and in the r-θ plane (right). The loop, comprises a core (dark grey), an outer layer (light grey) and a current neutralisation layer (blue); the whole loop is embedded in a potential envelope (white). The core radius is half the loop radius and 1/6 the envelope radius (R_1:R_2:$R_{\mathscr{b}}$:$R_{\mathscr{B}} = 0.5$:0.9:1:3). The loop aspect ratio ($L/R_{\mathscr{b}}$) in this figure is 20.

uous everywhere, whereas the current has discontinuities, and the outer surface of the potential envelope, representing the background corona, is placed at $R_{\mathscr{B}} = 3$ (thrice the loop radius).

The fields are once again expressed in terms of the well-known Bessel function model, generalised to the concentric layer geometry (Melrose, Nicholls, and Broderick, 1994; Browning and Van der Linden, 2003; Browning et al., 2008). The field equations for the four regions (core, outer layer, neutralisation layer and envelope) are as follows:

$$B_{1z} = B_1 J_0(|\alpha_1| r)\,, \tag{4.15}$$

$$B_{1\theta} = \sigma_1 B_1 J_1(|\alpha_1| r)\,, \qquad 0 \leq r \leq R_1\,, \tag{4.16}$$

$$B_{2z} = B_2 J_0(|\alpha_2| r) + C_2 Y_0(|\alpha_2| r)\,, \tag{4.17}$$

$$B_{2\theta} = \sigma_2 (B_2 J_1(|\alpha_2| r) + C_2 Y_1(|\alpha_2| r))\,, \qquad R_1 \leq r \leq R_2\,, \tag{4.18}$$

$$\begin{aligned} B_{3z} &= B_3 J_0(|\alpha_3| r) + C_3 Y_0(|\alpha_3| r)\,, \qquad && \qquad\qquad (4.19)\\ B_{3\theta} &= \sigma_3 (B_3 J_1(|\alpha_3| r) + C_3 Y_1(|\alpha_3| r))\,, && R_2 \le r \le R_{\mathscr{b}}\,, \qquad (4.20) \end{aligned}$$

$$\begin{aligned} B_{4z} &= B_4\,, \qquad && \qquad\qquad (4.21)\\ B_{4\theta} &= 0\,, && R_{\mathscr{b}} \le r \le R_{\mathcal{B}}\,, \qquad (4.22) \end{aligned}$$

where $\sigma_i = \frac{\alpha_i}{|\alpha_i|}$ $(i = 1, 2, 3)$ represent the sign of α_i. The fields must be continuous at the inner radial boundaries, R_1, R_2 and $R_{\mathscr{b}}$. (The positions are $R_1 = 0.5$, $R_2 = 0.9$ and $R_{\mathscr{b}} = 1$, so that most of the loop is similar to the one described earlier, with a thin current neutralisation layer between R_2 and $R_{\mathscr{b}}$.) Therefore, the constants B_j and C_j $(j = 2, 3, 4)$ can be expressed like so:

$$B_2 = \frac{\pi |\alpha_2| B_1 R_1}{2} \Big(\sigma_{1,2} J_1(|\alpha_1| R_1) Y_0(|\alpha_2| R_1) - J_0(|\alpha_1| R_1) Y_1(|\alpha_2| R_1) \Big)\,, \tag{4.23}$$

$$C_2 = \frac{\pi |\alpha_2| B_1 R_1}{2} \Big(J_0(|\alpha_1| R_1) J_1(|\alpha_2| R_1) - \sigma_{1,2} J_1(|\alpha_1| R_1) J_0(|\alpha_2| R_1) \Big)\,, \tag{4.24}$$

$$B_3 = \frac{\pi |\alpha_3| B_2 R_2}{2} \Big(\sigma_{2,3} F_1(|\alpha_2| R_2) Y_0(|\alpha_3| R_2) - F_0(|\alpha_2| R_2) Y_1(|\alpha_3| R_2) \Big)\,, \tag{4.25}$$

$$C_3 = \frac{\pi |\alpha_3| B_2 R_2}{2} \Big(F_0(|\alpha_2| R_2) J_1(|\alpha_3| R_2) - \sigma_{2,3} F_1(|\alpha_2| R_2) J_0(|\alpha_3| R_2) \Big)\,, \tag{4.26}$$

$$B_4 = B_3 G_0(|\alpha_3| R_{\mathscr{b}})\,, \tag{4.27}$$

$$C_4 = 0\,, \tag{4.28}$$

where

$$F_{0,1}(x) = J_{0,1}(x) + \frac{C_2}{B_2} Y_{0,1}(x)\,, \tag{4.29}$$

$$G_{0,1}(x) = J_{0,1}(x) + \frac{C_3}{B_3} Y_{0,1}(x)\,. \tag{4.30}$$

The value of α_3 (the neutralisation layer current) is found, for a given (α_1, α_2), by numerical solution of $B_{3\theta}(R_б) = 0$, ensuring that the net current is zero and that the azimuthal field vanishes outside the loop, see Equation 4.20.

The linear kink instability threshold for this current-neutralised loop was uncovered by the CILTS code (Section 3.2 and 5.2).

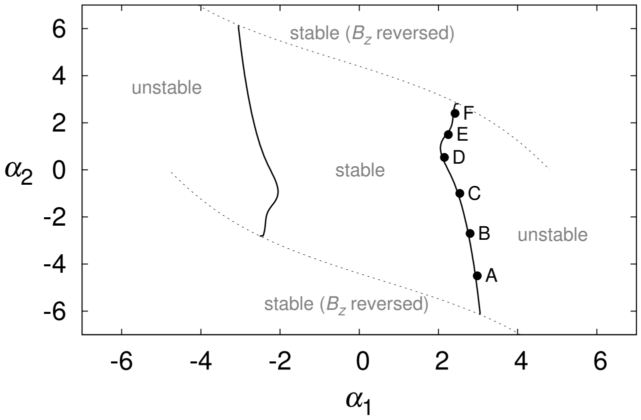

Figure 4.5: The linear kink instability thresholds for $L/R_б = 20$ are sampled by a selection of six marginally unstable configurations, indicated by the black circles. The dashed lines denote the thresholds for B_z reversal.

Table 4.1: The marginally kink unstable loop configurations chosen for numerical simulation.

Loop	α_1	α_2	α_3
F	2.42	2.4	-13.08
E	2.25	1.5	-8.71
D	2.15	0.53	-4.95
C	2.54	-1.0	-0.84
B	2.8	-2.7	3.82
A	2.98	-4.5	9.28

In contrast to the stability space for a loop of net current, the instability thresholds are open (Figure 4.5). The new stability space is closed by the thresholds for B_z reversal (dashed lines), which is a consequence of using Bessel functions (Section 3.2). The filled circles of Figure 4.5 identify the loop configurations (see also Table 4.1) that will be simulated by the LARE3D code (the initial field profiles for Loops E and B are presented in Appendix B.2). These configurations are expected to be unstable to the ideal kink instability and it is also expected that the magnetic field energy will decline to a level that is predicted by Taylor relaxation. In the analytical studies (Chapters 3 and 5), the magnetic field coefficient at the core (B_1) is initialised according to a normalised total axial flux. For convenience, the numerical code will instead set $B_1 = 1$.

4.1.3 Basic Operation

Each of the loops indicated in Figure 4.5 is subjected to a kink perturbation of the form,

$$v_r = c_1 \cos\left(\pi \frac{z}{L}\right) cos(kz)\,, \qquad r = 0\,, \tag{4.31}$$

$$v_r = c_1 \frac{e^{-4r^4}}{r} \left[\cos\left(\pi \frac{z}{L}\right)\Big(x\cos(kz) + y\sin(kz)\Big) \right], \qquad r > 0\,, \tag{4.32}$$

where v_r is the radial component of the perturbed velocity, L is the loop length, $r = \sqrt{x^2 + y^2}$ is the radial coordinate, $k = 1.1$ is the wave number, and the constant $c_1 = 0.01$ reduces the amplitude so that the perturbation is only a slight one. Assuming such a perturbation initiates an instability, the loop is expected to radially expand as it transitions towards a constant-α relaxed state (see Section 2.4). The numerical simulation should end with a (less than fully) relaxed loop that has zero net current.

The configurations listed in Table 4.1 encompass two types of loop; one where α_1 and α_2 have the same sign (D–F) and one where these parameters have opposing signs (A–C). Loop E has been chosen as representative of the first loop type and Loop B of the second. Henceforth, these two loops will be referred to as the first-quadrant loop (E) and the fourth-quadrant loop (B). First (and third) quadrant loops are a more likely result of *correlated* photospheric driving (Section 3.7), this is the reason why the part of the threshold curve where $\alpha_2 > 0$ is more finely sampled compared to $\alpha_2 < 0$. Both the first and fourth quadrant loops will be simulated for low and high resolutions; only the high resolution will be used for the other loop configurations. The simulations will proceed in steps of $0.034\,t_\mathrm{A}$ (low resolution) and $0.017\,t_\mathrm{A}$ (high resolution)[2]. LARE3D determines the size of the time step by applying the Courant-Friedrichs-Lewy condition: the solution is stable if $\delta t/\delta x \leq 1/c_\mathrm{s}$, where c_s is the sound speed (Anderson 1996). Each simulation runs until the magnetic field appears to have settled into a lower energy state and for all simulations, anomalous resistivity is switched on when $j_\mathrm{crit} > 15$.

Two third-party applications were used to plot and visualise the data produced by the LARE3D simulations, IDL version 7.1.1 (Lawrence Livermore Laboratory) and VisIt version 2.3.1 (ITT Visual Information Solutions) — in brackets are the institutions that maintain this software. The output from LARE3D is a collection of snapshot files; the size of a snapshot file depends on the resolution, 0.36 GB (low) or 3 GB (high). A number of other data files are also written by LARE3D, one of these contains the temporal variation of various forms of energy (in dimensionless units) throughout the simulation.

4.2 Simulation Results

4.2.1 Energy and Resistivity

The first-quadrant loop ($\alpha_1 = 2.25$, $\alpha_2 = 1.5$) is linearly kink unstable (Figure 4.4), and the numerical analysis shows that this loop is also *non-linearly* kink unstable: the magnetic energy undergoes a decline coincident with a rise in internal energy and with an increase in the maximum current (Figure 4.6). The non-linear instability starts at around $t = 50\,t_\mathrm{A}$ and within the next $50\,t_\mathrm{A}$, approximately 70% of the total energy release has been achieved. Magnetic energy reduces more slowly after $t = 100\,t_\mathrm{A}$. The

---

[2] $t_\mathrm{A} \approx 3$ s for a loop that has the following properties, $B_z = 100\,\mathrm{G}$, $L = 20\,\mathrm{Mm}$ and $\rho = \bar{m}n$, where $\bar{m} = 1.2\mathrm{m_p}$ and $n = 10^{15}\ \mathrm{m}^{-3}$.

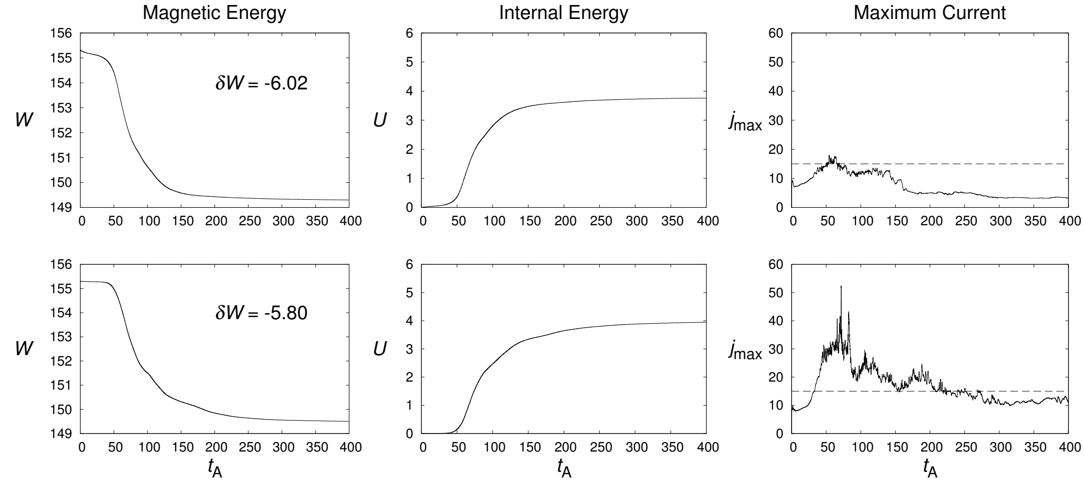

Figure 4.6: First-quadrant loop: the temporal variation of magnetic energy (left column), internal energy (middle column) and the maximum current (right column) for low resolution (top row) and for high resolution (bottom row). The critical current (i.e., the threshold for anomalous resistivity) is indicated by the horizontal dashed line (right column). The background resistivity is zero.

release of magnetic energy is of the same size for both resolutions[3]; however, at higher resolution, significantly larger currents are recorded. Spatially-confined changes in current are missed at the lower resolution and there is much less anomalous resistivity. The fact that the maximum current increases with resolution is indicative of current sheet formation. These structures have (possibly) infinite current density, so higher resolutions should reveal more and more current.

Ideal MHD (i.e., zero magnetic diffusivity) produces very similar results (Figure 4.7, top row); this emphasizes the dominance of the magnetic field, both before and after the instability. The adjective *ideal* is italicised because LARE3D cannot prevent some numerical resistivity (the decline in magnetic energy for a stable configuration under ideal conditions is too slow to be captured computationally, therefore any reduction seen is artificial, see Figure 4.12).

---

[3] At low resolution the energy release is slightly higher. This is possibly due to a higher numerical resistivity; a decline in energy is evident before the instability occurs, Figure 4.6 (top left).

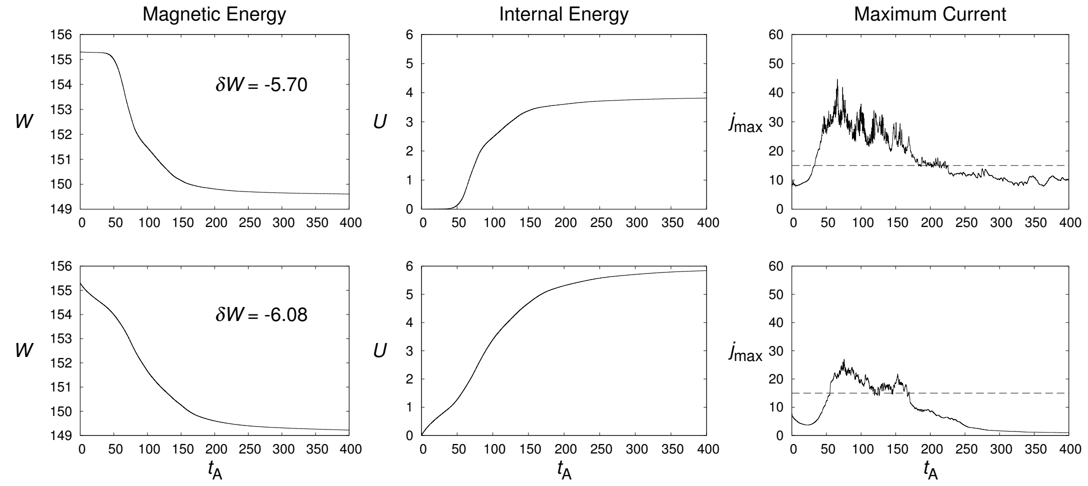

Figure 4.7: First-quadrant loop: the temporal variation of magnetic energy (left column), internal energy (middle column) and the maximum current (right column) for *ideal* MHD (top row) and for resistive MHD with $\eta_b = 0.0001$ (bottom row). The plots are from high resolution simulations.

A non-zero background resistivity ($\eta_b = 0.0001$) does alter the plots: energy release is slightly higher, the reduction in magnetic energy starts right away and is more drawn out, and the maximum current is much less than when $\eta_b = 0$ (Figure 4.7, bottom row). These differences are all consistent with an increased resistivity. In terms of energy conservation, LARE3D performs better when there is a constant background resistivity. The internal energy increases almost exactly by the same amount that the magnetic energy decreases; therefore, $\eta_b = 0.0001$ exceeds the numerical resistivity. Although, energy conservation should always be maximised, using even a low background resistivity means the simulation will less closely replicate the highly-conductive environment of the corona. When $\eta_b \neq 0$, energy dissipation is evident right from the start of the simulation (Figure 4.7, left column) — it is more likely that this slower initial decline is caused by global resistive diffusion rather than magnetic reconnection.

We will now investigate how the kinetic energy changes during the simulation and from this, estimate the growth rate of the instability. The kinetic energy peaks rapidly (at $\sim 75\, t_A$) for both low and high resolutions (Figure 4.8), which is a signature of reconnection: the rise in kinetic energy is caused by fast reconnective outflows. Note, the increase in kinetic energy begins before $t = 50\,t_{\mathrm{A}}$, the time when magnetic energy begins to decline. The former event indicates the start of the linear instability, whereas the latter heralds the non-linear phase.

The linear perturbation function (see Section 3.2) implies that the perturbed plasma velocity is proportional to $e^{\gamma t}$ and so, the kinetic energy, $E \propto e^{2\gamma t}$. Hence, the gradient of the natural logarithm of kinetic energy is in fact twice the growth rate of the instability. Figure 4.8 (right column) shows the growth rate to be more than double that calculated by the linear analysis ($\gamma = 0.04$). It is not clear why this discrepancy arises; Browning et al. (2008) generally found good agreement with linear growth rates. Perhaps it is caused by a different choice of initial disturbance.

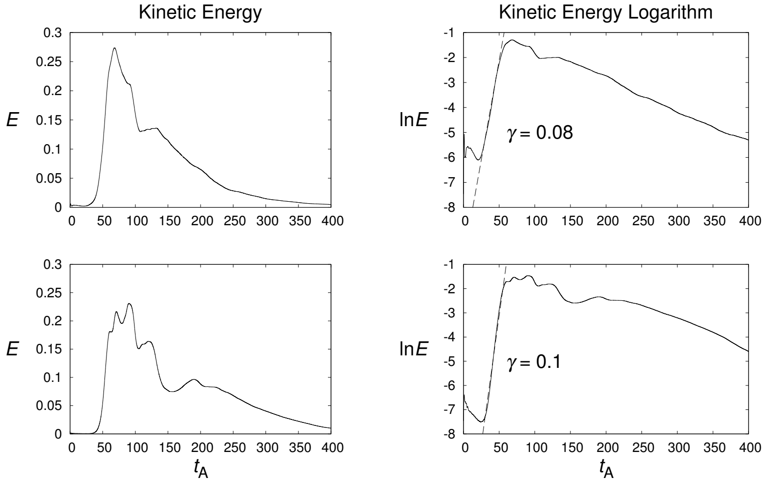

Figure 4.8: First-quadrant loop: the temporal variation of the kinetic energy (left column) and the natural logarithm of kinetic energy (right column) for low resolution (top row) and for high resolution (bottom row). The gradient of the dashed line in the plot of ln(E) is twice the instability growth rate, γ.

Figure 4.8 is repeated at high resolution for *ideal* MHD and for non-zero background resisitivity ($\eta_{\mathrm{b}} = 0.0001$), see Figure 4.9. Once again, there is little difference between *ideal* MHD and resistive MHD when $\eta_{\mathrm{b}} = 0$. Background resistivity has a marginal impact on the growth rate of the kink instability, but it will limit any sudden

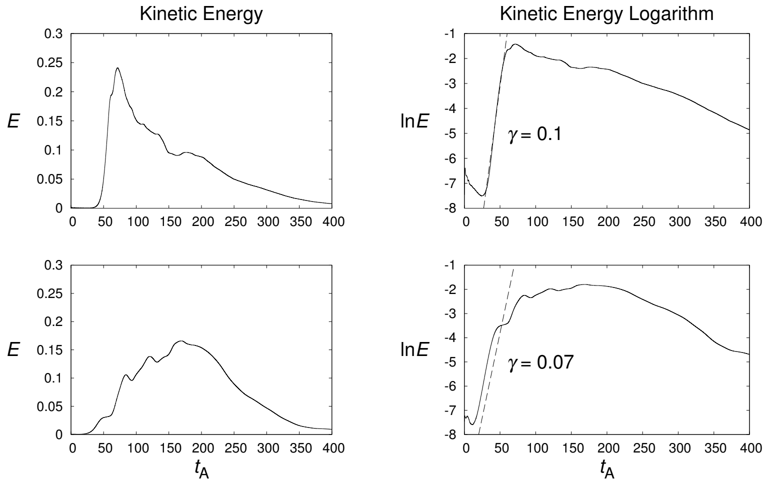

Figure 4.9: First-quadrant loop: the temporal variation of the kinetic energy (left column) and the natural logarithm of kinetic energy (right column) for *ideal* MHD (top row) and for resistive MHD with $\eta_b = 0.0001$ (bottom row). The plots are from high resolution simulations.

rises in kinetic energy.

The fourth-quadrant loop ($\alpha_1 = 2.8$, $\alpha_2 = -2.7$) has a core that is oppositely twisted with respect to its outer layer. Figure 4.10 shows the same correspondence between the magnetic and internal energies that was seen for the previous loop. Again, the magnetic

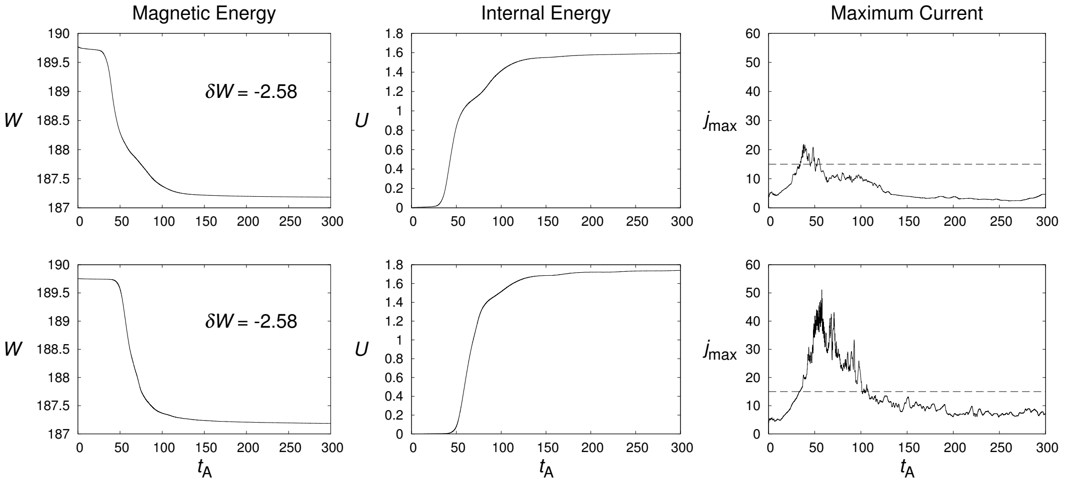

Figure 4.10: Fourth-quadrant loop: the temporal variation of magnetic energy (left column), internal energy (middle column) and the maximum current (right column) for low resolution (top row) and for high resolution (bottom row).

energy release is of the same size for both resolutions and, at the higher resolution, significantly larger currents are recorded. The linear analysis (Section 3.5.2) suggested that reversed α-profiles mitigate instability, and indeed, the decline in magnetic energy is around half of that for the first-quadrant loop.

The plot of the kinetic energy (Figure 4.11) reveals a weaker secondary instability that takes place at $t \approx 100\,t_{\mathrm{A}}$. The numerically-determined growth rate is again higher than that calculated by the linear analysis ($\gamma = 0.04$).

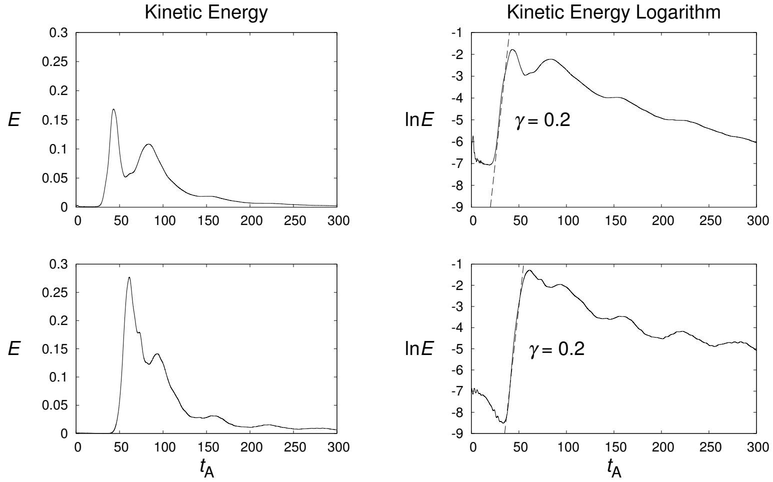

Figure 4.11: Fourth-quadrant loop: the temporal variation of the kinetic energy (left column) and the natural logarithm of kinetic energy (right column) for low resolution (top row) and for high resolution (bottom row).

The general trends for magnetic, internal and kinetic energies are consistent between resolutions (for both loops), and most importantly, so is the size of the magnetic energy release. Therefore, simulations at higher resolution are not required — this chapter will proceed with results taken only from the $256^2 \times 512$ simulations. Appendix C.1 gives the plots presented here for other loop configurations. For all these cases, the results suggest that linear instability gives way to non-linear growth, which gives rise to current sheets and magnetic reconnection. Thus, magnetic energy is dissipated and the loop is expected to evolve towards a Taylor-relaxed state.

Introducing a non-zero background resistivity does prevent the small (compared to the magnetic field) energy leak, at least for the first-quadrant loop; but such a resistivity is not realistic by coronal standards, and Figure 4.7 (right column) suggests that a substantial drop in field energy occurs before the kink instability has a chance to take effect. The fingerprints of numerical resistivity are noticeable within Figures 4.6 and 4.10, where $\eta_\text{b} = 0$. Only a small fraction ($\approx 3\%$) of the magnetic field energy is released by the kink instability. The slenderness of this energy release will mean that numerical (that is to say artificial) resistivity will be a factor during the conversion process: almost half of the loss in magnetic field energy is not accounted for by the rise in internal and kinetic energy. However, virtually all of this artificial resistivity is occurring during the energy conversion. The drop in magnetic energy is a robust result. To demonstrate further, Figure 4.12 shows the magnetic energy plot for a loop configuration ($\alpha_1 = 0.5$ and $\alpha_2 = 0.1$) that is well within the stable region (as shown in Figure 4.5) — this result is taken from an *ideal* MHD simulation. In the absence of an instability (and any applied resistivity), Figure 4.12, reveals the level of *numerical* resistivity that the magnetic field energy is subjected to over the course of the simulation. The energy declines by around one thousandth of one percent, which is three orders of magnitude smaller than the energy release caused by the kink instability.

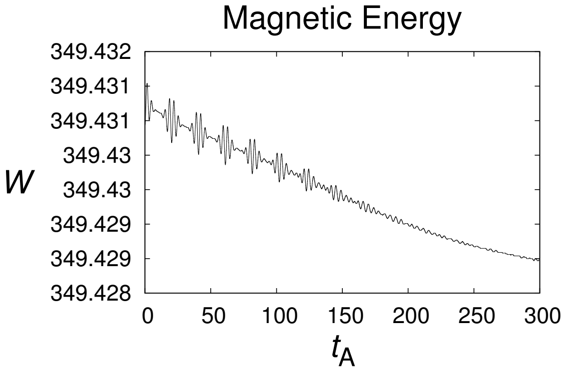

Figure 4.12: The temporal variation of magnetic energy for a linearly stable loop during a high resolution simulation.

The following sections will present results based on a current-dependent resistivity and zero background resistivity — this is more compatible with the coronal environment. The breakdown of energy conservation associated with this parameter choice is considered to be negligible.

4.2.2 Magnetic Field

Now we examine the magnetic field (and current distribution) at specific times during the simulations. Figure 4.13 shows how field lines, originally located within the core, become kinked as the instability takes hold and then relax as the magnetic energy is dissipated. The first and fourth quadrant loops follow the same course of events. Initially, the field lines are intertwined; then, during the growth of the instability, magnetic reconnection and anomalous resistivity (indicated by the red areas) start to occur. This phase is over quickly ($\Delta t \approx 50\, t_{\mathrm{A}}$) and by the end of the simulation the (reconnected) field lines have straightened considerably — the final state suggests a low constant-α configuration. The areas of anomalous resistivity must be dispersed throughout the loop volume in order for helicity to be more evenly redistributed and thereby create a linear α-profile.

The reduction in the azimuthal components of the field lines should cause a radial expansion of the loop. At the initial equilibrium, the inward tension force of the azimuthal field is balanced by the outward magnetic pressure of the axial field; thus, if the tension decreases, the loop must expand before equilibrium can be regained. This behaviour is clearly demonstrated by the plots in the next section.

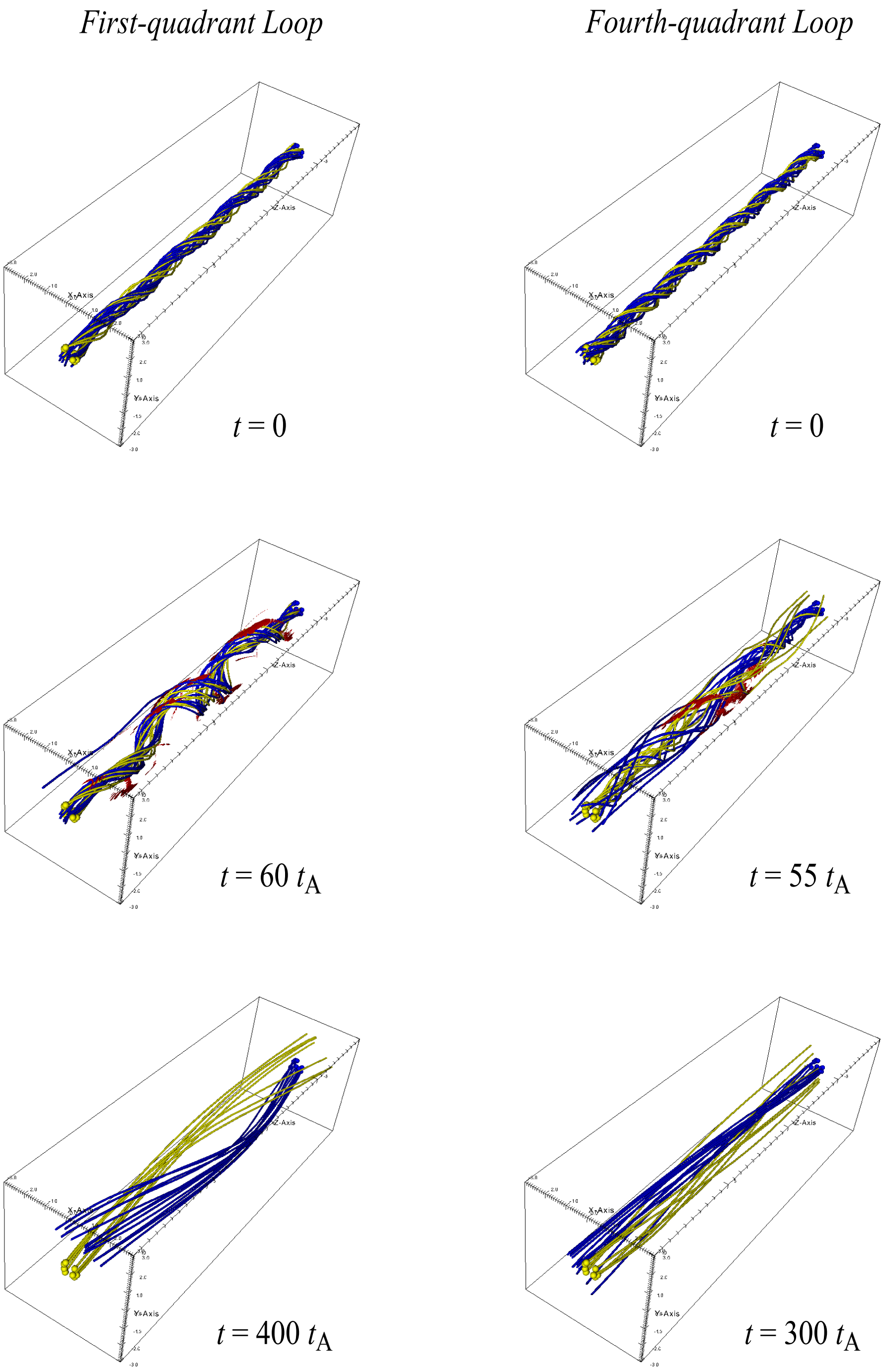

First-quadrant Loop

Fourth-quadrant Loop

$t = 0$

$t = 0$

$t = 60\ t_A$

$t = 55\ t_A$

$t = 400\ t_A$

$t = 300\ t_A$

Figure 4.13: Magnetic field lines originating from the front footpoint (yellow) and from the back footpoint (blue) are shown at three different times for the first-quadrant loop (left column) and for the fourth-quadrant loop (right column). Anomalous resistivity is indicated by the red areas.

4.2.3 Current Magnitude

Figure 4.14 shows the current magnitude for both loops over a cross section located at $z = 0$ (i.e., half way along the loop). The plot times are the same as those used for Figure 4.13. Hence, the plots in the middle column illustrate the time shortly after the start of the kink instability. At this time, current sheets of narrow width start to form, see the red areas of Figure 4.14 (middle row). The first-quadrant loop expands more than the fourth-quadrant loop, due to the fact that the former releases more energy. Notice also, that the relaxed loops maintain zero net current: the loops are always surrounded by white (i.e., zero current). The magnetic field plots of Figure 4.13 indicate that current magnitude plots at other z coordinates will be similar to the ones shown here.

The final states calculated by the numerical simulations are shown in the bottom row of Figure 4.14. These plots are overlaid with azimuthal magnetic field vectors, which are consistent with a cylindrical, constant-α configuration, bounded by a current-neutralising layer: the arrows all follow each other and the arrow sizes increase away from the axis, and then diminish before the loop edge.

4.2.4 Helicity

DeVore (2000) showed how to calculate the magnetic helicity over an entire coronal volume above a photospheric bounding surface. The first step is to work out the magnetic vector potential for a current-free field that has the same distribution of vertical magnetic flux at the lower boundary. DeVore begins by deriving an expression for the scalar potential, using Green's function for Laplace's equation as the integration kernel,

$$\phi_c(x, y, z, t) \;=\; \frac{1}{2\pi}\int_{-3}^{+3} dx' \int_{-3}^{+3} dy' \frac{B_z(x', y', -10, t)}{\sqrt{(x - x')^2 + (y - y')^2 + z^2}} \,. \qquad (4.33)$$

The grid domain used by LARE3D has a Cartesian geometry: the coronal loop is initially represented as a straight cylinder within a rectangular box. The x and y axes extend between -3 and +3; hence, the integral limits given above. The photospheric

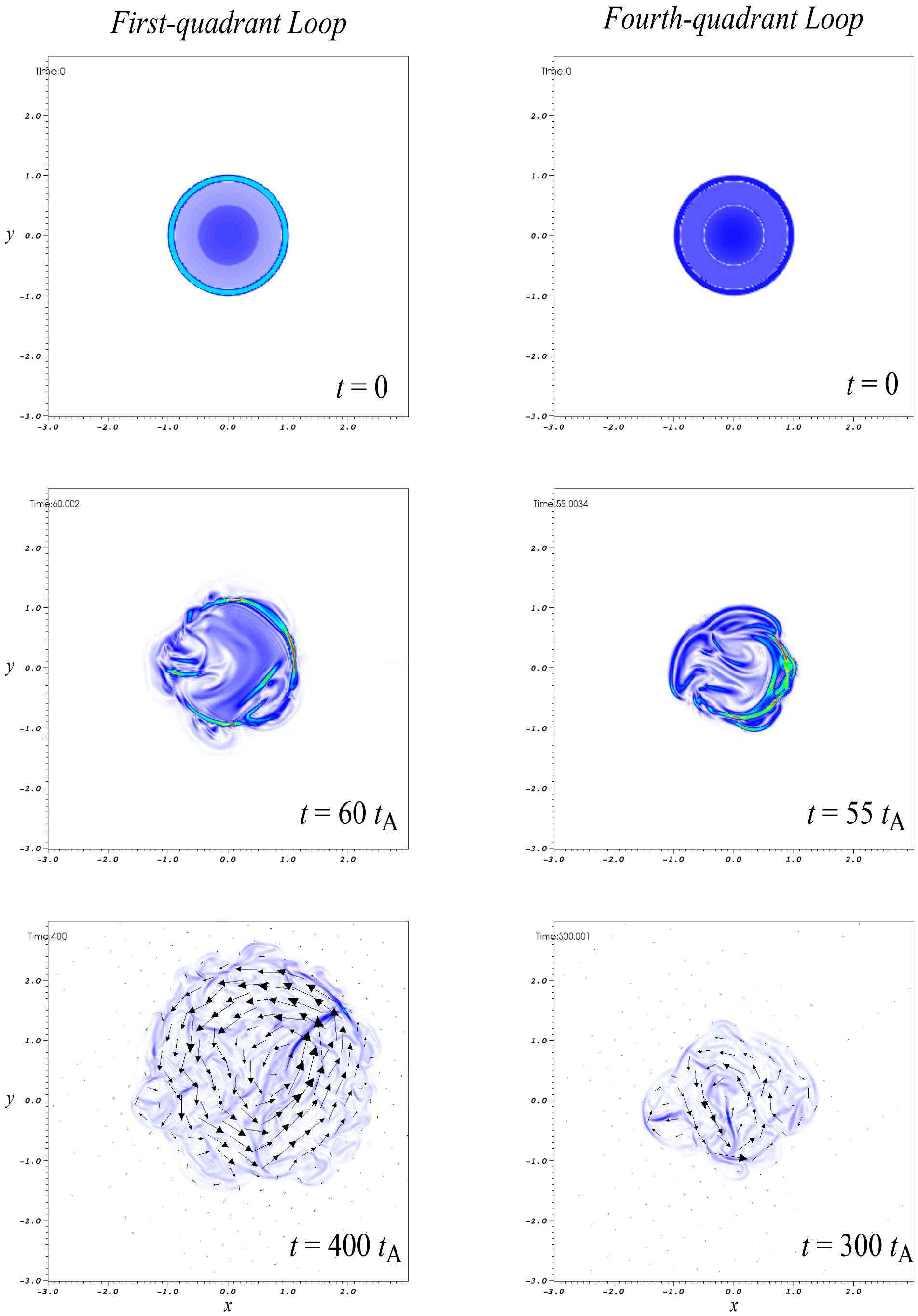

Figure 4.14: The spatial variation of current magnitude across the loop cross section at the apex (i.e., where $z = 0$) and at three different times for the first-quadrant loop (left column) and for the fourth-quadrant loop (right column). Low currents are represented by blue white colours and currents above the critical current ($j_{\mathrm{crit}} \geq 15$) are denoted by red pink colours. The black arrows in the final images (bottom) are magnetic field vectors.

boundaries are located at the limits of the z axis ($z = -10, +10$) and $z = 0$ is the loop apex. Equation 4.33 uses the first boundary position. The scalar vector potential is constructed like so,

$$\vec{A}_{\mathrm{c}}(x,y,-10,t) \;=\; \nabla \times \hat{z} \int_{z}^{+10} dz'\; \phi_{\mathrm{c}}(x,y,z',t)\,; \tag{4.34}$$

which becomes

$$\begin{aligned} \vec{A}_{\mathrm{c}}(x,y,-10,t) \;=\; & -\frac{1}{2\pi}\int_{z}^{+10} dz' \int_{-3}^{+3} dx' \int_{-3}^{+3} dy'\; \frac{B_z(x',y',-10,t)(y-y')}{\left[(x-x')^2+(y-y')^2+z^2\right]^{\frac{3}{2}}}\,\hat{x} \\ & +\frac{1}{2\pi}\int_{z}^{+10} dz' \int_{-3}^{+3} dx' \int_{-3}^{+3} dy'\; \frac{B_z(x',y',-10,t)(x-x')}{\left[(x-x')^2+(y-y')^2+z^2\right]^{\frac{3}{2}}}\,\hat{y}\,, \end{aligned} \tag{4.35}$$

when the curl differentials are moved inside the integral and applied to an expanded ϕ_{c}. Now the gauge-invariant vector potential can be specified as,

$$\vec{A}(x,y,z,t) \;=\; \vec{A}_{\mathrm{c}}(x,y,-10,t) - \hat{z} \times \int_{-10}^{z} dz'\; \vec{B}(x,y,z',t)\,, \tag{4.36}$$

by subtracting the helicity due to the potential field. Equation 4.36 can be re-expressed by expanding the cross product of the second term,

$$\begin{aligned} \vec{A}(x,y,z,t) \;=\; & \vec{A}_{\mathrm{c}}(x,y,-10,t) \\ & + \int_{-10}^{z} dz'\; B_y(x,y,z',t)\,\hat{x} - \int_{-10}^{z} dz'\; B_x(x,y,z',t)\,\hat{y}\,. \end{aligned} \tag{4.37}$$

Finally, the gauge-invariant magnetic helicity is

$$K \;=\; \int_V \vec{A}\cdot\vec{B}\; dV \;=\; \int_{-3}^{+3} dx \int_{-3}^{+3} dy \int_{-10}^{+10} dz\; \vec{A}(x,y,z,t)\cdot\vec{B}(x,y,z,t)\,. \tag{4.38}$$

The geometry used by DeVore differs significantly from that used in this thesis (Figure 4.4), which features two separate photospheric boundaries at the limits of the z axis. Fortunately, the relative positions of the two boundaries mean that if the flux is cancelled for one it will be cancelled for the other, and so the lower bound z coordinate can simply be set to -10.

Equations 4.33–4.38 have been implemented, using the five-point Newton-Cotes integration formula, in the IDL scripting language. A helicity calculation involving all the grid cells would take several days to complete on a dual-core desktop machine. For this reason, the IDL code has been modified so that the spatial dimensions can be sampled at regular intervals of specified length. For example, the x and y dimensions could be sampled at every fourth cell and the z dimension at every other cell. The level of sampling chosen should not prejudice the result, so the helicities will first be calculated using a coarse sampling; the sampling is then improved until the result converges.

Table 4.2: Helicity calculation for various levels of coordinate sampling at the most chaotic time, i.e., the moment of instability, $t = 60\,t_{\mathrm{A}}$ (first-quadrant loop) and $55\,t_{\mathrm{A}}$ (fourth-quadrant loop). All values are rounded to two decimal places.

Loop	$16 \times 16 \times 8$	$8 \times 8 \times 4$	$4 \times 4 \times 2$
First-quadrant	10.02	12.51	12.3
Fourth-quadrant	2.43	1.1	1.14

Table 4.2 shows the helicities (rounded to two decimal places) for the time when the loop is furthest from equilibrium — this is when the result is most likely to be affected by the sampling. The first sampling level is $16 \times 16 \times 8$: the x and y dimensions are sampled at every sixteenth cell and the z dimension at every eighth cell. Convergence is met when the sampling is $4{\times}4{\times}2$; these settings will be used to calculate the helicity at other times during the simulation[4].

The six loops (A–F) have zero net current initially and should continue to do so during the simulation; thus, outside the loop the helicity is zero. This means the helicity calculated using a straightforward cylindrical geometry can easily be compared to that calculated for a Cartesian geometry, where the loop is enclosed within a rectangular

---

[4] The sampling for the initial time need not be as fine, since, in the beginning, the fields will be z-invariant.

box. The helicity is zero everywhere in the additional volume between the surface of the rectangular box and the outer edge of the potential envelope.

Table 4.3: Helicity at three times during the simulations of the first and fourth quadrant loops. All values are rounded to two decimal places.

Loop	**Initial**	**Instability**	**Final**
First-quadrant	12.3	12.3	12.3
Fourth-quadrant	1.13	1.14	1.18

Again, the helicities are calculated for both loops, but now this property is also calculated at the start and end of the simulation (Table 4.3).

4.3 Comparison with Relaxation Theory

In order to continue the work of Chapter 3 for zero-net-current loops, it will first be necessary to examine the details of the relaxation process that are uncovered by numerical experiments. There is more than one way to calculate the relaxed state: choices must be made concerning the radial bounds over which helicity is conserved and energy release is calculated. The different relaxation *scenarios* will be compared with the numerical results and the one that best matches this data will be incorporated within an improved Taylor Relaxation model (Chapter 5).

4.3.1 Relaxation Scenarios

In Chapter 3, a loop with net current was relaxed such that it expanded to fill the entire potential envelope: the α-profile was invariant between $r = 0$ and $r = 3$ ($R_{\mathcal{B}}$). The *relaxed* alpha was identified by assuming that ψ (axial flux) and K/ψ^2 (helicity over axial flux squared) were conserved over the loop and envelope, in accordance with Taylor relaxation. Hence, the relaxed state always represented a threefold radial expansion of the initial state.

This model (Scenario 1) is the simplest relaxation scheme — ψ and K/ψ^2 are conserved from the axis to $R_{\mathcal{B}}$. It represents total relaxation and will have the lowest energy, according to Taylor's hypothesis. However, the expansion radius, R_e, could be anywhere in the range $\frac{9}{10}R_{\mathscr{b}} \leq R_e \leq R_{\mathcal{B}}$. The α-profile is invariant between the axis and R_e, and the field coefficients of the relaxed envelope (where $\alpha = 0$) are set such that the field is continuous at R_e; i.e., the relaxed state *has* net current. When $R_e = R_{\mathcal{B}}$, this scenario is identical to the relaxation scheme discussed in Chapter 3. This is likely to be a good model for fields with net current, since reconnection activity usually extends throughout the simulation volume (Browning et al. 2008).

Scenarios 2 and 3 are forms of partial relaxation, applicable to a range of expansion radii, see Figure 4.15. Some form of partial relaxation is more likely to be relevant to the zero-net-current case; it is known from simulation results, presented here and in Hood et al. (2009), that reconnection is of limited extent, leaving the external field undisturbed. Scenario 2 uses a neutralising loop surface (at $r = R_e$) to maintain zero net current, whereas the third scenario uses a neutralising layer. The neutralising surface of Scenario 2 is actually achieved by fixing the field coefficients of the potential envelope so that they do not change during relaxation. In the relaxed state, the envelope is the region between R_e and $R_{\mathcal{B}}$. Scenario 3 maintains the current neutralisation by retaining

Figure 4.15: Two possible relaxation states for a zero-net-current coronal loop. Both relaxations maintain a zero net current: Scenario 2 (left) achieves this via a neutralisation surface, whereas Scenario 3 (right) incorporates a current-neutralisation layer.

the current neutralisation layer (Figure 4.15, right). The relaxed neutralisation layer begins at R_e, which is always $\frac{9}{10}R_{en}$. Thus, for Scenario 3, the α-profile is α_e between the axis and R_e, α_{en} between R_e and R_{en}, and zero between R_{en} and $R_{\mathcal{B}}$ — α_{en} is fixed so that B_θ goes to zero at R_{en}. Again, the field coefficients of the potential envelope do not change between the initial and the relaxed states.

For Scenarios 2 and 3, the axial flux is conserved such that ψ_e of the threshold state is equal to ψ_e of the relaxed state (K/ψ^2 is conserved in the same manner). Whenever, ψ, K and W are used, the subscript e denotes the relaxation radius, R_e; it functions as the radial upper bound over which the associated property is calculated — the lower bound being the axis. For example, K_e is the helicity from $r=0$ to $r=R_e$, and $K_{\mathcal{B}}$ is the helicity from $r=0$ to $r=R_{\mathcal{B}}$, the outer edge of the potential envelope. Note, helicity is absent from the potential envelope surrounding a zero-net-current loop: $K_{b}=K_{\mathcal{B}}$ (unlike magnetic energy, $W_{b}\neq W_{\mathcal{B}}$). The energy release is given by Equation 4.39 for scenario 1 and by Equation 4.40 for the other two scenarios;

$$\delta W = W_{\mathcal{B}}(\alpha_{\mathrm{i}1},\alpha_{\mathrm{i}2}) - W_{\mathcal{B}}(\alpha_e)\,, \tag{4.39}$$

$$\delta W = W_e(\alpha_{\mathrm{i}1},\alpha_{\mathrm{i}2}) - W_e(\alpha_e)\,, \tag{4.40}$$

where $W(\alpha_{\mathrm{i}1},\alpha_{\mathrm{i}2})$ is the energy of the threshold state and $W(\alpha_e)$ is the energy of the relaxed state.

Figures 4.16 and 4.17 show how α_e and δW vary with relaxation radius (R_e). Scenarios 2 (long dashed) and 3 (short dashed) give similar results. As expected, these figures show an inverse relationship between α_e and δW, but only for relaxation scenarios that maintain current neutralisation (2 and 3). In general, δW increases with R_e, however, this relationship is not linear; beyond a moderate expansion of 50% ($R_e=1.5$) the energy release is ~99% of its maximum for the fourth-quadrant loop and ~80% for the first-quadrant loop. For Scenario 1, the energy release is almost independent of relaxation radius; the relaxed states have very similar energies for all values of R_e between $0.9R_{b}$ $(=0.9)$ and $R_{\mathcal{B}}$ $(=3)$.

The reason for this constancy, hinges on the fact that Scenario 1 relaxations have

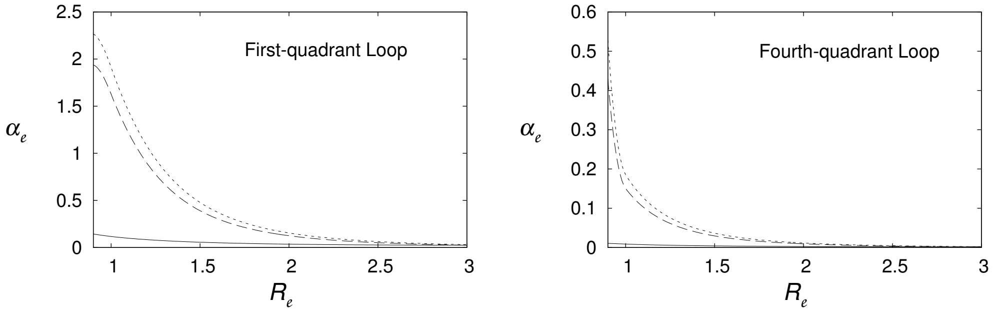

Figure 4.16: The variation of relaxed alpha (α_e) with relaxation radius (R_e) for the first-quadrant loop (left) and for the fourth-quadrant loop (right). Scenario 1 is represented by a solid black line; Scenario 2 is long dashed and Scenario 3 is short dashed.

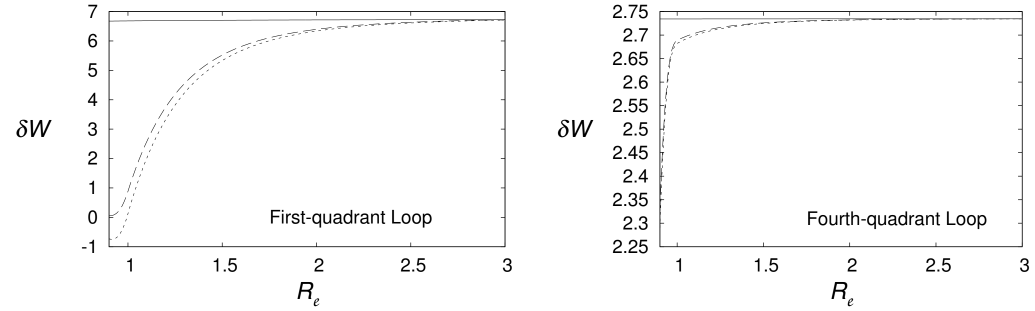

Figure 4.17: The variation of dimensionless energy release (δW) with relaxation radius (R_e) for the first-quadrant loop (left) and for the fourth-quadrant loop (right). The line types are the same as those used for Figure 4.16.

net current: the potential envelope of the relaxed state has helicity. Hence, in order for $K_{\mathcal{B}}$ to be conserved, the helicity from the relaxed loop (K_e) must be minimised; and therefore, the energy release is maximised. Figure 4.16 shows that, for Scenario 1, α_e is a very small when $R_e = R_{b}$. The relaxed alpha value can only get smaller (but never fall below zero) as the relaxation radius increases. If the codomain of $\alpha_e(r)$ is constrained, the same will be true of δW. The energy releases have also been calculated for Loops A, C, D and F, see Appendix B.2.1.

The next plots will be used to determine which relaxation scenario best matches the numerical results. Figures 4.18 and 4.19 compare the final field profiles from the numerical simulations of both loops, with those predicted by the three scenarios described above. The current magnitude plots of Section 4.2.3 suggested that the final

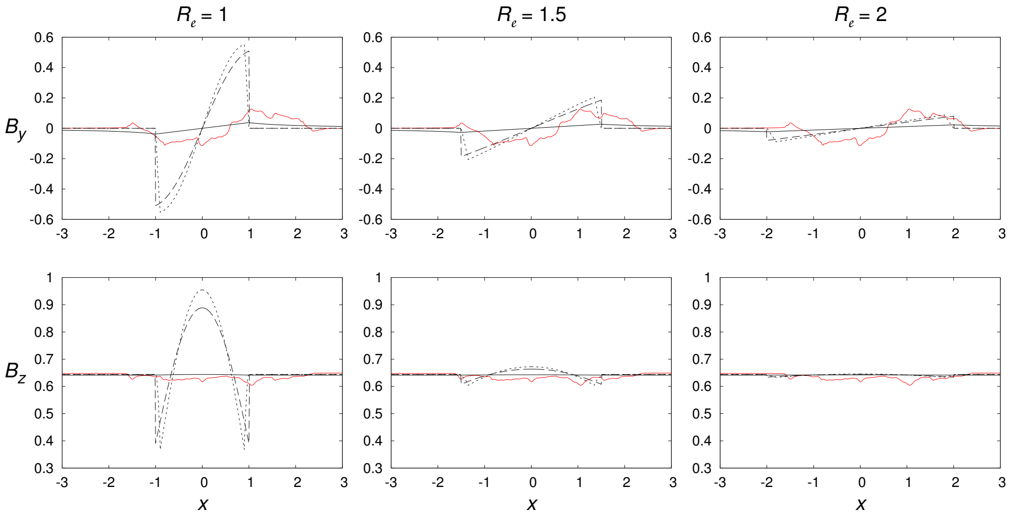

Figure 4.18: First-quadrant loop: a comparison between the B_y (top row) and B_z (bottom row) obtained analytically (black line) and numerically (red line). The numerical profiles are from the final frame of the high resolution LARE3D simulation (at $y = z = 0$). The comparisons are done for different relaxation radii, $R_e = 1$ (left column), 1.5 (middle column) and 2 (right column). Each plot compares the three relaxation scenarios, 1 is denoted by a solid line, 2 is long dashed and 3 is short dashed. The horizontal x-axis is equivalent to the radial axis.

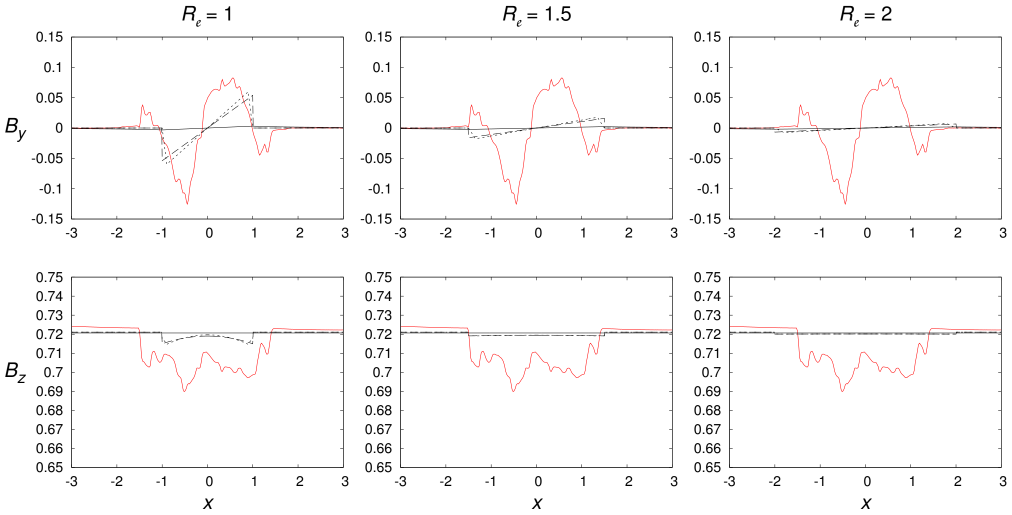

Figure 4.19: Fourth-quadrant loop: a comparison between magnetic field profiles; it is presented in the same way as Figure 4.18.

state maintained current neutralisation, and so those scenarios that have this feature are a better fit for the numerically-derived B_z and B_y profiles. The value of R_e is critical in achieving the best fit between the analytical and numerical results. For Scenarios 2 and 3, the closest correspondence will occur near to $R_e = 1.5$ for the first-quadrant loop (Figure 4.18) and near to $R_e = 1$ for the fourth-quadrant loop (Figure 4.19). The numerical (red) plots suggest that the loop axis has shifted from its initial $x = 0$ position, which is to be expected for a loop undergoing a kink instability; hence, the analytical (black) plots do not fit perfectly. However, the important point is that these comparisons do reveal the most accurate relaxation scenarios. Scenario 1 gives a weak match for the first-quadrant loop and a poor one for the fourth; however, the other two scenarios will, for the right value of R_e, achieve better matches for both loops. Figures 4.18 and 4.19 reveal scant difference between Scenarios 2 and 3; so, this thesis will continue with the scenario that has the more simple relaxed state (Scenario 2).

4.3.2 Final Magnetic Fields

Now that the details of the relaxation process have been decided, we can compare more thoroughly the final numerical results with the analytical predictions. The following figures show how well the field profiles produced by the numerical simulations match the configuration described by the Taylor-relaxed loop. These results cover an extensive series of positions within the loop volume. The aim of this section is to find the R_e and α_e values that best match the numerical results for all six loop configurations.

The final numerically-determined state is merely the last snapshot provided by the simulation; it is expected to be close to the analytically-determined relaxed state. Each loop is simulated for at least $300t_{\mathrm{A}}$; so, the sooner the instability occurs, the closer the loop will be to a fully relaxed state by the end of the simulation. A Taylor-relaxed loop is defined by some combination of R_e, B_1, α_e and σ_e (the sign of α_e). The Cartesian components of the relaxed field are as follows,

$$B_x(r) = -B_\theta(r)(y/r)\,, \tag{4.41}$$

$$B_y(r) = B_\theta(r)(x/r)\,, \tag{4.42}$$

$$B_z(r) = B_1 J_0(|\alpha_e| r)\,, \tag{4.43}$$

where $B_\theta(r) = \sigma_e B_1 J_1(|\alpha_e| r)$. An IDL code is used to generate unique relaxed configurations for every value of R_e between 0.9 and 3.0 in increments of 0.01. Hence, for each field component, it is checked which of the 211 possibilities has the lowest chi-squared value when compared with the numerical plot for the same component. These field comparisons (B_x, B_y and B_z) are performed over the x dimension for a selection of y-z coordinate pairs. Figures 4.20–4.22 compare the analytical and numerical relaxed field profiles for the first-quadrant loop.

Each of the following plots is associated with a particular x-axis, located at a specified y-z position. Note, the x-coordinate does not necessarily give the radial position, unless the x-axis intersects the loop axis. The actual radial positions at each x-coordinate can only be determined if the position of the loop axis is known. During the instability, the loop axis will become kinked and the amplitude of these kinks will vary with time. If the loop is sampled at a z-coordinate that has undergone a significant kink, the axis is likely to be far away from the origin in the x-y plane. Therefore, there will exist x-axes that (mostly) sample the potential envelope and little of the interior of the loop.

The location of the loop axis can be estimated if one assumes that the numerical relaxed loop is current neutralised, which appears to be the case (Figure 4.14). The loop boundary is crossed whenever α falls to zero. However, numerical inaccuracy means that the loop edge is in fact, wherever α is less than some previously determined residual value. After the first Lagrangian step, the loop will be almost undisturbed; i.e., it is extremely close to its initial state. Hence, one can reasonably assume, that all positions at a distance of twice the initial loop radius ($r = 1$) lie within the potential envelope. The α values within this region will of course be very small, but not zero,

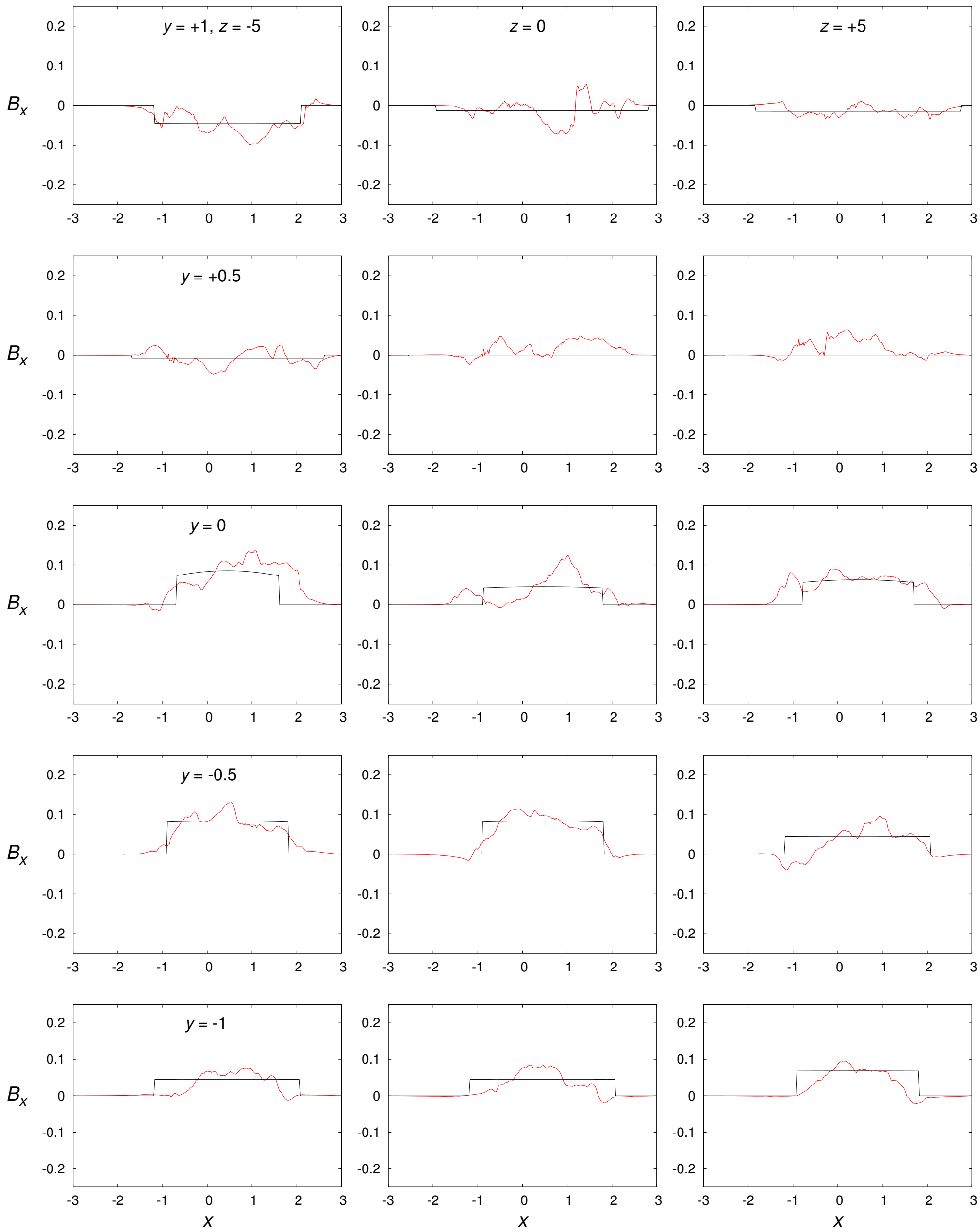

Figure 4.20: First-quadrant loop: a comparison between the B_x magnetic field profiles obtained numerically (red line) and analytically (black line). The latter is calculated from the α_e and R_e that best fit the numerical plot, which is taken from the final frame ($t = 400\,t_A$) of the high resolution LARE3D simulation. The comparisons are done for different z coordinates, $z = -5$ (left column), 0 (middle column) and 5 (right column); and for different y coordinates, $y = -1$ (bottom row), -0.5 (one above bottom row), 0 (middle row), 0.5 (one above middle row), and 1 (top row).

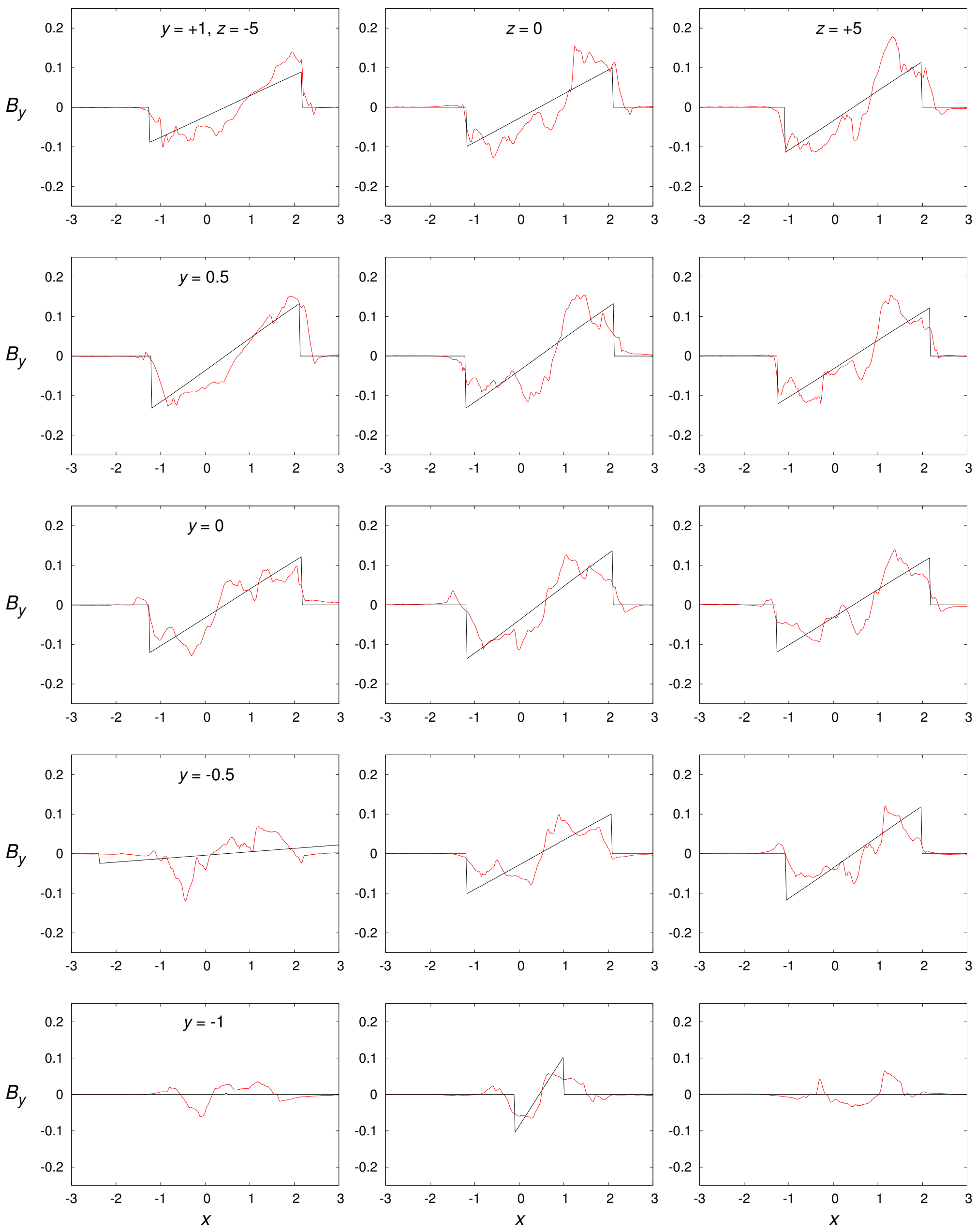

Figure 4.21: First-quadrant loop: a comparison between the B_y magnetic field profiles obtained numerically (red line) and analytically (black line). See Figure 4.20 for further details.

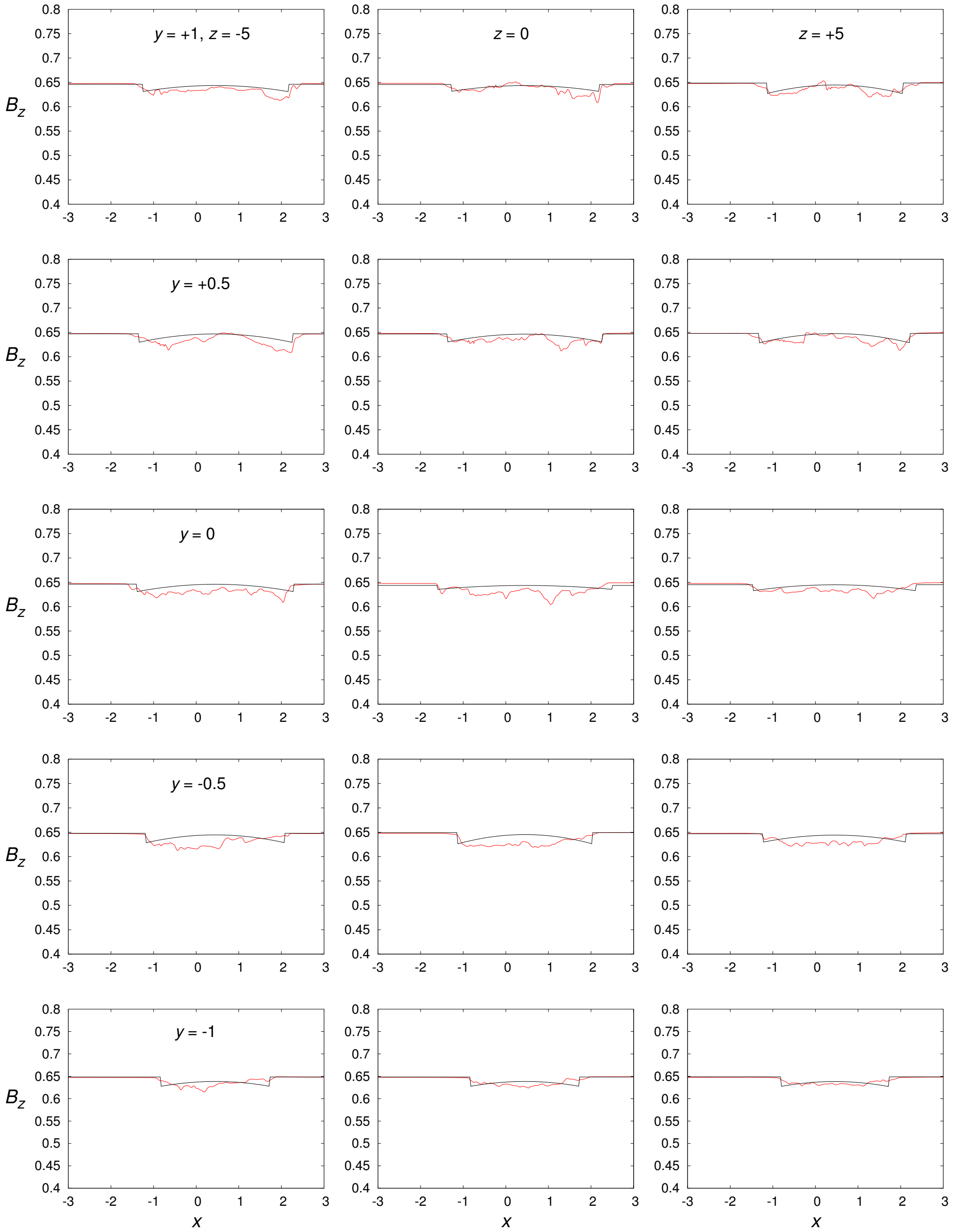

Figure 4.22: First-quadrant loop: a comparison between the B_z magnetic field profiles obtained numerically (red line) and analytically (black line). See Figure 4.20 for further details.

due to numerical inaccuracy. The greatest of these errors is the residual value used to determine the loop edge at later times in the simulation. Thus, a simple scan within the x-y plane can uncover the loop surface: the origin is the midpoint of the x-line that runs through the thickest part of the loop.

In general, the analytical plots of Figures 4.20–4.22 (first-quadrant loop) show a good agreement with the numerics; however, the R_e and α_e that best fit the red lines are independently chosen for each of the forty-five subplots. Figure 4.23 conveys the variation in the best fit parameters — some of the plots that failed to agree occupy (or are near to) the R_e limits. A disparity between the black and red B_x plots is noticeable when $z = 0.5, 1$. There are similiar issues with three of the B_y plots; these are located at the opposite end of the y-z grid to the failed B_x matches (Figures 4.20 and 4.21). The positions where the B_x plots fail to agree are $(y, z) = (1, 0), (1, 5), (0.5, -5), (0.5, 0)$ and $(0.5, 5)$; and for B_y, the positions are $(-0.5, -5), (-1, -5)$ and $(-1, 5)$. Common to all these positions is a noisy numerical plot that fluctuates around the zero line.

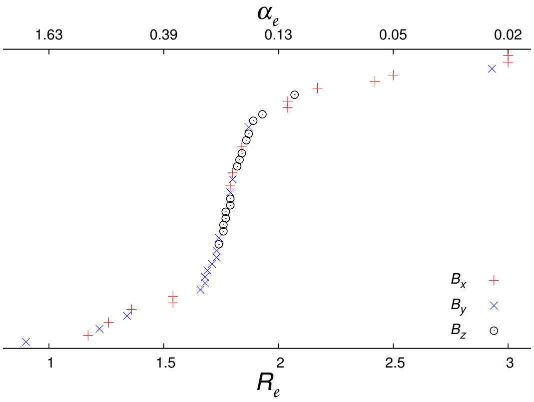

Figure 4.23: First-quadrant loop: the best-fit R_e and α_e used for each analytical plot in Figures 4.20–4.22. Black circles are for those best fits determined from B_z profiles, red plus signs are for B_x and blue crosses B_y.

The following averages are derived from the data presented in Figure 4.23, $\langle R_e \rangle = 1.83 \pm 0.42$ and $\langle \alpha_e \rangle = 0.28 \pm 0.32$. These two properties have a one-to-one mapping and there are many R_e, α_e pairs that provide the best fit for more than one numerical field plot. Hence, the slightly unusual form of Figure 4.23 is intended to distinguish the best-fit pairs for all forty-five field plots.

A similar treatment for the dimensionless energy release gives −5.87 ± 1.11. Despite the large scatter for α_e, the deviation for δW is comparatively modest, this is because $d(\delta W)/d(R_e)$ is small when $R_e \approx 1.8$ (Figure 4.17).

The impact of noisy plots and the fact that the final numerically-calculated state is only *partially* relaxed, can be appraised by re-running the simulation with background resistivity; once again, $\eta_{\mathrm{b}} = 0.0001$. The field profile comparisons can be found in Appendix C.3; below is the corresponding R_e-α_e scatter plot. Figure 4.24 yields

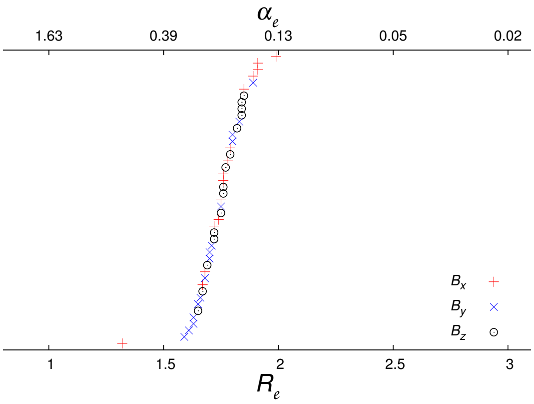

Figure 4.24: First-quadrant loop: the same as Figure 4.23, but this time a background resistivity has been applied.

$\langle R_e \rangle = 1.75 \pm 0.11$ and $\langle \alpha_e \rangle = 0.22 \pm 0.07$. The mean dimensionless energy release has also been calculated, $\langle \delta W \rangle = -6.07 \pm 0.25$. The resistivity smooths out low-level noise and thereby mitigates substantially the deviation associated with the analytical fit. Furthermore, the evolution towards a relaxed state starts earlier (Figure 4.7), so the final state is closer to full relaxation.

All of the above has been repeated for the fourth-quadrant loop. The numerous field-comparison plots have been left out; only the scatter plot (for the $\eta_{\mathrm{b}} = 0$ case) is presented. Figure 4.25 gives $\langle R_e \rangle = 1.29 \pm 0.69$ and $\langle \alpha_e \rangle = 0.17 \pm 0.11$; it also reveals a flaw in the IDL script used to decide the analytical fits. The bigger the increase in loop radius during relaxation, the lower the energy of the relaxed field; in particular, the magnitudes of B_x and B_y will be close to zero. Numerical plots that exhibit low-level

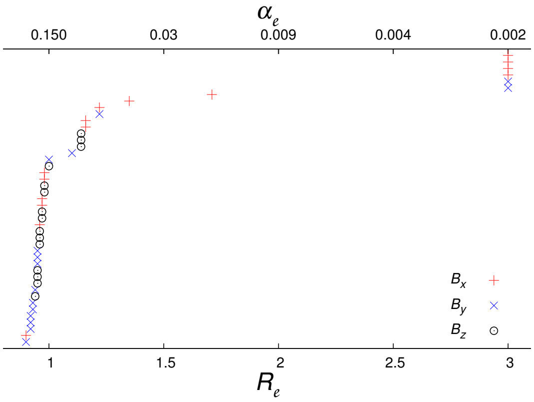

Figure 4.25: Fourth-quadrant loop: the plot format follows Figure 4.23.

noise along the entire x-axis have a tendency to be matched against a Taylor-relaxed field of $R_e = 3$ — there are six false matches of this type in Figure 4.25. These points have a disproportionate impact on the R_e average; nearly all of the other points are to the left of the average (1.29). Excluding the false matches, returns $\langle R_e \rangle = 1.03 \pm 0.15$, $\langle \alpha_e \rangle = 0.19 \pm 0.1$ and $\langle \delta W \rangle = -2.63 \pm 0.09$. The energy release is fairly insensitive to relaxation radius (Figure 4.17): before the exclusion, $\langle \delta W \rangle = -2.65 \pm 0.09$.

4.4 Summary

The overall impressive level of agreement demonstrated for the first and fourth quadrant loops, also extends to other positions along the instability threshold, see Table 4.4. This table also confirms that the analytically-calculated helicities (Appendix A.4.4) of Loops B–F are in approximate agreement with the numerical values, which were derived according to the procedure discussed in Section 4.2.4. The correspondence between the numerical and analytical energy releases is the most significant finding of this chapter. There is evidence to suggest that this correlation persists even when different settings are used for the LARE3D parameters controlling resistive MHD (Section 4.2.1 and Figure 4.7). In addition, these results are consistent with previous work (Browning et al. 2008; Hood et al. 2009).

Table 4.4: Analytical and numerical comparison involving the marginally kink-unstable Loops B–F. Numerical data are shown in red — the numerical helicities are an average over three times (initial, instability and final). All values are rounded to two decimal places.

Simulation	R_e	α_e	K	K	$\lvert\delta W\rvert$	$\lvert\delta W\rvert$
F	1.94	0.24	12.89	12.19	8.31	8.54 ± 0.36
E (first quadrant)	1.83	0.28	12.92	12.3	5.8	5.87 ± 1.11
D	1.68	0.3	11.03	10.52	3.15	3.41 ± 0.94
C	1.72	0.2	6.45	6.14	2.15	2.36 ± 0.37
B (fourth quadrant)	1.03	0.19	1.22	1.15	2.58	2.63 ± 0.09

It is interesting to compare the change in helicity ($\delta K/K$), over the course of the simulation, with the change in magnetic energy ($\delta W/W$). An approximate value for the helicity variation is $||K_{\text{final}}|/|K_{\text{initial}}| - 1|$; Tables 4.3 and C.1 provide the necessary data. For Loops E (first-quadrant) and C, $\delta K/K$ is two orders of magnitude smaller than $\delta W/W$, and for Loops D and F, this difference reduces to one order of magnitude. The fact that $\delta K/K \ll \delta W/W$, implies that magnetic energy dissipation is taking place within thin current sheets (Section 2.4). These results are comparable with (Browning et al. 2008); but for Loop B (fourth-quadrant), $\delta K/K$ is slightly larger than $\delta W/W$. This last result is not so surprising when one considers that the α parameters for Loop B have opposite sign and are almost equal in magnitude (Table 4.1). Consequently, Loop B contains regions of positive and negative helicity that sum to a value close to zero, making $\delta W/W$ large. In this case, a slightly different calculation should be used, one based on the helicity magnitude, $|K| = \int_V |\vec{A} \cdot \vec{B}|\, dV$.

The issue of false matches (see the end of Section 4.3.2) was a problem for Loop B only; the mean values for the other loops (i.e., R_e, α_e, δW) were calculated from a full set of analytical field fits. Loop A is not shown in Table 4.4 because it proved to be numerically unstable, even when the spatial resolution was increased to $512^2 \times 1024$.

It would appear that the assumption of a Taylor-relaxed state, subsequent to kink instability, has been vindicated by the results of the LARE3D numerical code. Although, the relaxation does not extend over the full numerical volume, but over a region of smaller extent (out to a radius R_e, which is less than the full radius, $R_{\mathcal{B}}$). In this sense, the relaxation is partial.

An improved TRoLE code, incorporating the most successful relaxation scheme (Scenario 2), and involving ensembles of zero-net-current loops can now be executed with some confidence. However, a relaxed state can only be identified if the relaxation radius is known; at present, it is unclear how R_e can be precisely determined from the threshold position. Although, the results of Section 4.3.1 (Figure 4.17) and Appendix B.2.1 (Figures B.7 and B.8) have revealed that for marginally-unstable loops, the energy release varies little with relaxation radius once $R_e \geq 1.5$. The next chapter will consider minimal ($R_e = 1$) and maximal ($R_e = 3$) relaxations.

5

The Properties and Consequences of Kink-unstable Ensembles of Zero-net-current Coronal Loops

Improving the realism of the loop ensemble model (TRoLE) is the focus of this chapter, which is based on the work published in Bareford et al. (2011). Previously, heating event distributions were calculated for ensembles of loops that possessed net current (Chapter 3). This was done using a simple cylindrical field model in which the current profile, $\alpha(r)$, of the stressed field is represented by a two parameter family. The resulting distributions were compatible with the energies required for coronal heating. However, as stated earlier (Section 4.1.2), a zero-net-current loop is more realistic. There are only two such fields on the marginal instability curve of Figure 3.2, for which the current due to α_2 cancels that due to α_1 (that is $\alpha_1 \approx \mp 2.48$, $\alpha_2 \approx \pm 0.95$). In the previous chapter, a new family of current-neutralised loops was introduced, see Section 4.1.2 (Figure 4.4). The linear stability of this new family of equilibria require further investigation.

There are other improvements that will also have a bearing on the energy release distributions. So far, the random nature of photospheric motions has been represented by allowing different parts of the loop interior to vary independently. However, it is more reasonable to assume some level of correlation, since it is likely that the whole of a loop footpoint will be subjected to the same convective eddy. Furthermore, this chapter also considers the consequences of varying the loop aspect ratio ($L/R_{\mathscr{b}}$), and it will continue the search for a twist-based parameter that can be used as a simple diagnostic for loop instability; see e.g., Hood and Priest (1979).

5.1 Equilibrium Fields

Section 4.1.2 presented the equilibrium fields for a zero-net-current loop (Equations 4.15–4.22). Essentially, the equilibrium parameter space remains 2D; i.e., it is determined by α_1, α_2. The field profiles for a selection of loop configurations are given in Appendix B.2.

Again, the magnetic flux through the loop and envelope is conserved:

$$\begin{aligned}\psi \quad = \quad \int_0^{R_{\mathcal{B}}} 2\pi r B_z \, dr = {} & \frac{2\pi B_1 R_1}{|\alpha_1|} J_1(|\alpha_1| R_1) \\ & + \frac{2\pi B_2 R_2}{|\alpha_2|} F_1(|\alpha_2| R_2) - 2\pi R_1 J_1(|\alpha_1| R_1) \left(\frac{\sigma_{1,2}}{|\alpha_2|} \right) \\ & + \frac{2\pi B_3}{|\alpha_3|} (R_{\mathscr{b}} G_1(|\alpha_3| R_{\mathscr{b}}) - R_2 G_1(|\alpha_3| R_2)) \\ & + \pi B_4 \left(R_{\mathcal{B}}^2 - R_{\mathscr{b}}^2 \right) . \end{aligned} \tag{5.1}$$

Hence, ψ is still normalised to 1 and B_1 is determined (noting that, in Equations 4.23–4.28, B_j and C_j are functions of B_1). The normalised coronal loop radius ($R_{\mathscr{b}} = 1$) is itself used to normalise the loop length (e.g., $L = 20R_{\mathscr{b}}$), see Figure 4.4.

The primary assumption of the TRoLE model is that the loop evolves through a sequence of two-α fields (Equations 4.15–4.22) as it is twisted by photospheric footpoint motions. The introduction of magnetic twist gives the coronal loop a circular cross section (Klimchuk et al. 2000). The TRoLE model presented here has the same cross-sectional shape, but the loop radius ($R_{\mathscr{b}}$) is held constant throughout the simulated photospheric driving. Purely azimuthal photospheric motions would cause a small expansion of the loop (Browning and Hood 1989) which are ignored here; alternatively, small radial footpoint motions must be allowed in order to maintain constant loop radius. In any case, the sequence of loop equilibria explored by TRoLE is clearly a small subset of the possible variation in field profiles that might arise from photospheric motions. As these random motions proceed, the loop continues to evolve through force-free equilibria until it becomes linearly unstable.

5.2 Linear Kink Instability Thresholds

The instability threshold is still a curve in 2D α-space (α_1, α_2). The properties of the loop (e.g., α_1, α_2 and α_3) at these threshold points can once again be found by substituting the perturbation function into the linearised MHD equations. A modified CILTS code, one that incorporates a current-neutralisation layer, is then able to uncover the threshold. Figure 5.1 shows the instability threshold curves mapped by the CILTS code for three values of loop aspect ratio ($L/R_б = 10$, 20, 30). The longer the loop the smaller the α-value required for instability, since, if the radius is held constant, longer loops are less affected by the stabilising influence of line-tying (Hood and Priest 1979). The addition of a current neutralisation layer prevents the threshold curves from clos-

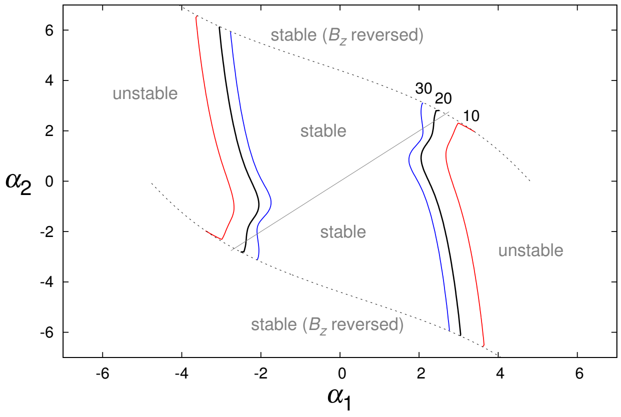

Figure 5.1: The instability thresholds for $L/R_б = 10$ (red), 20 (black) and 30 (blue). A closed stability region is formed by the B_z reversal lines (dashed). The relaxation line ($\alpha_1 = \alpha_2$) is also shown.

ing near the α-space origin; this is unlike the net current case, for which the threshold is a closed curve (Figure 3.2). The open shape is indeed similar to the instability curve for loops with a conducting wall at R_b (Browning and Van der Linden 2003), because the eigenfunctions almost vanish at this boundary; see Figure 5.3. Also, if α_1 is small, α_3 will be opposite in sign to α_2, and the outer layer is stabilised by the neutralisation layer. However, the loop configurations become unrealistic as we increase the magnitude of α_2 and the axial field reverses. Positions outside the B_z reversal lines (Figure 5.1) represent loops that have axial fields of mixed polarity. These configurations cannot represent states attained by the twisting of a unipolar loop.

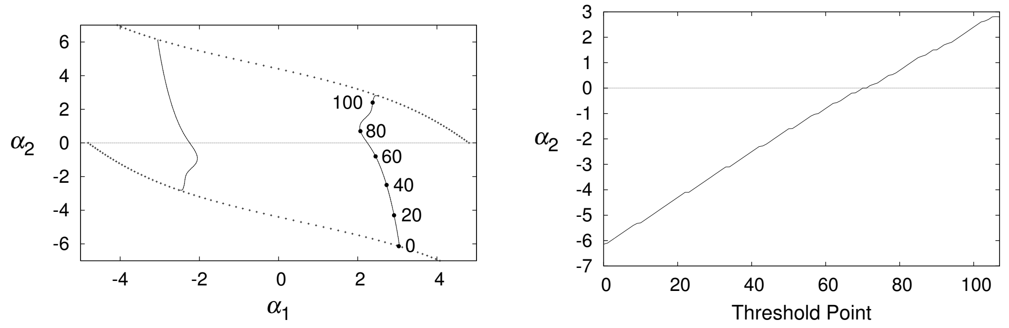

Figure 5.2: **Left**, the instability threshold for a loop of aspect ratio 20; the right half (i.e., where $\alpha_1 \geq 0$) is sampled by a selection of points. **Right**, is the variation in α_2 along the 1D representation of the instability threshold. The tick marks along the Threshold Point axis correspond with the numbers that follow the labelled threshold curve shown in the left plot.

Before proceeding to calculate the energy release properties, it is first of interest to analyse the marginally unstable states. The threshold curves shown in Figure 5.1 mirror each other. Thus, it will suffice to investigate the threshold where $\alpha_1 \geq 0$ (Figure 5.2). As in Section 3.2, the threshold curves can be represented in 1D form: the filled circles and associated numbers of Figure 5.2 (left) represent the tick marks and labels for the 1D threshold point axis, see Figures 5.5–5.9.

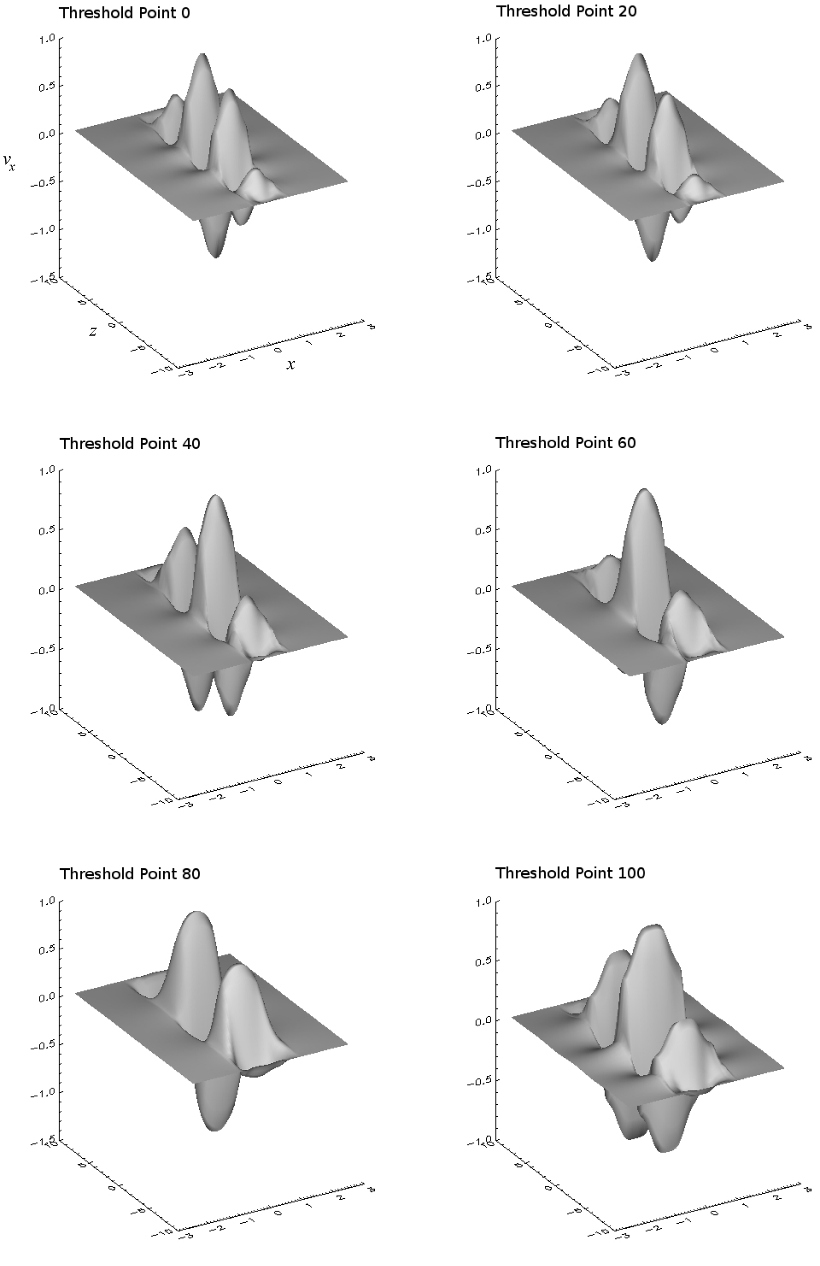

Figure 5.3: The linear eigenfunctions, $v_x(x,\ y = 0,\ z)$, for α-space points 0 (top left), 20 (top right), 40 (middle left), 60 (middle right), 80 (bottom left) and 100 (bottom right). The α coordinates associated with each eigenfunction are on the unstable side of the threshold point number (Figure 5.2). Cartesian coordinates are used, hence, the x-axis is equivalent to the radial axis.

First, we plot the linear eigenfunctions for a selection of marginally unstable α-space points that follow the instability threshold. The location of these points can be determined from the threshold point number given at the top of each plot in Figure 5.3. The eigenfunctions of the marginally unstable modes are strongly radially confined; that is, there is almost no disturbance beyond the loop radius ($R_b = 1$). This contrasts sharply with the situation for loops with net current, see Browning et al. (2008) and Chapter 3 (Figure 3.5), in which the eigenfunction can extend into the potential envelope.

Figure 5.4 shows how two types of mean magnetic shear (Equations 3.38 and 3.39) vary along the threshold. Between threshold points 20 and 90, the average shear at the threshold is again slightly higher than the limit suggested by Parker (Section 3.6.6). The ends of the threshold intersect the B_z reversal lines and this is why the shear values increase rapidly at the limits of the threshold point axis.

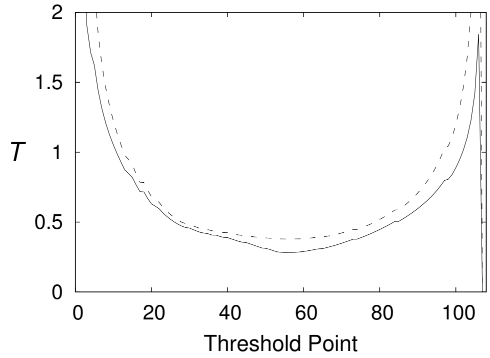

Figure 5.4: The mean absolute (solid) and root mean square (dashed) of the magnetic shear along the instability threshold. The shears are calculated over the loop volume, 0–R_b.

5.2.1 Instability Threshold and Critical Twist

Following Section 3.5.3, we look for a single twist-related parameter that takes on a critical value whenever the loop reaches the threshold (Appendix B.2 shows the twist profiles for a selection of loop configurations, stable and unstable). The average twist can be calculated in several ways; e.g., Equations 3.30, 3.31 and 3.32.

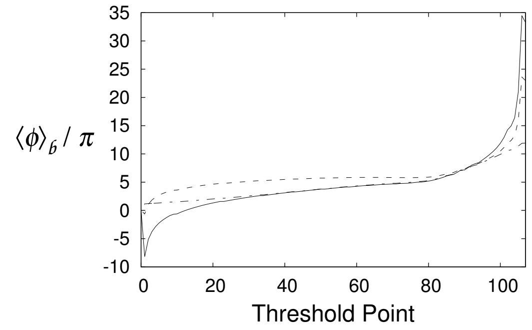

Figure 5.5: The variation in the loop average twist along the 1D representation of the instability threshold ($L/R_{\hat{b}} = 20$). The solid lines were calculated from Equation 3.32; the dashed from Equation 3.31 and the long-short dashed from Equation 3.30.

None of the twist averages (Figure 5.5) is invariant around the *whole* threshold curve, although $\langle\hat{\phi}\rangle_{\hat{b}} \approx 5\pi$ (Equation 3.31) for the majority of threshold points. This value is approximately in line with the oft-quoted result of 2.49π, the critical twist for a loop of aspect ratio 10 (Hood and Priest 1981). Each threshold point has a radial twist profile; these profiles feature reversed twist until around point 60, where the profile becomes single signed. After this point, the three average-twist plots converge to values between 5π and 10π. At higher threshold points, the plots diverge, and for Equation 3.31 and 3.32 the averages increase sharply.

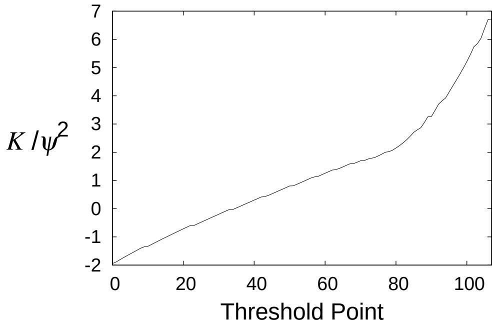

Figure 5.6: The variation in K/ψ^2 (over the range $0 - R_{\hat{b}}$) along the 1D representation of the instability threshold ($L/R_{\hat{b}} = 20$).

Again, the proposal of Malanushenko et al. (2009), that a critical value of normalised helicity indicates instability onset is considered. Figure 5.6 shows that the normalised helicity is certainly not the same for every threshold point, even if α_1 and α_2 have the same sign.

5.2.2 Path to Instability

Earlier a random walk process was used to simulate a loop being twisted by turbulent photospheric motions; i.e., a loop performed a sequence of fixed-length steps of random direction within α-space until the instability threshold was crossed. This process will now be followed for zero-net-current loops too. However, this time the random walks will be spatially correlated. In fact, it will be possible to vary the correlation between the inner and outer parts of the loop. Basically, it is more likely that the twisting will be fairly uniform across the loop (i.e., the change in α_1 is similar to the change in α_2).

When a loop begins its random walk (i.e., when it emerges from beneath the photosphere) it is assigned a random starting position within the stable region of α-space equilibria (i.e., the loop may have some initial twist). However, it is more likely that the initial twist will be small and that the initial value of α_2 will be similar to (or correlated with) the initial α_1-value. Furthermore, the change in α-coordinates that occurs whenever the loop steps through α-space, in response to photospheric driving, should also be correlated. The initial α_1-coordinate of the walk is chosen from a normal distribution centred on zero. A standard deviation is chosen such that the probability of the initial α_1-value representing an unstable configuration is negligible. Similarly, the initial α_2-coordinate is chosen such that the mean is the initial α_1-coordinate.

The step values, $\delta\alpha_1$ and $\delta\alpha_2$, are determined by assuming a step size, λ, and $\delta\alpha_1 \approx \delta\alpha_2$. Hence, $\delta\alpha_1$ is also chosen from a normal distribution, but this time the mean is $\frac{\lambda}{\sqrt{2}}$ and $\delta\alpha_2$ is chosen such that the mean is $\delta\alpha_1$. As the standard deviation of the normal distribution used to select $\delta\alpha_1$ and $\delta\alpha_2$ is decreased, the range of threshold crossings

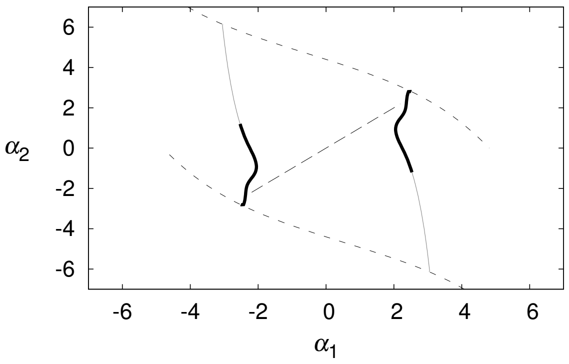

Figure 5.7: The stability region for a loop of aspect ratio 20 is demarcated by instability thresholds (solid lines) and B_z reversal lines (short dashed lines). The loop configurations along the threshold have single-signed twist (black) or reversed twist (grey). The relaxation line (long dashed) comprises the points within the stability region where $\alpha_1 = \alpha_2$.

narrows. In other words, the walks follow the $\alpha_1 = \alpha_2$ line more closely. A standard deviation of 0.1 will be used for the simulations presented in this chapter, since this value restricts the threshold crossings to points where the twist is single-signed; see Figure 5.7. Correlated[1] walks therefore are predisposed to maintaining the realism of loop configurations, since it is expected that in general photospheric motions do not create loops that have reversed twist. Four of the six marginally-unstable loops simulated in Chapter 4 have single-signed twist; loops A and B have reversed twist.

Contrary to the B_z profiles of Appendix B.2, the axial field at the loop footpoints should not change during the random walk or during relaxation. The reason for this discrepancy is that preservation of the footpoint axial field introduces a z dependency — the field becomes 2D. However, if the length of the loop exceeds its radius, a 1D field approximation, such as the one used by the model presented here, still remains adequate for a substantial portion of the loop. Zweibel and Boozer (1985) and Browning and Hood (1989) show that the z dependence is confined to thin boundary layers near the footpoints. Hence, the difference in energies for loops represented by 1D and 2D fields is negligible especially if $L/R_b > 10$ (see also Robertson et al. (1992); Lothian and Browning (2000)). Dalmasse, Browning, and Bareford (2011, in preparation)

---

[1] The reader may prefer drunk and sober to uncorrelated and correlated.

have investigated a simpler loop, having just a core and outer layer (with a conducting wall at $r = 1$), by calculating the energy releases according to Taylor relaxation for a representative sample of threshold configurations. This was done using both 1D and 2D fields, with the latter maintaining the axial field at the footpoints. The resulting energy releases differ by less than 1% between the 1D and 2D cases.

Figure 5.7 shows that a loop might cross a B_z reversal line before it reaches the instability threshold. If this happens, the loop is discarded and the simulation resumes with a new loop that has a stable α-configuration. Once a loop reaches the instability threshold, it becomes linearly unstable. At this point, the field releases energy and transitions to a lower energy state defined by Taylor relaxation: helicity is conserved and the α-profile relaxes to a single value.

5.2.3 Energy Release Calculation

In Chapter 3, a loop with net current was relaxed such that the α-profile became invariant over the range 0–$R_{\mathscr{B}}$. Hence, the relaxed state always represented a threefold radial expansion of the threshold state (i.e., from $R_{\mathscr{b}}$ to $R_{\mathscr{B}}$), the relaxation encompassed both the loop and the potential envelope. Numerical simulations (Browning et al. 2008) indicate that this is a good model for loops with net current. However, for loops with zero net current, the instability is more radially confined (Section 4.2.3) and the reconnection activity is correspondingly localised; it does not extend to the outer boundary (Hood et al. 2009).

This chapter will allow the relaxation radius, R_e, to be anywhere in the range $R_{\mathscr{b}}\,(=1) \leq R_e \leq R_{\mathscr{B}}\,(=3)$. If $R_e = R_{\mathscr{B}}$, *complete relaxation* is attained, as previously considered (Browning and Van der Linden 2003; Browning et al. 2008); otherwise relaxation is localised. α is constant between 0 and R_e and the fields in the remaining envelope (where $\alpha = 0$ and $R_e \leq r \leq R_{\mathscr{B}}$) are fixed so that they do not change during relaxation. This maintains current neutralisation, albeit via an infinitely thin current-neutralising surface. Axial flux is conserved, such that ψ (over 0–R_e) of the threshold state is equal to ψ (over 0–R_e) of the relaxed state. K/ψ^2 is conserved in an identical manner (in Chapter 3, conservation was always over 0–$R_{\mathcal{B}}$ and since the total axial flux was normalised to 1, conserving K/ψ^2 was identical to conserving K). Likewise, the energy release is the energy of the threshold state over 0–R_e minus the energy of the relaxed state over the same radial range. In fact, the energy of the remaining potential envelope is unchanged, so that the energy release could also be taken over the entire volume (0–$R_{\mathcal{B}}$); similarly, the envelope has zero helicity before and after relaxation. The scheme described above is known to be compatible with the results of non-linear MHD simulations, see Section 4.3.1.

5.3 Distribution of Energies and Coronal Heating Considerations

As with Chapter 3, the main task here is to calculate the distribution of magnitudes of the sequence of heating events generated by random photospheric driving. First, it must be shown how various properties vary along the instability threshold.

5.3.1 Helicity and Energy

The left plot of Figure 5.8 plots the total helicities of the threshold states. A total helicity (or flux) is one calculated over the range 0–$R_{\mathcal{B}}$, i.e., the loop and envelope. None of

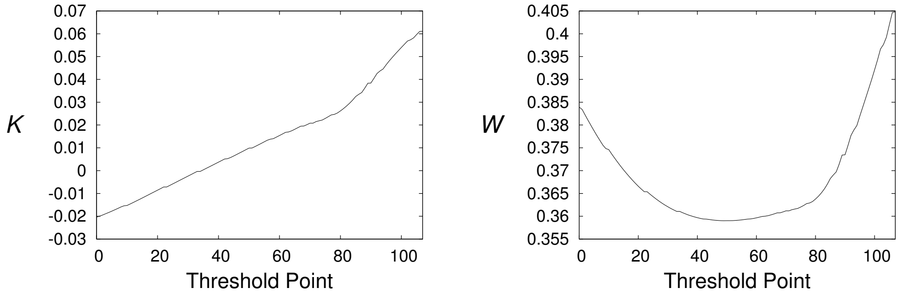

Figure 5.8: Total helicity (left) and total (dimensionless) magnetic energy (right) along the 1D representation of the instability threshold ($L/R_{b} = 20$).

the threshold states has sufficient helicity for the relaxed state to feature helical modes (Taylor 1986), and so all relaxed states are cylindrically symmetric. The left plot of

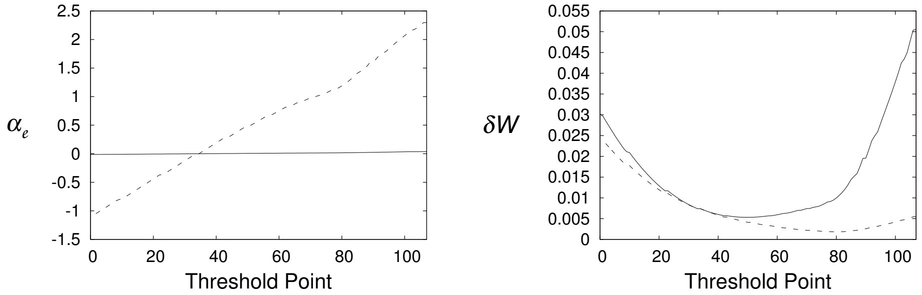

Figure 5.9: α_e (left) and energy release (right) along the 1D representation of the instability threshold ($L/R_{\mathfrak{b}} = 20$). These properties have been calculated for two relaxation radii, $R_e = R_{\mathfrak{b}}$ (dashed) and $R_e = R_{\mathcal{B}}$ (solid). When $R_e = R_{\mathcal{B}}$, α_e is of $O(10^{-2})$ and so the corresponding plot appears very close to the $\alpha_e = 0$ line.

Figure 5.9 confirms that each threshold state corresponds to a relaxed state. Both of the graphs in Figure 5.9 feature two plots; the dashed line represents minimum relaxation ($R_e = R_{\mathfrak{b}}$) and the solid line represents full relaxation ($R_e = R_{\mathcal{B}}$). The right plot shows that, in general, δW is affected by R_e (although, there is one part of the threshold where the energy release is insensitive to relaxation radius); hence, the energy distributions in the next section are calculated for minimum and maximum relaxation radii.

The energies shown in Figure 5.8 (right) and Figure 5.9 (right) are given as dimensionless quantities; using Equation 3.35 and assuming typical values, $R_{\text{cn}} = 1$ Mm (coronal radius) and $B_{\text{cn}} = 0.01$ T (mean axial coronal field), the dimensionalised energy values are $6 \times 10^{29}\,\delta W$ erg.

5.3.2 Flare Energy Distributions

An expression for the energy flux is derived by considering the loops in the ensemble as spatially separated but flaring simultaneously. All the energy input from the photosphere is dissipated, in a long-term time average over many events, since the instability threshold limits the accumulation of stresses within the coronal magnetic field. The energy flux, F, is repeated here for ease of referral;

$$F \; = \; \frac{81}{2}\frac{\pi}{\mu_0}R_{\mathrm{cn}}B_{\mathrm{cn}}^2\,\frac{1}{N\tau}\,\frac{1}{10^5}\sum_{i=1}^{10^5}\delta W\,, \tag{5.2}$$

where N is the average number of steps taken to reach the threshold and τ, is the time taken for α to change by $\lambda/R_{\mathscr{b}}$ and λ is the step length. A derivation based on the axial twist (Section 3.3) gives the following relationship between τ and λ;

$$\tau \; = \; \frac{L}{2}\frac{\lambda}{R_{\mathscr{b}}}\frac{R_{\mathrm{ft}}}{v_\theta}\,, \tag{5.3}$$

where, as before, R_{ft} is the footpoint radius and v_θ is the photospheric flow speed. A step time equivalent to a granule life time of order 10^3 (Zirker and Cleveland 1993) is obtained for $\lambda = 1$, $L = 20\,\mathrm{Mm}$, $R_{\mathrm{ft}} = 200\,\mathrm{km}$ and $v_\theta = 1\,\mathrm{km\,s^{-1}}$. The step time has a linear relationship with the loop length, $\tau = 100(L\,[\mathrm{Mm}])$. Applying the previously used values for B_{cn} and R_{cn}, gives a dimensional flux of $(10^8/N\tau)\sum\delta W$ erg cm^{-2} s^{-1}. This expression is applicable to active regions.

’Nanoflare’ Distributions

Examination of Figure 5.10 yields three key points. First, the total energy released increases with aspect ratio, but the average step count, N, decreases. This is expected since loop volume increases with aspect ratio, whereas the size of the stability region shrinks; see Figure 5.1. Second, as indicated before (Figure 5.9, right), increasing the relaxation radius increases the energy released. And third, correlated walks mean higher step counts. However, whether or not there is also an increased energy release depends on the relaxation radius.

If $R_e = R_{\mathscr{b}}\,(=\,1)$, the energy release from correlated walks is reduced compared to the uncorrelated distributions, whereas complete relaxation, $R_e = R_{\mathscr{B}}\,(=\,3)$, leads to an increased energy release. This less-than-straightforward point is consistent with the plot that shows the variation in energy release along the threshold for both values of R_e; see Figure 5.9 (right). A correlated walk would favour crossings around threshold point 90; when $R_e = R_{\mathscr{b}}$ the energy release is almost at its lowest for this part of the threshold, whereas the opposite is the case when $R_e = R_{\mathcal{B}}$. This is also true for the thresholds applicable to loops of aspect ratio 10 and 30.

For loops of aspect ratio 10, a correlated walk produces a distribution that has a high-energy cut off — this feature is an artefact of the simple two-α model. It is caused by the fact that when $L/R_{\mathscr{b}} = 10$, the relaxation line intersects the B_z reversal line before the instability threshold (Figure 5.1).

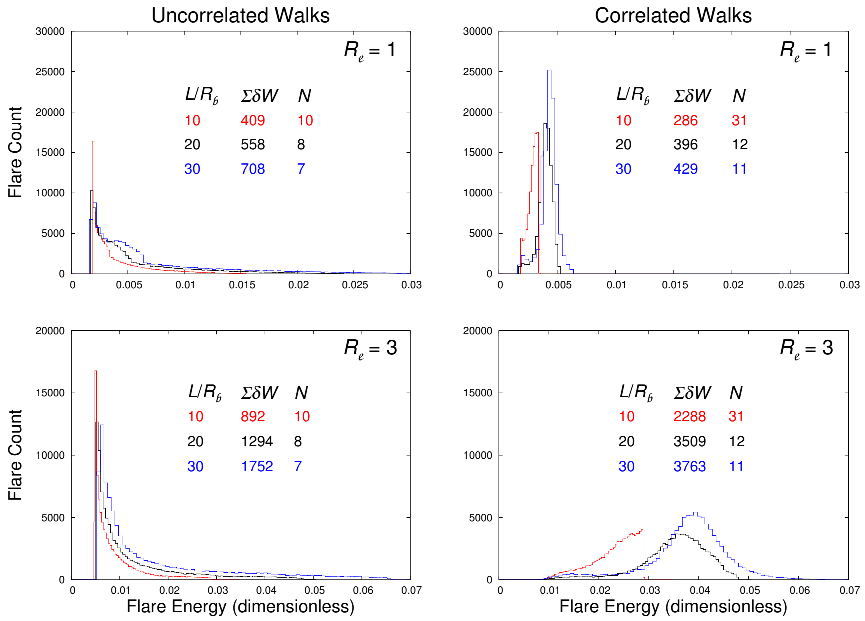

Figure 5.10: Flare energy distributions for a 10^5 loop ensemble, with each loop undergoing one relaxation event. The relaxation radius (R_e) associated with each event is $R_{\mathscr{b}}$ for the top two distributions and $R_{\mathcal{B}}$ for the bottom two. The plots on the left correspond to uncorrelated random walks, those on the right to correlated driving. Both walk types have step length $\lambda = 1$. The distribution curves are colour-coded according to aspect ratio: red denotes $L/R_{\mathscr{b}} = 10$, black $L/R_{\mathscr{b}} = 20$ and blue $L/R_{\mathscr{b}} = 30$. In addition, two properties are displayed for each plot, $\sum \delta W$, the total energy release (dimensionless) and N, the average number of steps taken to reach the threshold.

Calculating the dimensional heat fluxes (Equation 5.2) shows that the flux is weakly dependent on aspect ratio. Further examination reveals that any dependence on aspect ratio can only come from $\sum \delta W$, which is determined by the coordinates of the instability threshold. δW incorporates a length factor in units of the loop radius, i.e., $(L/R_{\mathrm{cn}})\,\delta w = \delta W$, where δw is the dimensionless energy release per unit of dimensionless length. Substituting the full expression for the step time $(\tau = (\lambda/2)(L/v_\theta)(R_{\mathrm{ft}}/R_{\mathrm{cn}}))$ into Equation 5.2 gives

$$F = \frac{81\pi}{10^5 \mu_0} \frac{R_{\mathrm{cn}}}{R_{\mathrm{ft}}} \frac{1}{N\lambda} B_{\mathrm{cn}}^2 v_\theta \sum_{i=1}^{10^5} \delta w\,; \tag{5.4}$$

again, applying previously used values, this simplifies to $F = (10^6/N) \sum \delta w\,\mathrm{erg\,cm^{-2}\,s^{-1}}$. The length terms cancel and the ratio $R_{\mathrm{cn}}\,/R_{\mathrm{ft}}$ is effectively a constant.

For distributions derived from uncorrelated walks and minimal relaxation $(R_{\mathscr{e}} = R_{\mathscr{b}})$, $F \approx 3\text{–}4 \times 10^6\,\mathrm{erg\,cm^{-2}\,s^{-1}}$. Using correlated walks instead, diminishes the fluxes to $0.9\text{–}2 \times 10^6\,\mathrm{erg\,cm^{-2}\,s^{-1}}$. Increasing the relaxation radius to $R_{\mathscr{B}}$ will reverse this reduction and yield $F \approx 7\text{–}10 \times 10^6\,\mathrm{erg\,cm^{-2}\,s^{-1}}$. This last result is also true for distributions based on uncorrelated walks and full relaxations. When $R_{\mathscr{e}} = R_{\mathscr{B}}$ correlated walks do lead to higher energy releases, however, these walks are longer and have higher step counts, which means the flux remains roughly constant.

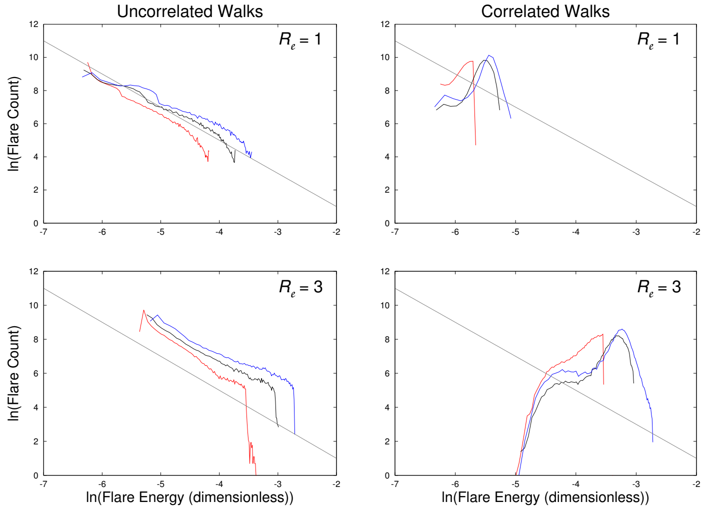

Figure 5.11: The logarithm of the flare energy distributions in Figure 5.10. The grey diagonal line in each plot is there for comparison; it has a gradient equal to the critical gradient for coronal heating, -2.

Finally, Figure 5.11 shows the natural logarithms of the flare energy distributions presented in Figure 5.10. The distributions calculated from uncorrelated walks give log plots that almost match the critical gradient for coronal heating. Although the log plots of the correlated (Gaussian-shaped) distributions do not follow power laws, these results have been included for completeness.

'Nanoflare' Distributions Derived from Twist Space

Section 3.6.4 showed that the 2D α-space can be translated to a parameter space more appropriate for photospheric driving. The instability thresholds of Figure 5.1 are re-plotted in terms of $\langle\phi\rangle_1/L$ and $\langle\phi\rangle_{1,2}/L$, the average magnetic twist (Equation 3.32) per unit length over the core and over the outer layer respectively (earlier, the stability space was represented in terms of twist boundary values; i.e., $\phi(R_1)$ and $\phi(R_2)$). Figure 5.12 (left) shows the results of such a translation – the vertical extents of the thresholds now vary substantially with loop size. A beneficial side effect of this translation is that correlated walks cease to be a problem for short loops ($L/R_{б} < 20$): for all three loop sizes, the $\langle\phi\rangle_1 = \langle\phi\rangle_{1,б}$ line intersects the threshold long before B_z reversal.

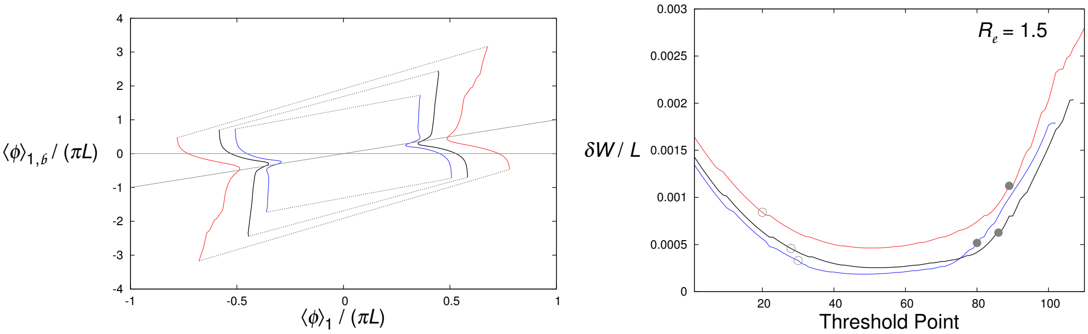

Figure 5.12: The instability thresholds of Figure 5.1 have been translated to ($\langle\phi\rangle/L$)-space (left); as before, the different colours represent the different aspect ratios and dashed lines represent B_z reversal. On the right is plotted the variation in dimensionless energy release (per unit length), achieved when $R_e = 1.5$, along the section of threshold where $\langle\phi\rangle_1 > 0$ — threshold point 1 is where $\langle\phi\rangle_{1,б}$ has its lowest value. The filled grey circles indicate where $\langle\phi\rangle_1 = \langle\phi\rangle_{1,б}$, which is the grey diagonal line in the left plot, and the empty circles locate $\langle\phi\rangle_{1,б} = 0$.

The energy release distributions generated from ($\langle\phi\rangle/L$)-space are presented for a relaxation radius of 1.5. As was discussed in Section 4.3.1 (Figure 4.17), modest expansions attain most of the energy release achieved by maximal relaxation ($R_e = 3$). This property of diminishing returns is also confirmed when one compares Figure 5.12 (right) with Figure 5.9 (right). In general, if one adds up the energy releases along a threshold, the sum for $R_e = 1$ is 50% of the sum for $R_e = 3$; however, this percentage rises to almost 90% when $R_e = 1.5$.

The dimensionlised energy fluxes (Equation 5.4) derived from Figure 5.13 are again independent of loop aspect ratio; and if $R_e = 1.5$ the correlated flux ($2 \times 10^6\,\mathrm{erg\,cm^{-2}\,s^{-1}}$) is lower than the uncorrelated one ($4 \times 10^6\,\mathrm{erg\,cm^{-2}\,s^{-1}}$). This difference is easily understood if one looks at the correlation points (the filled grey circles) in Figure 5.12 (right) — the energies associated with these points coincide with the peaks of the correlated distributions. Once again, the correlated walks are subject to a standard deviation that prevents the loop from reaching a reversed-twist threshold configuration. A consequence of this restriction is that correlated walks will not encounter the high energy parts of the threshold.

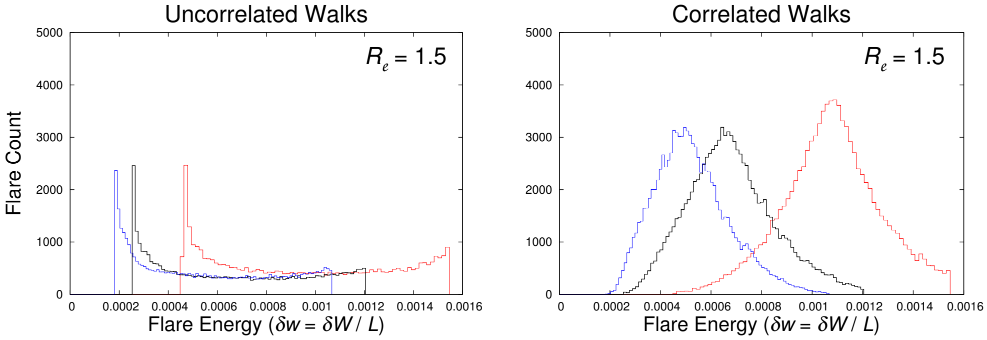

Figure 5.13: Flare energy distributions for a 10^5 loop ensemble, with each loop undergoing one relaxation event. The relaxation radius, R_e, associated with each event is 1.5 and the step length, λ, is 0.1π. The plots on the left correspond to uncorrelated random walks, those on the right to correlated driving.

The gradients of the corresponding log plots are slightly lower than the α-space ones (Figure 5.14), which means the correlated distributions are closer in shape to that suggested by observations. Unfortunately, the energy fluxes generated by a modest expansion do fall short of the required $1 \times 10^7 \, \mathrm{erg\,cm^{-2}\,s^{-1}}$. This could be rectified by increasing the mean axial field strength, B_{cn}, used in Equation 5.2, by a factor of $\sqrt{10}$; or, by adopting some distribution of B_{cn} over the loop ensemble that accounts for the shortfall. Increasing λ would also raise the energy flux.

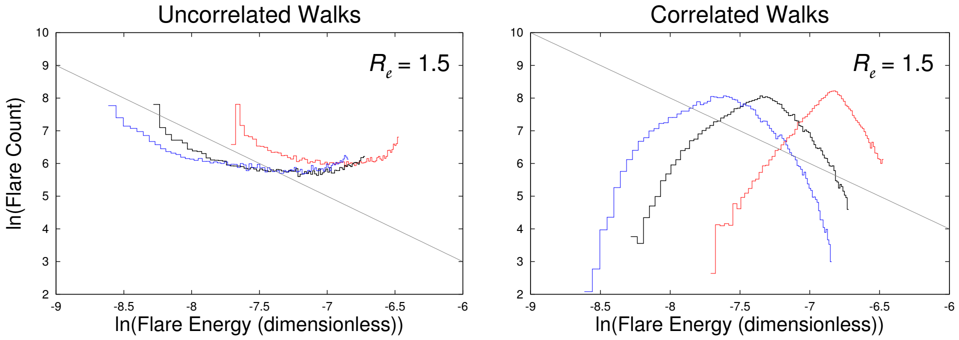

Figure 5.14: The logarithm of the flare energy distributions for a 10^5 loop ensemble, with each loop undergoing one relaxation event. The presentation of these plots follows the scheme used for Figure 5.13. The grey diagonal line in each plot is there for comparison; it has a gradient equal to the critical gradient for coronal heating, -2.

5.4 Conclusions

The twisting has been assumed to be localised within the loop cross section, so that the loop is always without net current (the azimuthal field vanishes at — and beyond — the loop boundary). This work is genuinely studying individual loops, rather than (unrealistically) allowing the potential envelope outside the loop to be twisted as the loop evolves.

A distribution of heating events, or nanoflares, is obtained for a variety of conditions. For spatially uncorrelated twisting motions, in which the motions may vary strongly across the loop cross section, a power-law distribution of energy versus occurrence frequency is obtained, with a slope slightly steeper than the critical value of -2 required for nanoflare heating to be effective (Hudson 1991). For strongly correlated twist motions, in which the twist in the outer part of the loop is close to that in the inner core, a peaked energy distribution is obtained, with almost Gaussian shape. The former case reflects the distribution of available energies around the instability threshold, whereas the latter is mainly determined by the allowable range of twist profiles. Note, these distributions (Figures 5.10 and 5.11) are obtained for an ensemble of identical loops: in reality, much broader distributions will result due to variations in axial field strengths and photospheric driving. The true nanoflare distribution is a convolution over more than one parameter.

The effect of loop aspect ratio has been found to have little impact on energy flux. The higher volume of large aspect ratio loops is counteracted by the smaller stability region (instability occurs at lower α-values). As the aspect ratio is increased beyond 30, the stability region is expected to reduce by smaller and smaller amounts, until the region converges to a minimum area. This has been shown for constant-α loops; see Figure 4 of Browning and Van der Linden (2003)). Hence, assuming that this expectation is verified, the energy flux will be independent of aspect ratio (Equation 5.4), assuming that the same axial field strength is applied to all members of the loop ensemble. Presumably, there is a dependence between loop size and $|B_{\mathrm{cn}}|$, so an ensemble that features some distribution of field strengths will still depend (albeit indirectly) on the aspect ratio.

One important consequence of considering loops with zero net current is that the reconnection activity tends to be localised near the loop and thus relaxation is likely to be incomplete (rather than including a large part of the surrounding potential field). Considered here are two limiting cases: localised relaxation, in which only the loop volume relaxes to a minimum energy (constant-α) state, and the surrounding potential envelope remains unaffected; and complete relaxation, in which the loop and the potential envelope relax out to the external boundary. The latter is clearly the true minimum energy state. The numerical simulations of Chapter 4 indicate an intermediate situation, but somewhat closer to the completely localised relaxation. In fact, the loop reconnects with some of the surrounding axial field, but only to a limited extent.

This is an important issue for understanding relaxation in the Sun, where the extent of relaxation is not defined by conducting walls — in contrast with laboratory plasmas (Taylor 1974). Future work will use numerical simulations to explore the transition to instability, and the effects of continual driving.

The results presented here are based on a loop model that has a thin current-neutralising layer (this approximates to a current sheet), in which the fields discontinuously change at the loop edge. This choice allows the fields inside the loop to be close to the previously studied two-α model of Chapter 3; thus, a comparison can be made. Also, such fields correspond to twisting within an isolated flux source, whilst the flux which surrounds the loop in the corona originates from untwisted separated sources. Interestingly, the ideal instability threshold in this case is very similar to that found for a close-fitting conducting wall at the loop edge, as originally used by Browning and Van der Linden (2003). This is because the thin current layer forces unstable perturbations to vanish (almost) at the loop edge. In numerical simulations, the choice of a thin current layer has consequences in allowing resistive modes to be significant; although for realistic values of the resistivity (unattainable in simulations) the growth rate of such modes is extremely slow. Preliminary studies have also been undertaken with a thicker current-neutralising layer. In this case, a closed stability threshold curve can be obtained, and the results are more similar to those presented in Chapter 3.

6

Final Discussion

6.1 Summary

The primary aim of this work is to investigate the distribution of energy releases in an ensemble of coronal loops driven by random photospheric footpoint motions, using Taylor relaxation theory. A relaxation event is triggered whenever the loop becomes unstable to an ideal kink instability; during this phase, current sheets form and subsequently, rapid reconnection occurs. A distribution of events is built up by allowing loop equilibria to evolve through a random walk, representing the effects of stochastic footpoint motions, until the linear stability threshold is reached. The advantage of the relaxation approach is that energy release is easily calculated for a wide family of profiles, which is extremely difficult with 3D numerical simulations. Furthermore, relaxation theory can better represent very high conductivities, which cannot be accessed by present day MHD codes. Of course, this approach can be extended to more complex field models than the simple cylindrical coronal loop models used here.

Chapter 3 followed these ideas with a deliberately simplistic procedure: an ensemble of release events was produced by a single loop, repeatedly encountering the threshold for linear kink instability; or an ensemble of identically-sized loops were each made to undergo a single instability. The energy-release distributions resulting from these two types of ensemble were found to be statistically stable for an ensemble population size of 10^5. The distributions are broadly similar between ensemble types and do not follow a simple power law. Although, the smallest flares are the most common - representing perhaps the elemental 'nanoflare' — there is a second smaller peak at higher energy, which is fitted by a power-law with an index of around -8, significantly higher than that required for coronal heating. These results were sufficiently interesting to warrant further study. A number of ways to improve the realism of the model were identified. Specifically, altering the loop model so that it would carry no net current, which is the expected outcome of a loop that has been twisted at the footpoints by spatially-localised photospheric motions.

A non-linear 3D MHD code was introduced (Section 4.1) and then applied to the simulaton of particular zero-net-current loops. These loop configurations had been identified by the linear analysis as being marginally kink unstable. The simulations showed that the linear instability quickly enters a non-linear phase and magnetic energy declines sharply before leveling off. Furthermore, the amount of energy release matched the amount predicted by Taylor relaxation. Evidence for helicity conservation was presented and in all but one case, the level of helicity variation was estimated to be smaller than the change in magnetic energy, by at least an order of magnitude. The implication of this result is that energy diffusion is occuring on much smaller scales than the global length scale; i.e., within the current sheets associated with magnetic reconnection. Relaxation theory also predicts that the final relaxed state should have a linear α-profile (that conserves helicity). The final field profiles (Figures 4.20–4.25) confirmed this expectation and also revealed (together with the current magnitude plots of Figure 4.14) that the property of zero net current was retained after the instability. Typically, the loop expands radially, the field reconnecting with that present in the potential envelope. This evidence was used to choose one of three relaxation scenarios, that gave a more precise description of how helicity is conserved and energy release determined.

The success of Chapter 4 in confirming the Taylor hypothesis, meant that it was worthwhile to return to the TRoLE model (Section 3.4). This time, ensembles of zero-net-current loops for different loop sizes were investigated (Chapter 5). In addition, a better representation of photospheric driving was included, alongside a more constrained process for Taylor relaxation. The resulting heat fluxes (dimensionlised for active regions) reach $10^7\,\mathrm{erg\,cm^{-2}\,s^{-1}}$ for a radially-expanded relaxed loop, which is just sufficient for coronal heating. The two types of photospheric driving, uniformly random and correlated, yielded different distribution shapes. A power-law distribution with index around -2 was produced by the first type and the second produced a Gaussian profile. The latter shape does not tally with observations of low-energy flares (Figure 1.9) and is probably an artefact of using one value for the mean axial field (B_{cn}) to dimensionalise the flare energy. In reality, a group of active-region loops will have some distribution of mean axial field strengths, which could be expressed as a probability function, thereby incorporating a random element in the energy calculation. It would be interesting to see if such a feature would alter the correlated distribution, so that it was closer to a power-law profile. Otherwise, the Gaussian correlated profile would suggest that uniformly random driving is the more realistic path to kink instability.

The calculation of the heat fluxes assumed 100% efficiency in the conversion between magnetic diffusion and heating. This is a reasonable assumption: the numerical simulations show that a small fraction of the energy released ($\lesssim 10\%$), is expressed as kinetic energy; but, by the end of the simulation, kinetic energy has declined to a negligible level. However, another way the energy release could be limited, is if the unstable loop attains an equilibrium that is less than fully relaxed (i.e., the α-profile remains non-linear) and still conserves helicity. There is perhaps, for some field configurations, another constraint that decides the relaxed state, such as the topological degree of the field line mapping between the ends of the loop, as investigated by Yeates et al. (2010). They examined two braided magnetic field configurations (one based on the simple pigtail braid and the other more complex). Both configurations underwent turbulent relaxation, leading to a final state that conserved topological degree and was *less* relaxed than that predicted by Taylor theory — the final state for the pigtail braid featured two flux tubes of opposite twist. Nevertheless, it is possible for the Taylor-relaxed state and the state that preserves topological degree to coincide. This could explain the level of agreement between the LARE3D simulations of Chapter 4 and Taylor relaxation. Moreover, the agreement is strongest for those parts of the instability threshold encountered by correlated photospheric driving.

6.2 Further Work

The previous chapter featured ensembles of loops, each one undergoing a single relaxation. This avoided having to resolve the issue of what happened to a loop afterwards. Would it remain a viable loop, albeit with a smaller aspect ratio? Is there a threshold value for the relaxed alpha (α_e) below which the loop simply merges into the background field? The numerical data presented in Chapter 4 (Figure 4.14) clearly show that relaxation is accompanied by loop expansion, and it would appear that the increase in loop radius is some function of α_1 and α_2.

Another question is whether or not photospheric driving is a factor during the relaxation process; the TRoLE model assumes that it is not. The LARE3D code could be used to help resolve this issue. It should be possible to choose a loop configuration (i.e., a set of α-parameters) that is just inside the threshold for linear kink instability and then, make the loop cross the threshold by applying a pre-determined velocity profile (v_θ) at both footpoints. Photospheric velocities are typically $1\,\mathrm{km\,s^{-1}}$, but in the corona the loop is wider and so the tangential motions there will be approximately $10\,\mathrm{km\,s^{-1}}$. Faster tangential velocities ($\sim 100\,\mathrm{km\,s^{-1}}$) may need to be applied in order for the simulation to complete in a reasonable amount of time. If there is enough flexibility in the initial parameters, LARE3D could be used to investigate the relationship between driving speed and energy release. This code could also continue to apply photospheric driving during the relaxation phase and show whether or not this had any consequences for the final loop configuration.

Loop curvature has not been considered by this thesis. The linear stability analysis (Section 3.2) and the TRoLE model require the magnetic fields to be solved analytically. If a loop is to retain its curvature, it can only be simulated numerically, which means choices have to be made concerning loop parameters (e.g., length, radius and α-profile). Fortunately, the work of Chapters 4 and 5, have uncovered those straightened loop configurations that are kink unstable and are likely to be reached by photospheric driving. These configurations could be adapted to include curvature and re-simulated within LARE3D. This would reveal what affect, if any, curvature has on the energy release precipitated by kink instability. A feature that improves the realism of the loop model may not be important as regards kink instability and Taylor relaxation. In essence, the results of this thesis can be used as a baseline against which the importance of additional features can be judged.

Appendix A

Loop Properties for All Values of α_1 and α_2

A loop is characterised by its α_1 and α_2 values. To calculate other properties (e.g., $\langle\tilde{\phi}\rangle$, K and W) it is first necessary to determine the axial fluxes and the magnetic field coefficients. These equations differ depending on whether or not the loop has a current-neutralisation layer, and on which of the α values is zero or non-zero. Expressions for constant-α fields can be recovered by setting $\alpha_1 = \alpha_2$, which gives more familiar formulae. The subscripts that accompany the quantity on the left hand side denote the upper and lower radial bounds over which the quantity is calculated. For example, $K_{0,1}$ is the helicity calculated over the loop core, which exists between R_0 (the axis) and R_1 (the core-outer layer boundary).

In each subsection, the expressions for a loop that has net current are presented first. These expressions are followed by those that are required if a current-neutralisation layer is inserted between the outer layer and the potential envelope. There is some overlap between the two sets of equations; specifically, the expression used to calculate a property over the range R_1–R_2 for the *zero* net current case is the same as that used for the net current case over the range R_1–R_b. (The auxiliary functions $F_{0,1}$ and $G_{0,1}$ are defined by Equations 4.29 and 4.30.)

A.1 Potential Loop: $\alpha_1 = 0$ and $\alpha_2 = 0$

A.1.1 Magnetic Field Coefficients

$$B_3 = B_2 = B_1 \tag{A.1}$$

$$C_3 = C_2 = 0 \tag{A.2}$$

Current Neutralisation Layer

$$B_4 = B_1 \tag{A.3}$$

$$C_4 = 0 \tag{A.4}$$

A.1.2 Axial Flux

$$\psi_{0,1} = \pi B_1 R_1^2 \tag{A.5}$$

$$\psi_{1,\mathscr{b}} = \pi B_2 \left(R_{\mathscr{b}}^2 - R_1^2\right) \tag{A.6}$$

$$\psi_{\mathscr{b},\mathscr{B}} = \pi B_3 \left(R_{\mathscr{B}}^2 - R_{\mathscr{b}}^2\right) \tag{A.7}$$

Current Neutralisation Layer

$$\psi_{2,\mathscr{b}} = \pi B_3 \left(R_{\mathscr{b}}^2 - R_2^2\right) \tag{A.8}$$

$$\psi_{\mathscr{b},\mathscr{B}} = \pi B_4 \left(R_{\mathscr{B}}^2 - R_{\mathscr{b}}^2\right) \tag{A.9}$$

A.1.3 Average Magnetic Twist

$$\langle\tilde{\phi}\rangle_{0,1} = \langle\tilde{\phi}\rangle_{1,\mathscr{b}} = \langle\tilde{\phi}\rangle_{\mathscr{b},\mathscr{B}} = 0 \tag{A.10}$$

Current Neutralisation Layer

$$\langle\tilde{\phi}\rangle_{2,\mathscr{b}} = \langle\tilde{\phi}\rangle_{\mathscr{b},\mathscr{B}} = 0 \tag{A.11}$$

A.1.4 Helicity

$$K_{0,1} = K_{1,\mathscr{b}} = K_{\mathscr{b},\mathscr{B}} = 0 \tag{A.12}$$

Current Neutralisation Layer

$$K_{2,\mathscr{b}} = K_{\mathscr{b},\mathscr{B}} = 0 \tag{A.13}$$

A.1.5 Energy

$$W_{0,1} = \frac{L\pi B_1^2}{2\mu_0} R_1^2 \tag{A.14}$$

$$W_{1,\mathscr{b}} = \frac{L\pi B_2^2}{2\mu_0} \left(R_{\mathscr{b}}^2 - R_1^2\right) \tag{A.15}$$

$$W_{\mathscr{b},\mathscr{B}} = \frac{L\pi B_3^2}{2\mu_0} \left(R_{\mathscr{B}}^2 - R_{\mathscr{b}}^2\right) \tag{A.16}$$

Current Neutralisation Layer

$$W_{2,\mathscr{b}} = \frac{L\pi B_3^2}{2\mu_0} \left(R_2^2 - R_{\mathscr{b}}^2\right) \tag{A.17}$$

$$W_{\mathscr{b},\mathscr{B}} = \frac{L\pi B_4^2}{2\mu_0} \left(R_{\mathscr{B}}^2 - R_{\mathscr{b}}^2\right) \tag{A.18}$$

A.2 Potential Core: $\alpha_1 = 0$ and $\alpha_2 \neq 0$

A.2.1 Magnetic Field Coefficients

$$B_2 = \frac{-\pi|\alpha_2|R_1}{2} B_1 Y_1(|\alpha_2|R_1) \tag{A.19}$$

$$C_2 = \frac{\pi|\alpha_2|R_1}{2} B_1 J_1(|\alpha_2|R_1) \tag{A.20}$$

$$B_3 = B_2 F_0(|\alpha_2|R_\flat) \tag{A.21}$$

$$C_3 = B_2 F_1(|\alpha_2|R_\flat) \tag{A.22}$$

Current Neutralisation Layer

$$B_3 = \frac{\pi|\alpha_3|R_2}{2} B_2 \Big(\sigma_{2,3} F_1(|\alpha_2|R_2) Y_0(|\alpha_3|R_2) - F_0(|\alpha_2|R_2) Y_1(|\alpha_3|R_2)\Big) \tag{A.23}$$

$$C_3 = \frac{\pi|\alpha_3|R_2}{2} B_2 \Big(F_0(|\alpha_2|R_2) J_1(|\alpha_3|R_2) - \sigma_{2,3} F_1(|\alpha_2|R_2) J_0(|\alpha_3|R_2)\Big) \tag{A.24}$$

$$B_4 = B_3 G_0(|\alpha_3|R_\flat) \tag{A.25}$$

$$C_4 = 0 \tag{A.26}$$

A.2.2 Axial Flux

$$\psi_{0,1} = \pi B_1 R_1^2 \tag{A.27}$$

$$\psi_{1,\mathscr{b}} = \frac{2\pi R_{\mathscr{b}}}{|\alpha_2|} B_2 F_1(|\alpha_2| R_{\mathscr{b}}) \tag{A.28}$$

$$\psi_{\mathscr{b},\mathcal{B}} = \pi B_2 F_0(|\alpha_2| R_{\mathscr{b}}) \Big(R_{\mathcal{B}}^2 - R_{\mathscr{b}}^2 \Big) \tag{A.29}$$

Current Neutralisation Layer

$$\psi_{2,\mathscr{b}} = \frac{2\pi}{|\alpha_3|} \Bigg[R_{\mathscr{b}} B_3 G_1(|\alpha_3| R_{\mathscr{b}}) - \sigma_{2,3} R_2 B_2 F_1(|\alpha_2| R_2) \Bigg] \tag{A.30}$$

$$\psi_{\mathscr{b},\mathcal{B}} = \pi B_4 \Big(R_{\mathcal{B}}^2 - R_{\mathscr{b}}^2 \Big) \tag{A.31}$$

A.2.3 Average Magnetic Twist

$$\langle \tilde{\phi} \rangle_{0,1} = 0 \tag{A.32}$$

$$\langle \tilde{\phi} \rangle_{1,\mathscr{b}} = \frac{\frac{\sigma_2 L}{|\alpha_2|} \Big[B_1 - B_2 F_0(|\alpha_2| R_{\mathscr{b}}) \Big]}{\frac{R_{\mathscr{b}} B_2}{|\alpha_2|} F_1(|\alpha_2| R_{\mathscr{b}})} \tag{A.33}$$

$$\langle \tilde{\phi} \rangle_{2,3} = \frac{\sigma_2 L R_{\mathscr{b}} (B_2 J_1(|\alpha_2| R_{\mathscr{b}}) + C_2 Y_1(|\alpha_2| R_{\mathscr{b}})) \log(R_{\mathcal{B}} / R_{\mathscr{b}})}{\frac{B_2 F_0(|\alpha_2| R_{\mathscr{b}})}{2} \Big({R_{\mathcal{B}}}^2 - {R_{\mathscr{b}}}^2 \Big)} \tag{A.34}$$

Current Neutralisation Layer

$$\langle\tilde{\phi}\rangle_{2,\mathscr{b}} = \frac{\frac{\sigma_3 L B_3}{|\alpha_3|}\Big[G_0(|\alpha_3|R_2) - G_0(|\alpha_3|R_{\mathscr{b}})\Big]}{\frac{B_3}{|\alpha_3|}\Big[R_{\mathscr{b}} G_1(|\alpha_3|R_{\mathscr{b}}) - R_2 G_1(|\alpha_3|R_2)\Big]} \tag{A.35}$$

$$\langle\tilde{\phi}\rangle_{\mathscr{b},\mathscr{B}} = \frac{\sigma_3 L B_3 G_1(|\alpha_3|R_{\mathscr{b}}) R_{\mathscr{b}} \log(R_{\mathscr{B}}/R_{\mathscr{b}})}{\frac{1}{2} B_4\Big[R_{\mathscr{B}}^2 - R_{\mathscr{b}}^2\Big]} = 0 \tag{A.36}$$

A.2.4 Helicity

$$K_{0,1} = 0 \tag{A.37}$$

$$\begin{aligned} K_{1,\mathscr{b}} = {} & \sigma_2 \frac{2\pi L B_2^2}{|\alpha_2|}\bigg(R_{\mathscr{b}}^2\Big(F_0^2(|\alpha_2|R_{\mathscr{b}}) + F_1^2(|\alpha_2|R_{\mathscr{b}})\Big) - \frac{2R_{\mathscr{b}}}{|\alpha_2|} F_0(|\alpha_2|R_{\mathscr{b}}) F_1(|\alpha_2|R_{\mathscr{b}})\bigg) \\ & - \sigma_2 \frac{2\pi L R_1^2}{|\alpha_2|} B_1 B_2 F_0(|\alpha_2|R_{\mathscr{b}}) \end{aligned} \tag{A.38}$$

$$K_{\mathscr{b},\mathscr{B}} = 2\sigma_2\bigg[L C_3 R_{\mathscr{b}}\Big(\Big(\psi_{0,\mathscr{b}} - \pi B_3 R_{\mathscr{b}}^2\Big)\log(R_{\mathscr{B}}/R_{\mathscr{b}}) + \frac{\pi B_3}{2}\Big(R_{\mathscr{B}}^2 - R_{\mathscr{b}}^2\Big)\Big)\bigg] \tag{A.39}$$

Current Neutralisation Layer

$$\begin{aligned} K_{2,\mathscr{b}} = {} & \sigma_3 \frac{2\pi L B_3^2}{|\alpha_3|}\bigg(R_{\mathscr{b}}^2\Big(G_0^2(|\alpha_3|R_{\mathscr{b}}) + 2G_1^2(|\alpha_3|R_{\mathscr{b}})\Big) - \frac{2R_{\mathscr{b}}}{|\alpha_3|} G_0(|\alpha_3|R_{\mathscr{b}}) G_1(|\alpha_3|R_{\mathscr{b}})\bigg) \\ & - \sigma_3 \frac{2\pi L B_3^2}{|\alpha_3|}\bigg(R_2^2\Big(G_0^2(|\alpha_3|R_2) + G_1^2(|\alpha_3|R_2)\Big) - \frac{2R_2}{|\alpha_3|} G_0(|\alpha_3|R_2) G_1(|\alpha_3|R_2)\bigg) \\ & + \sigma_3 \frac{2\pi L B_3}{|\alpha_3|}\Big(G_0(|\alpha_3|R_2) - G_0(|\alpha_3|R_2)\Big)\bigg[2R_2 B_2 F_1(|\alpha_2|R_2)\bigg(\frac{1}{|\alpha_2|} - \frac{\sigma_{2,3}}{|\alpha_3|}\bigg) + B_1 R_1^2\bigg] \end{aligned} \tag{A.40}$$

$$K_{3,4} = 0 \tag{A.41}$$

A.2.5 Energy

$$W_{0,1} = \frac{L\pi B_1^2 R_1^2}{2\mu_0} \tag{A.42}$$

$$\begin{aligned} W_{1,\mathscr{b}} &= \frac{L\pi B_2^2}{\mu_0}\left[R_{\mathscr{b}}^2\Big(F_0^2(|\alpha_2|R_{\mathscr{b}}) + F_1^2(|\alpha_2|R_{\mathscr{b}})\Big) - \frac{R_{\mathscr{b}}}{|\alpha_2|}F_0(|\alpha_2|R_{\mathscr{b}})F_1(|\alpha_2|R_{\mathscr{b}})\right] \\ &\quad - \frac{L\pi B_1^2 R_1^2}{\mu_0} \end{aligned} \tag{A.43}$$

$$W_{\mathscr{b},\mathscr{B}} = \frac{L\pi}{\mu_0}\left[\frac{B_3^2}{2}\Big(R_{\mathscr{B}}^2 - R_{\mathscr{b}}^2\Big) + C_3^2 R_{\mathscr{b}}^2 \log(R_{\mathscr{B}}/R_{\mathscr{b}})\right] \tag{A.44}$$

Current Neutralisation Layer

$$\begin{aligned} W_{2,\mathscr{b}} &= \frac{L\pi B_3^2}{\mu_0}\Bigg[R_{\mathscr{b}}^2\Big(G_0^2(|\alpha_3|R_{\mathscr{b}}) + G_1^2(|\alpha_3|R_{\mathscr{b}})\Big) - \frac{R_{\mathscr{b}}}{|\alpha_3|}G_0(|\alpha_3|R_{\mathscr{b}})G_1(|\alpha_3|R_{\mathscr{b}}) \\ &\qquad - R_2^2\Big(G_0^2(|\alpha_3|R_2) + G_1^2(|\alpha_3|R_2)\Big) + \frac{R_2}{|\alpha_3|}G_0(|\alpha_3|R_2)G_1(|\alpha_3|R_2)\Bigg] \end{aligned} \tag{A.45}$$

$$W_{\mathscr{b},\mathscr{B}} = \frac{L\pi}{\mu_0}\left[\frac{B_4^2}{2}\Big(R_{\mathscr{B}}^2 - R_{\mathscr{b}}^2\Big)\right] \tag{A.46}$$

A.3 Potential Outer Layer: $\alpha_1 \neq 0$ and $\alpha_2 = 0$

A.3.1 Magnetic Field Coefficients

$$B_2 = B_1 J_0(|\alpha_1|R_1) \tag{A.47}$$

$$C_2 = 0 \tag{A.48}$$

$$B_3 = B_2 \tag{A.49}$$

$$C_3 = C_2 \tag{A.50}$$

Current Neutralisation Layer

$$B_3 = \frac{\pi|\alpha_3|R_2}{2}\left(\sigma_{1,3}\frac{R_1}{R_2}B_1 J_1(|\alpha_1|R_1)Y_0(|\alpha_3|R_2) - B_2 Y_1(|\alpha_3|R_2)\right) \tag{A.51}$$

$$C_3 = \frac{\pi|\alpha_3|R_2}{2}\left(B_2 J_1(|\alpha_3|R_2) - \sigma_{1,3}\frac{R_1}{R_2}B_1 J_1(|\alpha_1|R_1)J_0(|\alpha_3|R_2)\right) \tag{A.52}$$

$$B_4 = B_3 G_0(|\alpha_3|R_{\mathscr{b}}) \tag{A.53}$$

$$C_4 = 0 \tag{A.54}$$

A.3.2 Axial Flux

$$\psi_{0,1} = \frac{2\pi R_1}{|\alpha_1|}B_1 J_1(|\alpha_1|R_1) \tag{A.55}$$

$$\psi_{1,\mathscr{b}} = \pi B_2\left(R_{\mathscr{b}}^2 - R_1^2\right) \tag{A.56}$$

$$\psi_{\mathscr{b},\mathscr{B}} = \pi B_1 J_0(|\alpha_1|R_1)\left({R_{\mathscr{B}}}^2 - {R_{\mathscr{b}}}^2\right) \tag{A.57}$$

Current Neutralisation Layer

$$\psi_{2,\mathscr{b}} = \frac{2\pi}{|\alpha_3|}\left[R_{\mathscr{b}} B_3 G_1(|\alpha_3|R_{\mathscr{b}}) - \sigma_{1,3}R_1 B_1 J_1(|\alpha_1|R_1)\right] \tag{A.58}$$

$$\psi_{\mathscr{b},\mathscr{B}} = \pi B_4\left(R_{\mathscr{B}}^2 - R_{\mathscr{b}}^2\right) \tag{A.59}$$

A.3.3 Average Magnetic Twist

$$\langle\tilde{\phi}\rangle_{0,1} \quad = \quad \frac{\frac{\sigma_1 L B_1}{|\alpha_1|}\Big[1 - J_0(|\alpha_1|R_1)\Big]}{\frac{R_1 B_1}{|\alpha_1|}J_1(|\alpha_1|R_1)} \tag{A.60}$$

$$\langle\tilde{\phi}\rangle_{1,\mathscr{b}} \quad = \quad \frac{\sigma_1 L B_1 J_1(|\alpha_1|R_1)R_1\log(R_{\mathscr{b}}/R_1)}{\frac{1}{2}B_2\Big[R_{\mathscr{b}}^2 - R_1^2\Big]} \tag{A.61}$$

$$\langle\tilde{\phi}\rangle_{\mathscr{b},\mathcal{B}} \quad = \quad \frac{\sigma_1 L R_1 B_1 J_1(|\alpha_1|R_1)\log(R_{\mathcal{B}}/R_1)}{\frac{B_2}{2}\Big({R_{\mathcal{B}}}^2 - {R_1}^2\Big)} \tag{A.62}$$

Current Neutralisation Layer

$$\langle\tilde{\phi}\rangle_{2,\mathscr{b}} \quad = \quad \frac{\frac{\sigma_3 L}{|\alpha_3|}\Big[B_2 - B_3 G_0(|\alpha_3|R_{\mathscr{b}})\Big]}{\frac{R_{\mathscr{b}} B_3}{|\alpha_3|}G_1(|\alpha_3|R_{\mathscr{b}}) - \frac{\sigma_{1,3} R_1 B_1}{|\alpha_3|}J_1(|\alpha_1|R_1)} \tag{A.63}$$

$$\langle\tilde{\phi}\rangle_{\mathscr{b},\mathcal{B}} \quad = \quad \frac{\sigma_3 L B_3 G_1(|\alpha_3|R_{\mathscr{b}})R_{\mathscr{b}}\log(R_{\mathcal{B}}/R_{\mathscr{b}})}{\frac{1}{2}B_4\Big[R_{\mathcal{B}}^2 - R_{\mathscr{b}}^2\Big]} \;=\; 0 \tag{A.64}$$

A.3.4 Helicity

$$K_{0,1} \quad = \quad \sigma_1\frac{2\pi L B_1^2}{|\alpha_1|}\left(R_1^2\Big(J_0^2(|\alpha_1|R_1) + J_1^2(|\alpha_1|R_1)\Big) - 2\frac{R_1}{|\alpha_1|}J_0(|\alpha_1|R_1)J_1(|\alpha_1|R_1)\right) \tag{A.65}$$

$$\begin{aligned} K_{1,\mathscr{b}} \quad = \quad & \sigma_1 \pi L B_2 B_1 J_1(|\alpha_1|R_1)R_1\Big(R_{\mathscr{b}}^2 - R_1^2\Big) \\ & + \sigma_1 2\pi L B_1 J_1(|\alpha_1|R_1)R_1^2\left(2\frac{B_1 J_1(|\alpha_1|R_1)}{|\alpha_1|} - B_2 R_1\right)\log(R_{\mathscr{b}}/R_1) \end{aligned} \tag{A.66}$$

$$\begin{aligned} K_{\mathscr{b},\mathcal{B}} \quad = \quad & \sigma_1 \pi L B_2 B_1 J_1(|\alpha_1|R_1)R_1\Big(R_{\mathcal{B}}^2 - R_{\mathscr{b}}^2\Big) \\ & + \sigma_1 2\pi L B_1 J_1(|\alpha_1|R_1)R_1^2\left(2\frac{B_1 J_1(|\alpha_1|R_1)}{|\alpha_1|} - B_2 R_1\right)\log(R_{\mathcal{B}}/R_{\mathscr{b}}) \end{aligned} \tag{A.67}$$

Current Neutralisation Layer

$$\begin{aligned}
K_{2,\mathscr{b}} &= \sigma_3 \frac{2\pi L B_3^2}{|\alpha_3|}\Big(R_{\mathscr{b}}^2\Big(G_0^2(|\alpha_3|R_{\mathscr{b}}) + G_1^2(|\alpha_3|R_{\mathscr{b}})\Big) - 2\frac{R_{\mathscr{b}}}{|\alpha_3|}G_0(|\alpha_3|R_{\mathscr{b}})G_1(|\alpha_3|R_{\mathscr{b}})\Big) \\
&\quad - \sigma_3 \frac{2\pi L}{|\alpha_3|}\Big(B_2^2 R_2^2 + B_1^2 J_1^2(|\alpha_1|R_1)R_1^2 - \sigma_{1,3}\frac{2B_2 B_1 J_1(|\alpha_1|R_1)R_1}{|\alpha_3|}\Big) \\
&\quad + \sigma_3 \frac{2\pi L B_3}{|\alpha_3|}\left[\frac{B_2}{B_3} - G_0(|\alpha_3|R_{\mathscr{b}})\right]\left[\frac{2B_1 J_1(|\alpha_1|R_1)R_1}{|\alpha_1|} - \frac{\sigma_{1,3}2B_1 J_1(|\alpha_1|R_1)R_1}{|\alpha_3|}\right. \\
&\qquad \left. + B_2(R_2^2 - R_1^2)\right] \qquad \text{(A.68)}
\end{aligned}$$

$$K_{3,4} = 0 \qquad \text{(A.69)}$$

A.3.5 Energy

$$W_{0,1} = \frac{L\pi B_1^2}{\mu_0}\left[R_1^2\Big(J_0^2(|\alpha_1|R_1) + J_1^2(|\alpha_1|R_1)\Big) - \frac{R_1}{|\alpha_1|}J_0(|\alpha_1|R_1)J_1(|\alpha_1|R_1)\right] \qquad \text{(A.70)}$$

$$W_{1,\mathscr{b}} = \frac{L\pi}{\mu_0}\left[\frac{B_2^2}{2}\Big(R_{\mathscr{b}}^2 - R_1^2\Big) + R_1^2 B_1^2 J_1^2(|\alpha_1|R_1)\log(R_{\mathscr{b}}/R_1)\right] \qquad \text{(A.71)}$$

$$W_{\mathscr{b},\mathscr{B}} = \frac{L\pi}{\mu_0}\left[\frac{B_2^2}{2}\Big(R_{\mathscr{B}}^2 - R_{\mathscr{b}}^2\Big) + R_1^2 B_1^2 J_1^2(|\alpha_1|R_1)\log(R_{\mathscr{B}}/R_{\mathscr{b}})\right] \qquad \text{(A.72)}$$

Current Neutralisation Layer

$$\begin{aligned}
W_{2,\mathscr{b}} &= \frac{L\pi}{\mu_0}\left[B_3^2\Big(R_{\mathscr{b}}^2\Big(G_0^2(|\alpha_3|R_{\mathscr{b}}) + G_1^2(|\alpha_3|R_{\mathscr{b}})\Big) - \frac{R_{\mathscr{b}}}{|\alpha_3|}G_0(|\alpha_3|R_{\mathscr{b}})G_1(|\alpha_3|R_{\mathscr{b}})\Big)\right. \\
&\qquad \left. - B_2^2 R_2^2 - B_1^2 J_1^2(|\alpha_1|R_1)R_1^2 + \frac{\sigma_{1,3}B_2 B_1 J_1(|\alpha_1|R_1)R_1}{|\alpha_3|}\right] \qquad \text{(A.73)}
\end{aligned}$$

$$W_{\mathscr{b},\mathscr{B}} = \frac{L\pi}{\mu_0}\left[\frac{B_4^2}{2}\Big(R_{\mathscr{B}}^2 - R_{\mathscr{b}}^2\Big)\right] \qquad \text{(A.74)}$$

A.4 Entirely Non-potential Loop: $\alpha_1 \neq 0$ and $\alpha_2 \neq 0$

A.4.1 Magnetic Field Coefficients

$$B_2 = \frac{\pi|\alpha_2|R_1}{2} B_1\Big(\sigma_{1,2} J_1(|\alpha_1|R_1) Y_0(|\alpha_2|R_1) - J_0(|\alpha_1|R_1) Y_1(|\alpha_2|R_1)\Big) \tag{A.75}$$

$$C_2 = \frac{\pi|\alpha_2|R_1}{2} B_1\Big(J_0(|\alpha_1|R_1) J_1(|\alpha_2|R_1) - \sigma_{1,2} J_1(|\alpha_1|R_1) J_0(|\alpha_2|R_1)\Big) \tag{A.76}$$

$$B_3 = B_2 F_0(|\alpha_2|R_b) \tag{A.77}$$

$$C_3 = B_2 F_1(|\alpha_2|R_b) \tag{A.78}$$

Current Neutralisation Layer

$$B_3 = \frac{\pi|\alpha_3|R_2}{2} B_2\Big(\sigma_{2,3} F_1(|\alpha_2|R_2) Y_0(|\alpha_3|R_2) - F_0(|\alpha_2|R_2) Y_1(|\alpha_3|R_2)\Big) \tag{A.79}$$

$$C_3 = \frac{\pi|\alpha_3|R_2}{2} B_2\Big(F_0(|\alpha_2|R_2) J_1(|\alpha_3|R_2) - \sigma_{2,3} F_1(|\alpha_2|R_2) J_0(|\alpha_3|R_2)\Big) \tag{A.80}$$

$$B_4 = B_3 G_0(|\alpha_3|R_b) \tag{A.81}$$

$$C_4 = 0 \tag{A.82}$$

A.4.2 Axial Flux

$$\psi_{0,1} = \frac{2\pi R_1}{|\alpha_1|} B_1 J_1(|\alpha_1|R_1) \tag{A.83}$$

$$\psi_{1,\mathscr{b}} = \frac{2\pi}{|\alpha_2|}\Big[R_{\mathscr{b}} B_2 F_1(|\alpha_2|R_{\mathscr{b}}) - \sigma_{1,2} R_1 B_1 J_1(|\alpha_1|R_1)\Big] \tag{A.84}$$

$$\psi_{\mathscr{b},\mathcal{B}} = \pi B_2 F_0(|\alpha_2|R_{\mathscr{b}})\Big(R_{\mathcal{B}}^2 - R_{\mathscr{b}}^2\Big) \tag{A.85}$$

Current Neutralisation Layer

$$\psi_{2,\mathscr{b}} = \frac{2\pi B_3}{|\alpha_3|}(R_{\mathscr{b}} G_1(|\alpha_3|R_{\mathscr{b}}) - R_2 G_1(|\alpha_3|R_2)) \tag{A.86}$$

$$\psi_{\mathscr{b},\mathcal{B}} = \pi B_4\Big(R_{\mathcal{B}}^2 - R_{\mathscr{b}}^2\Big) \tag{A.87}$$

A.4.3 Average Magnetic Twist

$$\langle\tilde{\phi}\rangle_{0,1} = \frac{\frac{\sigma_1 L B_1}{|\alpha_1|}\Big[1 - J_0(|\alpha_1|R_1)\Big]}{\frac{R_1 B_1}{|\alpha_1|} J_1(|\alpha_1|R_1)} \tag{A.88}$$

$$\langle\tilde{\phi}\rangle_{1,\mathscr{b}} = \frac{\frac{\sigma_2 L B_2}{|\alpha_2|}\Big[F_0(|\alpha_2|R_1) - F_0(|\alpha_2|R_{\mathscr{b}})\Big]}{\frac{B_2}{|\alpha_2|}\Big[R_{\mathscr{b}} F_1(|\alpha_2|R_{\mathscr{b}}) - R_1 F_1(|\alpha_2|R_1)\Big]} \tag{A.89}$$

$$\langle\tilde{\phi}\rangle_{\mathscr{b},\mathcal{B}} = \frac{\sigma_2 L R_{\mathscr{b}}\Big[B_2 J_1(|\alpha_2|R_{\mathscr{b}}) + C_2 Y_1(|\alpha_2|R_{\mathscr{b}})\Big]\log(R_{\mathcal{B}}/R_{\mathscr{b}})}{\Big[\frac{B_2 F_0(|\alpha_2|R_{\mathscr{b}})}{2}\Big({R_{\mathcal{B}}}^2 - {R_{\mathscr{b}}}^2\Big)\Big]} \tag{A.90}$$

Current Neutralisation Layer

$$\langle\tilde{\phi}\rangle_{2,\mathcal{b}} = \frac{\frac{\sigma_3 L R_2 B_3}{|\alpha_3|}\Big[G_0(|\alpha_3|R_2) - G_0(|\alpha_3|R_{\mathcal{b}})\Big]}{\frac{B_3}{|\alpha_3|}\Big[R_{\mathcal{b}} G_1(|\alpha_3|R_{\mathcal{b}}) - R_2 G_1(|\alpha_3|R_2)\Big]} \tag{A.91}$$

$$\langle\tilde{\phi}\rangle_{\mathcal{b},\mathcal{B}} = \frac{\sigma_3 L B_3 G_1(|\alpha_3|R_{\mathcal{b}}) R_{\mathcal{b}} \log(R_{\mathcal{B}}/R_{\mathcal{b}})}{\frac{1}{2}B_4\Big[R_{\mathcal{B}}^2 - R_{\mathcal{b}}^2\Big]} = 0 \tag{A.92}$$

A.4.4 Helicity

$$K_{0,1} = \sigma_1 \frac{2\pi L B_1^2}{|\alpha_1|}\Bigg(R_1^2\Big(J_0^2(|\alpha_1|R_1) + J_1^2(|\alpha_1|R_1)\Big) - 2\frac{R_1}{|\alpha_1|}J_0(|\alpha_1|R_1)J_1(|\alpha_1|R_1)\Bigg) \tag{A.93}$$

$$\begin{aligned} K_{1,\mathcal{b}} = {} & \sigma_2 \frac{2\pi L B_2^2}{|\alpha_2|}\Bigg(R_{\mathcal{b}}^2\Big(F_0^2(|\alpha_2|R_{\mathcal{b}}) + F_1^2(|\alpha_2|R_{\mathcal{b}})\Big) - 2\frac{R_{\mathcal{b}}}{|\alpha_2|}F_0(|\alpha_2|R_{\mathcal{b}})F_1(|\alpha_2|R_{\mathcal{b}})\Bigg) \\ & - \sigma_2 \frac{2\pi L B_2^2}{|\alpha_2|}\Bigg(R_1^2\Big(F_0^2(|\alpha_2|R_1) + F_1^2(|\alpha_2|R_1)\Big) - 2\frac{R_1}{|\alpha_2|}F_0(|\alpha_2|R_1)F_1(|\alpha_2|R_1)\Bigg) \\ & + \sigma_2 \frac{4\pi L B_2}{|\alpha_2|}\Big(F_0(|\alpha_2|R_1) - F_0(|\alpha_2|R_{\mathcal{b}})\Big)\Bigg[R_1 B_1 J_1(|\alpha_1|R_1)\Bigg(\frac{1}{|\alpha_1|} - \frac{\sigma_{1,2}}{|\alpha_2|}\Bigg)\Bigg] \end{aligned} \tag{A.94}$$

$$K_{\mathcal{b},\mathcal{B}} = 2\sigma_2\Bigg[L C_3 R_{\mathcal{b}}\Bigg(\Big(\psi_{0,2} - \pi B_3 R_{\mathcal{b}}^2\Big)\log(R_{\mathcal{B}}/R_{\mathcal{b}}) + \frac{\pi B_3}{2}\Big(R_{\mathcal{B}}^2 - R_{\mathcal{b}}^2\Big)\Bigg)\Bigg] \tag{A.95}$$

Current Neutralisation Layer

$$\begin{aligned}
K_{2,\mathcal{b}} \;=\;& \sigma_3 \frac{2\pi L B_3^2}{|\alpha_3|}\Big(R_{\mathcal{b}}^2 \Big(G_0^2(|\alpha_3| R_{\mathcal{b}}) + G_1^2(|\alpha_3| R_{\mathcal{b}})\Big) - 2\frac{R_{\mathcal{b}}}{|\alpha_3|} G_0(|\alpha_3| R_{\mathcal{b}}) G_1(|\alpha_3| R_{\mathcal{b}})\Big) \\
& - \sigma_3 \frac{2\pi L B_3^2}{|\alpha_3|}\Big(R_2^2 \Big(G_0^2(|\alpha_3| R_2) + G_1^2(|\alpha_3| R_2)\Big) - 2\frac{R_2}{|\alpha_3|} G_0(|\alpha_3| R_2) G_1(|\alpha_3| R_2)\Big) \\
& + \sigma_3 \frac{4\pi L B_3}{|\alpha_3|}\Big(G_0(|\alpha_3| R_2) - G_0(|\alpha_3| R_{\mathcal{b}})\Big)\Big[R_2 B_2 F_1(|\alpha_2| R_2)\Big(\frac{1}{|\alpha_2|} - \frac{\sigma_{2,3}}{|\alpha_3|}\Big) \\
& \qquad + R_1 B_1 J_1(|\alpha_1| R_1)\Big(\frac{1}{|\alpha_1|} - \frac{\sigma_{1,2}}{|\alpha_2|}\Big)\Big]
\end{aligned} \tag{A.96}$$

$$K_{\mathcal{b},\mathcal{B}} \;=\; \sigma_3 2 L B_3 G_1(|\alpha_3| R_{\mathcal{b}}) R_{\mathcal{b}}\Big[\Big(\psi_{0,3} - \pi B_4 R_{\mathcal{b}}^2\Big)\log(R_{\mathcal{B}}/R_{\mathcal{b}}) + \frac{\pi B_4}{2}\Big(R_{\mathcal{B}}^2 - R_{\mathcal{b}}^2\Big)\Big] \;=\; 0 \tag{A.97}$$

A.4.5 Energy

$$W_{0,1} \;=\; \frac{L\pi B_1^2}{\mu_0}\Big[R_1^2\Big(J_0^2(|\alpha_1| R_1) + J_1^2(|\alpha_1| R_1)\Big) - \frac{R_1}{|\alpha_1|} J_0(|\alpha_1| R_1) J_1(|\alpha_1| R_1)\Big] \tag{A.98}$$

$$\begin{aligned}
W_{1,2} \;=\;& \frac{L\pi B_2^2}{\mu_0}\Big[R_{\mathcal{b}}^2\Big(F_0^2(|\alpha_2| R_{\mathcal{b}}) + F_1^2(|\alpha_2| R_{\mathcal{b}})\Big) - \frac{R_{\mathcal{b}}}{|\alpha_2|} F_0(|\alpha_2| R_{\mathcal{b}}) F_1(|\alpha_2| R_{\mathcal{b}}) \\
& \qquad - R_1^2\Big(F_0^2(|\alpha_2| R_1) + F_1^2(|\alpha_2| R_1)\Big) + \frac{R_1}{|\alpha_2|} F_0(|\alpha_2| R_1) F_1(|\alpha_2| R_1)\Big]
\end{aligned} \tag{A.99}$$

$$W_{\mathcal{b},\mathcal{B}} \;=\; \frac{L\pi}{\mu_0}\Big[\frac{B_3^2}{2}\Big(R_{\mathcal{B}}^2 - R_{\mathcal{b}}^2\Big) + C_3^2 R_{\mathcal{b}}^2 \log(R_{\mathcal{B}}/R_{\mathcal{b}})\Big] \tag{A.100}$$

Current Neutralisation Layer

$$\begin{aligned} W_{2,\mathscr{b}} \;=\; & \frac{L\pi B_3^2}{\mu_0}\Bigg[R_{\mathscr{b}}^2\Big(G_0^2(|\alpha_3|R_{\mathscr{b}}) + G_1^2(|\alpha_3|R_{\mathscr{b}})\Big) - \frac{R_{\mathscr{b}}}{|\alpha_3|}G_0(|\alpha_3|R_{\mathscr{b}})G_1(|\alpha_3|R_{\mathscr{b}}) \\ & - R_2^2\Big(G_0^2(|\alpha_3|R_2) + G_1^2(|\alpha_3|R_2)\Big) + \frac{R_2}{|\alpha_3|}G_0(|\alpha_3|R_2)G_1(|\alpha_3|R_2)\Bigg] \end{aligned} \tag{A.101}$$

$$W_{\mathscr{b},\mathcal{B}} \;=\; \frac{L\pi}{\mu_0}\left[\frac{B_4^2}{2}\Big(R_{\mathcal{B}}^2 - R_{\mathscr{b}}^2\Big)\right] \tag{A.102}$$

Appendix B

Magnetic field profiles for a selection of α-space points

B.1 Net Current

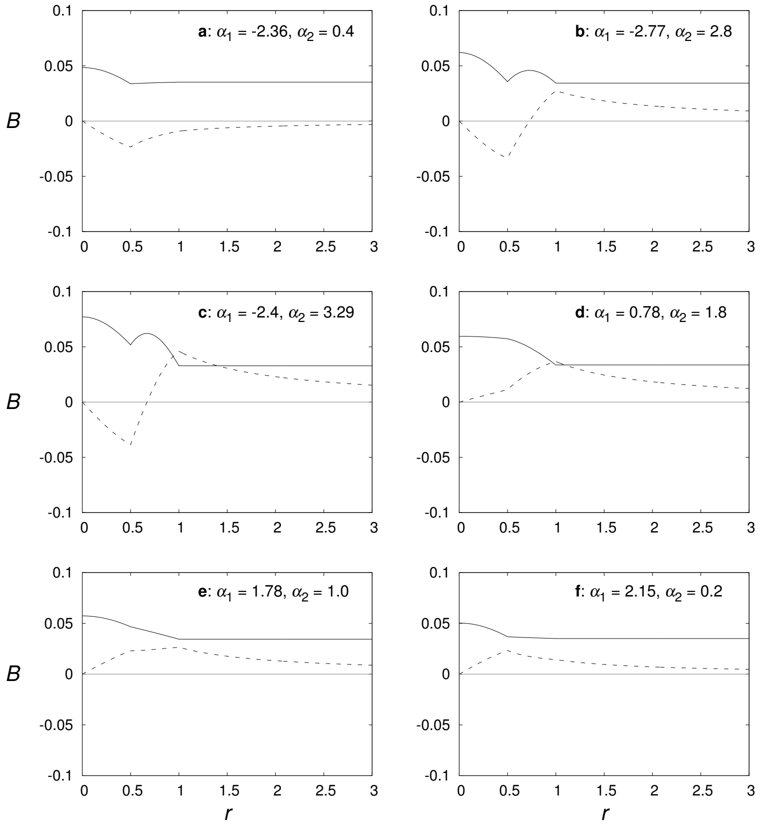

Figure B.1: The magnetic field profiles, B_z (solid) and B_θ (dashed), for the six α-space points identified in the top left plot of Figure 3.4.

B.2 Zero Net Current

The magnetic axial field, $B_z(r)$, azimuthal field, $B_\theta(r)$, and magnetic twist, $\phi(r)$, profiles are presented for a selection of stable and unstable loop configurations, see Figure B.2. The empty circles on the $\alpha_1 = \alpha_2$ line are the relaxed states of the unstable configurations identified by the filled circles on the threshold. Both relaxed states have a radius of 1.5. Figures B.5 and B.6 are arranged such that each threshold profile is immediately to the left of the corresponding relaxed profile. The fields are constructed such that $B_1 = 1$.

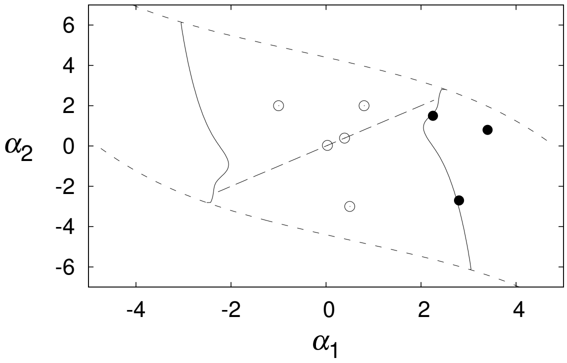

Figure B.2: The stability region for a loop of aspect ratio 20 is demarcated by instability thresholds (solid lines) and B_z reversal lines (short dashed lines). The relaxation line (long dashed) comprises the points within the stability region where $\alpha_1 = \alpha_2$. Stable configurations are indicated by empty circles and unstable ones by filled circles.

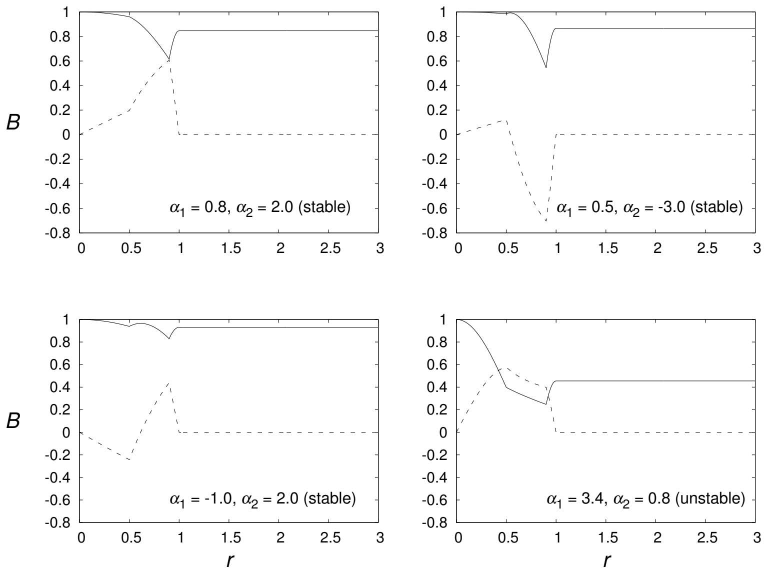

Figure B.3: The B_z (solid) and B_θ (dashed) profiles for some of the configurations (3 stable, 1 unstable) located in Figure B.2.

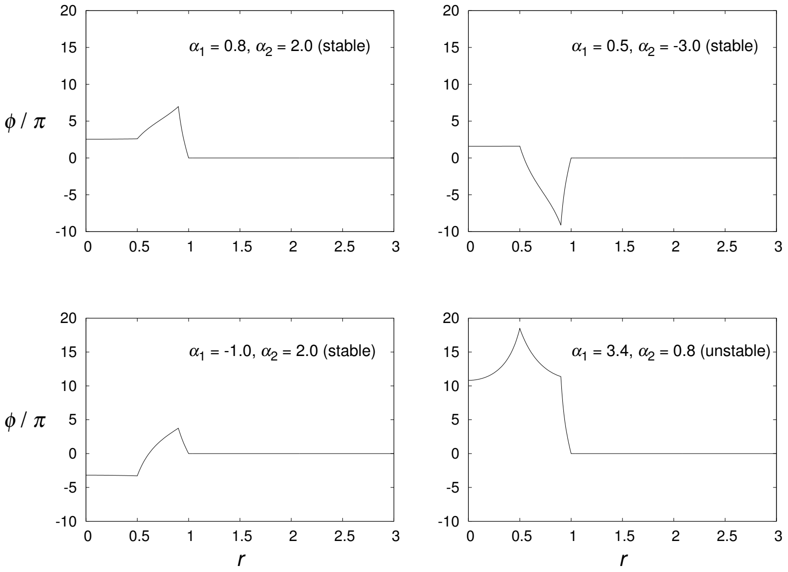

Figure B.4: The magnetic twist profiles for some of the configurations (3 stable, 1 unstable) located in Figure B.2.

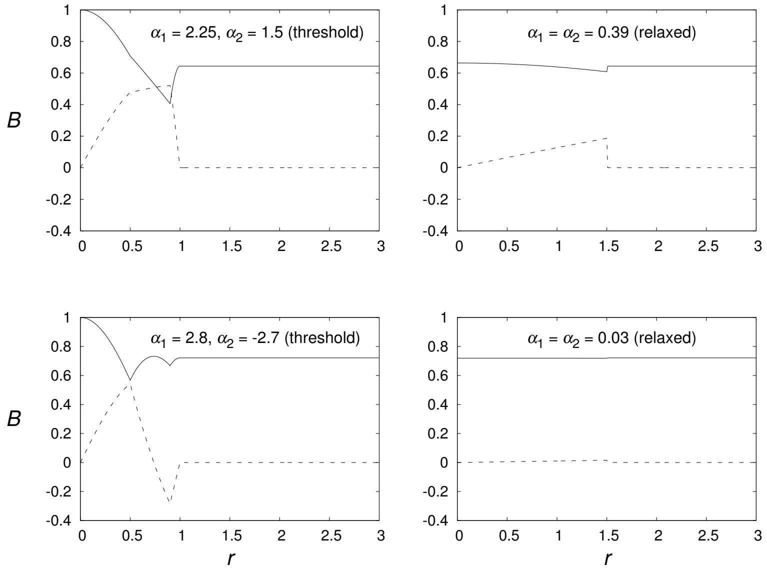

Figure B.5: The B_z (solid) and B_θ (dashed) profiles for the threshold and relaxed configurations located in Figure B.2. For the second relaxed configuration (bottom right), the B_θ profile is just above zero between $r = 0.0$ and $r = 1.5$.

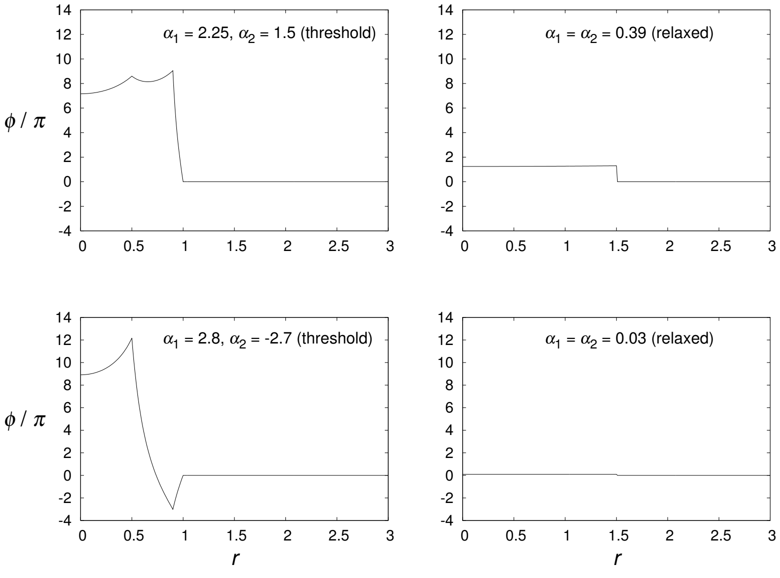

Figure B.6: The magnetic twist profiles for the threshold and relaxed configurations located in Figure B.2.

B.2.1 Relaxation Radius and Energy Release

This subsection shows how the energy release varies with relaxation radius for the loop configurations identified by Figure 4.5, but not directly considered in Chapter 4; namely Loops A, C, D and F. The energy releases have all been calculated according to Relaxation Scenario 2, see Section 4.3.1.

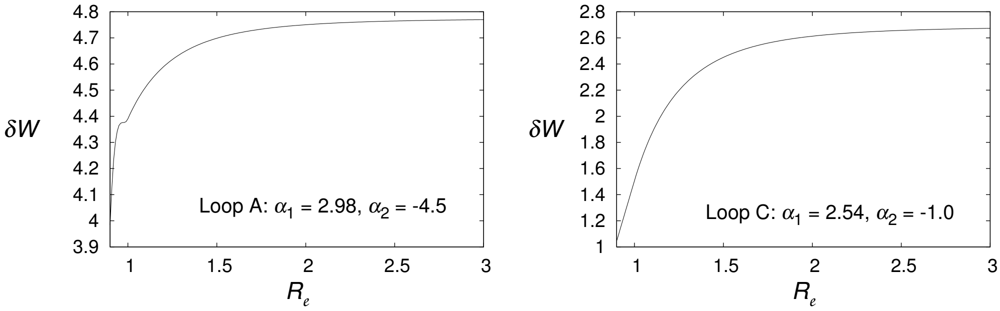

Figure B.7: The variation of energy release (δW) with relaxation radius (R_e) for Loop A (left) and Loop C (right).

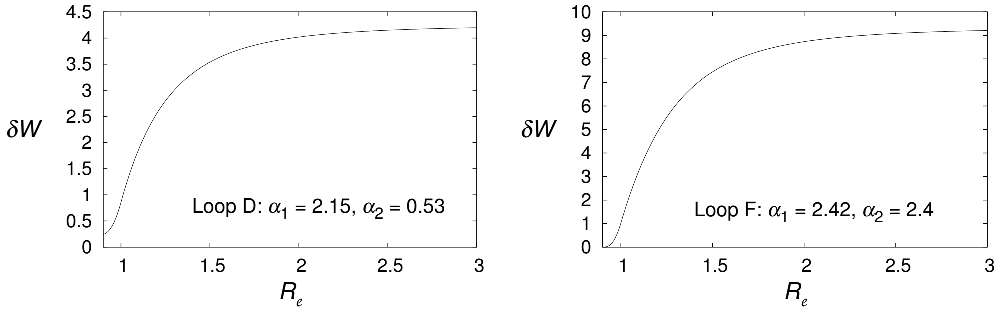

Figure B.8: The variation of energy release (δW) with relaxation radius (R_e) for Loop D (left) and Loop F (right).

Appendix C

Miscellaneous Numerical Results

C.1 Energy

Here are shown the energy plots taken from the loop simulations (high resolution) identified by Figure 4.5, but not directly considered in Chapter 4; namely Loops C, D and F. The results for Loop A are not shown, since this simulation proved to be numerically unstable.

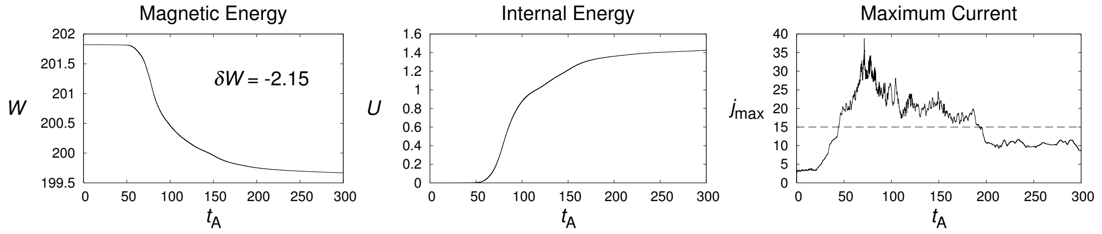

Figure C.1: **Loop C**, the temporal variation of magnetic energy (left column), internal energy (middle column) and the maximum current (right column). The critical current (i.e., the threshold for anomalous resistivity) is indicated by the horizontal dashed line (right column).

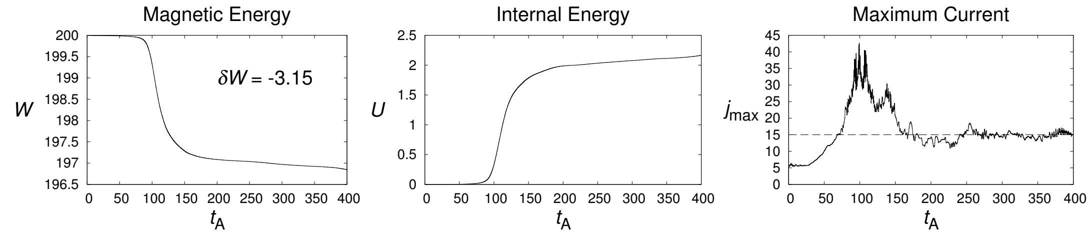

Figure C.2: **Loop D**, the temporal variation of magnetic energy (left column), internal energy (middle column) and the maximum current (right column).

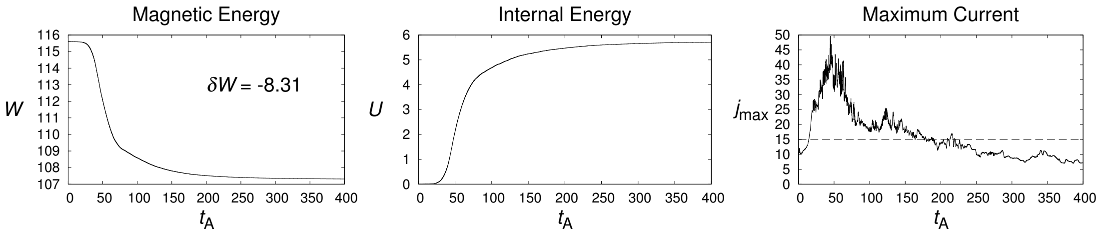

Figure C.3: **Loop F**, the temporal variation of magnetic energy (left column), internal energy (middle column) and the maximum current (right column).

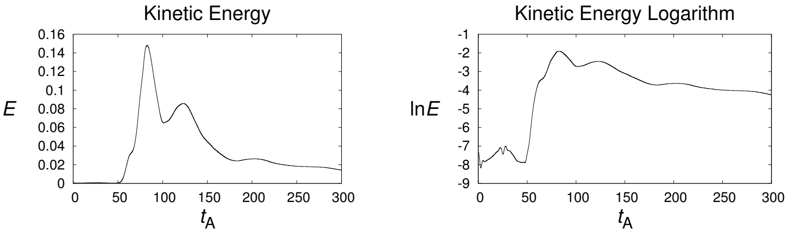

Figure C.4: **Loop C**, the temporal variation of the kinetic energy (left column) and the natural logarithm of kinetic energy (right column).

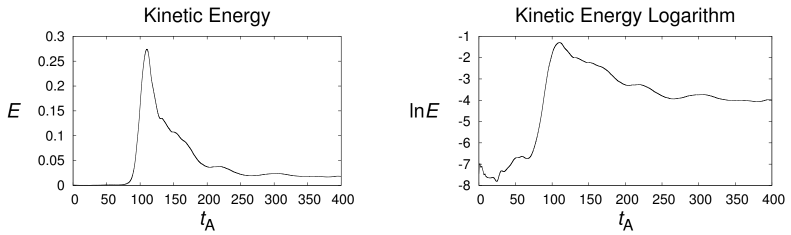

Figure C.5: **Loop D**, the temporal variation of the kinetic energy (left column) and the natural logarithm of kinetic energy (right column).

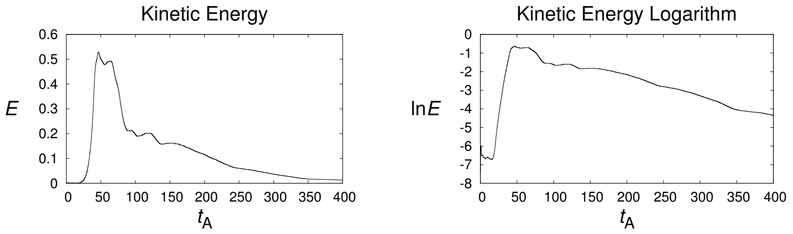

Figure C.6: **Loop F**, the temporal variation of the kinetic energy (left column) and the natural logarithm of kinetic energy (right column).

C.2 Helicity

Table C.1: Helicity at three times during the simulations of Loops C, D and F (Figure 4.5).

Loop	**Initial**	**Instability**	**Final**
C	6.15	6.13 ($t = 75t_A$)	6.15
D	10.54	10.54 ($t = 105t_A$)	10.48
F	12.31	12.03 ($t = 50t_A$)	12.22

C.3 Final Field Profiles with Background Resistivity

Here are shown the final magnetic field profiles (B_x, B_y, B_z) taken from a first-quadrant loop simulation (Section 4.3.2) with a background resistivity of 0.0001. The best-fit analytical plots are also given.

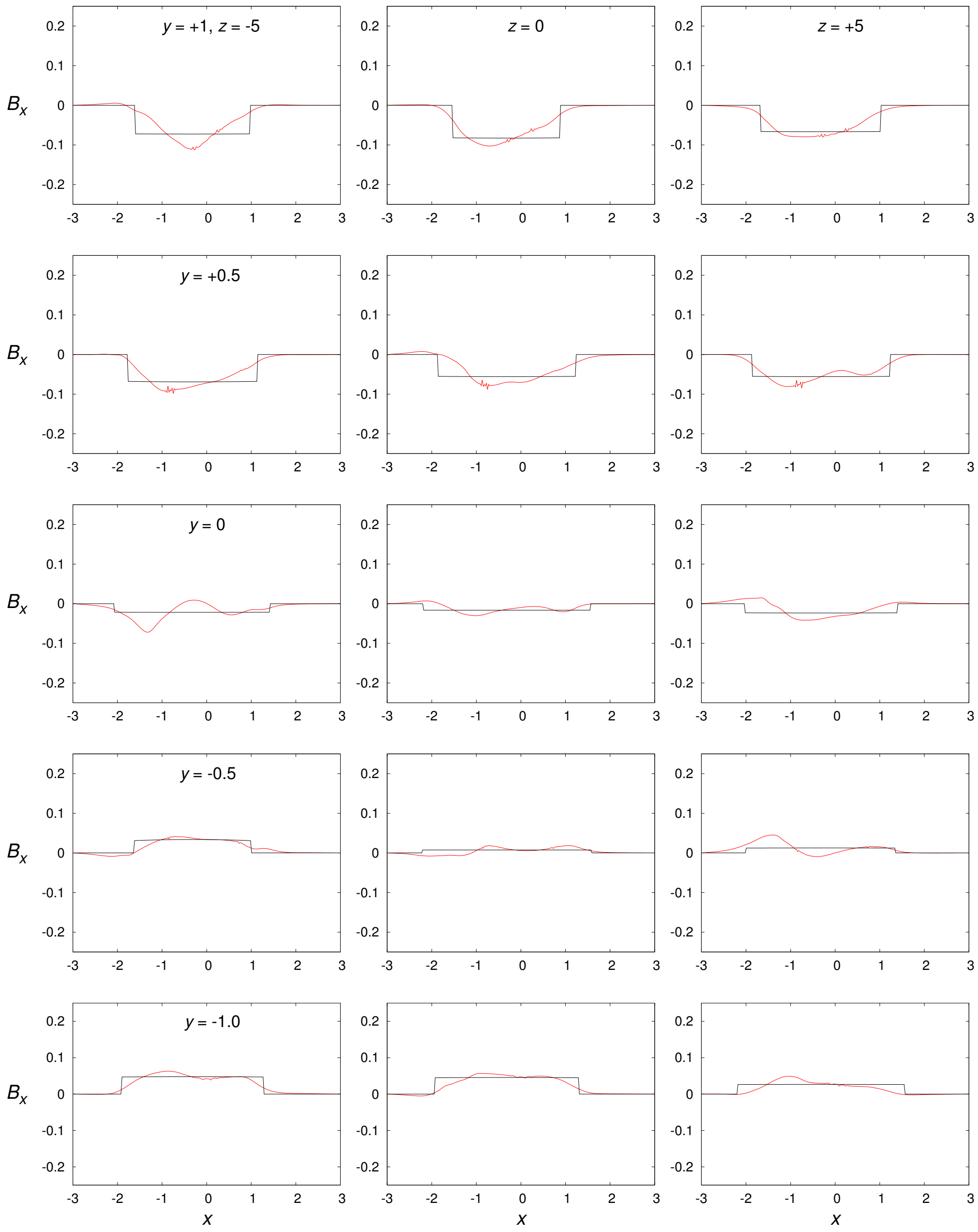

Figure C.7: First-quadrant loop: a comparison between the B_x magnetic field profiles obtained numerically (red line) and analytically (black line). The latter is calculated from the α_e and R_e that best fit the numerical plot, which is taken from the final frame ($t = 400\,t_A$) of the high resolution LARE3D simulation. The comparisons are done for different z coordinates, $z = -5$ (left column), 0 (middle column) and 5 (right column); and for different y coordinates, $y = -1$ (bottom row), -0.5 (one above bottom row), 0 (middle row), 0.5 (one above middle row), and 1 (top row).

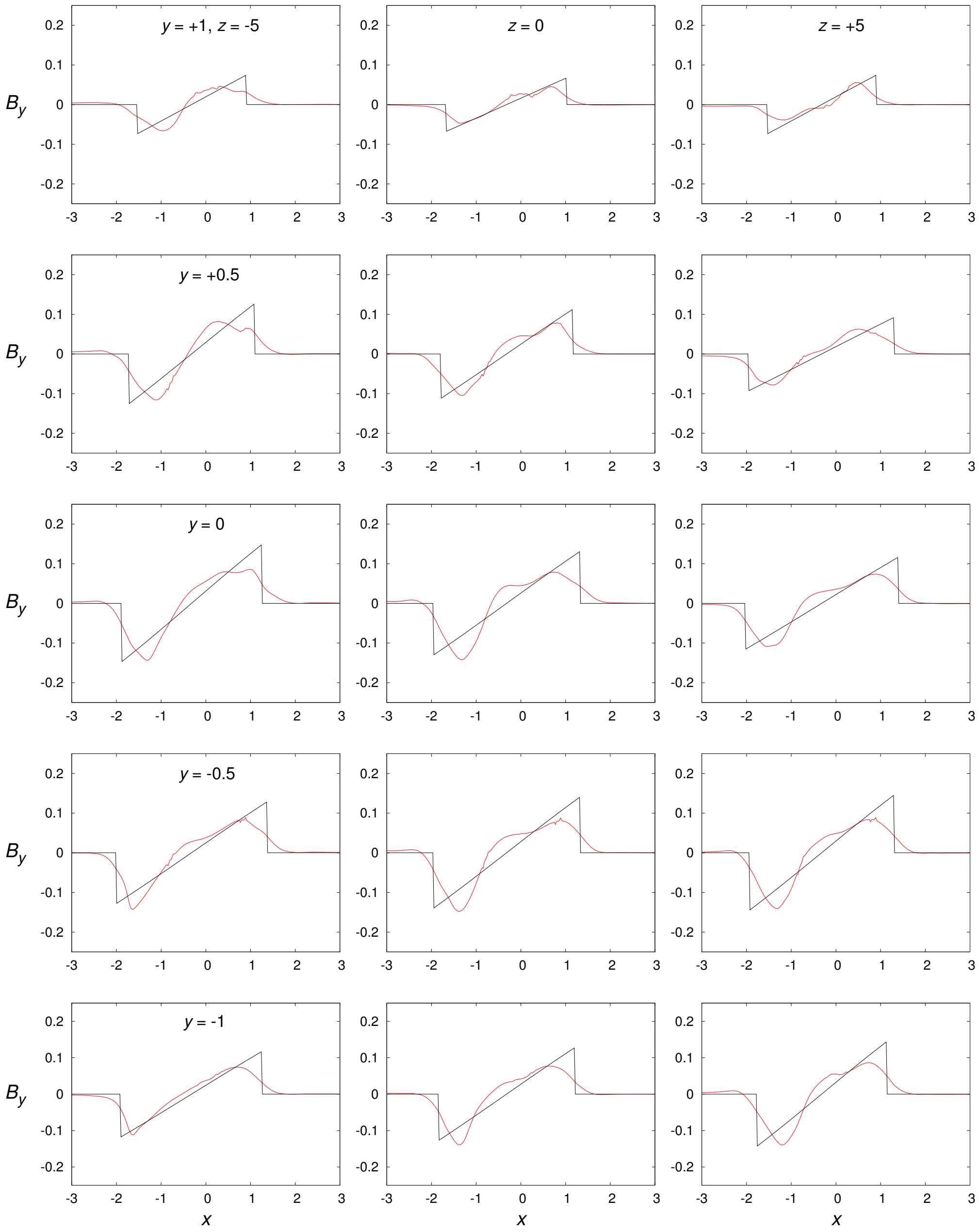

Figure C.8: First-quadrant loop: a comparison between the B_y magnetic field profiles obtained numerically (red line) and analytically (black line). See Figure C.7 for further details.

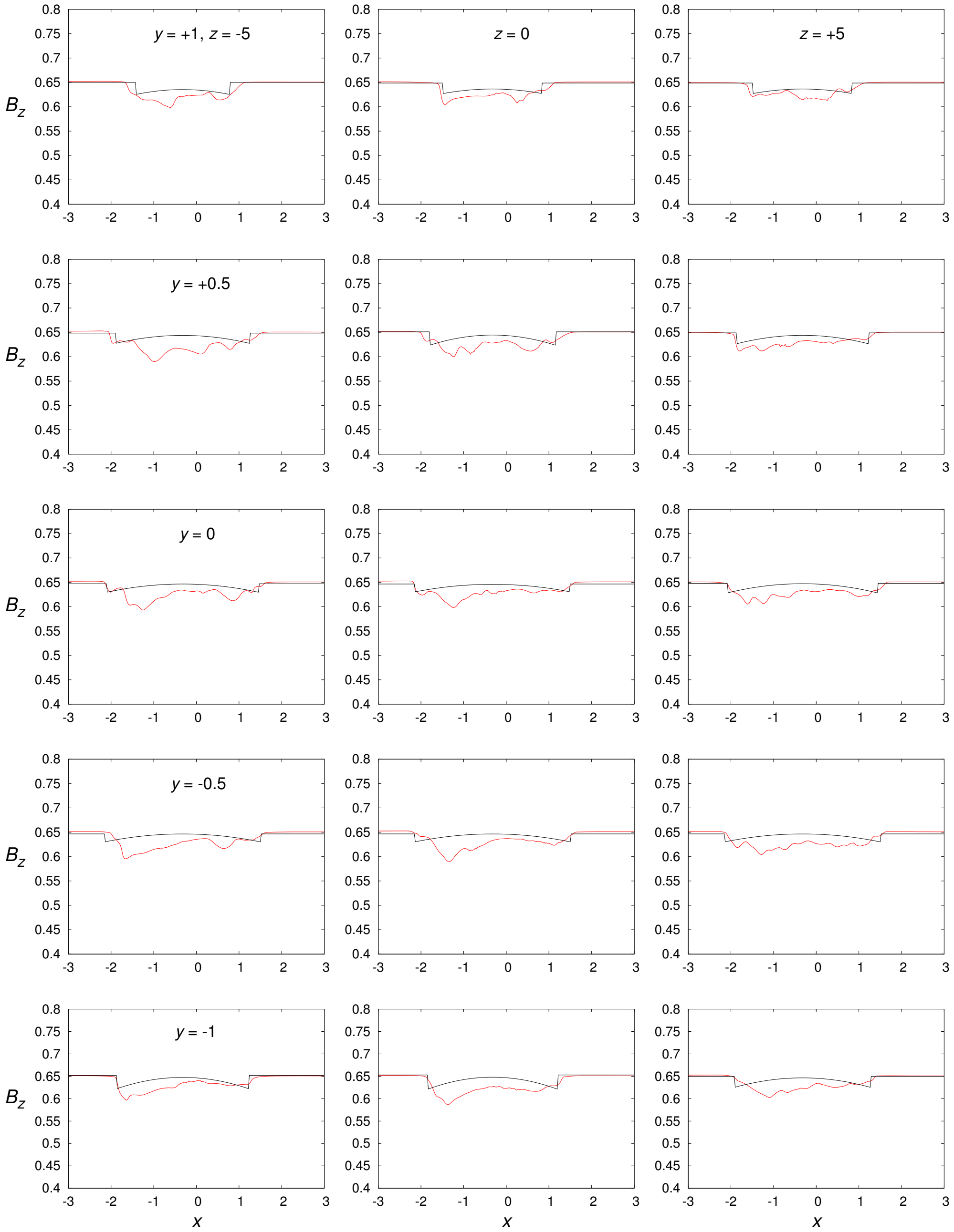

Figure C.9: First-quadrant loop: a comparison between the B_z magnetic field profiles obtained numerically (red line) and analytically (black line). See Figure C.7 for further details.

List of Figures

List of Tables

References

V. I. Abramenko, A. A. Pevtsov, and P. Romano. Coronal Heating and Photospheric Turbulence Parameters: Observational Aspects. *The Astrophysical Journal*, 646 (1):L81–L84, July 2006. ISSN 0004-637X. doi: 10.1086/506592. URL `http://stacks.iop.org/1538-4357/646/i=1/a=L81`.

H. Alfvén. On the Existence of Electromagnetic-Hydrodynamic Waves. *Arkiv for Astronomi*, 29:1–7, 1943.

J. D. Anderson. *Computational Fluid Dynamics*. Springer, 2nd edition, 1996.

P. Antolin, K. Shibata, and G. Vissers. Coronal Rain as a Marker for Coronal Heating Mechanisms. *ApJ*, 716:154–166, June 2010. doi: 10.1088/0004-637X/716/1/154.

T. D. Arber, A. W. Longbottom, and R. A. M. van der Linden. Unstable Coronal Loops: Numerical Simulations with Predicted Observational Signatures. *ApJ*, 517: 990–1001, June 1999. doi: 10.1086/307222.

T. D. Arber, A. W. Longbottom, C. L. Gerrard, and A. M. Milne. A Staggered Grid, Lagrangian-Eulerian Remap Code for 3-D MHD Simulations. *Journal of Computational Physics*, 171:151–181, July 2001. doi: 10.1006/jcph.2001.6780.

M. J. Aschwanden. *Physics of the Solar Corona*. Springer-Praxis Books in Astronomy and Planetary Sciences. Praxis Publishing Ltd, Chichester, UK, 2nd edition, 2009. ISBN 3540307656.

M. J. Aschwanden and L. W. Acton. Temperature Tomography of the Soft X-Ray Corona: Measurements of Electron Densities, Tempuratures, and Differential Emission Measure Distributions above the Limb. *ApJ*, 550:475–492, March 2001. doi: 10.1086/319711.

M. J. Aschwanden, R. W. Nightingale, T. D. Tarbell, and C. J. Wolfson. Time Variability of the "Quiet" Sun Observed with TRACE. I. Instrumental Effects, Event Detection, and Discrimination of Extreme-Ultraviolet Microflares. *ApJ*, 535:1027–

1046, June 2000a. doi: 10.1086/308866.

M. J. Aschwanden, T. D. Tarbell, R. W. Nightingale, C. J. Schrijver, A. Title, C. C. Kankelborg, P. Martens, and H. P. Warren. Time Variability of the "Quiet" Sun Observed with TRACE. II. Physical Parameters, Temperature Evolution, and Energetics of Extreme-Ultraviolet Nanoflares. *ApJ*, 535:1047–1065, June 2000b. doi: 10.1086/308867.

D. Banerjee, E. O'Shea, A. de Groof, and S. Poedts. Active Region Oscillations as Observed by CDS, EIT and TRACE. In H. Lacoste, editor, *SOHO 13 Waves, Oscillations and Small-Scale Transients Events in the Solar Atmosphere: Joint View from SOHO and TRACE*, volume 547 of *ESA Special Publication*, pages 39–+, January 2004.

M. R. Bareford, P. K. Browning, and R. A. M. van der Linden. A nanoflare distribution generated by repeated relaxations triggered by kink instability. *A&A*, 521:A70+, October 2010. doi: 10.1051/0004-6361/201014067.

M. R. Bareford, P. K. Browning, and R. A. M. van der Linden. The Flare-Energy Distributions Generated by Kink-Unstable Ensembles of Zero-Net-Current Coronal Loops. *Sol. Phys.*, 273:93–115, October 2011. doi: 10.1007/s11207-011-9832-4.

H. Baty. Magnetic topology during the reconnection process in a kinked coronal loop. *A&A*, 360:345–350, August 2000.

H. Baty. On the MHD stability of the vec m = 1 kink mode in solar coronal loops. *A&A*, 367:321–325, February 2001. doi: 10.1051/0004-6361:20000412.

H. Baty and J. Heyvaerts. Electric current concentration and kink instability in line-tied coronal loops. *A&A*, 308:935–950, April 1996.

P. M. Bellan. *Fundamentals of Plasma Physics*. Cambridge University Press, Cambridge, UK, 1st edition, 2006. ISBN 0521821169.

M. A. Berger. Generation of coronal magnetic fields by random surface motions. I - Mean square twist and current density. *A&A*, 252:369–376, December 1991.

M. A. Berger. Introduction to magnetic helicity. *Plasma Physics and Controlled Fusion*, 41:167–+, December 1999. doi: 10.1088/0741-3335/41/12B/312.

M. A. Berger and G. B. Field. The topological properties of magnetic helicity. *Journal of Fluid Mechanics*, 147:133–148, October 1984. doi: 10.1017/S0022112084002019.

T. E. Berger and A. M. Title. On the Dynamics of Small-Scale Solar Magnetic Elements. *ApJ*, 463:365–+, May 1996. doi: 10.1086/177250.

J. Birn and E. R. Priest, editors. *Reconnection of Magnetic Fields*. Cambridge University Press, 2007.

G. J. J. Botha, T. D. Arber, and A. W. Hood. Thermal conduction effects on the kink instability in coronal loops. *A&A*, 525:A96+, January 2011. doi: 10.1051/0004-6361/201015534.

S. J. Bradshaw and P. J. Cargill. A New Enthalpy-Based Approach to the Transition Region in an Impulsively Heated Corona. *ApJL*, 710:L39–L43, February 2010. doi: 10.1088/2041-8205/710/1/L39.

J. Braithwaite. The stability of toroidal fields in stars. *A&A*, 453:687–698, July 2006. doi: 10.1051/0004-6361:20041282.

D. Brennan. *Stability Studies of Helicity Injected Spheromaks and Spherical Tokamaks*. PhD thesis, University of Manchester, Manchester, United Kingdom, 2000.

P. K. Browning. Helicity injection and relaxation in a solar-coronal magnetic loop with a free surface. *Journal of Plasma Physics*, 40:263–280, October 1988. doi: 10.1017/S002237780001326X.

P. K. Browning and A. W. Hood. The shape of twisted, line-tied coronal loops. *Sol. Phys.*, 124:271–288, September 1989. doi: 10.1007/BF00156270.

P. K. Browning and R. A. M. Van der Linden. Solar coronal heating by relaxation events. *A&A*, 400:355–367, March 2003. doi: 10.1051/0004-6361:20021887.

P. K. Browning, T. Sakurai, and E. R. Priest. Coronal heating in closely-packed flux tubes - A Taylor-Heyvaerts relaxation theory. *A&A*, 158:217–227, April 1986.

P. K. Browning, C. Gerrard, A. W. Hood, R. Kevis, and R. A. M. van der Linden. Heating the corona by nanoflares: simulations of energy release triggered by a kink instability. *A&A*, 485:837–848, July 2008. doi: 10.1051/0004-6361:20079192.

N. Brynildsen, P. Maltby, T. Fredvik, and O. Kjeldseth-Moe. Oscillations Above the Umbra of Sunspots. In H. Lacoste, editor, *SOHO 13 Waves, Oscillations and Small-Scale Transients Events in the Solar Atmosphere: Joint View from SOHO and TRACE*, volume 547 of *ESA Special Publication*, pages 45–+, January 2004.

J. Christensen-Dalsgaard, W. Däppen, S. V. Ajukov, E. R. Anderson, H. M. Antia, S. Basu, V. A. Baturin, G. Berthomieu, B. Chaboyer, S. M. Chitre, A. N. Cox, P. Demarque, J. Donatowicz, W. A. Dziembowski, M. Gabriel, D. O. Gough, D. B. Guenther, J. A. Guzik, J. W. Harvey, F. Hill, G. Houdek, C. A. Iglesias, A. G.

Kosovichev, J. W. Leibacher, P. Morel, C. R. Proffitt, J. Provost, J. Reiter, Jr. E. J. Rhodes, F. J. Rogers, I. W. Roxburgh, M. J. Thompson, and R. K. Ulrich. The Current State of Solar Modeling. *Science*, 272:1286–1292, May 1996. doi: 10.1126/science.272.5266.1286.

R. B. Dahlburg, J.-H. Liu, J. A. Klimchuk, and G. Nigro. Explosive Instability and Coronal Heating. *ApJ*, 704:1059–1064, October 2009. doi: 10.1088/0004-637X/704/2/1059.

A. de Groof, C. Bastiaensen, D. A. N. Müller, D. Berghmans, and S. Poedts. Detailed comparison of downflows seen both in EIT 30.4 nm and Big Bear Hα movies. *A&A*, 443:319–328, November 2005. doi: 10.1051/0004-6361:20053129.

I. de Moortel. Longitudinal Waves in Coronal Loops. *Space Sci. Rev.*, 149:65–81, December 2009. doi: 10.1007/s11214-009-9526-5.

I. De Moortel, J. Ireland, R. W. Walsh, and A. W. Hood. Longitudinal intensity oscillations in coronal loops observed with TRACE I. Overview of Measured Parameters. *Sol. Phys.*, 209:61–88, September 2002. doi: 10.1023/A:1020956421063.

C. E. DeForest. On the Size of Structures in the Solar Corona. *ApJ*, 661:532–542, May 2007. doi: 10.1086/515561.

C. R. DeVore. Magnetic Helicity Generation by Solar Differential Rotation. *ApJ*, 539:944–953, August 2000. doi: 10.1086/309274.

S. Di Giorgio, F. Reale, and G. Peres. CDS/SoHO multi-line observation of a solar active region: Detection of a hot stable loop and of a cool dynamic loop. *A&A*, 406:323–335, July 2003. doi: 10.1051/0004-6361:20030492.

B. Edlén. Die Deutung der Emissionslinien im Spektrum der Sonnenkorona. Mit 6 Abbildungen. *ZAp*, 22:30–+, 1943.

C. R. Evans and J. F. Hawley. Simulation of magnetohydrodynamic flows - A constrained transport method. *ApJ*, 332:659–677, September 1988. doi: 10.1086/166684.

D. A. Falconer, R. L. Moore, J. G. Porter, and D. H. Hathaway. Network Coronal Bright Points: Coronal Heating Concentrations Found in the Solar Magnetic Network. *ApJ*, 501:386–+, July 1998. doi: 10.1086/305805.

L. Feng, B. Inhester, S. K. Solanki, T. Wiegelmann, B. Podlipnik, R. A. Howard, and J.-P. Wuelser. First Stereoscopic Coronal Loop Reconstructions from STEREO SECCHI Images. *ApJL*, 671:L205–L208, December 2007. doi: 10.1086/525525.

J. M. Finn and T. M. Antonsen. Magnetic helicity: What is it, and what is it good for? *Comments Plasma Phys. Control. Fusion*, 9:111–126, 1985.

L. Fletcher. Ultra-violet footpoints as tracers of coronal magnetic connectivity and restructuring during a solar flare. *A&A*, 493:241–250, January 2009. doi: 10.1051/0004-6361:20077972.

C. L. Gerrard and A. W. Hood. Kink unstable coronal loops: current sheets, current saturation and magnetic reconnection. *Sol. Phys.*, 214:151–169, May 2003.

C. L. Gerrard, T. D. Arber, and A. W. Hood. The triggering of MHD instabilities through photospheric footpoint motions. *A&A*, 387:687–699, May 2002. doi: 10.1051/0004-6361:20020491.

J. P. Goedbloed and S. Poedts. *Principles of Magnetohydrodynamics with Applications to Laboratory and Astrophysical Plasmas*. Cambridge University Press, 2004.

L. Golub and J. M. Pasachoff. *The Solar Corona*. Cambridge University Press, Cambridge, UK, 1st edition, 1997. ISBN 9780521882019.

W. Grotian. Zur Frage der Deutung der Linien im Spektrum der Sonnenkorona. *Naturwissenschaften*, 27:214–214, March 1939. doi: 10.1007/BF01488890.

D. A. Gurnett and A. Bhattacharjee. *Introduction to Plasma Physics: With Space and Laboratory Applications*. Cambridge University Press, 1st edition, 2005.

M. Haynes and T. D. Arber. Observational properties of a kink unstable coronal loop. *A&A*, 467:327–333, May 2007. doi: 10.1051/0004-6361:20066922.

W. W. Heidbrink and T. H. Dang. Magnetic Helicity is Conserved at a Tokamak Sawtooth Crash. *APS Meeting Abstracts*, pages 1095P–+, October 2000.

J. Heyvaerts and E. R. Priest. Coronal heating by phase-mixed shear Alfven waves. *A&A*, 117:220–234, January 1983.

J. Heyvaerts and E. R. Priest. Coronal heating by reconnection in DC current systems - A theory based on Taylor's hypothesis. *A&A*, 137:63–78, August 1984.

A. W. Hood. Instabilities in the solar corona. *Plasma Physics and Controlled Fusion*, 34:411–442, April 1992. doi: 10.1088/0741-3335/34/4/002.

A. W. Hood and E. R. Priest. Kink instability of solar coronal loops as the cause of solar flares. *Sol. Phys.*, 64:303–321, December 1979. doi: 10.1007/BF00151441.

A. W. Hood and E. R. Priest. Critical conditions for magnetic instabilities in force-free coronal loops. *Geophysical and Astrophysical Fluid Dynamics*, 17:297–318, 1981.

doi: 10.1080/03091928108243687.

A. W. Hood, P. K. Browning, and R. A. M. van der Linden. Coronal heating by magnetic reconnection in loops with zero net current. *A&A*, 506:913–925, November 2009. doi: 10.1051/0004-6361/200912285.

H. S. Hudson. Solar flares, microflares, nanoflares, and coronal heating. *Sol. Phys.*, 133:357–369, June 1991. doi: 10.1007/BF00149894.

D. E. Innes, A. Genetelli, R. Attie, and H. E. Potts. Quiet Sun mini-coronal mass ejections activated by supergranular flows. *A&A*, 495:319–323, February 2009. doi: 10.1051/0004-6361:200811011.

Å. M. Janse and B. C. Low. Coronal hydromagnetic implosions. *A&A*, 472:957–965, September 2007. doi: 10.1051/0004-6361:20077532.

H. Ji, S. Terry, M. Yamada, R. Kulsrud, A. Kuritsyn, and Y. Ren. Electromagnetic Fluctuations during Fast Reconnection in a Laboratory Plasma. *Physical Review Letters*, 92(11):115001–+, March 2004. doi: 10.1103/PhysRevLett.92.115001.

J. Jing, P. F. Chen, T. Wiegelmann, Y. Xu, S.-H. Park, and H. Wang. Temporal Evolution of Free Magnetic Energy Associated with Four X-Class Flares. *ApJ*, 696: 84–90, May 2009. doi: 10.1088/0004-637X/696/1/84.

Y. Katsukawa and S. Tsuneta. Small Fluctuation of Coronal X-Ray Intensity and a Signature of Nanoflares. *ApJ*, 557:343–350, August 2001. doi: 10.1086/321636.

Rudolf Kippenhahn. *Discovering the Secrets of the Sun.* John Wiley & Sons Ltd, Chichester, UK, 1st edition, 1994. ISBN 0471943630.

J. A. Klimchuk. Cross-Sectional Properties of Coronal Loops. *Sol. Phys.*, 193:53–75, April 2000.

J. A. Klimchuk. On Solving the Coronal Heating Problem. *Sol. Phys.*, 234:41–77, March 2006. doi: 10.1007/s11207-006-0055-z.

J. A. Klimchuk, S. K. Antiochos, and D. Norton. Twisted Coronal Magnetic Loops. *ApJ*, 542:504–512, October 2000. doi: 10.1086/309527.

R. A. Kopp, G. Poletto, G. Noci, and M. Bruner. Analysis of loop flows observed on 27 March, 1980 by the UVSP instrument during the solar maximum mission. *Sol. Phys.*, 98:91–118, July 1985. doi: 10.1007/BF00177201.

A. G. Kosovichev, J. Schou, P. H. Scherrer, R. S. Bogart, R. I. Bush, J. T. Hoeksema, J. Aloise, L. Bacon, A. Burnette, C. De Forest, P. M. Giles, K. Leibrand, R. Nigam, M. Rubin, K. Scott, S. D. Williams, S. Basu, J. Christensen-Dalsgaard, W. Däppen, Jr. E. J. Rhodes, Jr. T. L. Duvall, R. Howe, M. J. Thompson, D. O. Gough, T. Sekii, J. Toomre, T. D. Tarbell, A. M. Title, D. Mathur, M. Morrison, J. L. R. Saba, C. J. Wolfson, I. Zayer, and P. N. Milford. Internal structure and rotation of the Sun: First results from MDI data. In J. Provost & F.-X. Schmider, editor, *Sounding Solar and Stellar Interiors*, volume 181 of *IAU Symposium*, pages 203–+, 1997.

S. Krucker and A. O. Benz. Energy Distribution of Heating Processes in the Quiet Solar Corona. *ApJL*, 501:L213+, July 1998. doi: 10.1086/311474.

R. Y. Kwon and J. Chae. Magnetic Twist of EUV Coronal Loops Well-traced in TRACE Images: Evidence for Magnetic Reconnection Origin of Coronal Loops? *ApJL*, 677:L141–L144, April 2008. doi: 10.1086/587981.

R. H. Levine. A New Theory of Coronal Heating. *ApJ*, 190:457–466, June 1974. doi: 10.1086/152898.

R. P. Lin, S. Krucker, G. J. Hurford, D. M. Smith, H. S. Hudson, G. D. Holman, R. A. Schwartz, B. R. Dennis, G. H. Share, R. J. Murphy, A. G. Emslie, C. Johns-Krull, and N. Vilmer. RHESSI Observations of Particle Acceleration and Energy Release in an Intense Solar Gamma-Ray Line Flare. *ApJL*, 595:L69–L76, October 2003. doi: 10.1086/378932.

R. Lionello, M. Velli, G. Einaudi, and Z. Mikic. Nonlinear Magnetohydrodynamic Evolution of Line-tied Coronal Loops. *ApJ*, 494:840–+, February 1998. doi: 10.1086/305221.

M. C. López Fuentes, J. A. Klimchuk, and C. H. Mandrini. The Temporal Evolution of Coronal Loops Observed by GOES SXI. *ApJ*, 657:1127–1136, March 2007. doi: 10.1086/510662.

M. C. López Fuentes, P. Démoulin, and J. A. Klimchuk. Are Constant Loop Widths an Artifact of the Background and the Spatial Resolution? *ApJ*, 673:586–597, January 2008. doi: 10.1086/523928.

R. M. Lothian and P. K. Browning. Energy dissipation and helicity in coronal loops of variable cross-section. *Sol. Phys.*, 194:205–227, June 2000.

B. Lyot. The study of the solar corona and prominences without eclipses (George Darwin Lecture, 1939). *MNRAS*, 99:580–+, June 1939.

D. H. Mackay, L. M. Green, and A. van Ballegooijen. Modeling the Dispersal of an Active Region: Quantifying Energy Input into the Corona. *ApJ*, 729:97–+, March 2011. doi: 10.1088/0004-637X/729/2/97.

A. Malanushenko, D. W. Longcope, Y. Fan, and S. E. Gibson. Additive Self-helicity as a Kink Mode Threshold. *ApJ*, 702:580–592, September 2009. doi: 10.1088/0004-637X/702/1/580.

S. W. McIntosh, B. de Pontieu, M. Carlsson, V. Hansteen, P. Boerner, and M. Goossens. Alfvénic waves with sufficient energy to power the quiet solar corona and fast solar wind. *Nature*, 475:477–480, July 2011. doi: 10.1038/nature10235.

D. B. Melrose, J. Nicholls, and N. G. Broderick. Surface currents on models of force-free solar magnetic flux tubes. *Journal of Plasma Physics*, 51:163–176, February 1994. doi: 10.1017/S0022377800017451.

Z. Mikic, D. D. Schnack, and G. van Hoven. Dynamical evolution of twisted magnetic flux tubes. I - Equilibrium and linear stability. *ApJ*, 361:690–700, October 1990. doi: 10.1086/169232.

D. J. Mullan. *Physics of the Sun*. CRC Series in Pure and Applied Physics. CRC Press, Boca Raton, Florida, US, 1st edition, 2010. ISBN 9781420083071.

R. Muller, T. Roudier, J. Vigneau, and H. Auffret. The proper motion of network bright points and the heating of the solar corona. *A&A*, 283:232–240, March 1994.

V. M. Nakariakov and E. Verwichte. Coronal Waves and Oscillations. *Living Reviews in Solar Physics*, 2:3–+, July 2005.

D. Nandy, M. Hahn, R. C. Canfield, and D. W. Longcope. Detection of a Taylor-like Plasma Relaxation Process in the Sun. *ApJL*, 597:L73–L76, November 2003. doi: 10.1086/379815.

U. Narain and P. Ulmschneider. Chromospheric and Coronal Heating Mechanisms II. *Space Sci. Rev.*, 75:453–509, February 1996. doi: 10.1007/BF00833341.

J. B. Noglik, R. W. Walsh, and J. Cirtain. Comparison of High-Resolution TRACE Data to Spectroscopic CDS Data for Temperature Determination. *ApJ*, 674:1191–1200, February 2008. doi: 10.1086/525012.

E. N. Parker. Nanoflares and the solar X-ray corona. *ApJ*, 330:474–479, July 1988. doi: 10.1086/166485.

E. N. Parker. Heating solar coronal holes. *ApJ*, 372:719–727, May 1991. doi: 10.1086/170015.

C. E. Parnell. The Role of Dynamic Brightenings in Coronal Heating. In R. W. Walsh, J. Ireland, D. Danesy, & B. Fleck, editor, *SOHO 15 Coronal Heating*, volume 575 of *ESA Special Publication*, pages 227–+, December 2004.

C. E. Parnell. 3D magnetic reconnection, flares and coronal heating. *Mem. Soc. Astron. Italiana*, 78:229–+, 2007.

C. E. Parnell and P. E. Jupp. Statistical Analysis of the Energy Distribution of Nanoflares in the Quiet Sun. *ApJ*, 529:554–569, January 2000. doi: 10.1086/308271.

C. E. Parnell, A. L. Haynes, and K. Galsgaard. Structure of magnetic separators and separator reconnection. *Journal of Geophysical Research (Space Physics)*, 115: A02102, February 2010. doi: 10.1029/2009JA014557.

S. Patsourakos and J. A. Klimchuk. The Cross-Field Thermal Structure of Coronal Loops from Triple-Filter TRACE Observations. *ApJ*, 667:591–601, September 2007. doi: 10.1086/520713.

H. E. Petschek. *Magnetic field annihilation, in The Physics of Solar Flares*. NASA SP-50, 1964.

J. E. Plowman, C. C. Kankelborg, and D. W. Longcope. Coronal Loop Expansion Properties Explained Using Separators. *ApJ*, 706:108–112, November 2009. doi: 10.1088/0004-637X/706/1/108.

F. Portier-Fozzani, M. Aschwanden, P. Démoulin, W. Neupert, J.-P. Delaboudinière, and the EIT Team. Measurement of coronal magnetic twists during loop emergence of NOAA 8069. *Sol. Phys.*, 203:289–308, November 2001. doi: 10.1023/A:1013329626327.

E. R. Priest. *Solar Magnetohydrodynamics*, volume 21 of *Geophysics and Astrophysics Monographs*. D. Reidel Publishing Company, P.O. Box 17, 3300 AA Dordrecht, Holland, The Netherlands, 3rd edition, 1987. ISBN 902771374X.

E. R. Priest and T. G. Forbes. *Magnetic Reconnection MHD Theory and Applications*. Cambridge University Press, 2000.

E. R. Priest and V. S. Titov. Magnetic Reconnection at Three-Dimensional Null Points. *Royal Society of London Proceedings Series A*, 354:2951–2992, December 1996.

E. R. Priest, D. W. Longcope, and J. Heyvaerts. Coronal Heating at Separators and Separatrices. *ApJ*, 624:1057–1071, May 2005. doi: 10.1086/429312.

J. Qiu. Observational Analysis of Magnetic Reconnection Sequence. *ApJ*, 692:1110–1124, February 2009. doi: 10.1088/0004-637X/692/2/1110.

M. A. Raadu. Suppression of the Kink Instability for Magnetic Flux Ropes in the Chromosphere. *Sol. Phys.*, 22:425–433, February 1972. doi: 10.1007/BF00148707.

F. Reale. Coronal Loops: Observations and Modeling of Confined Plasma. *Living Reviews in Solar Physics*, 7:5–+, November 2010.

F. Reale, S. Parenti, K. K. Reeves, M. Weber, M. G. Bobra, M. Barbera, R. Kano, N. Narukage, M. Shimojo, T. Sakao, G. Peres, and L. Golub. Fine Thermal Structure of a Coronal Active Region. *Science*, 318:1582–, December 2007. doi: 10.1126/science.1146590.

S. Régnier and E. R. Priest. Nonlinear force-free models for the solar corona. I. Two active regions with very different structure. *A&A*, 468:701–709, June 2007. doi: 10.1051/0004-6361:20077318.

J. A. Robertson, A. W. Hood, and R. M. Lothian. The evolution of twisted coronal loops. *Sol. Phys.*, 137:273–292, February 1992. doi: 10.1007/BF00161850.

J. Sánchez Almeida and M. Martínez González. The Magnetic Fields of the Quiet Sun. In J. R. Kuhn, D. M. Harrington, H. Lin, S. V. Berdyugina, J. Trujillo-Bueno, S. L. Keil, & T. Rimmele, editor, *Astronomical Society of the Pacific Conference Series*, volume 437 of *Astronomical Society of the Pacific Conference Series*, pages 451–+, April 2011.

A. W. Sandman, M. J. Aschwanden, M. L. Derosa, J. P. Wülser, and D. Alexander. Comparison of STEREO/EUVI Loops with Potential Magnetic Field Models. *Sol. Phys.*, 259:1–11, October 2009. doi: 10.1007/s11207-009-9383-0.

J. T. Schmelz, K. Nasraoui, V. L. Richardson, P. J. Hubbard, C. R. Nevels, and J. E. Beene. All Coronal Loops Are the Same: Evidence to the Contrary. *ApJL*, 627: L81–L84, July 2005. doi: 10.1086/431950.

C. J. Schrijver. Catastrophic cooling and high-speed downflow in quiescent solar coronal loops observed with TRACE. *Sol. Phys.*, 198:325–345, February 2001. doi: 10.1023/A:1005211925515.

C. L. Selhorst, A. Silva-Válio, and J. E. R. Costa. Solar atmospheric model over a highly polarized 17 GHz active region. *A&A*, 488:1079–1084, September 2008. doi: 10.1051/0004-6361:20079217.

A. K. Srivastava, T. V. Zaqarashvili, P. Kumar, and M. L. Khodachenko. Observation of Kink Instability During Small B5.0 Solar Flare on 2007 June 4. *ApJ*, 715:292–299, May 2010. doi: 10.1088/0004-637X/715/1/292.

P. A. Sturrock and Y. Uchida. Coronal heating by stochastic magnetic pumping. *ApJ*, 246:331–336, May 1981. doi: 10.1086/158926.

Z. Svestka, B. V. Jackson, and M. E. Machado, editors. *Eruptive Solar Flares*, volume 399 of *Lecture Notes in Physics, Berlin Springer Verlag*, 1992.

J. B. Taylor. Relaxation of Toroidal Plasma and Generation of Reverse Magnetic Fields. *Physical Review Letters*, 33:1139–1141, November 1974. doi: 10.1103/PhysRevLett.33.1139.

J. B. Taylor. Relaxation and magnetic reconnection in plasmas. *Reviews of Modern Physics*, 58:741–763, July 1986. doi: 10.1103/RevModPhys.58.741.

S. Terzo, F. Reale, M. Miceli, J. A. Klimchuk, and R. Kano S. Tsuneta. WIDESPREAD NANOFLARE VARIABILITY DETECTED WITH HINODE/X-RAY TELESCOPE IN A SOLAR ACTIVE REGION. *ApJ*, 736, July 2011. doi: 10.1088/0004-637X/736/2/111.

Y. T. Tsap, Y. G. Kopylova, A. V. Stepanov, V. F. Melnikov, and K. Shibasaki. Ballooning Instability in Coronal Flare Loops. *Sol. Phys.*, 253:161–172, December 2008. doi: 10.1007/s11207-008-9199-3.

D. Utz, A. Hanslmeier, R. Muller, A. Veronig, J. Rybák, and H. Muthsam. Dynamics of isolated magnetic bright points derived from Hinode/SOT G-band observations. *A&A*, 511:A39+, February 2010. doi: 10.1051/0004-6361/200913085.

D. A. Uzdensky. The Fast Collisionless Reconnection Condition and the Self-Organization of Solar Coronal Heating. *ApJ*, 671:2139–2153, December 2007. doi: 10.1086/522915.

R. A. M. Van der Linden. *The thermal instability in the solar corona: a mechanism for the formation of cool condensations (prominences)*. PhD thesis, Katholieke Universiteit, Leuven, Belgium, 1991.

R. A. M. Van der Linden and A. W. Hood. A complete coronal loop stability analysis in ideal magnetohydrodynamics. II. Force-free cylindrical equilibria. *A&A*, 346:303–312, June 1999.

B. van Leer. Towards the ultimate conservative difference scheme. V - A second-order sequel to Godunov's method. *Journal of Computational Physics*, 32:101–136, July 1979. doi: 10.1016/0021-9991(79)90145-1.

G. Vekstein. Probing nanoflares with observed fluctuations of the coronal EUV emission. *A&A*, 499:L5–L8, May 2009. doi: 10.1051/0004-6361/200911872.

G. Vekstein and Y. Katsukawa. Scaling Laws for a Nanoflare-Heated Solar Corona. *ApJ*, 541:1096–1103, October 2000. doi: 10.1086/309480.

G. E. Vekstein and R. Jain. Signatures of a nanoflare heated solar corona. *Plasma Physics and Controlled Fusion*, 45:535–545, May 2003. doi: 10.1088/0741-3335/45/5/302.

G. E. Vekstein, E. R. Priest, and C. D. C. Steele. On the Problem of Magnetic Coronal Heating by Turbulent Relaxation. *ApJ*, 417:781–+, November 1993. doi: 10.1086/173358.

M. Velli, A. W. Hood, and G. Einaudi. Ideal kink instabilities in line-tied coronal loops - Growth rates and geometrical properties. *ApJ*, 350:428–436, February 1990. doi: 10.1086/168397.

M. Velli, R. Lionello, and G. Einaudi. Kink Modes and Current Sheets in Coronal Loops. *Sol. Phys.*, 172:257–266, May 1997.

N. Viall and J. Klimchuk. Patterns of Nanoflare Heating Exhibited by Active Regions Observed with SDO/AIA. In *AAS/Solar Physics Division Abstracts #42*, pages 2103–+, May 2011.

H. P. Warren, A. R. Winebarger, and D. H. Brooks. Evidence for Steady Heating: Observations of an Active Region Core with Hinode and TRACE. *ApJ*, 711:228–238, March 2010. doi: 10.1088/0004-637X/711/1/228.

M. S. Wheatland. Do Solar Flares Exhibit an Interval-size Relationship? *Sol. Phys.*, 191:381–389, February 2000.

M. L. Wilkins. Use of artificial viscosity in multidimensional fluid dynamic calculations. *Journal of Computational Physics*, 36:281–303, July 1980. doi: 10.1016/0021-9991(80)90161-8.

G. L. Withbroe and R. W. Noyes. Mass and energy flow in the solar chromosphere and corona. *ARA&A*, 15:363–387, 1977. doi: 10.1146/annurev.aa.15.090177.002051.

M. Yamada. Review of controlled laboratory experiments on physics of magnetic reconnection. *J. Geophys. Res.*, 104:14529–14542, July 1999. doi: 10.1029/1998JA900169.

M. Yamada, R. Kulsrud, and H. Ji. Magnetic reconnection. *Reviews of Modern Physics*, 82:603–664, January 2010. doi: 10.1103/RevModPhys.82.603.

A. R. Yeates, G. Hornig, and A. L. Wilmot-Smith. Topological Constraints on Magnetic Relaxation. *Physical Review Letters*, 105(8):085002–+, August 2010. doi: 10.1103/PhysRevLett.105.085002.

M. Zhang and B. C. Low. Magnetic Flux Emergence into the Solar Corona. III. The

Role of Magnetic Helicity Conservation. *ApJ*, 584:479–496, February 2003. doi: 10.1086/345615.

J. B. Zirker and F. M. Cleveland. Nanoflare mechanisms - Twisting and braiding. *Sol. Phys.*, 144:341–347, April 1993. doi: 10.1007/BF00627598.

E. G. Zweibel and A. H. Boozer. Evolution of twisted magnetic fields. *ApJ*, 295: 642–647, August 1985. doi: 10.1086/163407.

E. G. Zweibel and M. Yamada. Magnetic Reconnection in Astrophysical and Laboratory Plasmas. *ARA&A*, 47:291–332, September 2009. doi: 10.1146/annurev-astro-082708-101726.